CHARGE TRANSFER DYNAMICS IN BRIDGED DONOR-ACCEPTOR MOLECULAR ASSEMBLIES

ABDELMENEIM EL-DALI


CENTRE FOR NFLD. STUDIES
MEMORIAL UNIVERSITY
OF NEWFOUNDLAND

Charge Transfer Dynamics in Bridged Donor-Acceptor Molecular Assemblies

by

Abdelmeneim El-Dali

(B.Sc., M.Sc.) University of Garyounis,
Benghazi, Libya

Submitted to the Department of Chemistry in Partial Fulfillment of the

Requirements for the Degree of

Doctor of Philosophy

at the

Memorial University of Newfoundland
St. John's, Newfoundland and Labrador, Canada

January 7, 2011

Dedication

To my parents
To my brothers and sisters
To my wife
To my children Bilgase, Osaid, Abdulla and...

Abstract

The metabolic processes inherent to life on earth are driven by chemical transformations that are too numerous to count. Important classes of reactions involve the transfer of charge, i.e. electron transfer and proton transfer as well as group transfer reactions. The recent X-ray crystal structure reveled that proton coupled electron transfer reactivity plays crucial rule in the photosynthetic apparatus. The theory to describe proton coupled electron transfer is not as evolved to that which described electron transfer. There exist a number of unresolved issues. The primary goal of this work was to understand at a very fundamental level, the molecular properties that dictate chemical reactivity so as to quantify the important factors which influence the charge transfer excited-state dynamics. In this work, we have applied a variety of different techniques to study the properties and the mechanism of ground state and excited state intermolecular and intramolecular proton transfer and charge transfer in chromosphere assemblies.

The bbim system was studied to outline fundamental investigation with respect to the excited state intramolecular proton transfer. The ground state potential energy surface was characterized by temperature dependent ^{1}H NMR to establish the energetics of the enol / keto inter-conversion in the ground state. Analysis of the temperature dependent ^{1}H NMR yielded $\Delta H^{\ddagger} = 27\ kJmol^{-1}$, $\Delta S^{\ddagger} = -133\ JK^{-1}mol^{-1}$. Upon excitation, bbim is a dual emitter with high energy emission band at 427 nm and 550 nm respectively. The intensity of transitions was found to be solvent dependent. Addition of D_2O resulted in dramatic changes in the intensity and energetics of emission spectrum envelope. The emission spectra were subjected to a Franck-Condon line shape analysis and provide

structural and electronic of the excited states.

The photophysical properties of bbim were dependent on the electrolyte. Dramatic changes in the absorption and emission spectra were observed with [NBu$_4$]F and [NBu$_4$]OH. Titration experiment with a number of $[N(Bu)_4]X$, where X is fluoride (F^-), chloride (Cl^-), bromide (Br^-), iodide (I^-), acetate (Ac^-), hydrogen sulphate ($HSO_4{}^-$), hexafluorophosphate ($PF_6{}^-$). The equilibrium constants were valuated using singular value decomposition, or global analysis. The analysis suggests a complex equilibrium consisting of eight distinct species in the ground stat. For the excited state bbim a similar analysis describe above yielded six step equilibra. The potential application of bbim as a anion sensor which can discriminate the anion however this compound are air sensitive when excited in present of air.

A second distinct study was focused on the 3-aminocoumarin (3-AC). The emission spectral fitting results were consistent with a small change in the structural in the ground and excited state. This study was first to use emission spectral fitting as a tool to probe the excited state and was consistent with expectation of the energy gap law was obeyed. At the present time more experiments are required to understand the position of substituent and the nature of emitting state. The data suggests the intervention of a ICT and TICT state in excited state decay. DFT calculations were carried out to understand the electronic structure in the ground state.

Acknowledgment

Above all, I give my thanks to Allah, who has inspired me all through my life. Next, I offer thanks to the people who have helped me along the way to make this thesis possible.

First of all, I would like to thank to my supervisor, Dr. David Thompson, for his guidance of this work throughout the past six years. My second and deep sense of gratitude must go to the members of my thesis committee, Prof. Robert Davis, and Prof. Erika Merschrod for their carful reviewing of my thesis. I could not have completed this thesis without their constant support.

I would like to show my gratitude to Dr. Csaba Szakacs, Shaheen Fatima and Dr. Javier Concepcion (The University of North Carolina, Chapel Hill) for theoretical calculations. Also I wish to thank Ms. L. Winsor for HPLC and MS spectra and Dr. Louise Dawe for providing the crystal structure of the bbim molecule. I would like to acknowledge Dr. Paris Georghiou who has done collaborative work with me.

The kindest appreciation is to the financial support from the Libyan government for the scholarship, and big thanks to Memorial University, for their help and support.

I'd also like to thank Dr. Peter Pickup, Dr. Hongchao Li and Dr. Graham Bodwell's group as well as Jamie Kendall and Amit Kudale for providing bbim and coumarins samples with excellent quality. Thanks should also go to the other members of the Thompson research group for the exchange of ideas and lab equipment.

Finally, and most importantly, I would like to express my deepest gratitude for the continuous support and encouragement that I received from my wife Karima, my lovely

kids Bilgase, Osaid and Abdulla, my parents, brothers and sisters in Libya. I have to admit that I cannot forget to thank my friends who have helped even with as little as kind word throughout my working time.

Abdelmeneim El-Dali

January 2011

Contents

Table of Contents

List of Schemes xxix

A	Electron acceptor
A_{std}	Standard absorbance at the excitation wavelength
A_{un}	Sample absorbance at the excitation wavelength
bbim	2,5-Bis(benzimidazoly)-1,4-dihydroxybenzene
C	Chromophore
CT	Charge transfer
D	Electron donor
d	Electron-transfer distance between the electron donor and acceptor
DFT	Density functional theory
DMF	Dimethylformamide
DMSO	Dimethyl sulfoxide
D_{op}	Optical dielectric constants
D_s	Static dielectric constants
EDG	Electron-donating groups
ESIPT	Excited state intramolecular proton transfer
ESPT	Excited state proton transfer
E_{ss}	Stokes shift between the absorbing and emitting states
E_LT	Electron transfer
ET	Energy transfer
EWG	Electron-withdrawing group
E_0	Energy gap

$E^o(D^+/D)$	Oxidation potential energy of the donor
$E^o(A/A^-)$	Reduction potential energy of the acceptor
E_{oo}	Electronic excitation energy to the lowest vibrational state
$FCWD$	Franck-Condon weighted density of states
[F(calc)]	Franck-Condon factors
fs	Femtosecond
f_{osc}	Oscillator strength
HBI	2-(2′-hydroxyphenyl)benzimidazole
HF	Hartree-Fock
HPLC	High-performance liquid chromatography
H_{DA}	Electronic coupling element
H_{el}	Born-Oppenheimer Hamiltonian for the system
ICT	Intramolecular charge transfer
IRF	Instrument response function
ISC	Intersystem crossing
I_o	Fluorescence intensity at the $time = 0$
I_{std}	Standard integrated emission intensities
I_{un}	Sample integrated emission intensities
K	Equilibrium constant
k_B	Boltzmann Constant
k_{ET}	Electron transfer rate constant
κ_{el}	Electronic factor

k_c	Rates of the dynamic chemical exchange
k_{isc}	Rate constants for intersystem crossing
k_{nr}	Rate constants for non-radiative decay
k_{obs}	Observed rate constant of electron transfer
k_r	Rate constants for radiative
MeCN	Acetonitrile
ns	Nanosecond
n_{std}	Refractive indices of standard
n_{un}	Refractive indices of sample
PET	Photoinduced electron transfer
PMT	Photomultiplier tube
PPT	Photoinduced proton transfer
ps	Picosecond
PSII	Photosystem II
PT	Proton transfer
r_A	Radius for the acceptor
r_D	Radius for the donor
r_{DA}	Separation distance between the donor and the acceptor
S	Electron vibration coupling constant
SOC	Spin-orbit coupling
SVD	Singular value decomposition
T	Absolute temperature

TD-DFT	Time dependent density functional theory
THF	Tetrahydrofuran
TICT	Twisted intramolecular charge transfer
TMS	Tetramethylsilane
TS	Transition state
T_c	Coalescence temperature
2-NpOH	2-Naphthol
3-AC	3-aminocoumarin
Ψ_P^o	Electron wavefunctions of the product
Ψ_R^o	Electron wavefunctions of the reactant
λ_0	Solvent reorganization energy
λ_i	Intramolecular (vibrational) reorganization energy
ν_{ET}	Frequency factor for electron transfer
χ^2	Chi square
ϕ_{em}	Fluorescence quantum yields
$\Delta G^{\ddagger}$	Free energy of activation
ΔG^o	Gibbs free energy
ΔG°	Free energy change
ΔOD	Optical density change
Δq	Difference in the equilibrium bond lengths in the reactant and product
$\Delta \nu$	Half linewidths of the resonance frequency
$\Delta \vec{\mu}$	Change in dipole moment

$\Delta\bar{\nu}_{1/2}$	Full width at half-maximum
Δf	Mataga parameter
$\hbar\omega$	Vibrational spacing
$I(t)$	Fluorescence intensity at $t = i$
$fwhm$	Full width at half maximum
λ	Total reorganization energy
τ	Lifetime
ω	Vibrational angular frequency

Chapter 1

Introduction:

Electron Transfer and Proton Transfer Reactions

1.1 Electron Transfer

1.1.1 Preamble

The study and understanding of the principles of energy conversion in nature can provide important ideas for improving our lives.[1] Photosynthesis converts sunlight into chemical energy forming carbohydrates and oxygen from carbon dioxide as shown in Eq 1.1.

$$6CO_2 + 6H_2O \overset{h\nu}{\rightarrow} C_6H_{12}O_6 + 6O_2 \qquad (1.1)$$

The photosynthetic reaction center, i.e. Photosystem II (PSII) is an elaborate apparatus and an integral part of the photosynthetic process. In PSII, the oxidation of water takes place producing molecular oxygen in green plants and providing electrons to P_{680}^{+} which are utilized to drive important metabolic reactions which provide chemical energy to the organism.[1] The process is initiated when sunlight is absorbed by an antenna system that is arranged in large light harvesting complexes (the light harvesting apparatus LHI and LHII). The structural arrangement of LHI and LHII facilitate rapid energy transfer to the reaction center on picosecond time scale. Energy transfer results in the sensitization and electronic excitation of a special pair of chlorophyll molecules called P_{680} of the PSII reaction center.

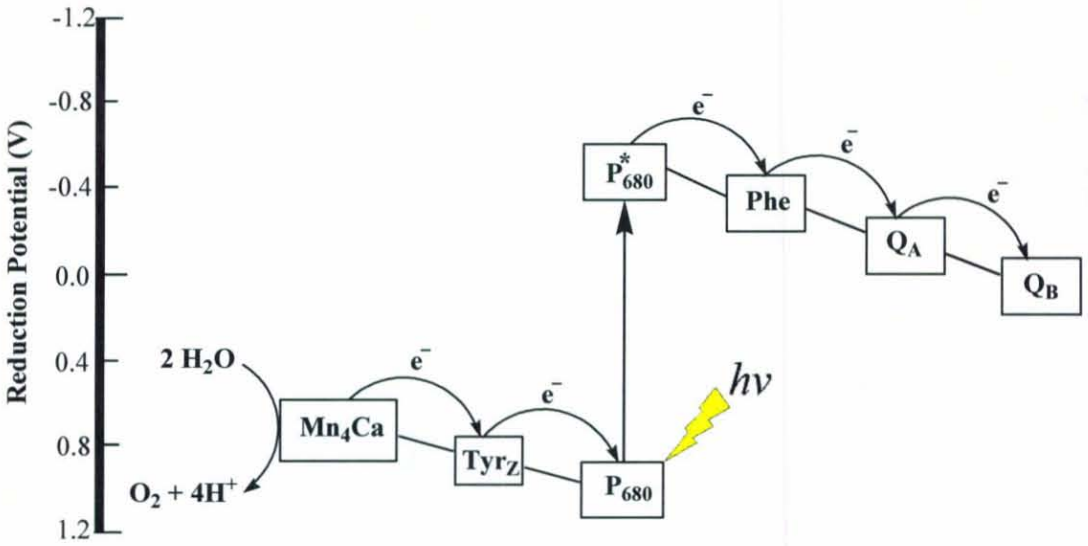

Figure 1.1. Schematic picture of electron-flow and approximate reduction potential in PSII.

After light excitation, the P_{680}^{*} excited state is a strong reducing agent, Eq 1.2, which triggers an electron transfer to a nearby electron acceptor pheophytin (*Phe*) in 2-21 ps.[1] The charge recombination in $P_{680}^{+} - Phe^{-}$ takes place in 30-40 ns[1] in genetically modified assemblies where Q_A has been removed or altered.[1,2]

$$Phe + P_{680} \xrightarrow{h\upsilon} Phe + P_{680}^{*} \underset{k_{ET}}{\longrightarrow} P_{680}^{\cdot+} + Phe^{\cdot-} \qquad (1.2)$$

However, the electron travels further down from *Phe* to plastoquinones, A (Q_A), in a few hundreds of ps.[3] The radical cation $P_{680}^{+\bullet}$ is regenerated by electron transfer tyrosine (Tyr_Z) on the donor side of PSII which prevents the collapse of redox separated Q_A^- to P_{680}^{+} assemblies.[4-7] Also in the donor side is the Mn_4 cluster, which is responsible for the catalytic water oxidation to generate oxygen and electrons which are used to restore P_{680}^{+}

to P_{680} (Figure 1.1). The oxidations at the Mn-cluster occur in four steps called the S-cycle or Kok-cycle.[8,9]

The diagram below illustrates that the charge separated state is produced after an electron is transferred within picoseconds from the electron donor (D) to the electron acceptor (A) of the reaction center, resulting in a charge-separated state or redox separated state.

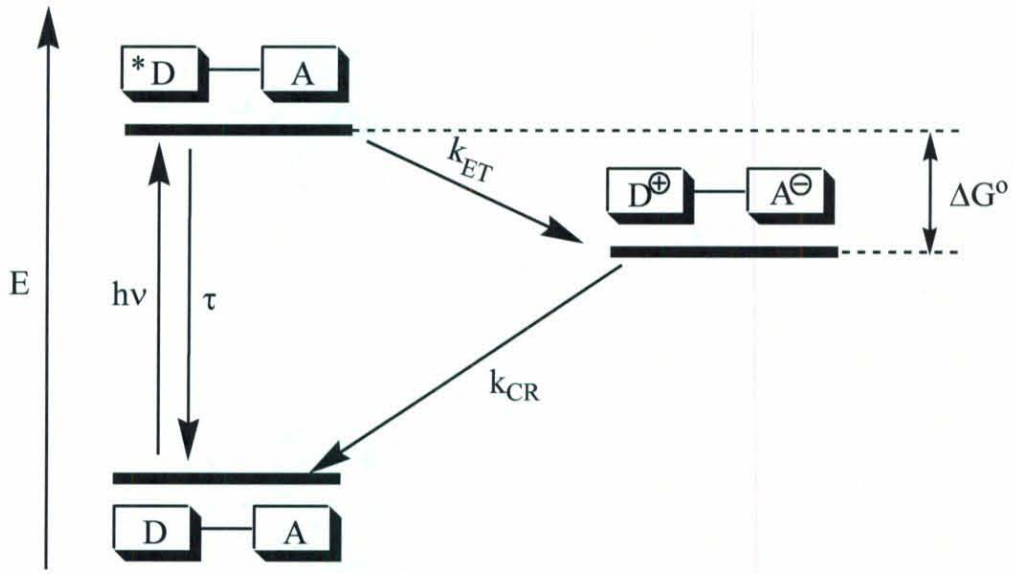

Figure 1.2. Energy diagram illustrating photo-excitation followed by an electron-transfer step resulting in charge separated species.

At this juncture, it is critical to recognize and understand the wide ranging importance of E_LT phenomena in both chemistry and life. We have briefly described the role of electron transfer in the natural conversion of solar energy into chemical potential. A brief insight into the history and fundamentals of electron transfer in particular

photoinduced electron transfer will also be given below in section 1.1.2 and 1.1.3. The theories and mechanisms of electron transfer will be described in section 1.1.4.

1.1.2 History of Electron Transfer

Electron transfer reactions have been intensively investigated since the late 1940s[10-18]. In 1983, Henry Taube was awarded the Nobel Prize in chemistry for his work in the elucidation of inner sphere and outer sphere electron transfer reaction mechanisms in metal complexes. In 1952, Libby discussed electron transfer processes between isotopically labeled ions and gave a qualitative discussion on the basis of the Franck-Condon principle with a focus on the neglected role of solvent reorganization outside the inner coordination shell.[19] From 1956 to 1965, Marcus wrote a series of pioneering papers which described the development of a quantitative theory for electron transfer using statistical mechanics.[20] The first recognition of an electronic absorption corresponding to a charge-transfer transition in solution was for a new absorption band of an aromatic organic compound and halogen (iodine) by Benesi-Hildebrand in 1949 (Eq 1.3).[21]

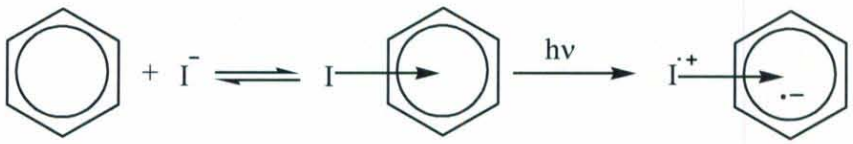

(1.3)

In 1952, Mulliken designed a conceptual theoretical model for a system consisting of electron donor / acceptor complexes. In 1954, Förster and Kaspar observed the formation of an excimer (a combination of an atom or molecule that exists in an excited state with another identical atom or molecular entity in its ground state)[22]. This work ultimately

formed the basis of a massive field of study for photoinduced electron donor/acceptor interactions resulting in a systematic understanding of charge transfer. The evolution of electron transfer theory occurred over a relatively short time frame due to a surety between experimentalists and theoreticians. From Marcus's first paper[13] published in the 1950's to the 1990's, several predictions from Marcus have been verified. These include selected milestones as outlined below:

- Recognition of the self-exchange reaction.
- The connection between optical and thermal electron transfer in mixed valence complexes was considered by Noel Hush who pioneered electron transfer theory for charge transfer processes.
- The role of molecular vibrations involved in the transfer of an electron was clarified following the valuable contribution of Norman Sutin who recognized the role of bond length changes in the electron transfer.
- The role of solvent in electron transfer.
- The dependence of the rate of electron transfer ($\boldsymbol{k_{et}}$) on $\boldsymbol{\Delta G^o}$ and prediction of the inverted region.
- Rehm-Weller's contribution in understanding the $\boldsymbol{\Delta G^o}$ dependence of the electron transfer process and the problem of diffusional masking.
- Verification of the inverted region by Miller and Hutcheson for bimolecular reactions in rigid media by pulse radiolysis.
- Closs, Miller, Meyer, and Sutin who designed chromophore-quencher donor/acceptor adducts that gave definitive evidence of the inverted region.

- Inverted region for Dexter energy transfer.

Marcus theory is now seen to contribute to an understanding of chemical reactivity in a very wide range of ET phenomena in chemistry and was recognized by the Nobel Prize awarded to R. A. Marcus in 1992.[13,15,23,24]

1.1.3 Electron Transfer

Electron transfer (ET) is a fundamental chemical process for moving an electron from an electron donor to electron acceptor. These reactions do not necessarily break or form chemicals bonds which are the basis of the outer sphere mechanism. In inner-sphere ET the electron transfer from reductant to oxidant occurs via a covalent bond; this is the so-called bonded electron transfer. A famous example of an inner sphere ET process that proceeds via a transitory bridged intermediate is the reduction of $[CoCl(NH_3)_5]^{2+}$ by $[Cr(H_2O)_6]^{2+}$. The electron transfer that occurs is mediated by a chlorine ligand bridge and is termed intramolecular electron transfer.[25] Here the individual chemical moieties exhibit a strong electronic interaction.[26,27] In outer-sphere electron transfer, the redox partners are in direct contact with one another in the precursor complex and the coupling of the donor and the acceptor electron wavefunctions are orders of magnitude smaller than the inner-sphere electron transfer mechanism. The media that account for long range electron transfer processes including solvents, non-covalent bonds or covalent bonds or salt bridges which provide routes for the migration of an electron from donor to acceptor. As an example, self-exchange describes the degenerate reaction between two substitution-inert complexes.

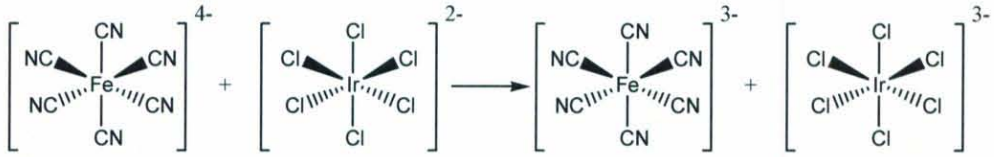

(1.4)

In such cases, one sees very weak electronic interactions before the ET event occurs between the reactants in the transition state.[26,28] Another example for long-range ET is a major step in photosynthesis in green plants.[29] Despite the fact that solvent or bonds mediate ET between D and A, ET can also occur through incoherent hopping processes between localized electronic states.[30]

Electron transfer can initiate by photoexcitation whereby a photon of light promotes an electron to a high energy orbital leaving a low energy orbital half full. Figure 1.3 shows the energy gap (ΔE) between the highest occupied molecular orbital (HOMO) of the donor and the lowest unoccupied molecular orbital (LUMO) of the acceptor, and illustrates the promotion of an electron from the HOMO to the LUMO.

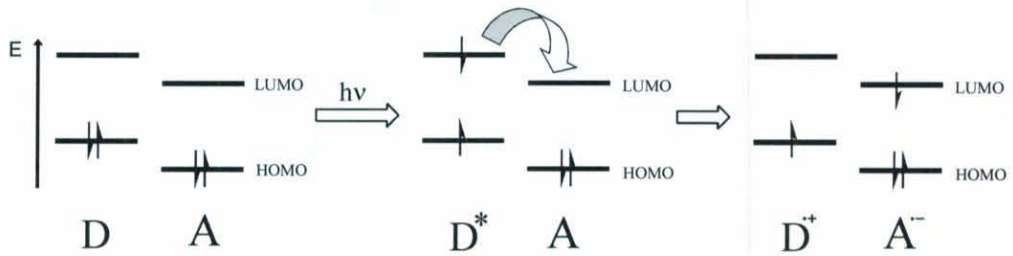

Figure 1.3. Excitation of a donor followed by electron transfer.

Essentially there are three distinct categories of electron transfer reactions that can be divided as follows: thermal, optical and photoinduced electron transfer. Figure 1.4 shows three categories of the ET processes which may involve either a charge shift ($D^- + A \rightarrow D + A^-$) or the formation of a charge separated state ($D + A \rightarrow D^+ + A^-$).[31]

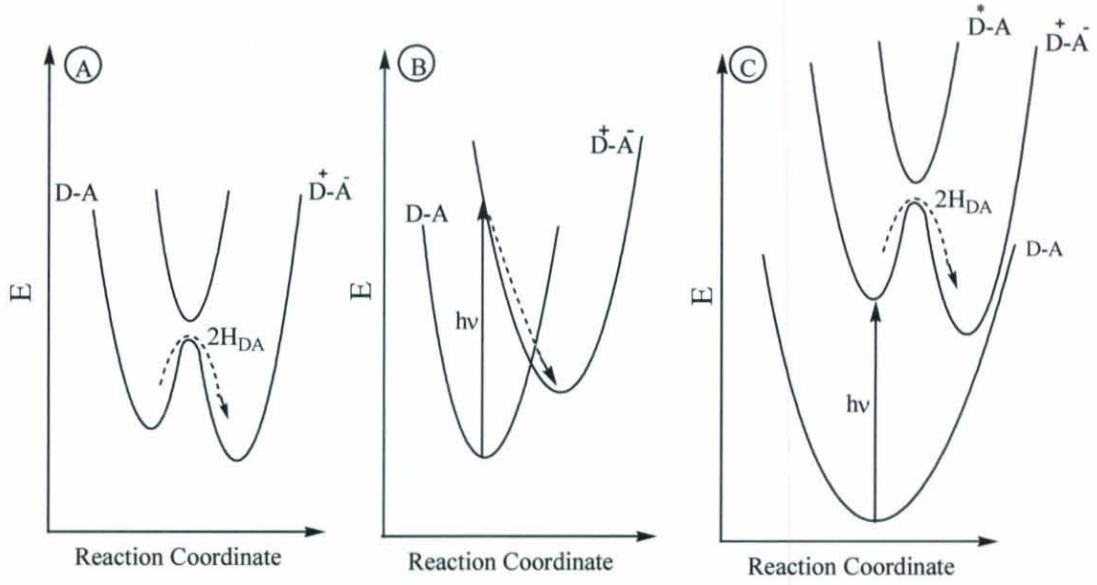

Figure 1.4. Schematic diagram representing electron transfer categories: (A) thermal ET, (B) optical ET, and (C) photoinduced ET.

The first category of electron transfer reaction is thermal electron transfer. In this case the free energy of the reactant is higher than the free energy of the product ($\Delta G^o < 0$) which is thermodynamically favored as shown in Figure 1.4 (A). The second category of electron transfer is optical electron transfer, Figure 1.4 (B). In this case the free energy change (ΔG^o) between reactant and product is greater than zero, and therefore additional or excess energy is required to create the product. In this case photoexcitation results in a vertical transition into the charge separated state from the reactant (D-A) to the product surface (D^+-A^-). The optical electron transfer is represented as a direct electronic transition from the reactants to products surface as a given in Eq 1.5.[31]

$$[D - A] + h\nu \rightarrow [D^+ - A^-] \qquad (1.5)$$

The third category of electron transfer reaction is photoinduced electron transfer (PET). Figure 1.4 (C) displays the potential energy curves for photoinduced electron transfer to

form a product (charge-separated species). Upon excitation, the excited state species $(D^* - A)$ is formed and this species will undergo electron transfer to form the product (charge separated state, $D^+ - A^-$). Relaxation of the charge separated state by either a radiative or non-radiative pathway leads to repopulation of the ground state.

Photoinduced electron transfer (PET) between an excited donor or acceptor and the ground state of a donor or acceptor creates redox separated intermediates whose lifetime is dictated by structure (electronic, vibronic and solvent interactions) as well as chemical bonding in the donor-acceptor pair. The behavior of these intermediates in the limit of formation of a large dipole is strongly dependent on the polarity and nature of the solvent, i.e. solvent glasses, rigid films etc. For example, PSII still undergoes photoinduced electron transfer at 4 K. However, most donor/acceptor adducts will not transfer electrons once the solvent is frozen.[32]

The PET reaction is one of the most critical processes of conversion of light into transiently stored redox energy,[33-35] and in efficiently moving electrons during key steps in photosynthesis,[36] metabolism,[36] and organic reaction mechanisms.[37] Many examples of chemical reactions exist that are driven by PET processes.[36-48] It is unsurprising therefore, that much effort has been expended to achieve an understanding of the fundamental principles of PET and that PET is the focus of a myriad of review articles.

1.1.4 Electron Transfer Theory

1.1.4.1 Introduction

Electron transfer reactions can be divided into three steps. In the first step the electron donor (D) and the electron acceptor (A) form an encounter complex in bimolecular systems. This is essential in order to improve the orbital-overlap between acceptor and donor. In a second step the electron transfer takes place, in which the donor and acceptor reorganize their nuclear configuration such that the redox partners are isoenergetic. In the final step, dissociation of the activated complex occurs to form the separated products of the electron transfer reaction.[49,50]

1.1.4.2 Classical Theory of Electron Transfer

Marcus proposed a quantitative physical model that predicts the rate constant of an electron transfer reaction from an electron donor to an electron acceptor using the expressions that were derived from transition state theory. Marcus theory provides a general framework for understanding the relationship between the kinetic barrier and its thermodynamic driving force for a charge transfer reaction. Marcus treated the solvent as a dielectric continuum and, most critically, his model met the requirement for conservation of energy by having the electron transfer occur at or near nuclear configurations for which the total potential energy of the reactants and the surrounding solvent is equal to that of the products and the surrounding solvent.[13-15,20,23,24,51-54]

Electron transfer between pairs of cations in aqueous solution shown in Eq 1.6 may be discussed using quantitative elements of Marcus theory. This reaction is a typical self-exchange electron transfer process, where the asterisk denotes a radioactive isotope.

$$Fe^{2+} + Fe^{*3+} \rightarrow Fe^{3+} + Fe^{*2+} \qquad (1.6)$$

The above equation shows the formation of new ions as a consequence of electron transfer at the microscopic level however, at the macroscopic level, there is no chemical change. As a result of electron transfer, the solvation spheres of each metal ion need to reorganize (see Figure 1.5). This produces a solvation barrier for the electron transfer process. Therefore, the reaction coordinate for this reaction is the change in the solvation spheres around the two metal ions. The electron transfer occurs in three stages: (i) the coordination shells of the two ions are reorganized in the transition state, labelled TS, by contracting the bonds length of the donor and expanding the bond lengths of the acceptor; a process known as inner sphere reorganization. (ii) Once the redox partners are isoenergetic, electron transfer takes place. (iii) the coordination shells of the two ions relax from the TS geometry to the equilibrium geometry of the product (Figure 1.5).

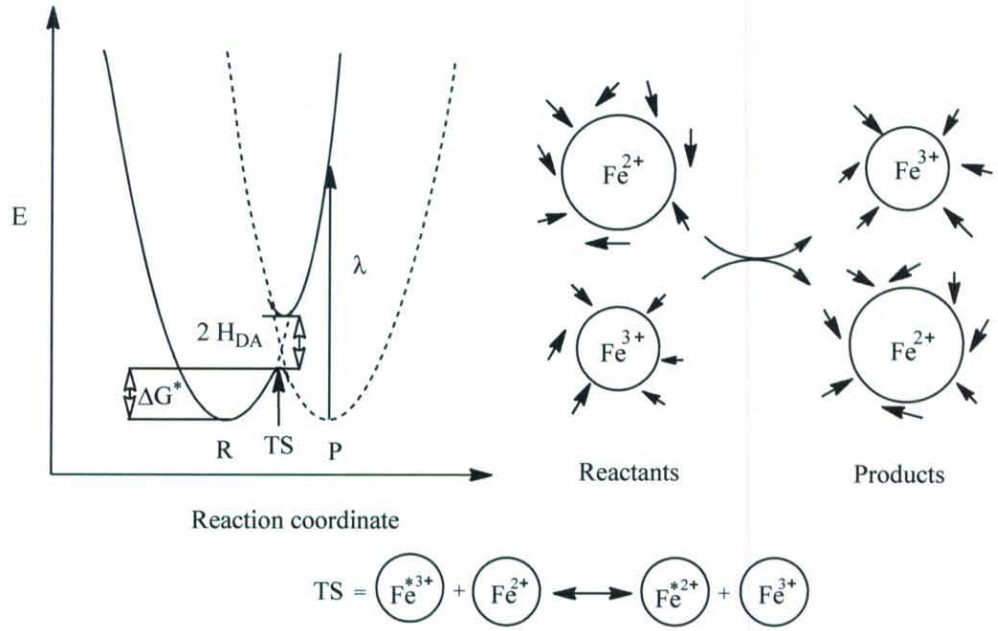

Figure 1.5. Representation of the energy diagram of reactants and products showing electron transfer where the reactive species are surrounded by solvent molecules.

The transition state (TS) is an essential intermediary between the reactant and product states because of two conditions during electron transfer: (a) energy must be conserved and (b) the nuclei must remain stationary on the time scale of electron transfer (the Franck-Condon principle).

Marcus theory was proposed to estimate the rate constant of intramolecular electron transfer reactions (k_{ET}) in terms of the free energy of activation ($\Delta G^{\ddagger}$) of the reaction, as given by Eq 1.7.[13-15,50,54-58]

$$k_{ET} = \nu_{ET} exp\left(\frac{-\Delta G^{\ddagger}}{RT}\right) = \kappa_{el}\nu_n exp\left(\frac{-\Delta G^{\ddagger}}{RT}\right) \qquad (1.7)$$

where ν_{ET} is the frequency factor for electron transfer, κ_{el} is the electronic factor which represents the probability of the electron transfer occurring ($\kappa_{el} = 1$ for adiabatic and $\kappa_{el} < 1$ for nonadiabatic processes) and ν_n is the effective frequency of nuclear motion through the transition state ($\nu_n \cong 10^{13} s^{-1}$). The $\Delta G^{\ddagger}$ for electron transfer can be calculated from the Gibbs free energy of the reaction (ΔG^o) and the reorganization energy (λ) and is given by

$$\Delta G^{\ddagger} = \frac{(\lambda + \Delta G^o)^2}{4\lambda} \qquad (1.8)$$

where λ is the total reorganization energy required for the system to reach the optimum configuration given in Eq 1.9.

$$\lambda = \lambda_i + \lambda_0 \qquad (1.9)$$

where λ_i and λ_0 are the intramolecular and solvent reorganization energies respectively. Thus, the reorganization energy (λ) can be observed as a vertical displacement of the product free energy surface when the two parabolas cross each other (Figure 1.6).

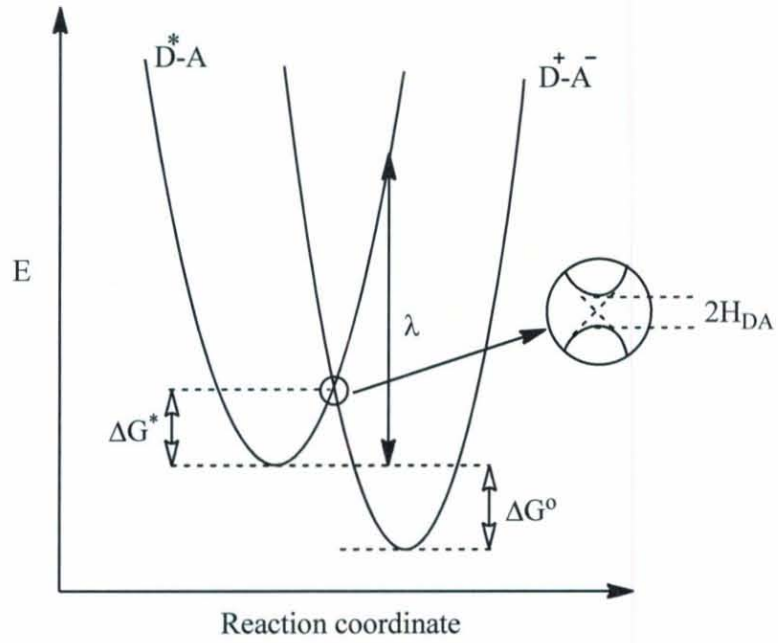

Figure 1.6. Schematic one dimensional parabolic curves of the reactant and product state according to Marcus theory.

The value of the internal reorganization energy, λ_i, that depends on the difference in bond lengths can be estimated using Eq 1.10.[14]

$$\lambda_i = \sum_i \left[\frac{f(R)_i f(P)_i}{f(R)_i + f(P)_i}\right][\Delta q_i]^2 \qquad (1.10)$$

where $f(R)_i$ and $f(P)_i$ are the reduced force constants for the ith vibration of reactant and product molecules and Δq_i is the difference in the equilibrium bond lengths in the reactant and product molecules respectively.

The outer sphere (solvent) reorganizational energy λ_0 value can be estimated using the dielectric continuum model that treats solvents at the microscopic level as having their bulk characteristics characterized by their optical and static dielectric constant values. The λ_0 value is given by Eq 1.11.[59]

$$\lambda_0 = (\Delta e)^2 \left(\frac{1}{2r_D} + \frac{1}{2r_A} - \frac{1}{r_{DA}}\right)\left(\frac{1}{D_{op}} - \frac{1}{D_s}\right) \qquad (1.11)$$

where r_D and r_A are the hard sphere radii for the donor and acceptor respectively, r_{DA} is the separation distance between the donor and the acceptor, D_{op} and D_s are the optical and static dielectric constants of the solvent, and Δe refers to the charge transferred from donor to acceptor. λ_0 is influenced by a number of factors including the distance separating the reactants, as well as the polarity of the solvent. Estimates for the value of λ_0 for intramolecular electron transfer may be calculated by dielectric continuum theory, where λ_0 is given by

$$\lambda_o = \frac{(\Delta\vec{\mu})^2}{a^3}(\Delta f) \qquad (1.12)$$

where $\Delta\vec{\mu}$ is the change in dipole moment on forming the $D^{\cdot+} - A^{\cdot-}$ adduct, Δf is the Mataga parameter and a^3 is the volume of the DA system. The dipole in a sphere assumes a point change in a spherical void that is defined by the radius of the DA system. However, the role of the solvent is very poorly understood[60]. While the dielectric continuum model works well for absorption in the D/A adduct, it fails to model how solvent interactions are manifested in radiative decay, the temperature dependence of λ_o and neglects that the solvent may mediate electron transfer by increasing the electronic matrix coupling constant H_{DA}. More sophisticated models are slowly emerging that are quantitatively accurate in describing λ_o.

According to Eq 1.7 and 1.8, the rate constant of electron transfer (k_{ET}) will increase with driving force (ΔG^o) due to decreased activation energy, where $-\Delta G^o < \lambda$ (the Marcus normal region). At $-\Delta G^o = \lambda$ the k_{ET} value reaches its maximum, where

electron transfer occurs without activation (activationless regime), (the Marcus optimal region). At large ΔG^o $(-\Delta G^o > \lambda)$ the k_{ET} value decreases with the increasing driving force, ΔG^o, (inverted region). This region was confirmed by Closs and Miller.[61] Three regimes are illustrated Figure 1.7.

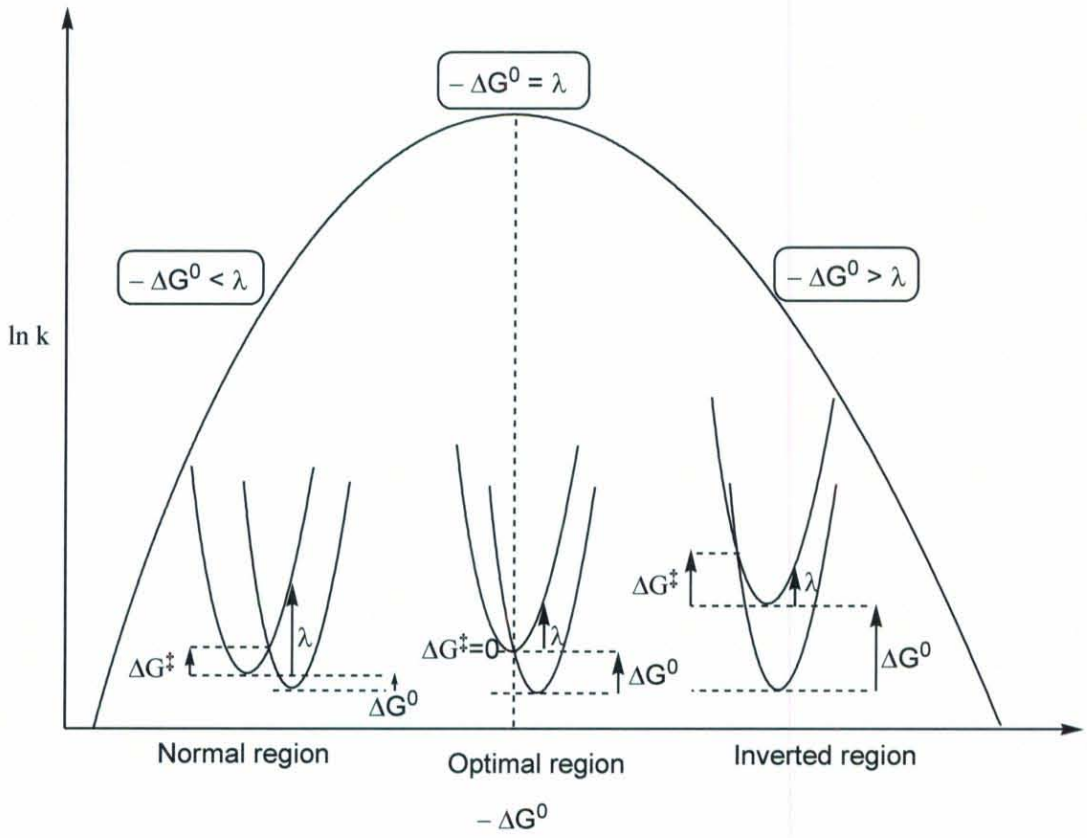

Figure 1.7. The parabolic curve plot of logarithm of the rate of electron transfer as a function of driving force based on the classical Marcus model.

According to Marcus theory, the electron transfer rate constant (k_{ET}) for a non-adiabatic electron transfer reaction is proportional to the magnitude of the electronic coupling element or electron-transfer matrix element (H_{DA}) between the donor (D) and the acceptor (A) and the Franck-Condon weighted density of states ($FCWD$).[15] This is

often reasonably accurate at the high temperature limit with $\hbar\omega_j \ll k_B T$. In the case of electron transfer at the lower temperature limit, a semiclassical expression of the Marcus theory can be used.[24,55,62,63]

$$k_{ET} = \frac{2\pi}{\hbar}|H_{DA}|^2 \frac{1}{\sqrt{4\pi\lambda k_B T}} exp\left(\frac{-(\lambda + \Delta G^o)^2}{4\lambda k_B T}\right) \quad (1.13)$$

Eq 1.13 is called the semiclassical Marcus equation which works accurately for the normal region ($-\Delta G^o < \lambda$) as well as in the high temperature limit. The result is that this equation predicts that k_{ET} is directly proportional to $-\Delta G^o$ in the normal region until a maximum is reached for the optimal region, and then any further increase in the driving force leads to a decrease in the rate of electron transfer.

1.1.4.3 Adiabatic and Non-adiabatic ET Process

In the absence of interactions between the reacting species, the potential energy surfaces of the reactants and the products are unperturbed at their intersection point. When the electron transfer takes place, the molecules are rather close to each other and some electronic interaction is expected. Such an electronic coupling leads to a reconfiguration of the energy surfaces at the crossing point (Figure 1.8). If one applies the Fermi Golden Rule,[15] in which the rate constant of electron transfer is proportional to the magnitude of the electronic coupling element or electron-transfer matrix element (H_{DA}) and the Franck-Condon weighted density of states ($FCWD$) one has, Eq 1.14

$$k_{et} = \frac{2\pi}{\hbar}|H_{DA}^2|FCWD \quad (1.14)$$

The magnitude of H_{DA} is rather different for the cases of nonadiabatic (diabatic) and adiabatic ET. H_{DA} can be defined by Eq 1.15.[49]

$$H_{DA} = \langle \Psi_R^o | H_{el} | \Psi_P^o \rangle \quad (1.15)$$

where Ψ_R^o, Ψ_P^o are the diabatic electron wavefunctions of the reactant and product respectively and H_{el} is the Born-Oppenheimer Hamiltonian for the system. In the case of adiabatic ET, the magnitude of H_{DA} is large ($\geq 200\ cm^{-1}$). On the other hand, for nonadiabatic ET the magnitude of H_{DA} is small ($< 200\ cm^{-1}$).

The diagram below shows two different types of electron transfer reactions, non-adiabatic, and adiabatic.[64] In both cases, the system consists of a donor/acceptor pair, in which the donor (D) is excited by absorbing photon of light at an appropriate wavelength and then electron transfer occur giving a product (charge separated state).

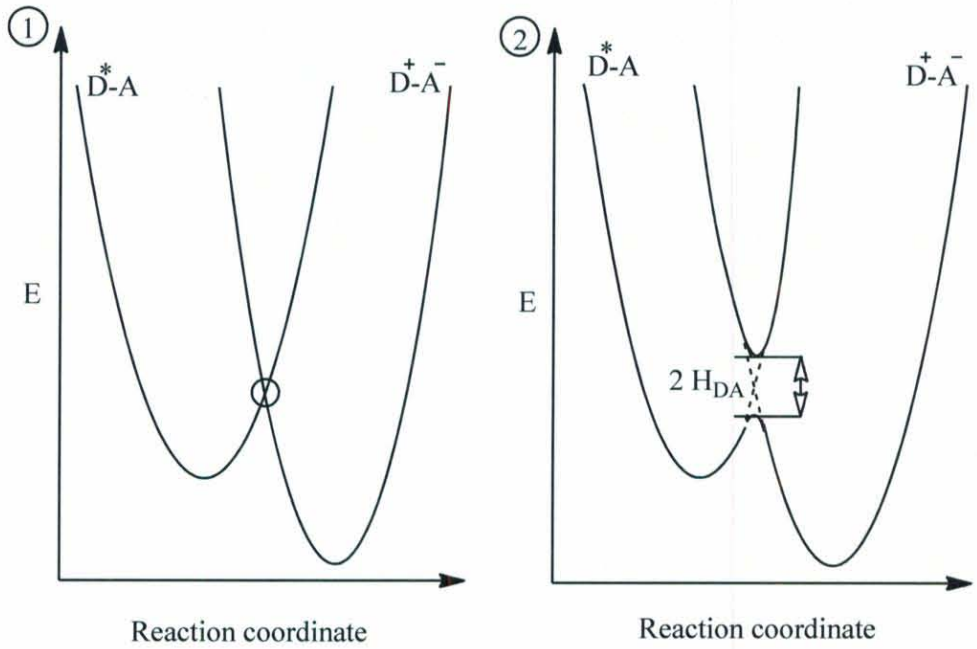

Figure 1.8. Schematic showing one dimensional potential energy surfaces for two different electron transfer regimes, (1) non-adiabatic and (2) adiabatic Gibbs free energy surfaces.

1.1.4.4 Electron Transfer Variables

As shown above, semiclassical Marcus theory predicts the dependence of the electron transfer rate constant (k_{ET}) on several parameters such as the electronic coupling element (H_{DA}), the free energy or the driving force of the reaction (ΔG^o), the total reorganization energy (λ), and the absolute temperature (T). These parameters can be affected by various factors including the types of chromophores, the distance between the two chromophores, the orientation of the chromophores, the effect of the bridge that connects chromophores, and solvent effects. Changes in all of these variables can affect k_{ET} values observed. These effects will briefly be described in the following paragraphs.

1.1.4.4.1 Chromophore Dependence

The extent of the donor and acceptor character varies from one chromophore to another on account of their redox potentials. The relationship between the free energy of reaction and the redox potentials is given by the Rehm-Weller equation for infinite charge separation between donor-acceptor and is given by Eq 1.16.[65,66]

$$\Delta G^o = E^o(D^+/D) - E^o(A/A^-) - E_{oo} \quad (1.16)$$

where $E^o(D^+/D)$, $E^o(A/A^-)$ are the oxidation and reduction potential energies of D and A, respectively, and E_{oo} is the electronic excitation energy to the lowest vibrational state as shown in Figure 1.9. In the case of finite distance between donor and acceptor, one has to take into account the Coulombic attraction energy, ΔG_{ip}, between D^+ and A^-. The modified Rehm-Weller equation is given in Eq 1.17

$$\Delta G^o = E^o(D^+/D) - E^o(A/A^-) - E_{oo} + \Delta G_{ip} \quad (1.17)$$

The Coulombic attraction energy is defined by

$$\Delta G_{ip} = \frac{-e^2}{4\pi D_{op} D_s r_{DA}} \qquad (1.18)$$

where D_{op}, D_s are the optical dielectric and static dielectric constants of the solvent. According to Eq 1.13, the electron transfer rate constant depends on the ΔG^o value, and according to Eq 1.17, the ΔG^o value depends on the donor- acceptor redox potential as shown in Figure 1.9.

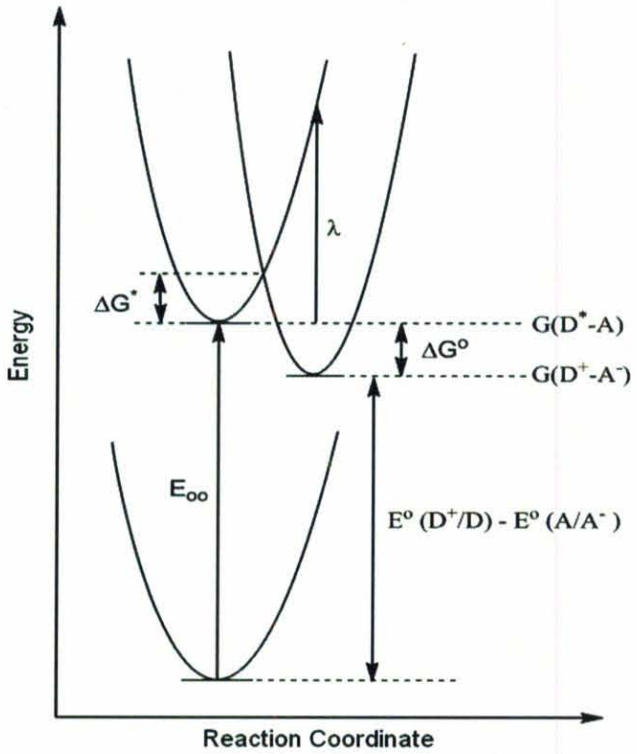

Figure 1.9. Schematic one dimensional parabolic energy curves for the photoinduced electron transfer reaction.

1.1.4.4.2 Geometry Dependence

The geometric orientation of the chromophores can be effected by the overlap of the π system which directly alters the magnitude of the electronic coupling element

(H_{DA}).[67,68] For example (Figure 1.10), in the folded conformation of a molecule, there is the possibility of exciplex formation (a combination of two different atoms or molecules that exists only in an excited state)[69] between the two chromophores linked together by long chains. The dependence on geometry has been experimentally and theoretically investigated for both organic and inorganic compounds.[68,70-76] The study by Wasielewski *et al.*[77] has shown that for four chromophores edge-to-edge, distance varies based on their orientation. It was shown that the rate of the electron transfer change due to different orientations affects the H_{DA} value.

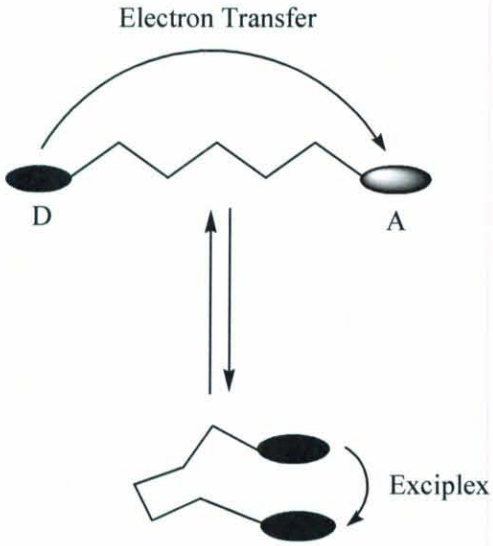

Figure 1.10. Molecular schematic showing the effects of geometry and conformation on electron transfer and exciplex formation.

1.1.4.4.3 Solvent Dependence

The solvent effect on the rate constants and activation parameters of the electron transfer reactions has been widely investigated.[73,75,76,78-83] Marcus has proposed that the solvent may influence the k_{ET} by two parameters. First, the Gibbs free energy of the reaction (ΔG^o) can be changed by varying solvent polarity.[84-86] Second, the solvent

reorganization energy (λ_o) varies according to the magnitude of the optical and the static dielectric constant (D_{op}, D_s), both of which are directly proportional to λ_o as shown in Eq 1.11. In the case of a high dielectric constant, the molecule assumes a change in its conformation, which might increase the H_{DA} magnitude by bringing the donor and acceptor close together. In addition, the size and shape of solvent molecules as well as of solvent viscosity have been correlated with k_{et}.[87-89] Figure 1.11 shows that ground and excited states are surrounded by solvent molecules. State (b) illustrates the activated encounter complex and (c) shows the charge separated state. Since the electron transition take place in a fixed nuclear configuration, states (b) and (c) have the same molecular distance between the D and A. After electron transfer, state (c) produces an ion pair. Solvent molecules will reorganize, stabilizing the ion pair. The stabilization that occurs increase with increased solvent polarity.

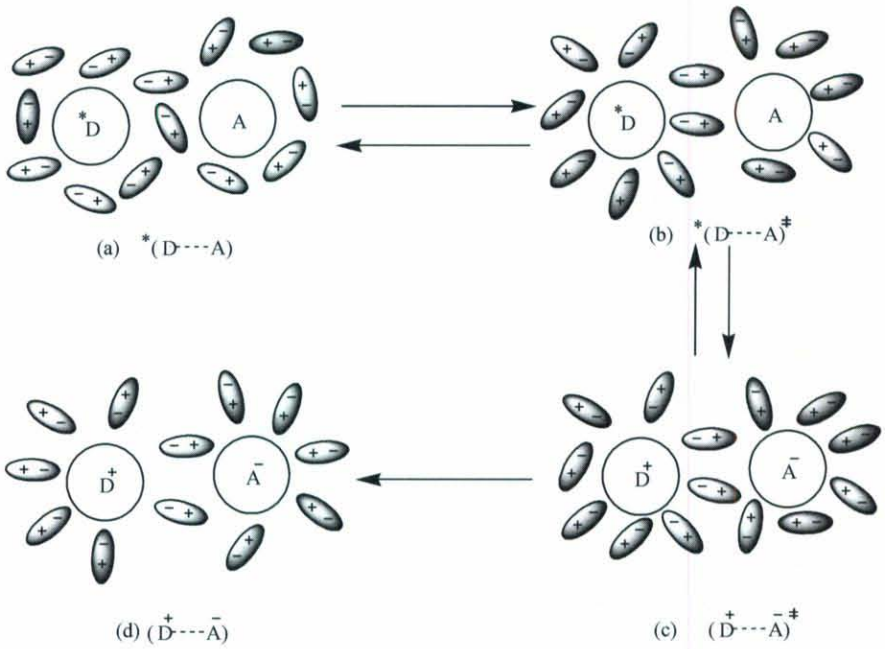

Figure 1.11. Solvent orientation effects on the donor-acceptor electron transfer system.

1.2 Proton-transfer

1.2.1 Introduction

Proton transfer (PT) between a donor and acceptor is a critical reaction in both chemical and biological processes.[90-98] Proton transfer in acid-base reactions is a well known ground state phenomenon that is different from excited state proton transfer (ESPT) because the excited molecules undergo a dramatic change in their acidity due to a new electronic redistribution of the π electron cloud upon excitation. The electronic redistribution reduces the electron density on the acidic moiety, making proton dissociation more facile. Therefore photo-acids increase acidity, while photo-bases increase basicity upon electronic excitation. This is illustrated in scheme 1.1[90] which shows the 2-Naphthol (2-NpOH) excitation and photo-dissociation in the well known Förster cycle.

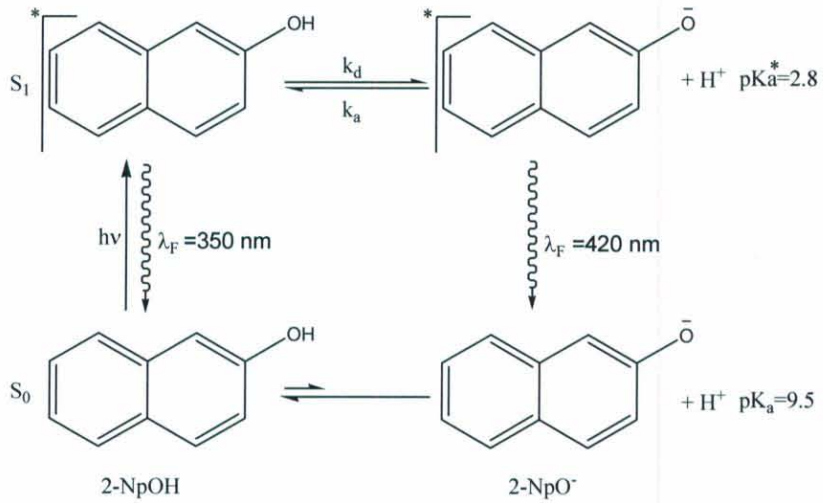

Scheme 1.1. Förster cycle of 2-NpOH excitation and photo-dissociation.

More than 50 years ago, pioneering work was undertaken by Weller,[99-101] Förster,[102,103] and Weber[104] to study this phenomenon. In this case, the photoexcitation may trigger a photoinduced proton transfer (PPT). For molecules with both acidic and basic moieties in the same molecule, one often sees hydrogen bonding between the acidic hydrogen and the basic electron pair.[105,106]

1.2.2 Excited state Intramolecular Proton Transfer (ESIPT)

In 1955, Weller reported the first example of ESIPT reactions,[107,108] in which he noticed an unusually large Stokes shift (~ $1x10^4$ cm^{-1}) in the dual fluorescence emission spectrum of the methyl salicylate molecule. Weller proposed that upon excitation, the ESIPT process occurred through an intramolecular hydrogen bond between the oxygen atom and the hydroxyl proton of the molecule as shown in scheme 1.2.

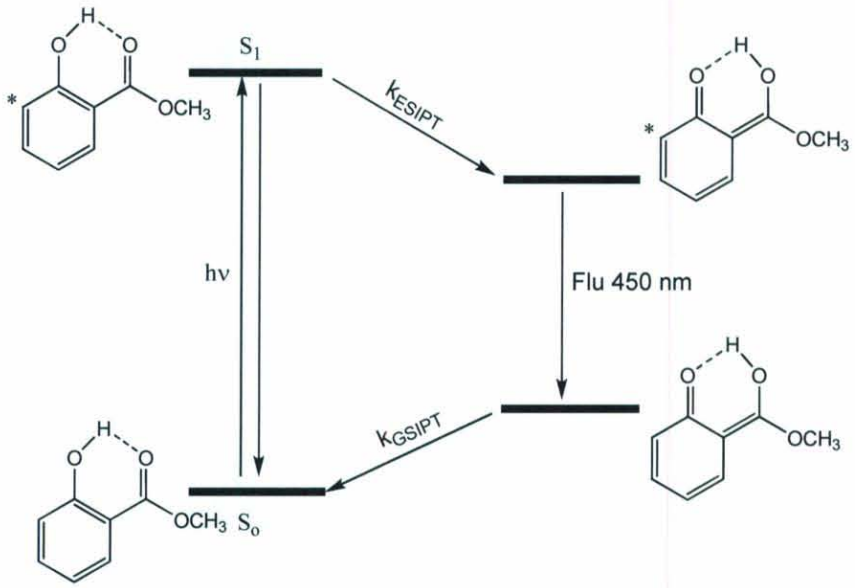

Scheme 1.2. Excited-sate intramolecular proton transfer in the methyl salicylate molecule.

In the simplest four state cycle, the mechanism starts with the photoexcitation of a hydrogen-bonded complex to an excited state having a different pK_a value from the ground electronic state. The excited state species rapidly transfers a proton across the hydrogen bond producing an excited tautomeric species, and then relaxes to the ground state where proton transfer occurs to restore the ground state and complete the cycle. Weller proposed that the blue fluorescence emission at 450 nm is due to the tautomeric form which is often the case in ESIPT reactions. Further experimental and theoretical details will be found in Chapter 3. ESIPT reactions have received extensive attention by a number of research groups around the world. This is because of its characteristically large Stokes shift which leads to interesting applications such as the proton-transfer laser,[109-112] fluorescence micropatterning,[113] chemosensors,[114-116] photostabilizers,[117,118] electroluminescence organic laser diodes,[119] and DNA complexing agents.[120] These types of reactions have been broadly described in a number of excellent reviews covering different aspects of ESIPT process, both experimentally[98,121-128] and theoretically.[125,129-135] Ultrafast techniques such as laser flash photolysis and time-resolved fluorescence have been used to determine the populations of different species on nanosecond (ns), picosecond (ps) or femtosecond (fs) time scales in order to understand the underlying kinetics.

ESIPT reactions are often the first step in the sensitization of enol-keto tautomerization which causes a large electronic and structural rearrangement. As Figure 1.12[136] shows, the proton transfer is due to changes in the potential energy surface upon excitation in which the proton is transferred in the fs time scale.

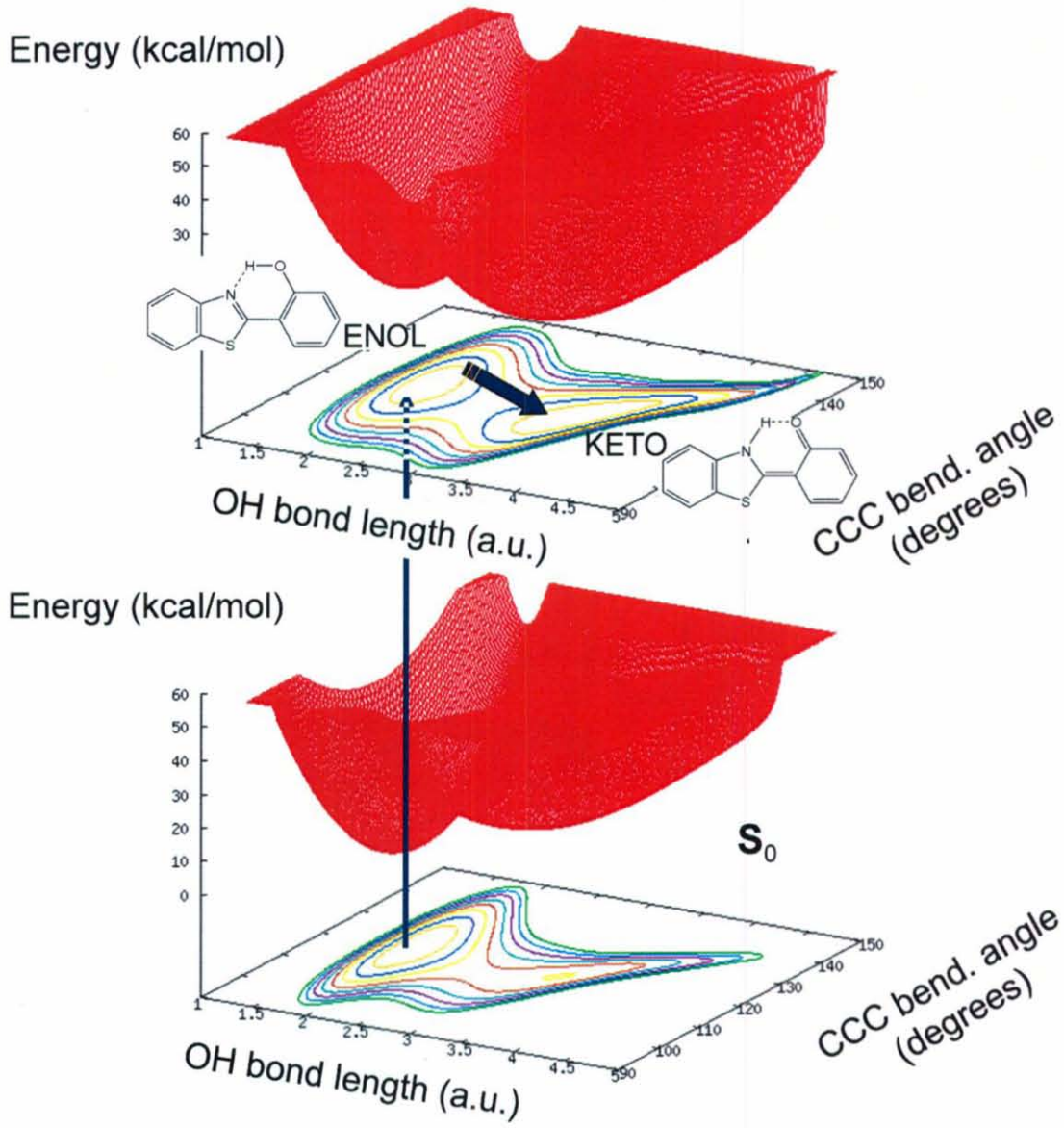

Figure 1.12. Schematic illustration of potential energy surfaces for the ground (S_0) and excited (S_1) electronic states of HBT as a function of the enol-keto isomerization. The vertical arrow indicates photoexcitation of the ground states from S_0 to S_1.[136]

1.2.3. Solvent-mediated ESIPT

ESIPT usually occurs when the proton donor site is distal to the proton acceptor site, and there is no intramolecular hydrogen bond between the acidic and basic moieties. In such cases, clusters of solvent molecules (e.g., water and hydroxylic solvent) clusters can accept or donate protons and mediate ESIPT. Numerous examples of such ESIPT processes mediated by solvent exist. Wolfbeis *et al.*[137] observed green fluorescence emission (λ_{max} 540 nm) where 7-hydroxyflavone was photoexcited in acidic aqueous media. The authors proposed that the long wavelength fluorescence emission is due to either the formation of an exciplex or to the phototautomer that would arise from an ESIPT reaction (Scheme 1.3).

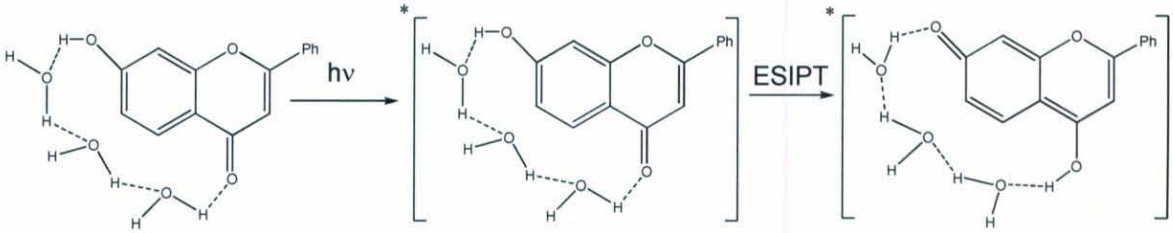

Scheme 1.3. The proposed excited-state behavior of 7-hydroxyflavone in water.

Scheme 1.3 suggests that H_2O assisted excited-state proton transfer may take place, allowing a water cluster to serve as a suitable molecular probe. Additional insight was provided by Wan *et al.*[138] and Itoh *et al.*[139] who proposed that the excited state of their compounds undergoes an ESIPT mediated by a water cluster.

1.3 Scope of this Thesis

The work presented in this thesis is divided into five self-contained chapters including the introduction.

In our studies, chromophores are composed of a covalently linked donor and acceptor unit, some of these chromophores also containing either electron withdrawing or electron donating groups.

Chapter 1 provides a detailed and fundamental overview of the basic chemical processes of ET and PT to help understand the excited state behavior of the molecules studied. In Chapter 2 the experimental details were described. In Chapter 3, the studies were designed aimed at understanding the fundamental photophysical properties of 2,5-Bis(benzimidazoly)-1,4-dihydroxybenzene (bbim). Bbim exhibits excited state intramolecular proton transfer (ESIPT) and CT behavior in DMSO and THF solvents. In Chapter 4, an investigation of the effect of electrolyte (anions) on the ground and excited states of bbim, and inter-intramolecular proton transfer from bbim is discussed. In this work, the nature of the interaction of the hydroquinone OH and benzimidazole NH subunits with different anions was examined. In Chapter 5, a detailed investigation into the photophysical properties of 3-aminocoumarin (3-AC) and some of its derivative dyes, in solvents of varying polarity was reported. Electronic excitation of 3-AC results in the locally excited singlet state which then undergoes intramolecular charge transfer (ICT). In this chapter, the excited state dynamics of 3-AC are studied in an attempt to determine the presence of twisted intramolecular charge transfer (TICT) states and their influence on deactivating derivatised 3-AC excited states.

1.4 References

(1) Deisenhofer, J.; Norris, J. R. *In the Photosynthetic Reaction Center*; Academic press: San Diego, 1993; Vol. Vol 1-2.

(2) Britt, R. D. *Oxygenentic Photosynthesis: The light reactions*; Eds. Ort, R.D. and Yocum, C.F., Kluwer Academic Publishers, Dordrecht,: The Netherlands, 1996.

(3) Wijin, R.; Gorkom, H. J. *Biochim. Biophys. Acta* **2002**, *1553*, 302-308.

(4) Ruttinger, W.; Dismukes, G. C. *Chem. Rev.* **1997**, *97*, 1-24.

(5) Renger, G. *Biochim. Biophys. Acta* **2001**, *1503*, 210-228.

(6) McEvoy, J. P.; Brudvig, G. W. *Phys. Chem. Chem. Phys* **2004**, *6*, 4754-4763.

(7) Mukhopadhyay, S.; Mandal, S. K.; Bhaduri, S.; Armstrong, W. *Chem. Rev.* **2004**, *104*, 3981-4026.

(8) Joliot, P.; Barbieri, G.; Chabaud, R. *Photochem. Photobiol.* **1969**, *10*, 309-329.

(9) Kok, B.; Forbush, B.; McGloin, M. *Photochem. Photobiol.* **1970**, *11*, 457-475.

(10) Frauenfelder, H.; Wolynes, P. G. *Science* **1985** *229*, 337.

(11) Garg, A.; Onuchic, J. N.; Ambegaokar, V.; Zusman, L. D. *J. Chem. Phys.* **1985**, *83*, 4491.

(12) Hynes, J. T. *Annu. Rev. Phys. Chem.* **1985**, *36*, 573.

(13) Marcus, R. A. *J. Chem. Phys.* **1956**, *24*, 966.

(14) Marcus, R. A. *J. Chem. Phys.* **1965**, *43*, 679.

(15) Marcus, R. A.; Sutin, N. *Biochim. Biophys. Acta* **1985**, *811*, 265-322

(16) Wolynes, P. G. *J. Chem. Phys.* **1987**, *86*, 1957.

(17) Zusman, L. D. *Chem. Phys. Lett.* **1980**, *49*, 295.

(18) Zusman, L. D. *Chem. Phys. Lett.* **1983**, *80*, 29.

(19) Marcus, R. A. *Pure & Appl. Chern.* **1997**, *69*, 13-29.

(20) Marcus, R. A. *Angew. Chem. Int. Ed. Engl.* **1993**, *32*, 1111-1121.

(21) Benesi, H. A.; Hildebrand, J. H. *J. Am. Chem. Soc.* **1949**, *71*, 2703–2707.

(22) Förster, T.; Kasper, K. *Phys. Chem. (N. F.)* **1954**, *1*, 19.

(23) Marcus, R. A. *J. Chem. Phys.* **1963**, *39*, 1734

(24) Marcus, R. A. *Annu. Rev. Phys. Chem.* **1964**, *15*, 155.

(25) Wittekindt, C.; Schwarz, M.; Friedrich, T.; Koslowski, T. *Journal of the American Chemical Society* **2009**, *131*, 8134-8140.

(26) BARR, S. W.; WEAVER, M. J. *Inorg. Chem.* **1984**, *23*, 1657-1663.

(27) Marusak, R. A.; Ivanca, M. A.; Haller, K. J.; Graham, L., A. *Inorg. Chem.* **1991**, *30*, 618-623.

(28) Mohsin, A. B.; Ingole, P. P.; Chaudhari, V. R.; Haram, S. K. *J. Phys. Chem. B* **2009**, *113*, 2848–2853.

(29) Huynh, M. H. V.; Meyer, T. J. *Chem. Rev.* **2007**, *107*, 5004-5064.

(30) Berlin, Y. A.; Ratner, M. A. *Radiat. Phys. Chem.* **2005**, *74*, 124-131.

(31) Balzani, V.; Juris, A.; Venturi, M. *Chem. Rev.* **1996**, *96*, 759-833.

(32) Moore, G. F.; Hambourger, M.; Gervaldo, M.; Poluektov, O. G.; Rajh, T.; Gust, D.; Moore, T. A.; Moore, A. L. *J. Am. Chem. Soc.* **2008**, *130*, 10466-10467.

(33) Castellano, F. N.; Meyer, G. J. *J. Phys. Chem.* **1995**, *99*, 14742.

(34) Fox, M. A.; Chanon, M. *Eds. Photoinduced Electron Transfer*; Elsevier: Amsterdam, 1988.

(35) Gratzel, M. *Heterogeneous Photochemical Electron Transfer*; CRC: Boca Raton, FL, 1989.

(36) Huynh, M. H. V.; Meyer, T. J. *Chem. Rev.* **2007**, *107*, 5004-5064.

(37) MIller, J. B.; Salvador, J. R. *J. Org. Chem.* **2002**, *67*, 435-442.

(38) Chen, L.; Wood, P. D.; Mnyusiwalla, A.; Marlinga, J.; Johnston, L. J. *J. Phys. Chem. B* **2001**, *105*, 10927.

(39) Fukuzumi, S.; Nishimine, M.; Ohkubo, K.; Tkachenko, N. V.; Lemmetyinen, H. *J. Phys. Chem. B* **2003**, *107* 12511.

(40) Kang, Y. S.; Kevan, L. *J. Phys. Chem.* **1994**, *98*, 2478.

(41) Miyashi, T.; Ikeda, H.; Takahashi, Y. *Acc. Chem. Res.* **1999**, *32* 815–824.

(42) Mukherjee, T. K.; Mishra, P. P.; Datta, A. *Chem. Phys. Lett.* **2005**, *407*, 119.

(43) Sadhiya, I. B.; Ramamurthy, P. *Journal of Photochemistry and Photobiology A: Chemistry* **2009**, *201*, 175-182.

(44) Tachiya, M. C. *J. Phys. Chem.* **1990**, *68* 797.

(45) Tavernier, H. L.; Barzykin, A. V.; Tachiya, M.; Fayer, M. D. *J. Phys. Chem. B* **1998**, *102*, 6078.

(46) Tavernier, H. L.; xLaine, H. L.; Fayer, M. D. *J. Phys. Chem. A* **2001**, *105*, 8944.

(47) Weidemaier, K.; Fayer, M. D. *J. Phys. Chem.* **1996**, *100* 3767.

(48) Weidemaier, K.; Tavernier, H. L.; Fayer, M. D. *J. Phys. Chem. B* **1997** *101* 9352.

(49) Bolton, J. R.; Mataga, N.; McLendon, G. *"In Electron Transfer in Inorganic, Organic, and Biological Systems"*; Eds, Am. Chem. Soc.: Washington, DC, 1991.

(50) Newton, M. D.; Sutin, N. *Annu. Rev. Phys. Chem.* **1984**, *35*, 437-480.

(51) Marcus, R. A. *Discuss. Faraday Soc.* **1960**, *29*, 21.

(52) Marcus, R. A. *Discuss. Faraday Soc.* **1982**, *74*, 7.

(53) Marcus, R. A. *J. Chem. Phys.* **1984**, *81*, 4494.

(54) Marcus, R. A. *Rev. Mod. Phys.* **1993**, *65*, 599.

(55) Barbara, P. F.; Meyer, T. J.; Ratner, M. A. *J. Phys. Chem.* **1996**, *100*, 13148.

(56) Hush, N. S. *Coord. Chem. Rev.* **1985**, *64*, 135.

(57) Sutin, N. *Acc. Chem. Res.* **1982**, *15*, 275.

(58) Sutin, N. *Prog. Inorg. Chem.* **1983**, *30*, 441.

(59) Wasielewski, M. R. *Chem. Rev.* **1992**, *92*, 435-461.

(60) Barbara, P. F.; Meyer, T. J.; Ratner, M. A. *J. Phys. Chem.* **1996**, *100*, 13148-13168.

(61) Closs, G. L.; Miller, J. R. *Science* **1988**, *240*, 440.

(62) Chen, P.; Meyer, T. J. *Chem. Rev.* **1998**, *98*, 1439-1477.

(63) Cukier, R. I.; Nocera, D. G. *Annu. Rev. Phys. Chem.* **1998**, *49*, 337–69

(64) Sparpaglione, M.; Mukamel, S. *J. Phys. Chem.* **1987**, *91*, 3938-3943.

(65) Rehm, D.; Weller, A. *Isr. J. Chem.* **1970**, *8*, 259 –271.

(66) Rehm, D.; Weller, A.; Ber, B. *Phys. Chem.* **1969**, *73*, 834.

(67) Cave, R. J.; Siders, P.; Marcus, R. A. *J. Phys. Chem.* **1986**, *90*, 1436-1444.

(68) Helms, A.; Heiler, D.; McLendon, G. *J. Am. Chem. Soc.* **1991**, *113*, 4325-4327.

(69) BRASLAVSKY, S. E. *Pure Appl. Chem.* **2007**, *79*, 293–465.

(70) Fahrni, C. J.; Yang, L.; VanDerveer, D. G. *Journal of the American Chemical Society* **2003**, *125*, 3799-3812.

(71) Heiler, D.; McLendon, G.; Rogalsky, P. *J. Am. Chem. Soc.* **1987**, *109*, 604-606.

(72) Lendzian, F.; Schluepmann, J.; Gersdorff, J. v.; Moebius, K.; Kurreck, H. *Angew. Chem. Int. Ed. Engl.* **1991**, *30*, 1461-1463.

(73) Lewis, F. D.; Letsinger, R. L.; Wasielewski, M. R. *Accounts of Chemical Research* **2001**, *34*, 159-170.

(74) Prezhdo, O. V.; Duncan, W. R.; Prezhdo, V. V. *Accounts of Chemical Research* **2008**, *41*, 339-348.

(75) Rosokha, S. V.; Kochi, J. K. *J. Am. Chem. Soc.* **2007**, *129*, 3683-3697.

(76) Rosokha, S. V.; Kochi, J. K. *Accounts of Chemical Research* **2008**, *41*, 641-653.

(77) Sakata, Y.; Tsue, H.; O'Neil, M. P.; Wiederrecht, G. P.; Wasielewski, M. R. *J. Am. Chem. Soc.* **1994**, *116*, 6904-6909.

(78) Barthel, E. R.; Martini, I. B.; Keszei, E.; Schwartz, B. J. *J. Chem. Phys.* **2003**, *118*, 5916-5931.

(79) Nad, S.; Kumbhakar, M.; Pal, H. *The Journal of Physical Chemistry A* **2003**, *107*, 4808-4816.

(80) Niwa, T.; Kikuchi, K.; Matsusita, N.; Hayashi, M.; Katagiri, T.; Takahashi, Y.; Miyashi, T. *J. Phys. Chem.* **1993**, *97*, 11960-11964.

(81) Previtali, C. M. *Pure & Appl. Chern.* **1995**, *67*, 127-134.

(82) Schuster, G. B. *Accounts of Chemical Research* **2000**, *33*, 253-260.

(83) Sonoyama, N.; Karasawa, O.; Kaizu, Y. *J. Chem. Soc., Faraday Trans.* **1995**, *91*, 437 - 443.

(84) Liu, J.-Y.; Bolton, J. R. *J. Phys. Chem.* **1992**, *96*, 1718-1725.

(85) Schmidt, J. A.; Liu, J.-Y.; Bolton, J. R.; Archer, M. D.; Gadzekpo, V. P. Y. *J. Chem. Soc., Faraday Trans.* **1989**, *85*, 1027-1041.

(86) Schmidt, J. A.; Siemiarczuk, A.; Weedon, A. C.; Bolton, J. R. *J. Am. Chem. Soc.* **1985**, *107*, 6112-614.

(87) Davis, K. L.; Waldeck, D. H. *J. Phys. Chem. B* **2008**, *112*, 12498-12507.

(88) Gladkikh, V. S.; Burshtein, A. I.; Tavernier, H. L.; Fayer, M. D. *J. Phys. Chem. A* **2002**, *106*, 6982-6990.

(89) Lockard, J. V.; Wasielewski, M. R. *J. Phys. Chem. B* **2007**, *111*, 11638-11641.

(90) Agmon, N. *J. Phys. Chem. A* **2004**, *109*, 13-35.

(91) Baiz, C. R.; Ledford, S. J.; Kubarych, K. J.; Dunietz, B. D. *J. Phys. Chem. A* **2009**, *113*, 4862-4867.

(92) Chattoraj, M.; King, B. A.; Bublitz, G. U.; Boxer, S. G. *Proc. Natl. Acad. Sci. U.S.A.* **1996**, *93*, 8362.

(93) Choudhury, S. D.; Pal, H. *J. Phys. Chem. B* **2009**, *113*, 6736-6744.

(94) Cox, M. J.; Timmer, R. L. A.; Bakker, H. J.; Park, S.; Agmon, N. *J. Phys. Chem. A* **2009**, *113*, 6599-6606.

(95) Horner, G.; Lewandowska, A.; Hug, G. L.; Marciniak, B. *J. Phys. Chem. C* **2009**, *113*, 11695-11703.

(96) Plasser, F.; Barbatti, M.; Aquino, A. l. J. A.; Lischka, H. *J. Phys. Chem. A* **2009**.

(97) Tolbert, L. M.; Solntsev, K. M. *Acc. Chem. Res.* **2001**, *35*, 19-27.

(98) Zhong, D.; Douhal, A.; Zewail, A. H. *Proc. Natl. Acad. Sci. U.S.A.* **2000**, *97*, 14056.

(99) Weller, A. *Electrochemie* **1952**, *56*, 662.

(100) Weller, A. *Electrochemie* **1957**, *61*, 956.

(101) Weller, A. *Discuss Faraday Soc.* **1959**, *27*, 28.

(102) Förster, T. *Naturwissenschaften* **1949**, *36*, 186.

(103) Förster, T. *Electrochem* **1950**, *54*, 531.

(104) Weber, K. *Phys. Chem. B* **1931**, *15*, 18.

(105) Douhal, A.; Lahmani, F.; Zewail, A. H. *Chem. Phys. Lett.* **1996**, *207*, 477.

(106) Formosinho, S. J.; Arnaut, L. G. *J. Photochem. Photobiol. A* **1993**, *75*, 21.

(107) Weller, A. *Naturwiss.* **1955**, *42*, 175.

(108) Weller, A. *Elektrochemia* **1956**, *60*, 1144.

(109) Acuna, A. U.; Costela, A.; Munoz, J. M. *J. Phys. Chem.* **1986**, *90*, 2807-2808.

(110) Chou, P.-T.; McMorrow, D.; Aartsma, T. J.; Kasha, M. J. *Phys. Chem.* **1984**, *88*, 4596.

(111) Park, S.; Kwon, O.-H.; Kim, S.; Park, S.; Choi, M.-G.; Cha, M.; Park, S. Y.; Jang, D.-J. *J. Am. Chem. Soc.* **2005**, *127*, 10070.

(112) Parthenopoulos, D. A.; McMorrow, D. P.; Kasha, M. *J. Phys. Chem.* **1991**, *95*, 2668.

(113) Kim, S.; Park, S. *Advanced Materials* **2003**, *15*, 1341.

(114) Kim, S. K.; Lee, D. H.; Hong, J.-I.; Yoon, J. *Acc. Chem. Res.* **2008**, *42*, 23-31.

(115) Liu, Z.-Q.; Shi, M.; Li, F.-Y.; Fang, Q.; Chen, Z.-H.; Yi, T.; Huang, C.-H. *Org. Lett.* **2005**, *7*, 5481-5484.

(116) Martínez-Máñez, R.; Sancenón, F. *Chem. Rev.* **2003**, *103*, 4419-4476.

(117) Keck, J.; Kramer, H. E. A.; Port, H.; Hirsch, T.; Fischer, P.; Rytz, G. *J. Phys. Chem.* **1996**, *100*, 14468.

(118) Sobolewski, A. L.; Domcke, W.; Hattig, C. *J. Phys. Chem. A* **2006**, *110*, 6301-6306.

(119) Kim, S.; Chang, D. W.; Park, S. Y.; Kim, K.; Jin, J.-I. *Bull. Korean Chem. Soc.* **2001**, *22*, 1407.

(120) Joubert, A.; Sun, X.-W.; Johansson, E.; Bailly, C.; Mann, J.; Neidle, S. *Biochemistry* **2003**, *42*, 5984-5992.

(121) Chudoba, C.; Riedle, E.; Pfeiffer, M.; Elsaesser, T. *Chem. Phys. Lett.* **1996**, *263*, 622.

(122) Douhal, A.; Fiebig, T.; Chacisvilis, M.; Zewail, A. H. *J. Phys. Chem. A* **1998**, *102*, 1657.

(123) Frey, W.; Laermer, F.; Elsaesser, T. *J. Phys. Chem.* **1991**, *95*, 10391.

(124) Garcı´a-Ochoa, I.; Dı´ez-Lo´pez, M.-A.; Vin˜as, M. H.; Santos, L.; Martı´nez-Ata´z, E.; Amat-Guerri, F.; Douhal, A. *Chem-Eur. J.* **1999**, *5*, 897.

(125) Guallar, V.; Moreno, M.; Lluch, J. M.; Amat-Guerri, F.; Douhal *A. J. Phys. Chem.* **1996**, *100*, 19789.

(126) Herek, J. L.; Pedersen, S.; Baares, L.; Zewail, A. H. *J. Chem. Phys.* **1992**, *97*, 9046.

(127) Lochbrunner, S.; Wurzer, A. J.; Riedle, E. *J. Chem. Phys.* **2000**, *112*, 10699.

(128) Sytnik, A.; Valle, J. C. D. *J. Phys. Chem.* **1995**, *99*, 13028.

(129) Casadesus, R.; Moreno, M.; Lluch, J. M. *Chem. Phys. Lett.* **2002**, *356*, 423.

(130) Granucci, G.; Hynes, J. T.; Millie´, P.; Tran-Thi, T.-H. *J. Am. Chem. Soc.* **2000**, *122*, 12243.

(131) Guallar, V.; Batista, V. S.; Miller, W. H. *J. Chem. Phys.* **2000**, *113*, 9510.

(132) Nagaoka, S.; Nagashima, U. J. *Phys. Chem.* **1991**, *95*, 4006.

(133) Nagashima, U.; Nagaoka, S.; Katsumata, S. *J. Phys. Chem.* **1991**, *95*, 3532.

(134) Scheiner, S. *J. Phys. Chem. A* **2000**, *104*, 5898.

(135) Sobolewski, A. L.; Domcke, W. *Chem. Phys. Lett* **1999**, *300*, 533.

(136) Justin, K.; Wu, Y.; Brédas, J.-L.; Batista, V. S. *Israel Journal of Chemistry* **2009**, *49*, 187-197.

(137) Schipfer, R.; Wolfbeis, O. S.; Knierzinger, A. *J. Chem. Soc., Perkin Trans. 2* **1981**, 1443 - 1448.

(138) Fischer, M.; Wan, P. *J. Am. Chem. Soc.* **1999**, *121*, 4555-4562.

(139) Itoh, M.; Adachi, T. *J. Am. Chem. Soc.* **1984**, *106*, 4320-4324.

Chapter 2

Experimental Methods, Methodologies and Analysis

2.1 Introduction to Excited States

2.1.1 Introduction

This chapter is divided into two sections. In the first section general concepts of excited state formation and decay will be introduced and a general description of the techniques used in this work will be described. The second section describes the experimental and technical details of the measurements and instrumentation, the experimental methodologies employed in the data acquisition, and the description of the data analysis.

2.1.2 Excited State Formation

Absorption of a photon or photon capture by a molecule leads to formation of an excited state which contains the energy of the photon. Once formed, the excited system will distribute the incorporated energy via a number pathways as shown in Figure 2.1

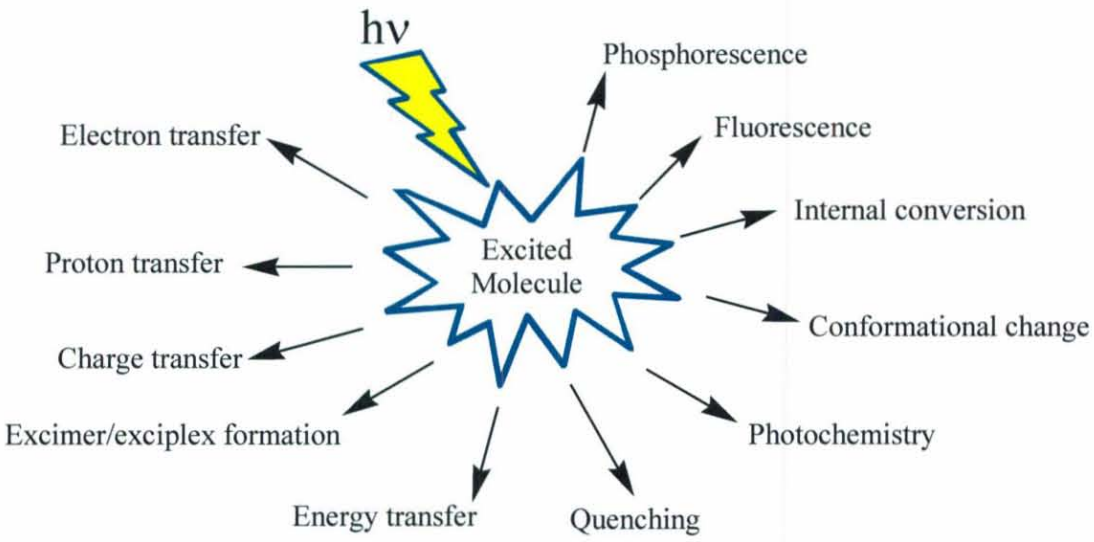

Figure 2.1. The possibilities that can occur when a molecule absorbs UV radiation.

Photon capture or photon absorption is a non-adiabatic process which redistributes electron density from the ground state to form an excited state on a time scale of 1-10 fs. Absorption is a vertical transition in the Franck-Condon sense[1] yielding a new electron configuration on a higher lying potential energy surface, Figure 2.2.

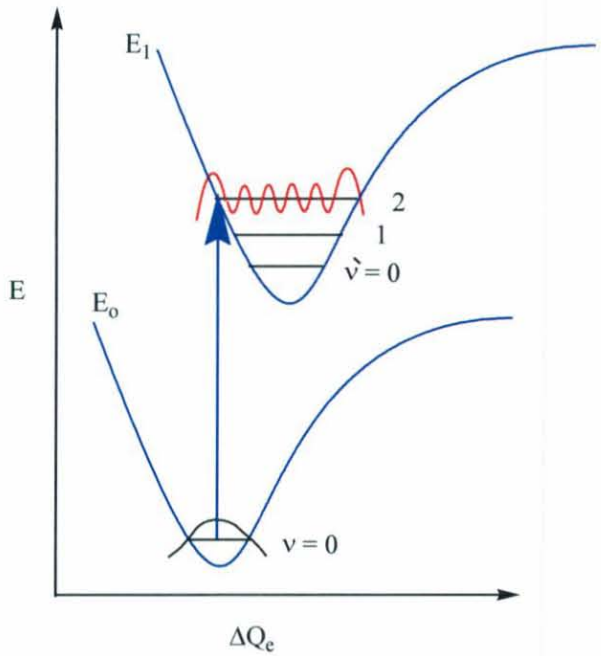

Figure 2.2. The Franck-Condon Principle.

Immediately after photon absorption, the newly formed excited state has the electron co-ordinates of the excited state (i.e. S_1, S_2 etc) and the nuclear and solvent co-ordinates of the ground state. The absorption spectrum can be viewed as a superposition of all transitions from the ground state of varying conformation, solvation and low energy vibrational levels that are Boltzmann populated (levels for which $k_B T \gg \hbar\omega$). Taken together, the full width at half maximum ($fwhm$) for each transition is broadened due to the distribution of conformers and solvation environments.

Once the excited state is formed, vibrational modes within the excited state potential energy surface start to oscillate leading to vibrational cooling and solvent reorganization appropriate to the excited state electronic structure. The Jablonski diagram shown in Figure 2.3 illustrates the energies and spin parentage of the various states which may be accessed as the excited state relaxes.

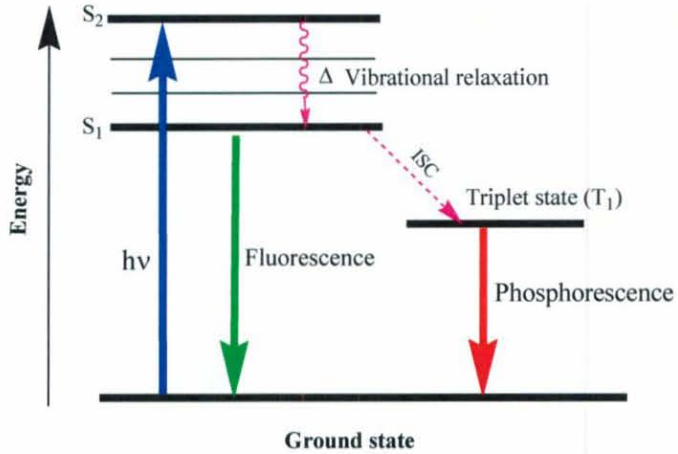

Figure 2.3. The Jablonski diagram which illustrates the energy difference between the excited state and ground state.

Each process that deactivates the excited state is time dependent as illustrated in Figure 2.4.

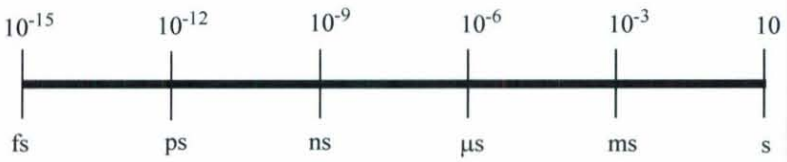

fs Light absorption

fs Proton transfer

ps Solvent rotations

ps Translational motion of solvents

ps to μs Fluorescence

μs to s Phosphorescence

Figure 2.4. Time scales line for some events of photochemical and photophysical interest.

2.1.3 Photophysical Processes

Kasha's rule[2] dictates that all reactivity arises from the lowest lying excited state. The population of the lowest energy excited state following absorption of a photon is described by the differential equations expressed in the following sections: steady-state kinetics and emission are described in section 2.1.3.1 and the time dependence of excited state dynamics is described in sections 2.1.3.2 and 2.1.3.3. A brief overview of instrumental techniques is found in section 2.5.

2.1.3.1 Steady-State Kinetics

Steady-state excitation leads to a distribution of excited states which depends on:

(1) Light intensity.

(2) The magnitude of the rate constants that interconvert the excited states.

The implicit assumption is that each of the excited states is thermally equilibrated with the solvent. Under these conditions, one may analyze the kinetics in a steady-state experiment knowing the number of photons absorbed and the quantum efficiencies for each transition that interconverts excited states and ultimately leads to relaxation to the ground state.

(1) Absorption $C + h\nu \xrightarrow{k_1} {}^1C^* \quad \frac{d[^1C^*]}{dt} = k_1[C]$ (2.1)

(2) Fluorescence ${}^1C^* \xrightarrow{k_r} C + h\nu \quad \frac{d[^1C^*]}{dt} = -k_r[^1C^*]$ (2.2)

(3) Non-radiative decay ${}^1C^* \xrightarrow{k_{nr}} C + \Delta \quad \frac{d[^1C^*]}{dt} = -k_{nr}[^1C^*]$ (2.3)

(4) Intersystem crossing ${}^1C^* \xrightarrow{k_{isc}} {}^3C^* \quad \frac{d[^1C^*]}{dt} = -k_{isc}[^1C^*]$ (2.4)

(5) Phosphorescence ${}^3C^* \xrightarrow{k_p} C + h\nu \quad \frac{d[^3C^*]}{dt} = k_p[^3C^*]$ (2.5)

(6) Photochemistry ${}^1C^* \xrightarrow{k_p} Chemical\ products$ (2.6)

$$\frac{d[^1C^*]}{dt} = k_1[C] - k_r[^1C^*] - k_{nr}[^1C^*] - k_{isc}[^1C^*] \quad (2.7)$$

where C = chromophore. Under steady-state conditions

$$\frac{d[^1C^*]}{dt} = 0 \quad (2.8)$$

$$k_1[C] = \left(k_r + k_{nr} + k_{isc} + \sum_0^i k_i\right)[^1C^*] \quad (2.9)$$

$$[^1C^*] = k_1[C]\left(k_r + k_{nr} + k_{isc} + \sum_0^i k_i\right)^{-1} \quad (2.10)$$

Therefore $[^1C^*]$ is dependent on the k_1 formation step of the excited state and the sum of the kinetic pathways that deactivate the excited state.

With the mechanism illustrated above, the steady-state emission intensity is governed by $[^1C^*]$ and characterized by ϕ_{em} as given by

$$\phi_{em} = \phi_i \frac{k_r}{k_r + k_{nr} + k_{isc} + \sum_0^i k_i} \qquad (2.11)$$

where ϕ_i, is the quantum efficiency for the reacting photoactive state. k_r, k_{nr}, *and* k_{isc} are the rate constants for radiative, non-radiative and intersystem crossing ($\Delta S \neq 0$) respectively. The parameter $\sum_0^i k_i$ is the sum of all other processes which deactivate the excited state.

In many systems, intersystem crossing ($\Delta S \neq 0$) to form a triplet state is possible provided there is spin-orbit coupling or another mechanism that allows spin interconversion to occur while conserving energy and spin-orbit angular momentum.[3,4] Formation of a triplet state or other states with different spin multiplicity is driven by the requirement to reduce electron-electron repulsion and is a consequence of Hund's rule. Thus the quantum yield for triplet formation is

$${}^3\phi_{em} = \phi_{isc} \frac{{}^3k_r}{{}^3k_r + {}^3k_{nr} + {}^3k_{isc} + \sum_0^i {}^3k_i} \qquad (2.12)$$

where the left hand superscript denotes spin multiplicity and the subscript is associated with each rate process defined above. ϕ_{isc} is the quantum yield for intersystem crossing.

$$\phi_{isc} = \frac{{}^1k_{isc}}{{}^1k_r + {}^1k_{nr} + \sum_0^i k_i} \qquad (2.13)$$

If the system is subjected to laser pulse excitation, a non-equilibrium mixture of excited states is created. These states undergo relaxation with a characteristic rate constant dependent on the system. The rate constant for excited state decay k_d is given by

$$k_d = \left(k_r + k_{nr} + k_{isc} + \sum_0^i k_i \right) \qquad (2.14)$$

2.1.3.2 Emission Lifetimes

Time resolved or pulsed light excitation gives kinetic information directly. The excited state lifetime of a fluorophore is defined as the time required for the system to return to the ground state energy via radiative and non-radiative decay pathways. Time-resolved fluorescence spectroscopy can be used in cases where radiative decay occurs providing a measure of k_{obs} for the system. Irradiation of a sample using a pulsed laser produces an electronic excited state which then relaxes after the laser pulse has passed through the sample. The excitation laser pulses should be shorter than the radiative lifetime of the sample under investigation. After pulsed excitation, emission from the excited state is monitored as a function of time, providing dynamic information about the system under study. In the kinetic limit where a single species decays from $S_1 \rightarrow S_0$, the data are adequately fit by

$$I(t) = I_o exp\left(-t/\tau\right) \quad (2.15)$$

where I_o is the fluorescence intensity at time $t = 0$ after the laser excitation, $I(t)$ is the fluorescence intensity at $t = i$, and τ is the fluorescence lifetime. $\tau = (k)^{-1}$ for systems that exponentially decay and k_{obs} is the linear combination of rate constants for all processes that deactivate the excited state, e.g. Eq 2.16.

$$(\tau)^{-1} = k_{obs} = \sum_{0}^{i} k_i \qquad (2.16)$$

2.1.3.3 Laser Flash Photolysis

Flash photolysis is a pump-probe technique used to generate and study excited states over some 15 orders of magnitude in time, depending on the apparatus. The premise of the laser flash experiment is the use of a very short laser pulse to create excited states or other reactive species and to follow the fate of these transients over time by absorption spectroscopy techniques.

2.2 Materials

2.2.1 Compounds

The compound 2,5-bis(benzimidazolyl)-1,4-dihydroxybenzene (bbim) was prepared by the reaction shown in Scheme 2.1.[5] The author thanks Dr. Hongchao Li for synthetic work and donation of high quality materials. The excited state properties of these systems are described in Chapter 3.

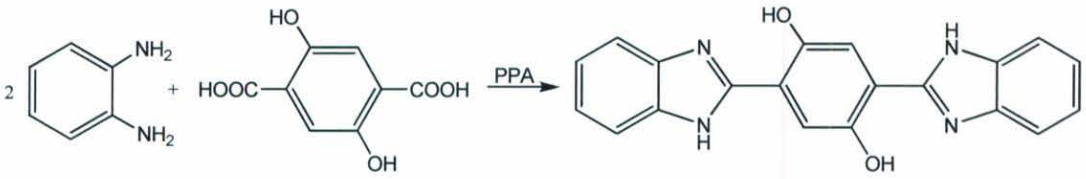

Scheme 2.1. General synthesis of 2,5-bis(benzimidazolyl)-1,4-dihydroxybenzene (bbim).

The photophysical characterization of the coumarin based assemblies is described in Chapter 5 of this dissertation. The preparation and characterization of the coumarins and their derivatives were accomplished using the protocols developed by Dr. Amit Kudale, Mr. Jamie Kendall and Dr. Graham J. Bodwell as shown in Scheme 2.2.[6]

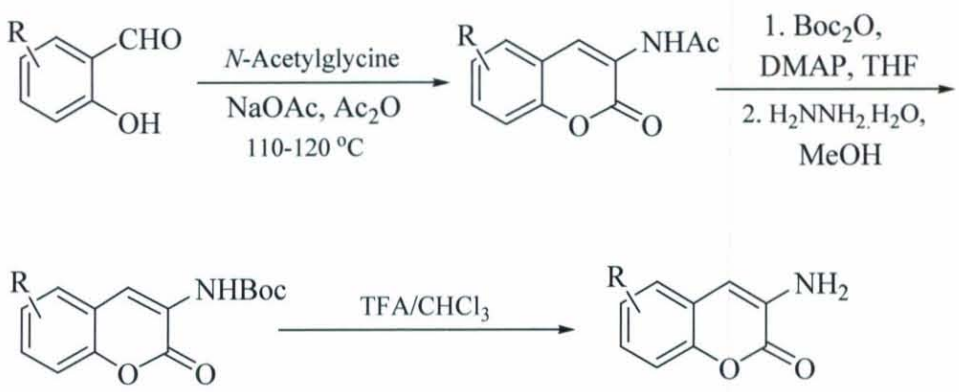

Scheme 2.2. General synthesis of 3-Aminocoumarins (3-AC).

The coumarin based chromophores were prepared as precursors for more complex assemblies to study electron-proton transfer. The purity of compounds that were used in this work has been assessed by HPLC that was performed by using an Agilent Eclipse XDB-CIB 5μ (4.6 x 250 mm) column in 30 % H_2O and 70 % MeCN (70% to 100% in 10 min). Tetra-*n*-butylammonium $[N(nC_4H_9)_4]X$, (X^-= fluoride (F^-), chloride (Cl^-), bromide (Br^-), iodide (I^-), acetate (Ac^-), hydrogen sulphate (HSO_4^-), hexafluorophosphate (PF_6^-) salts were obtained from Aldrich and used as received.

2.2.2 Solvents

High purity spectroscopic grade solvents from Burdick and Jackson (B & J) were used because the demonstrated purity > 99.9% by GC analysis as determined by the manufactuer was critical to the photophysical measurements. Deuterated solvents (99.9 % D atom), such as DMSO-d_6, CD_3CN and D_2O were purchased commercially from Aldrich and used without further purification.

2.3 Sample Preparation

The following protocol was followed for all excited state measurements.

A. The absorption spectrum of the solvent was obtained using air as a reference. This allowed the immediate assessment of solvent purity if the solvent contained absorbing impurities.

B. The emission spectrum of the solvent was obtained to check for emitting impurities in the solvent, using 2-3 excitation wavelengths from 320 nm to 600 nm depending on the nature of the chromophore.

C. Once the solvent was screened, the sample was dissolved and the absorption spectrum was obtained. If the sample was air sensitive, the absorption spectrum was obtained before and after purging with N_2.

The advantage of the stated standard protocols was that if there were emitting impurities, the only source would be the sample. This procedure leads to less time expended for trouble shooting for anomalous behaviour during analysis of the data.

Samples were prepared gravimetrically and dissolved in solvents using the screening procedure given above. All samples were purged by using N_2 (99.9%). Depending on the solubility required of bbim, the solvent employed was either DMSO (B & J), DMF (B & J) or THF that was distilled from Na (s) without benzophenone. The experimental results were found to be independent of the source of THF; i.e. Burdick and Jackson or freshly distilled THF. The concentration of the bbim solution was adjusted at λ_{max} to produce an absorbance value of 0.5. The bbim samples were N_2-purged for 50 minutes to reduce the

O_2 concentration due to the extreme sensitivity of this compound to oxygen under the conditions employed. For more details, see Chapter 3. 15-20 minutes of N_2 purging were sufficient to minimize the amount of O_2 for the study of coumarins and their derivatives. For all of the transient absorption measurements, the ground state absorption spectra were recorded before and after flash photolysis experiments (~ 10 laser shots). If any changes were observed over the course of the experiment, a fresh sample was prepared. In all cases, the data were taken such that there were extensive overlapping data sets.

2.4 Determination of Equilibrium Constant

2.4.1 ^{1}H NMR Titration

^{1}H NMR spectra were measured on a 500 MHz NMR spectrometer. A solution of bbim in DMSO-d_6 was prepared (1.0 x 10^{-4} M), and one ml was transferred to a 5-mm NMR tube. A small aliquot of tetra-*n*-butylammonium fluoride ($[N(nC_4H_9)_4]F^-$) in DMSO-d_6 was introduced in an incremental fashion, and the corresponding spectra of these mixtures were recorded.

2.4.2 UV-Vis and Fluorescence Titrations

Spectrophotometric titrations were performed using a 1.0 x 10^{-5} M concentration of BBIM in DMSO with a fresh tetrabutylammonium salt ([TBA]X, where X= F^-, Cl^-, Br^-, I^-, Ac^-, HSO_4^-, and PF_6^-). Acid titrations were performed using a 1.0 x 10^{-5} M concentration of 3-AC in MeCN with a fresh trifluoroacetic acid (TFA) solution added, and the UV-vis spectra of the samples were recorded. All spectrophotometric titration curves were fitted by global kinetic analysis protocols which were used to determine the association constants.

2.5 Ground State Measurements

2.5.1 Absorption Spectra

Absorption spectra with a wavelength range from 190 nm to 1100 nm, were obtained using 1.0 cm quartz cuvettes supplied by Starna (catalog number 1/Q/10-GL14-S/C). Spectra were acquired using an Agilent 8543 diode array spectrophotometer interfaced to a computer. Data analysis and manipulation of spectra were carried out by using Chem-Station software provided by Agilent. The extinction coefficients were determined from gravimetrically prepared solutions that were systematically diluted to insure that the absorption spectra were linear with concentration according to Beer's law. The procedure used would readily identify if aggregation / precipitation was a problem. The estimated error in extinction coefficients was $\pm$ 10% .

2.5.2 Temperature-Dependent Absorption Spectra

Temperature dependent absorption spectra data were obtained using a thermostatted Hewlett Packard diode array 8452A spectrophotometer interfaced with a computer (PC) system with HP 89532A software. Temperature was controlled by using a refrigerated circulating bath, (NESLAB) RTE-8. The solution was stirred in a 1.0 cm quartz cuvette by pumping N_2 gas, and the temperature of samples was monitored using a thermoelectric voltage in millivolts and using a reference table that conformed to NIST standards to convert voltage to the corresponding temperature. The sample was equilibrated at each temperature for 15 min before the spectroscopic measurement. The author thanks Dr. L. K. Thompson for loan of the temperature bath.

2.5.3 ^{1}H NMR and Temperature-Dependant ^{1}H NMR

Proton nuclear magnetic resonance (^{1}H NMR) spectra were obtained using a Bruker Avance 500 MHz NMR spectrometer, and all shifts are referenced to TMS. Temperature dependant ^{1}H NMR data were measured for BBIM in DMSO-d_6 (99.9 atom % D atom) using the same NMR spectrometer. Temperature was increased at 5 °C increments from 25 °C to 95 °C, and allowed to equilibrate for 10 min. The ^{1}H NMR spectra were taken at each desired temperature. The sample was then cooled to room temperature and the ^{1}H NMR spectra remeasured to insure that no adventitious side reactions had occurred at higher temperatures.

2.6 Excited State Measurements

2.6.1 Emission and Emission Quantum Yields

Emission and excitation spectra were obtained using a Photon Technology International (PTI) Quantamaster 6000 emission spectrometer. Excitation light was provided by a 175W Xe arc lamp. The emitted light was collected 90° to the excitation beam and detected by a Hammamatsu R-928 photomultiplier tube (PMT) in photon counting mode. The PMT was housed in a Products for Research (PR) water-cooled PMT housing. All measurements were recorded using a 1.0 cm quartz cuvette supplied by Starna. The schematic diagram of the Quantamaster 6000 emission spectrometer is shown in Figure 2.5. Emission and excitation spectra were corrected using correction factors supplied by the manufacturer. All components of the steady-state spectrofluorometer are illustrated in Figure 2.5.[7]

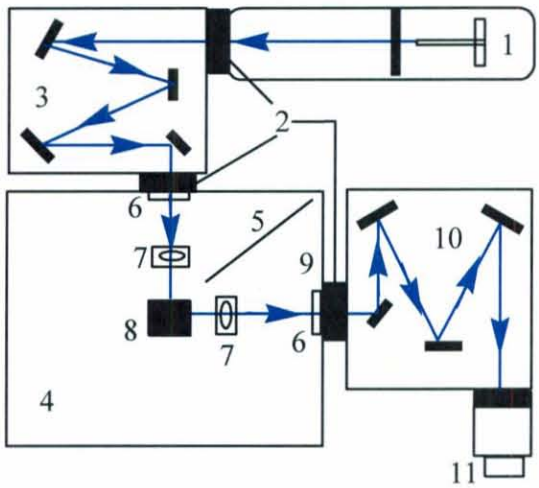

1 Arc lamp housing, **2** Adjustable slits, **3** Excitation monochromator, **4** Sample compartment, **5** Baffle, **6** Filter holders, **7** Excitation/emission optics, **8** Cuvette holder, **9** Emission port shutter, **10** Emission monochromator, and **11** PMT detector.

Figure 2.5. Optical system of the Quantamaster 6000 spectrofluorometer. The light source is usually a high pressure xenon arc lamp. The monochromator is used to select the excitation wavelength, and the fluorescence is detected through a monochromator by a photomultiplier (PMT).

Fluorescence quantum yields (ϕ_{em}) were determined by relative actinometry from corrected spectra of the samples. The samples were optically dilute with Abs. < 0.2 at the excitation wavelength. The quantum yields of standard solutions of quinine bisulfate were measured using aqueous H_2SO_4 (0.1 M) ($\lambda_{ex} = 365\,nm$, and ϕ_{std}= 0.54). The fluorescence quantum yield is given by Eq. 2.17 [8]

$$\phi_{em} = \phi_{std}\left(\frac{A_{std}}{A_{un}}\right)\left(\frac{I_{un}}{I_{std}}\right)\left(\frac{n_{un}}{n_{std}}\right)^2 \qquad (2.17)$$

where I_{un} and I_{std} are the sample and standard integrated emission intensities respectively; A_{un} and A_{std} are the sample and standard absorbance at the excitation wavelength respectively, and n_{un} and n_{std} are the refractive indices of samples and standard solvents respectively. A list of actinometers and the photophysical data are summarized in Table 2.1.

Table 2.1. Standard materials and their literature quantum yield values.

Compound	Solvent	Lit. ϕ_{em}	Em range, nm	Reference
Cresyl violet	Methanol	0.54	600-650	*J. Phys. Chem.*, 1979, **83**, 696
Rhodamine 101	Ethanol + 0.01% HCl	1.00	600-650	*J. Phys. Chem.*, 1980, **84**, 1871
Quinine bisulfate	**0.1M H_2SO_4**	**0.54**	**400-600**	*J. Phys. Chem.*, 1961, **65**, 229
Fluorescein	0.1M NaOH	0.79	500-600	*J. Am. Chem. Soc.*, 1945, 1099
Norharmane	0.1M H_2SO_4	0.58	400-550	*J. Lumin.*, 1992, **51**, 269-74
Harmane	0.1M H_2SO_4	0.83	400-550	*J. Lumin.*, 1992, **51**, 269-74
Harmine	0.1M H_2SO_4	0.45	400-550	*J. Lumin.*, 1992, **51**, 269-74
2-methylharmane	0.1M H_2SO_4	0.45	400-550	*J. Lumin.*, 1992, **51**, 269-74
Chlorophyll A	Ether	0.32	600-750	*Trans. Faraday Soc.*, 1957, **53**, 646
Zinc phthalocyanine	1% pyridine in toluene	0.30	660-750	*J. Chem. Phys.*, 1971, **55**, 4131
Benzene	Cyclohexane	0.05	270-300	*J. Phys. Chem.*, 1968, **72**, 325
Tryptophan	Water, pH 7.2, 25C	0.14	300-380	*J. Phys. Chem.*, 1970, **74**, 4480
2-Aminopyridine	**0.1M H_2SO_4**	**0.60**	**315-480**	*J. Phys. Chem.*, 1968, **72**, 268
Anthracene	Ethanol	0.27	360-480	*J. Phys. Chem.*, 1961, **65**, 229
9,10-diphenyl anthracene	Cyclohexane	0.90	400-500	*J. Phys. Chem.*, 1983, **87**, 83

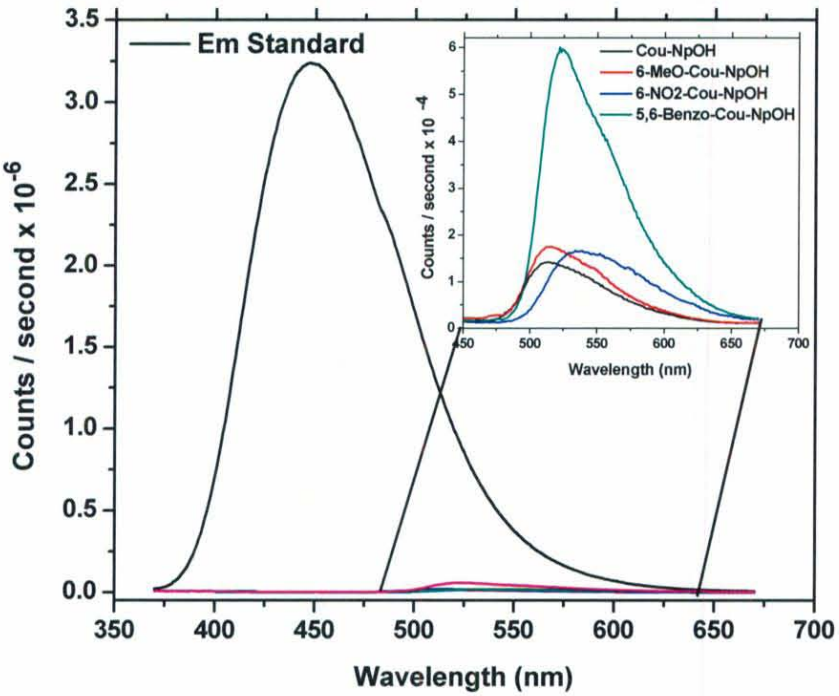

Figure 2.6. Fluorescence of Cou-NpOH and its derivatives measured relative to quinine bisulfate standard solution to determine fluorescence quantum yield at room temperature in a chloroform solution.

2.6.2 Emission Lifetime

The PTI laser subsystem equipped with a N_2 GL-3300 laser (fundamental line at 337.1 nm) was used as the excitation source. Data collection was accomplished using a proprietary stroboscopic technique which requires a 40 ns delay lime provided by a 40-foot fiber optic delay line. The intensity vs. time profiles are collected in a manner similar to a boxcar data acquisition system. The time intervals for data integration are computer controlled; and the kinetic trace is a histogram of the photons emitted per time interval at set time delays. The stroboscopic technique then allows acquisition of decay data that

occurs within the laser pulse. The pulsewidth of the N_2 laser is $450 \pm 50\ ps$ on a shot per shot basis. The integration coupled to prior acquisition of a high quality instrument response function (IRF) allows for the deconvolution of $\tau < 400\ ps$ to be extracted from the data, using the procedure outlined below.

The timing of the laser pulse and data acquisition was performed using a Stanford Research System Model DG535 four-channel digital delay pulse generator. Kinetic analysis of the lifetime data was accomplished using software provided by PTI or was exported and fit using Origin software. The IRF data were collected prior to data acquisition for the sample by use of a scattering solution (coffee mate in water).

2.6.3 Laser Flash Photolysis

The excitation source of the instrument utilized the third harmonic of a Q-switched Quanta-Ray Brilliant B DCR-2A Nd-YAG (neodymium-doped yttrium aluminum garnet) laser that generates pulses of light at 355 nm with duration of 8 ns.

Time-resolved transient absorption signals were acquired using pulsed laser excitation from a Quantel Brilliant B laser coupled to a tripling NLO crystal, for 355 nm (8 ns pulse width; 5-10 mJ/pulse; 20 Hz) pulsed excitation. The probe beam was oriented 90^{o} to the excitation source. The time sequence for the laser flash experiments is illustrated in Figure 2.8

2.6.3.1 Experimental Setup

The Applied Photophysics LKS 60 laser flash photolysis apparatus and the optical pulse profile are schematically shown in Figure 2.7 and 2.8 respectively.

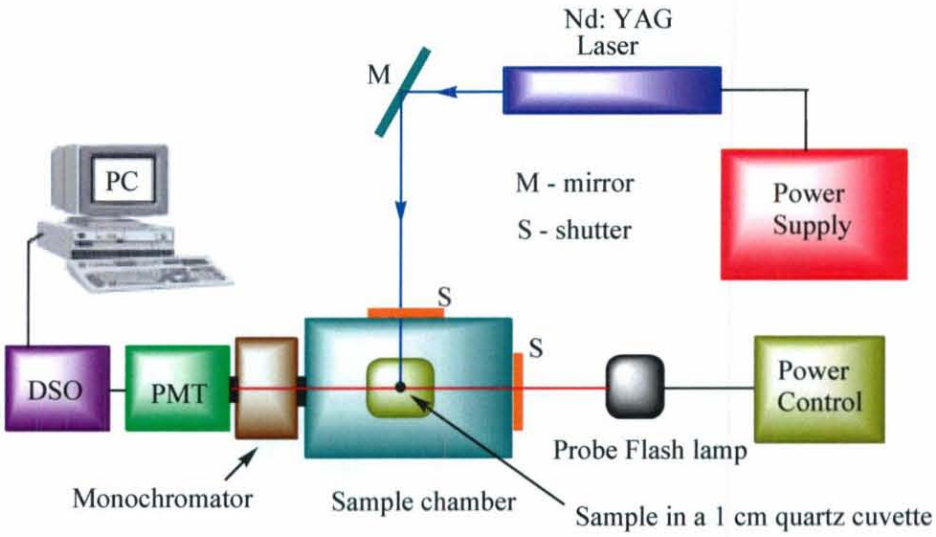

Figure 2.7. A schematic representation of the nanosecond transient absorption set-up.

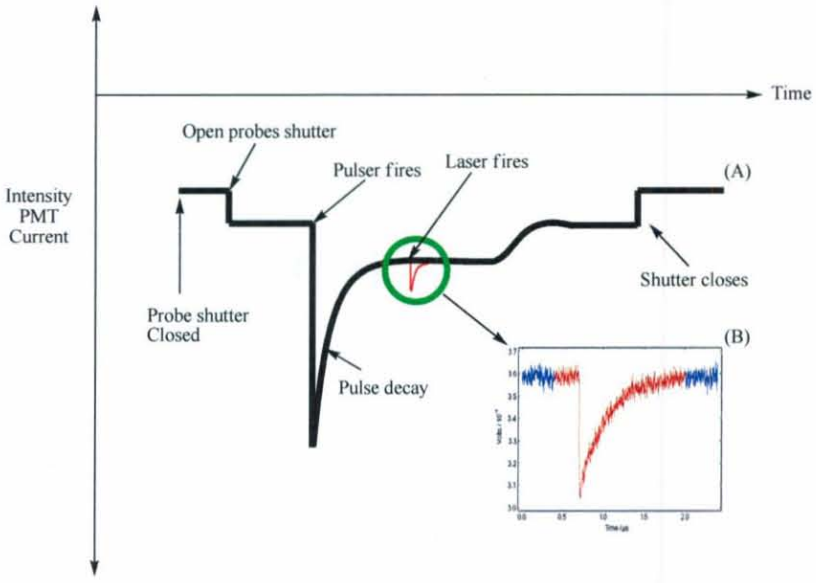

Figure 2.8. (A) Typical optical pulse profile generated from the probe pulse as detected at the photomultiplier (PMT). (B) is the transient species produced by the laser pulse.

The fundamental of a Nd-YAG laser is at 1046 nm (2.87×10^{14} s^{-1}), which is usually doubled (532nm) (5.64×10^{14} s^{-1}), tripled (355nm) (8.45×10^{14} s^{-1}), or quadrupled (266nm) (1.13×10^{15} s^{-1}). The excitation wavelength used in this work was the third harmonic of a 1064 nm pulse coupled to a frequency triple at 355 nm with pulse width 5-8 ns (*fwhm*). The output power of the laser was ~ 5-8 mJ/pulse at a repetition rate of 20 Hz. The probe beam was produced by a 150 W Xe arc lamp operated in pulsed mode. The detection wavelength was monitored using an f/3.4 grating monochromator and the resulting beam was detected by a five-stage photomultiplier tube (PMT) which was used to measure the intensity of the light at each wavelength of analysis. The PMT output is current vs time. The conversion to voltage vs. time was accomplished by terminating the PMT output across a 50 Ω resistor. In order to protect the sample against unnecessary radiation exposure between measurements, a shutter was placed between the lamp and the laser to prevent complications due to photostationary states. A digital oscilloscope recorded the signal resulting from the laser pulse. This signal was then sent to a computer provided by Applied Photophysics used to analyse the data.

A computer controlled the timing of the laser oscillator, Q-switch, lamp, shutters and trigger. Kinetic traces were obtained by signal averaging of a number of traces to get high spectral resolution. The lifetimes of transient absorption were averaged at each wavelength. The average decay curves were fit to a suitable exponential decay function. The transient absorption data were plotted as ΔA versus time using OriginPro 7 software.[9]

2.7 Data Analysis

2.7.1 Absorption Deconvolution

Deconvolution of the absorption spectral data may be necessary if information about the position, height and width of individual component bands is required. There are a number of methods designed for absorption band deconvolution. The method employed in this work to locate the maxima is moment analysis, allowing the bandwidth to vary until a satisfactory fit was found as described below.

The procedure for deconvolution of electronic absorption spectra can be described as follows:

- Create a table and a figure for wavenumber vs. absorption data.
- Determine the number of absorption bands that are necessary to describe the spectrum. Those numbers can chosen by the program using the first and second derivatives of the spectrum, dA/dv and d^2A/dv^2. Except for hidden bands, the first derivative is zero but the second derivative is negative.
- Calculate the band profile for each contributor by using the first and second derivatives of the absorption spectrum.

The energies for each of the transitions were fixed and only the bandwidths of the individual Gaussian curves were allowed to vary in the fitting procedure to achieve an adequate fit as shown in Figure 2.9. In some cases, manual adjustment is required if the spectrum has more than four or five strongly overlapped bands to make the calculated and experimental spectra coincide.

An example of deconvolution of an absorption spectrum is shown in Figure 2.9.

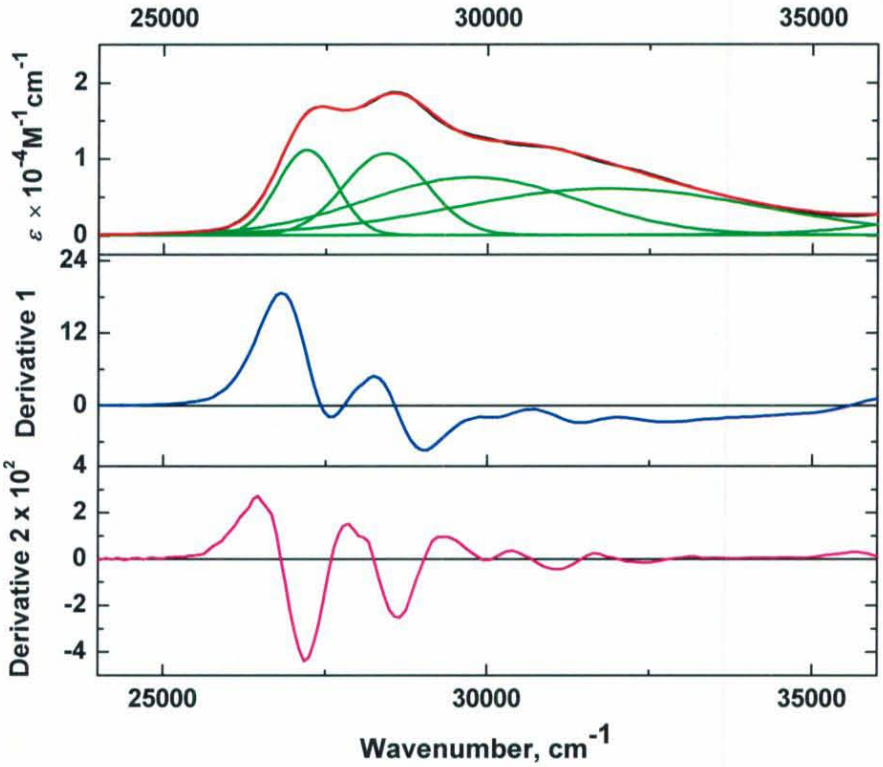

Figure 2.9. Deconvolution spectrum illustrating the energy of 4 transitions.

Figure 2.9 illustrates that the fitted and experimental spectra are seen to be in good agreement on the low energy side of the spectral band envelopes. In some other cases there is increasing uncertainty in the fits of the spectra as the energy is increased, where the calculated residuals start to exhibit differences between the experimental and fitted data. As such, a cautious interpretation of the fitting parameters in the higher energy transitions is warranted.

2.7.1.1 Mathematical Functions for Spectral Bands

The absorption spectral band is usually described by the frequency corresponding to the absorption maximum, the intensity or the molar absorptivity at the absorption maximum and the bandwidth which is usually determined at half height.

Absorption spectra usually have a Gaussian line shape, in which the overall absorbance, $\bar{A}$, at a wavenumber $\bar{\nu}$ can be expressed in terms of the Gaussian sum given by Eq 2.18.[10]

$$\bar{A} = A_0 + \sum_{j=1}^{n} \alpha_j \frac{A_{jmax}}{w_j \cdot \sqrt{\frac{\pi}{2}}} exp\left[-\frac{2(\bar{\nu} - \nu_j)^2}{w_j^2}\right] \qquad (2.18)$$

Where the $\bar{A}$ value can be determined experimentally, A_{jmax} is the total area under the curve from the baseline for an individual absorption band, α_j is the fraction of the i^{th} component and ν_j is the position of the peak's center, w is 2 "sigma", approximately 0.849 the width of the peak at half height.[11] The local maximum of an individual Gaussian curve is given by Eq 2.19.[10,12]

$$\bar{A} = A_0 + \frac{A_{max}}{w \cdot \sqrt{\frac{\pi}{2}}} exp\left[-\frac{2(\bar{\nu} - \nu)^2}{w^2}\right] \qquad (2.19)$$

2.7.2 Emission Spectral Fitting

The emission spectral fits were based on a single mode Franck-Condon analysis of the reduced emission spectra.[13-15] The emission spectra were corrected with the emission abscissa converted by the method described by Parker and Rees.[16] The theoretical

quantity required is the number of photons emitted per energy interval. The spectral fitting program was generously provided by Juan Pablo Claude and uses procedures and algorithms described elsewhere.[17,18,19] The emission spectra fitting provides information on the electron vibration coupling constant or Huang-Rhys factor,[20] S, quantum spacing, $\hbar\omega$, the zero→zero energy gap, E_0, and the full width at half-maximum of the individual vibronic components, $\Delta\bar{\nu}_{1/2}$. As a result of the fitting procedure, the vibrational spacing, $\hbar\omega$, was fixed while the other emission spectral fitting parameters (E_0, S, and $\Delta\bar{\nu}_{1/2}$) were allowed to vary until a minimum was found.[18]

2.7.2.1 Physical Model

The emission spectral fitting can be carried out using one- and two-mode spectral fits.[13,15,18,21] For the emission spectra that have one accepting vibrational mode, the emission spectral fitting was carried out by using one-mode spectral fitting. The emitted light intensity, $I(\bar{\nu})$ at the average energy $\bar{\nu}$ in wavenumbers relative to the intensity of the 0-0 transition, is given by

$$I(\bar{\nu}) = \sum_{\nu_M}\left[\left(\frac{E_0 - \nu_M\hbar\omega}{E_0}\right)^3\left(\frac{S^\nu}{\nu!}\right)exp\left(-4ln2\left(\frac{\bar{\nu} - E_0 + \nu_M\hbar\omega}{\Delta\bar{\nu}_{1/2}}\right)^2\right)\right] \qquad (2.20)$$

where E_0 is the energy gap between the first vibrational level of the ground and excited states and $\hbar\omega$ is the quantum spacing for the medium frequency acceptor mode. The E_0 and $\hbar\omega$ parameters of the one-mode fits are described in Figure 2.10. The full-width at half-maximum of the individual vibronic components is $\Delta\bar{\nu}_{1/2}$ is given in cm^{-1}, and S is the electron vibration coupling constant or Huang-Rhys factor as given in Eq 2.21.[20]

$$S = \frac{M\omega}{2\hbar}(\Delta q)^2 = \frac{\lambda_i}{\hbar\omega} \qquad (2.21)$$

where M is the reduced mass of the atoms,[22] ω is the vibrational angular frequency, and λ_i is the intramolecular reorganizational energy.

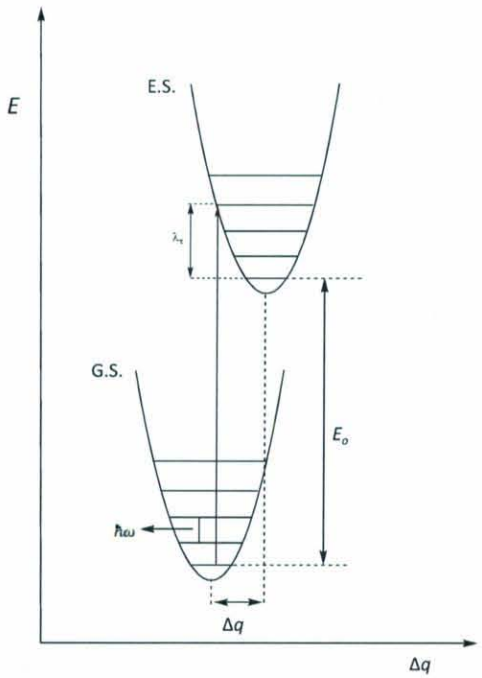

Figure 2.10. Two dimensional energy-coordinate diagram for one-mode spectral fitting illustrating the energy gap, E_0, quantum spacing, $\hbar\omega$, reorganization energy, λ_t, and nuclear displacement, Δq.

The observed emission spectra originate from the overlap of different transition states of the excited state. Figure 2.11 illustrates all of the emission spectral fitting parameters E_0, $\hbar\omega$, and $\Delta\bar{\nu}_{1/2}$

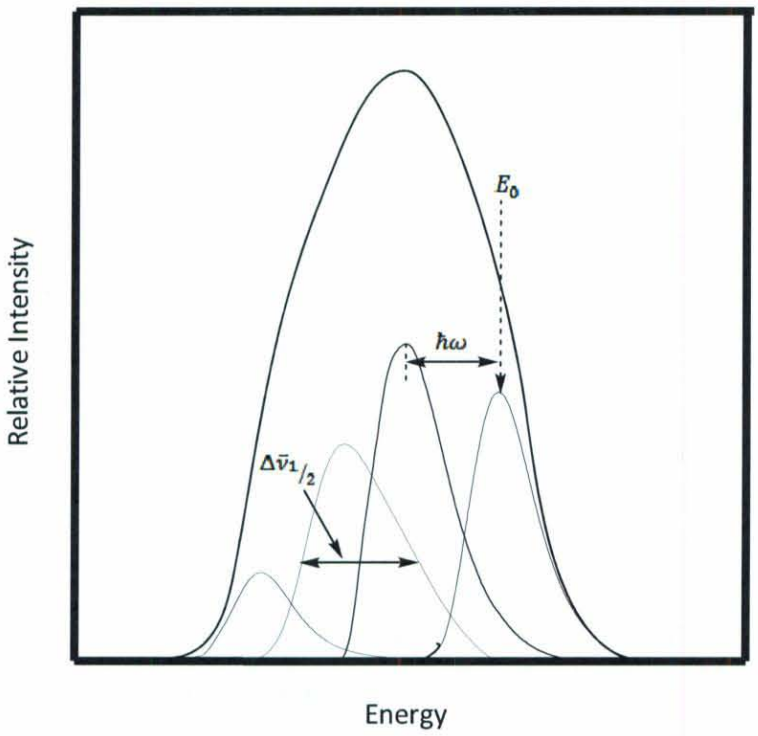

Figure 2.11. One-mode model of the emission spectra depiction of emission spectral fitting parameters.

The bandwidth at half-height ($\Delta\bar{\nu}_{1/2}$) is related to the contributions from the solvent reorganization energy, (λ_o), and low frequency solute modes treated classically ($\hbar\omega \ll k_BT$). It also includes inhomogeneous band broadening $\left(\Delta\bar{\nu}_{1/2}\right)_o$. In the classical limit, ($\Delta\bar{\nu}_{1/2}$) is predicted to vary with temperature as shown in Eq 2.22.[23]

$$\lambda_o = \frac{\left(\Delta\bar{\nu}_{1/2}\right)^2}{16k_BTln(2)} \qquad (2.22)$$

2.7.3 Kinetics

2.7.3.1 Time Resolved Data Analysis

The analysis equations and the procedure for deconvolution of $(I(t))$ from the laser required removal of the temporal convolution distortion contained in the IRF measurements. Where the lifetime of the excited state is less than the laser pulse time, the assumption that the laser excitation may be treated as a delta function is not valid. The IRF is recorded using laser scatter which yields the time profile of the laser pulse. The convolution of the instrument response function is given by Eq 2.23.[24]

$$I(t) = \int_0^t D(s)L\,(t-s)ds \qquad (2.23)$$

where $I(t)$ is the recorded profile (fluorescence intensity decay at time t), $L(t)$ is the instrument response function (IRF), and $D(s)$ is the delta (δ) which models the laser excitation. For a single-exponential function, the time dependent intensity is given by

$$I(t) = A\,exp(^{-t}/_{\tau}) \qquad (2.24)$$

where τ is the decay time and A is the pre-exponential factor. Using equation 2.23 and 2.24 yields the following relationship which has been solved in closed form.

$$A\,exp(^{-t}/_{\tau}) = \int_0^t D(s)L\,(t-s)ds \qquad (2.25)$$

This provides a mechanism for removal of the IRF from the observed $I(t)$ time profile. For more complex decay data, the multi-exponential decay, the δ pulse response, is given by Eq 2.26.[25]

$$I(t) = \sum_{i=1}^{n} A_i\,exp(^{-t}/_{\tau_i}) \qquad (2.26)$$

A_i is the amplitude of the process that contributes to kinetic decay at $t = 0$ and τ_i is the associated lifetime for A_i.

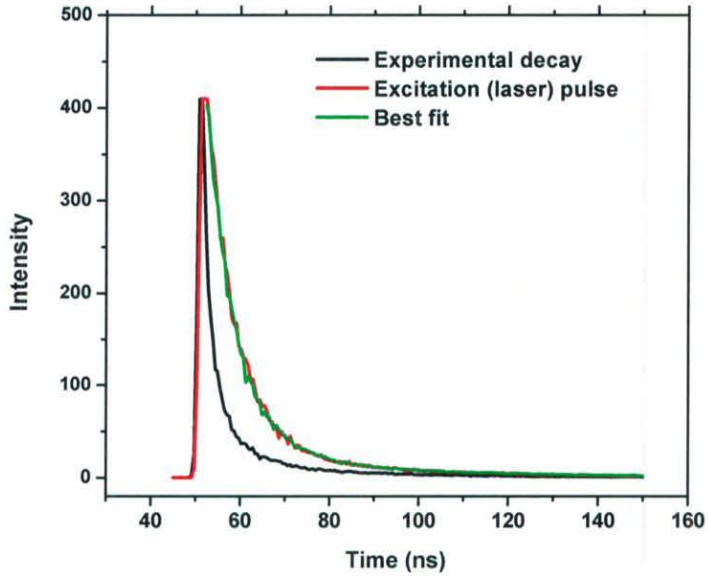

Figure 2.12. Laser pulse (red line), experimental decay (black line), the best numerical fit (true experimental function convoluted with laser pulse) green line.

The most widely used method to extract the true fluorescence response function from the deconvolution methods of analysis is the nonlinear least squares method (iterative deconvolution).

2.7.3.2 Transient Absorption

From the theoretical equations described above, the transient absorption from the transmitted light intensity passing through the sample as a function of time, I_t, can be calculated. The transmitted light intensity changes with time and the intensity of the incident light I_o is constant. By Beer's law, the absorbance before and after excitation is given by

$$\Delta A = A_{ES} - A_{GS} \qquad (2.27)$$

where A_{ES} and A_{GS} are the absorbance after and before excitation (pump pulse) respectively, and the transient absorption at a given wavelength λ is given by Eq 2.28.[26]

$$\Delta A \; or \; \Delta OD = -log \frac{I_t(t,\lambda)}{I_0(t,\lambda)} \qquad (2.28)$$

where I_t and I_0 are the probe intensity measured with and without the pump pulse respectively. The optical density change, ΔOD, obtained from nanosecond laser flash photolysis can be analysed using the Marquardt fitting algorithm producing transient lifetimes or rate constants. However, fitting of transient decay can involve single-exponential, dual-exponential fits, and multi-exponential assumptions. Once the ΔOD has been calculated, the lifetime can be extracted by single-exponential fits according to

$$\Delta OD = \Delta OD_0 exp - \frac{t}{\tau_1} \qquad (2.29)$$

where, ΔOD_0 is the initial absorbance difference. The rate constant values can be extracted as the reciprocal of the lifetime.

$$k = \frac{1}{\tau} \qquad (2.30)$$

Fitting of the absorption change can be conducted by employing a multi-exponential equation.

$$\Delta OD = A \; exp - \frac{t}{\tau_1} + B \; exp - \frac{t}{\tau_2} + C \; exp - \frac{t}{\tau_3} \qquad (2.31)$$

2.7.4 Global Kinetic Analysis

2.7.4.1 Introduction

Kinetic analysis using global analysis software to fit datasets is a powerful technique used in very diverse fields of science such as kinetic analysis[27,28] and equilibrium systems.[29,30] The data sets of multiwavelength absorption and emission data were analyzed by using SPECFIT/32™ (Spectrum Software Associates).[31,32] SPECFIT/32™ is based on the algorithms developed by Zuberbühler and coworkers described in references [33-36]. SPECFIT/32™ is a sophisticated, multivariate spectra treatment program for modeling and fitting a diversity of kinetic systems and equilibrium titration 3D data sets that are obtained from multiwavelength spectrophotometric studies. Typically 3D data sets consist of simultaneous measurements of absorbance versus wavelength. This program handles multiwavelength and multivariate spectra for equilibrium and kinetic systems with singular value decomposition (SVD) and nonlinear regression modeling to determine the stability constants from spectrophotometric titration data by using the Levenberg–Marquardt method.[37] The details and advantages of this program are clearly described by Ward *et al.*[38]

The simultaneous calculations of the equilibrium constants were completed using SPECFIT/32™ software. The 3D data obtained from absorption and emission for a multiwavelength spectrophotometric titration were used with the known concentration of the sample under investigation (host) which is maintained constant and the concentration of the ligand such as anions (guest) which varied. A new spectrum was obtained after each addition of guest, taking the dilution factor into account. The experimental titration data set was imported into the SPECFIT/32™ program as multiple data set files in CSV

format, giving the initial concentration of the host and the volume of the first addition of the guest. All titrations had the same volume added for each spectrum, and the SPECTFIT/32^{TM} program automatically calculated the new concentration of the host. The critical step is choosing the right model by knowing in advance the chemical nature of the system under investigation or the model that can be justified by the eigenvector factor analysis of the data set automatically performed by SPECFIT/32^{TM}. SPECFIT/32TM uses the Newton-Raphson method, solving equations numerically to determine the speciation equilibria for complexiметric equilibria. More details of the Newton-Raphson method can be found elsewhere.[39] In the model, various states of interactions between the host and the guest are represented by overall stability constants β_n, where n =1, 2, 3,..., n which are specified in terms of titration stoichiometry. The assumed model has two titratable components (M, L) involved in six different stoichiometric states, such as bbim (host) titrated with tetrabutylammonium acetate (guest), (see Chapter 4). In this model, there are two free states, M_1L_0 and M_0L_1 and four complexes M_1L_1, M_1L_2, M_1L_3, and M_1L_4, where M represents the first species and is denoted as a host, and L is the second species, which can be considered as a guest. For the spectroscopic titrations, all species except M_0L_1 are coloured and may contribute to the observed spectrum. For the bbim titrations with tetrabutylammonium acetate, the coloured species were the four complexes, M_1L_1, M_1L_2, M_1L_3, and M_1L_4. The equilibrium constants (β) may also be taken as fixed values.

2.7.4.2 Singular Value Decomposition (SVD)

SVD is a specialized technique for analysis of multivariate data in many matrix computations and analyses, and also is an important factorization of a rectangular real or complex matrix. Additionally, the SVD exposes the geometric structure of a matrix, an important aspect of many matrix calculations. The global fitting of time dependent data of spectroscopic results is made more efficient by SVD.[40,41]

Let Y denote a matrix A, containing spectral data for m wavelength and n time delays after photolysis, which can be expressed as the product of three matrices. The equation for singular value decomposition of Y is given as:

$$Y = USV^T \qquad (2.32)$$

where U and V both consist of columns of orthonormal vectors (V^T is the transpose of V), and S is an $n\ x\ n$ diagonal matrix. The factor S is the square root of the eigenvalues, which contains the non-negative singular values of Y. The term U is called a singular vector, (U_k), and V^T contains the elements of the singular vectors,(V_k). The nonzero elements of S are the so-called singular values. $S_k > 0$ for $1 \leq k \leq r$ and $S_i = 0$ for $(r+1) \leq k \leq n$ where, without loss of universality, $m \geq n$ and therefore $r \leq n$. The determination of the singular vectors can be obtained by high-to-low sorting of singular values. One important result of the SVD of Y is given by

$$Y^l = \sum_{k=1}^{l} U_k S_k V_k^T \qquad (2.33)$$

In order to calculate the SVD, it is necessary to calculate V^T and S by $Y^T Y$ as follows:

$$Y^T Y = V S^2 V^T \qquad (2.34)$$

and then follow by calculating U as given below

$$U = YVS^{-1} \qquad (2.35)$$

There are several more methods for calculating the SVD that have as good an accuracy and speed and which can be found in the literature on the mathematics and computation of SVD.[42,43]

2.7.4.3 Nonlinear Fitting of Multi-wavelength Data.

Non-linear least squares fitting is a mathematical optimization technique. This technique is an integral part of the analysis which attempts to find a best fit to a set of data by attempting to minimize the sum of the squares of the differences between the fitted function and the data which are called residuals. Therefore the goal of a nonlinear least squares fit is to find the parameters of an expression that yield the best fit between data pairs (X, Y) and the value of the expression for each value of X. The Levenberg-Marquardt algorithm is an iterative procedure that provides a numerical solution to non-linear least squares fitting.

Multidimensional nonlinear least-squares fitting requires the minimization of the squared residuals R' which are given by the differences between $C\hat{A}'$ and a reduced matrix (Y')

$$R' = C\hat{A}' - Y' \qquad (2.36)$$

$\hat{A}'$ is a linear least squares estimate which is given by

$$\hat{A}' = C^{+}Y' \qquad (2.37)$$

where C^+ is the pseudo-inverse of C, and C is the matrix of the concentration.

Non-linear least squares fitting parameters are determined using an iterative process by using a fitting algorithm to minimize the difference between the square of measured and calculated values (Y_{meas}, Y_{calc}), which is the sum of the squares of all components of R, as given by

$$ssq = \sum_i \sum_j R_{i,j}^2 \quad (2.38)$$

where ssq is the quality of the fit as given by the sum of squares, and R is the residual matrix. Fitting the non-linear parameters gives a measure of the stability constants of the system under investigation that define the matrix of concentration profiles C which is given by

$$ssq = \sum_i \sum_j R_{i,j}^2 = C \quad (2.39)$$

In spectrophotometric studies, the relationship between the concentrations and the measurements can be described according to Beer's law using the following equation

$$Y_{meas} = Y_{calc} + R \quad (2.40)$$

Non-linear least squares fitting parameters are a function of nonlinear parameters of K. The parameter K represents the equilibrium constants in the case of equilibrium systems under study and R is the matrix of rate constants in a kinetics system study. A shift vector Δk can be calculated by

$$\Delta k = (J^t J)^{-1} J^t R' \quad (2.41)$$

where J is the Jacobian.

$$J = \frac{\delta R}{\delta p} \qquad (2.42)$$

The shift vector Δpar is given by

$$\Delta par = -J^{+}R \quad (2.43)$$

where J^{+} is the pseudo inverse that can be calculated by

$$J^{+} = (J^{t}J)^{-1}J^{t} \quad (2.44)$$

2.7.4.4 Error Analysis

The Newton-Gauss algorithm allows a straightforward evaluation of the errors in the non-linear parameters.[44] The inverse of the Hessian matrix contains information about the standard errors and is given by

$$H^{-1} = (J^{t}J)^{-1} \qquad (2.45)$$

The standard error σ_i of the fitting parameters can be obtained by the equation

$$\sigma_i = \sigma_R\sqrt{d_{i,i}} \qquad (2.46)$$

where $d_{i,i}$ is the i^{th} diagonal element of the inverted Hessian matrix H^{-1}, and σ_R is the standard deviation of the measurement error in Y_{meas}.

$$\sigma_R = \sqrt{\frac{ssq}{df}} \qquad (2.47)$$

where df specifies the degrees of freedom, which is equal to $df = m - np$, where m represents the number of experimental values, and np is the number of optimised parameters. More details of the software and the related non-linear algorithms can be found in the literature.[45] In summary, global analysis has a unique power to provide a mechanism to analyze data and determine the rate constant and stability constants in a more powerful manner than other fitting methods. Global fitting includes a large number

of data points and besides fitting the global analysis has the ability to simulate product formation as a function of time.

2.7.5 Theoretical Calculation

DFT and TD-DFT theoretical calculations were performed by Shaheen Fatima, and Dr. Csaba Szakacs. The author thanks Shaheen Fatima, Prof. Erika Merschrod, and Dr. Csaba Szakacs for help in assigning the bbim and 3-AC based transitions. The MP2/6-31G(d) basis set was used for subsequent single point calculations. DFT and HF geometry optimizations and electronic structure calculations provided qualitative information about the HOMO-LUMO energy gap. Time dependent density functional theory (TDDFT) calculations were performed on the gas phase optimized geometry of the ground state (S_0) by using the B3LYP functional and 6-31+G(d) basis set. The theoretical calculations are included for completeness.

2.8 References

(1) Lakowicz, J. R. *"Principles of fluorescence spectroscopy"* 3ed.; Springer Berlin / Heidelberg: New York, 2006.

(2) Rohatgi-Mukherjee, K. K. *"Fundamentals of photochemistry"*; Wiley Inc.: New York, 1978.

(3) Khudyakov, I. V.; Serebrennikov, Y. A.; Turro, N. J. *Chem. Rev.* **1993**, *93*, 537-570.

(4) Turro, N. J. *"Modern Molecuar Photochemistry"*; University Science Books: Sausalito, California, 1991.

(5) Colin, C.; Ph.D. Thesis, Memorial University of Newfoundland and Labrador, 2000.

(6) Jamie, K.; M.Sc. Thesis, Memorial University of Newfoundland and Labrador, 2003.

(7) PTI [Web page] http://www.pti-nj.com/UVvis/UV-Vis.html.

(8) Demas, J. N.; Crosby, G. A. *J. Phys. Chem.* **1991**, *75*, 991.

(9) ORIGIN; OriginLap Corporation, One Roundhouse Plaza, Suite 303, Northampton, MA 01060, : USA, 2003.

(10) Zimina, G. M.; Zolotarevskii, V. I.; Krasnyi, D. V.; Revina, A. A. *High Energy Chemistry* **2004**, *38*, 226-230.

(11) Dong, J.-L.; Li, X.-H.; Zhao, L.-J.; Xiao, H.-S.; Wang, F.; Guo, X.; Zhang, Y.-H. *J. Phys. Chem. B* **2007**, *111*, 12170-12176.

(12) Caraman, I.; Vatavu, S.; Rusu, G.; Gasina, P. *Chalcogenide Letters* **2006**, *3*, 1-7.

(13) Caspar, J. V.; Meyer, T. J. *J. Inorg. Chem.* **1983**, *22*, 2444.

(14) Claude, J. P.; Meyer, T. J. *J. Phys. Chem.* **1995**, *99*, 51-54.

(15) Kober, E. M.; Casper, J. V.; Lumpkin, R. S.; Meyer, T. J. *J. Phys. Chem.* **1986**, *90*, 3722.

(16) Parker, C. A.; Rees, W. T. *Analyst (London),* **1960**, *85*, 857.

(17) Barbara, P. F.; Meyer, T. J.; Ratner, M. A. *J. Phys. Chem.* **1996**, *100*, 13148-13168.

(18) Claude, J. P., Ph.D. Dissertation, University of North Carolina at Chapel Hill,, 1995.

(19) Kestell, J. D.; Williams, Z. L.; Stultz, L. K.; Claude, J. P. *J. Phys. Chem. A* **2002**, *106*, 5768-5778.

(20) Huang, K.; Rhys, A. *Proc. Roy. Soc.* **1950**, *A204*, 406.

(21) Caspar, J. V.; Meyer, T. J. *J. Am. Chem. Soc.* **1983**, *105*, 5583-5590.

(22) Hsu, J.-H.; Hayashi, M.-t.; Lin, S.-H.; Fann, W.; Rothberg, L. J.; Perng, G.-Y.; Chen, S.-A. *J. Phys. Chem. B* **2002**, *106*, 8582-8586.

(23) Thompson, D. W.; Fleming, C. N.; Myron, B. D.; Meyer, T. J. *J. Phys Chem. B* **2007**, *111*, 6930-6941.

(24) In *Photon Technology International (PTI); [Web page]* *http://www.pti-nj.com/LaserStrobe/LaserStrobe.pdf*.

(25) Bernard, V. *"Molecular Fluorescence Priciples and Applications"*; Wiley-Vch, 2002.

(26) David, L. A.; Andret, A. D. *"An Introduction to Laser Specrtoscopy"* Kluwer Academic / Plenum Publishers: New York, 2002.

(27) Cruse, R. W.; Kaderli, S.; Karlin, K. D.; Zuberbuehler, A. D. *Journal of the American Chemical Society* **1988**, *110*, 6882-6883.

(28) Knutson, J. R.; Beechem, J. M.; Brand, L. *Chem. Phys. Lett.* **1963**, *702*, 501-507.

(29) Gampp, H.; Maeder, M.; Meyer, C. J.; ZuberbOhler, A. D. *Talenta* **1986**, *33*, 943-951.

(30) Kankare, J. *J. Anal. Chem.* **1970**, *42*, 1322-1326.

(31) SPECFIT/32; Spectrum Software Associates, M. B. P. R. W., Marlborough, MA 01752, USA, 2004, [Web page] http://www.biologic.info/rapid-kinetics/specfit.html., Ed.

(32) Binstead, R. A.; Jung, B.; Zuberbühler, A. D.; SPECFIT/32TM V3.0.33 Program for Multivariate Data Analysis Spectrum Software Associates Marlborough (USA). 1993.

(33) Maeder, M.; Zuberbu¨hler, A. D. *Anal. Chem.* **1990**, *62*, 2220.

(34) Gampp, H.; Maeder, M.; Zuberbu¨hler, A. D. *Trends Anal. Chem.* **1988**, *7*, 147.

(35) Gampp, H.; Maeder, M.; Meyer, C. J.; Zuberbu¨hler, A. D. *Talantu* **1985**, *32*, 257.

(36) Gampp, H.; Maeder, M.; Meyer, C. J.; Zuberbu¨hler, A. D. *Tulunta* **1985**, *32*, 95.

(37) Marquardt, D. W. *Journal of Applied Mathematics* **1963**, 11.

(38) Loosli, A.; Rusbandi, U. E.; Gradinaru, J.; Bernauer, K.; Schlaepfer, C. W.; Meyer, M.; Mazurek, S.; Novic, M.; Ward, T. R. *Inorganic Chemistry* **2006**, *45*, 660-668.

(39) Miguel, A.; Veron, H. *Ser. Mat.* **1992**, *22*, 159-166.

(40) Eckhart, C.; Young, G. *Bull. Am. Math. Soc.* **1939**, *45*, 118-121.

(41) Hendler, R. W.; Shrager, R. I. *J. Biochem. Biophys. Methods* **1994**, *28*, 1-33.

(42) Strang, G. *"Introduction to Linear Algebra"*; Wellesley-Cambridge Press: Wellesley, MA, 1993.

(43) Jessup, E. R.; Sorensen, D. C. *Journal on Matrix Analysis and Applications* **1994**, *15*, 530-548.

(44) Bevington, P. R. *"Data Reduction and Error Analysis for the Physical Sciences"*; McGraw-Hill: New York, 2003.

(45) Bazaraa, M. S.; Sherali, H. D.; Shetty, C. M. *"Nonlinear Programming: Theory and Algorithms"*; 3 ed.; John Wiley & Sons, Inc.: New York, 2006.

Chapter 3

Excited Electronic State Intramolecular Proton Transfer in 2,5-Bis(benzimidazoyl)-1,4-dihydroxybenzene (bbim)

3.1 Introduction

The main principles of proton transfer in the ground and excited electronic states are described below. The coverage of the literature is limited only to selected systems that illustrate the important features of proton transfer in ground and excited states.

3.1.1 Ground State Proton Transfer (GSPT)

Proton transfer (PT) between molecules in the ground state has a rich and diverse literature, Scheme 3.1.[1] Mechanistic details in aqueous media are in many respects well documented. For example, the free energies of proton transfer (usually quoted as pK_a) are known for a massive array of molecules.[2] The dynamics of proton transfer are not as well documented. For instance, the equilibrium for $H_2O \leftrightharpoons H^+ + OH^-$ has $pK_a =$ 14 and $pK_w = 15.7$ using the concentration description, $\left(K_w = \frac{[H^+][OH^-]}{[H_2O]}\right)$ with $k_f = 1 \times 10^{10} s^{-1}$and $k_r = 5 \times 10^{-3}\, M^{-1}s^{-1}$,[1] in aqueous media. If the reaction is studied in non-aqueous media, then pH, pK_a, etc are no longer meaningful and are poor indicators of acidity based on H_2O as a proton acceptor. However, the problem may be understood within the confines of proton donor-acceptor interactions, i.e. Brønsted acid-base theory or Lewis electron pair donor/acceptor interactions.

Marcus[3-5] understood that there was an intimate connection between thermally activated electron and proton transfer processes. The theoretical expressions for proton transfer from donor to acceptors may be understood by using concepts such as driving force (ΔG^o) and reorganization energies. For excited states, the kinetics of PT can be rapid, with the key microscopic elements in understanding PT being the quantum nature of nuclear motion and the electrostatic coupling with surrounding solvent molecules. In

this kinetic limit, the barrier for PT is dictated by solvent rearrangement and tunneling.

3.1.2 Excited State Proton Transfer (ESPT)

Absorption of a photon of light by a molecule results in the formation of a Franck-Condon excited state where electron density has been redistributed forming an electronic structure appropriate to the higher energy excited state. The newly formed excited state possesses the nuclear and solvent co-ordinates of the ground state and the electronic configuration of the excited state (Franck-Condon state). This is a consequence of electron motion being much faster than nuclear motion. With time ($10^{-15} \rightarrow 10^{-12}\ s$), changes in the electronic and nuclear configuration of the molecule will occur, along with longer time scale solvent dynamics ($10^{-12} \rightarrow 10^{-9}\ s$), dissipating energy as light (emission) and heat (non-radiative). The mechanisms for excited state decay may be broadly separated into two categories: radiative decay (k_r) with emission of light and non-radiative relaxation (k_{nr}) with the excess energy from photon capture being released to the solvent as heat. For molecules with an ionizable proton, another pathway for non-radiative relaxation is introduced which involves proton transfer to an appropriate acceptor as illustrated in Scheme 3.1. The excited state pK_a^* is defined as the ratio of k_+^*/k_-^*, with k_+^* the rate constant for H^+ transfer from donor (D) to acceptor (A), and k_-^*, the rate constant for the proton transfer from HA^+ to D^{-*}.

Proton transfer from an excited molecule to an acceptor is called Excited State Proton Transfer (ESPT). Chemical compounds featuring intramolecular hydrogen bonding within a molecule result in Excited State Intramolecular Proton Transfer (ESIPT). ESIPT occurs in molecules when the acidic hydrogen and the basic electron pair

of the molecules are spatially very close together. Scheme 3.1.

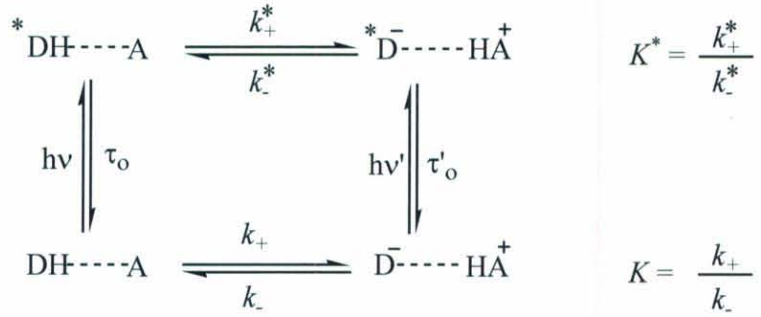

Scheme 3.1. Bimolecular proton transfer mechanism.

3.1.3 Excited State Intramolecular Proton Transfer (ESIPT)

ESIPT reactions have received a lot of attention and have been intensively investigated for several decades.[6-21] ESIPT occurs in molecules with the ground and excited states having two different structures. The relevant dynamics in this work involve both proton transfer (PT) and formation of an excited state tautomer. This class of ESIPT reactions is characterized by the transfer of a proton across a π −bonded molecular fragment which initiates the formation of a tautomer in an electronic excited state. The keto-enol tautomer isomeration is one subclass of possible ESPT and ESIPT excited state proton transfer reactions and is the focus of the investigations described below.

In the ground state, proton transfer (PT) to initiate a keto-enol tautermization is endergonic with positive Gibbs free energy change and the enol isomer is the dominating form. The enol form is stabilized by intramolecular hydrogen bonding and in order to induce isomerization, thermal energy is required in the adiabatic limit and photonic energy in the non-adiabatic limit. Upon photoexcitation, a proton transfer reaction takes place on an ultrafast time scale leading to rearrangement of the excited enol form to give

the excited "keto form" tautomer.[22]

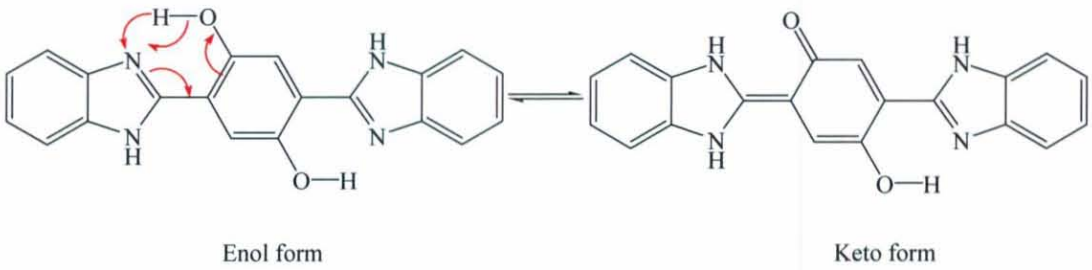

Figure 3.1. Structures of the tautomeric isomers of bbim.

The excited state keto isomer reverts to the ground state by release of energy either by radiative or non-radiative relaxation mechanisms yielding the keto tautomer with a ground state electronic configuration. Reverse proton transfer then results in reformation of the enol isomer as illustrated in Figure 3.2

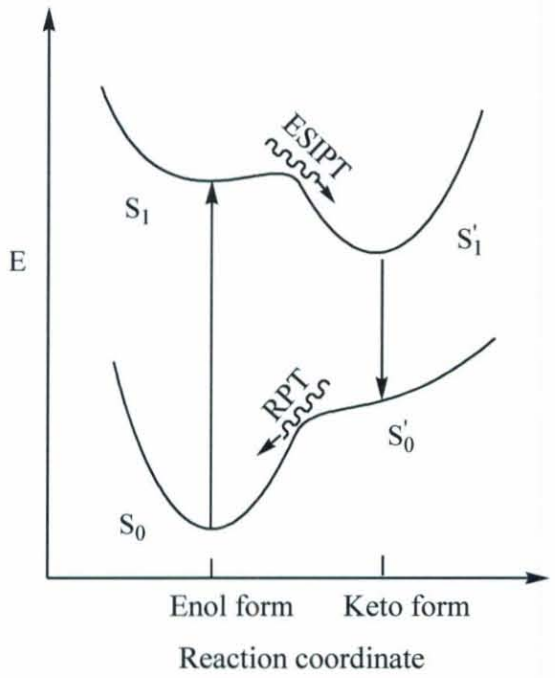

Figure 3.2. Potential energy diagram for the ESIPT mechanism.[23]

Increasing acidity and basicity of acid and base groups in a molecule following

electronic excitation is the driving force for increasing the rate of intramolecular proton transfer in the excited state.[24,25] These different species in the ground and excited states in the ESIPT sequence result in a large Stokes' shift between the ground state enol absorption and the excited state tautomer emission which accrue from the large structural changes. Based on these properties, molecules that undergo ESIPT have been utilized in device applications such as the proton-transfer laser,[26] in fluorescence micropatterning,[27] in chemosensors,[28] in photostabilizers,[29] in electroluminescent organic laser diodes,[30] and in DNA complexing agents.[31]

In molecular assemblies that possess both an acidic and a basic group in close proximity, an intramolecular hydrogen-bond is usually observed. Following light excitation, an intramolecular proton transfer between the acidic and basic sites in the molecule may occur.

For high polarity solvents, able to form a hydrogen-bond or other solvent-specific interactions with a solute molecule, ESPT is a bimolecular process with the solvent acting as a proton acceptor.[32,33] There are several studies where intermolecular proton transfer to solvent, or an added base, competes with intramolecular proton transfer.[34] These studies will be discussed in Chapter 4.

The discussion outlined above has focused on the general features of ground and excited state proton transfer reactions. Detailed investigations into structure reactivity relationships in ESIPT reactions have revealed several factors that dictate the dynamics involved in ESPT and ESIPT reactions. The relevant literature is outlined below.

3.1.4 Overview of Pertinent Literature for Proton Transfer

Proton transfer reactions have been extensively investigated and the literature published in this area is vast. Structures of investigated molecules relevant to this dissertation are shown in Figure 3.3 and the corresponding ground and excited state spectroscopic data are compiled in Table 3.1.

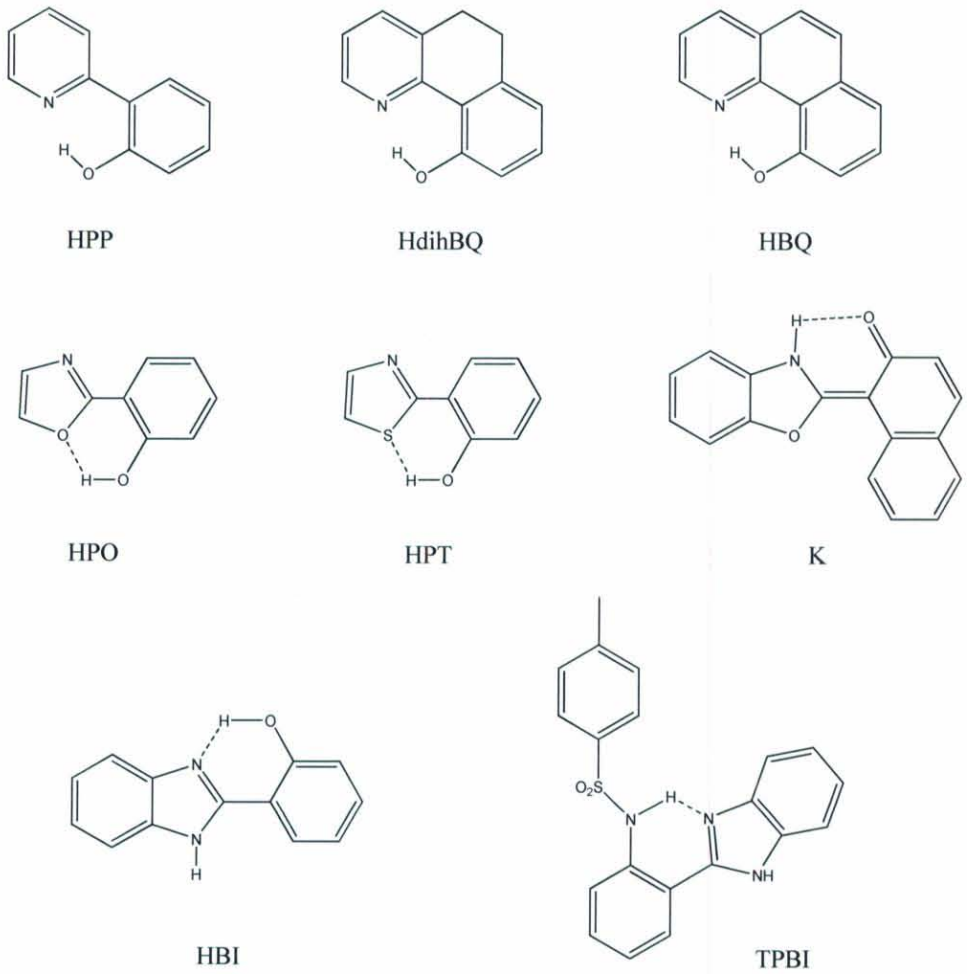

Figure 3.3. Literature structures of compounds that exhibit excited state proton transfer.

Table 3.1. Photophysical properties data from this thesis (bbim) and from literature examples.

Quantity	Solvent	λ_{Abs} (nm)	E_{op} (cm^{-1})	ε_{max} $M^{-1}cm^{-1}$	λ_{em}, (nm)	E_{em}, cm^{-1}	ϕ_{em}	τ, ns	pK_1 [(i)]	pK_1^*	pK_2 [(ii)]	pK_2^*
bbim	DMSO	318	31447	3.9×10^4								
		334	29940	5.2×10^4	427	23420	0.027	1.9				
		385	25974	3.5×10^4	550	18182	0.091	7.4				
		404	24752	3.8×10^4								
HPP [a]	Ethanol	318	31447	6.6×10^3	500	20000	-	1.9	4.1	7.8	10.2	7.1
HdihBQ[a]	Ethanol	320	31250	6.6×10^3	605	16530	<0.001	0.01	4.4	8.3	>12-13	-
HBQ [a]	Ethanol	370	27027	6.6×10^3	630	15873	0.0057	0.35	3.7	7.0	14.2	-
HPO [b]	Ethanol	306	32680	7.6×10^3	345	28986	0.0035	1.55	2.0	7.9	9-9.5	1.7-2.2
HPT [b]	Ethanol	326	30675	6.3×10^3	360	27778	0.010	0.69	2.7	6.6	8.8	0.54
K [c]	Benzene	356	28000	-	468	21400	0.11	0.96				
TPBI [d]	MeCN	299	33445	1.69×10^4	480	20833	0.49	6.04				
		315	31746	1.74×10^4								
HBI [e]	MeOH	279	35842	-					5.48		8.83	
		286	34965	1.62×10^4	356	28090	0.0623	0.34				
		316	31646	1.35×10^4	473	21142	0.1355	1.74				
		325	30770	-								

[(i)] Ground and excited state pK values of protonation (pK_1). [(ii)] Ground and excited state pK values of deprotonation (pK_2)
[a] Reference 65, [b] Reference 66, [c] Reference 42, [d] Reference 8 and [e] Reference 7.

3.1.4.1 Pioneering Studies

Over 50 years ago, Weller[35-37] first suggested the occurrence of the ESIPT reaction in methyl salicylate (MS). The author noticed dual fluorescence with an unusually large Stokes shift in the fluorescence emission spectrum of MS while the methyl ether derivative exhibited only one fluorescence emission peak with the expected mirror-image relationship between the absorption and fluorescence spectra. The author proposed that, on excitation, the ESIPT reaction occurred in the enol form between the oxygen in the carbonyl group and hydrogen of the OH group to give the keto form as shown in Figure 3.4 and that the fluorescence emission observed was from a tautomeric species (keto form) as shown in Figure 3.4.

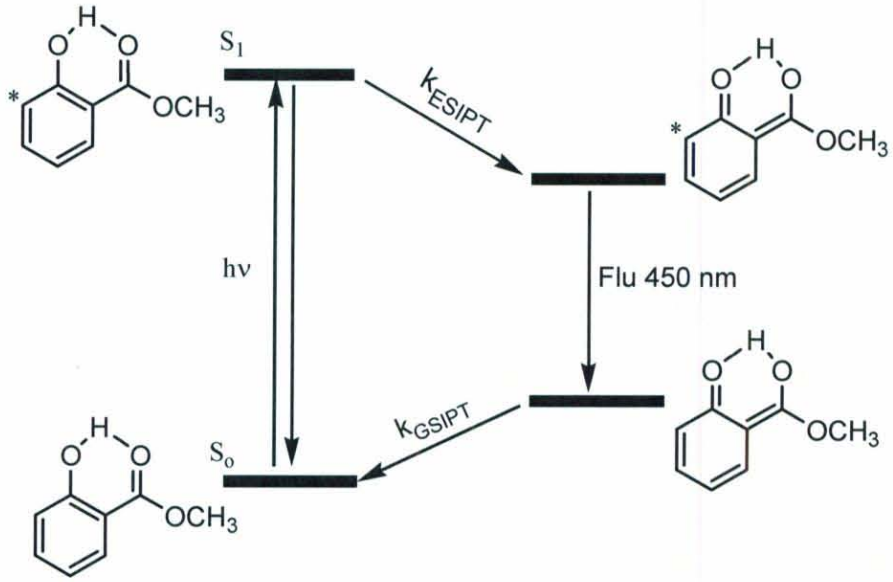

Figure 3.4. Potential energy diagram for the ESIPT mechanism of methyl salicylate.

One of the applications of ESIPT was noted by Acuna *et al.*[26]; the authors reported that o-hydroxybenzamide (salicylamide) was effective as a laser dye, in which excitation

of the salicylamide phototautomer generated by ESIPT produced intense stimulated emission at 439 nm. The excited phototautomer of salicylamide generated by ESIPT shows strong fluorescence with emission quantum yield (ϕ_{em}) = 0.27.

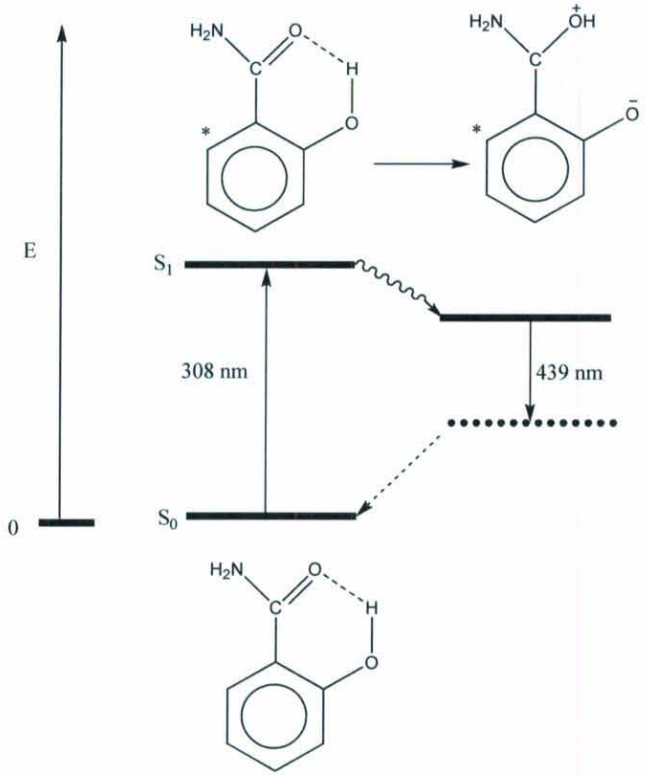

Figure 3.5. Proposed photochemical mechanism.[26]

The chemical structures of compounds containing intramolecular hydrogen bonds between a phenolic group and a heteroatom group such as oxygen, nitrogen or sulphur have been extensively studied primarily as a result of their use as photostabilizers in polymers. The role of a photostabilizer is to intercept a photon which undergoes rapid relaxation thereby extending the lifetime of a polymer and stabilizing the materials from photodegradation of the matrix. Incorporation of stabilizers into plastic prevents the

formation of radicals and other direct photoreactions of the matrix. For example, 2-(2′-hydoxyphenyl)benzoxazole (structure HBO shown below), has been studied by several authors,[38-42] who observed a strong tautomer emission with absent or very weak emission for the normal species.

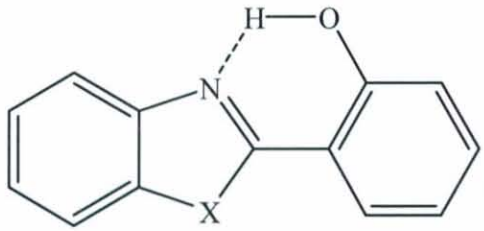

X = O or S

Scheme 3.2. Chemical structure of 2-(2′-hydoxyphenyl)benzoxazole (HBO) molecule.

Initially Itoh *et al.*[43] observed one fluorescence emission peak in the HBO emission spectrum which they assigned to the phototautomer, but this assignment was later disputed by Mordzinski *et al.*[40] who reassigned this species as a triplet state. Mordzinski assumed that ESIPT occurs from the excited enol form to produce the excited keto form which was deactivated by intersystem crossing yielding a triplet state. They found the rise time of this state to be about 200 ps at room temperature and about 10 ps below 160 K. These pioneering experiments are interesting due to the laser power dependence of the excitation. At high laser fluence, the kinetics become 2nd order, consistent with a bimolecular triplet-triplet annihilation process. The paper also contains a wealth of temperature dependent transient absorption data. However, the observed behaviour of the excited chromophores points to a complex excited state manifold whose dynamics are not clearly understood.

3.1.4.2 Solvent Effects on Inter and Intramolecular Proton Transfer

Abou-Zied *et al.*[44] have studied the ground state equilibrium, excited state dynamics and solvent dependent dynamics of HBO. These authors proposed that HBO exists in equilibrium between the syn- and anti-rotational isomers as shown in Scheme 3.3. Abou-Zied *et al.* conclude that the phenyl hydroxyl proton may interact with solvent forming either an intermolecular hydrogen bond or an intramolecular hydrogen bond between the benzoazole nitrogen and the phenyl hydroxyl proton. The intermolecular hydrogen bond (solvated form) possesses a longer lifetime in highly polar solvents like DMSO. In the case of the intramolecular hydrogen bond lifetime of the tautomer species, this is dramatically longer in a solvent of low polarity such as hexane relative to polar solvents such as MeOH and DMSO.

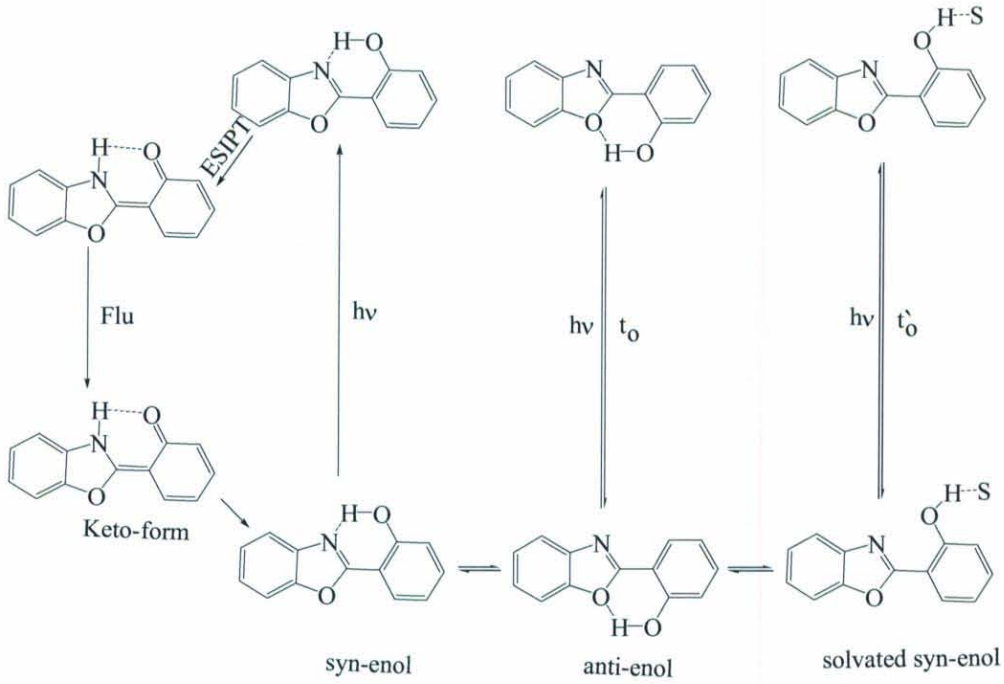

Scheme 3.3. Proposed photochemical mechanism describing excitation, proton transfer and ESIPT in HBO.[44]

Roberts *et al.*[19] have studied the HBI molecule in various solvents that facilitate the formation of an intermolecular hydrogen bond which weakens the intramolecular proton transfer as illustrated in Figure 3.6.

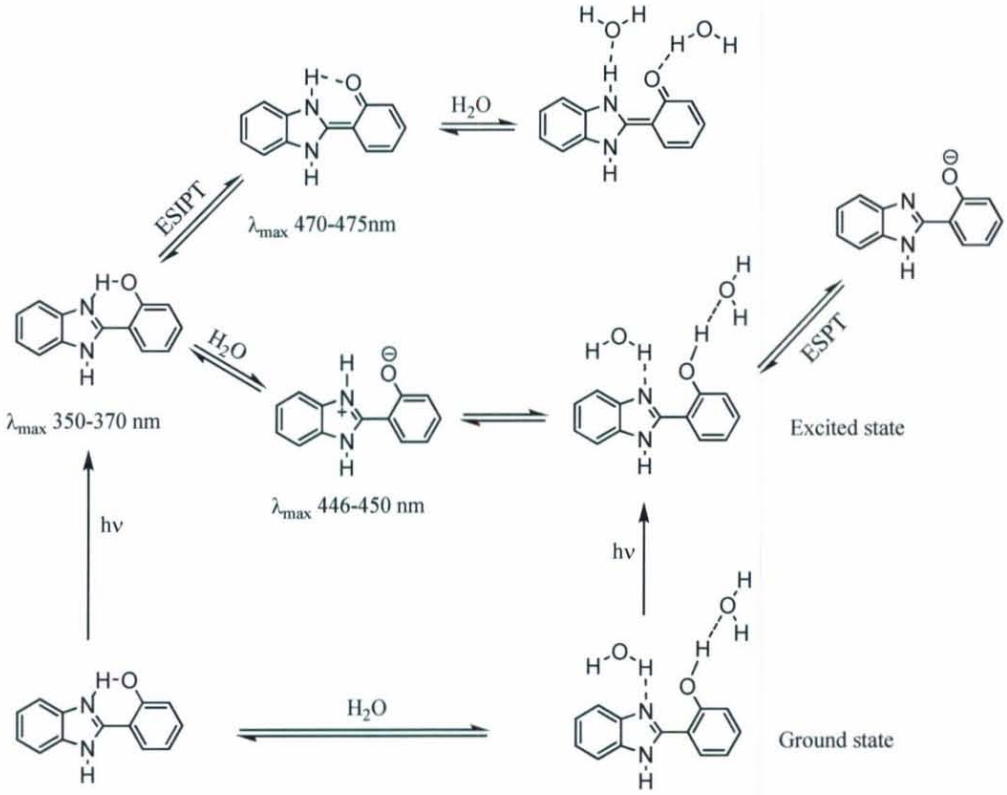

Figure 3.6. Ground and excited-state PT reactions of HBI in various binary solvents.[19]

Recently, Iijima *et al.*[45] proposed a new family of ESIPT molecules, 2-(2′-hydroxynaphthyl)benzazoles (1-3) shown in Scheme 3.4. These molecules revealed dual emission at 405 and 500 nm due to the keto-tautomer and an excited rotamer for compounds number 1 and 3; in contrast compound 2 exhibits one emission peak at 468 nm due to the keto tautomer form. Comparing compounds 1, 2 and 3 with HBO, it is seen that 1, 2 and 3 contain the naphthalene moiety which leads to an extension of the

aromatic ring structure. The naphthalene ring should decrease the energy gap between the ground and excited states for the keto-tautomer which should cause a red shift in both the absorption and fluorescence bands, but emitted fluorescence from the excited keto-tautomer was observed at shorter wavelengths than for the HBO compound. The authors conclude that the introduction of the naphthalene moiety in place of the phenol moiety increases the energy gap between the ground and excited states for the keto-tautomer. The authors could not give a plausible mechanism for these effects.

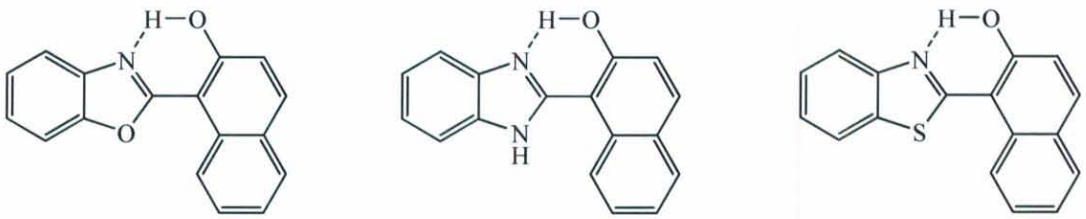

(1) (2) (3)

Scheme 3.4. Chemical structures of 1, 2 and 3 molecules.[45]

3.1.4.3 1 Photon-2 Proton Transfer: Single vs Double Proton Transfer

Various experiments were performed by Anna Grabowska and her co-workers[10,11,14,20,22,46-48] to study the nature of the single and double proton transfer in the excited state. Double derivatives of benzoxazole, bis-2,5-(2-benzoxazolyl)hydroquinone (2,5-BBHQ) and bis-3-6-(2-benzoxazolyl)pyrocatochol (3,6-BBPC) were reported as dually fluorescent systems. The 2,5-BBHQ undergoes an excited state single proton transfer (SPT) producing the keto tautomer and might also produce zwitterionic or biradical structures. In contrast, 3,6-BBPC was reported to undergo an excited state double proton transfer reaction producing the diketo tautomer. Figure 3.7.

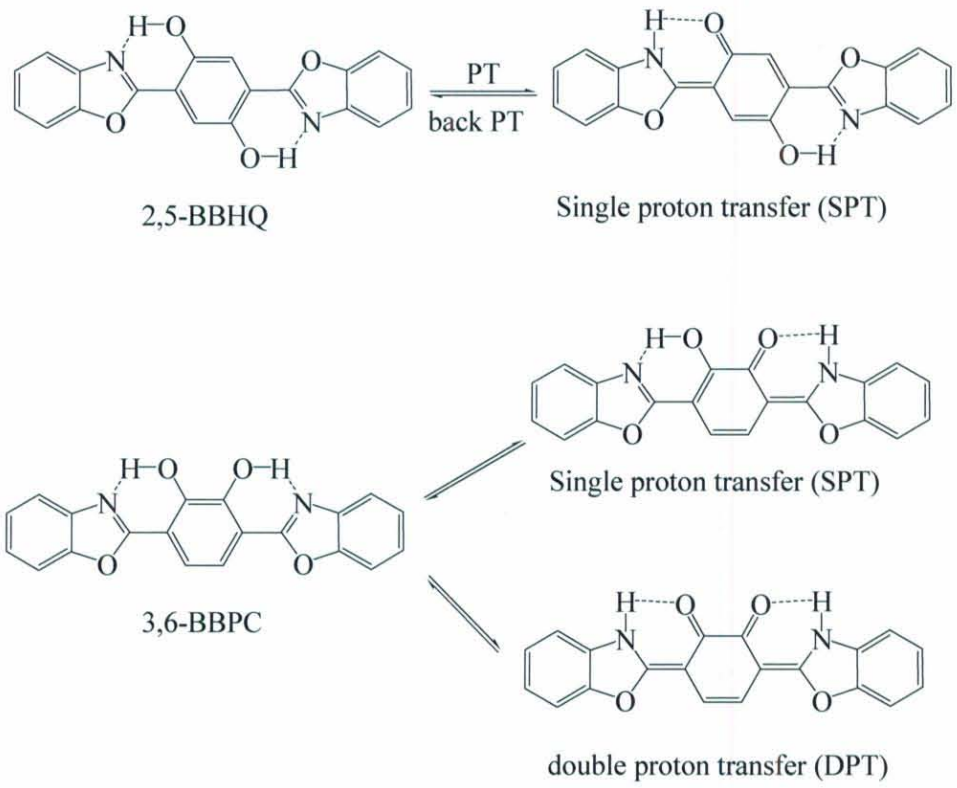

Figure 3.7. Single and double excited state proton transfer in 2,5-BBHQ and 3,6-BBPC respectively.

Picosecond transient absorption difference spectra of 2,5-BBHQ and 3,6-BBPC were reported, which gave a negative absorption or a prompt bleach at 645 nm and revealed a positive absorption peak at 560 nm for 2,5-BBHQ. In the 3,6-BBPC system a prompt bleach at 550 nm, a prompt absorption peak at 490 nm, and a broad absorption peak at 600-770 nm were observed. These results were assigned as due either to a single or a double proton transfer as shown above in Figure 3.7.

Weiß *et al.*[49] have suggested that 2,5-BBHQ undergoes double proton transfer at the two ESIPT reactive sites instead of single proton transfer. The authors said this argument was confirmed by semiempirical quantum chemical calculations. For more

details see the reference.

Grabowska *et al.*[10,11] have discussed the computational methods used to study the proton transfer processes in the first excited singlet state of both 2,5-BBHQ and 3,6-BBPC. The computational study demonstrated that 2,5-BBHQ and 3,6-BBPC exhibit only single proton transfer in the excited state in each case, because the di-keto tautomer has on a relative basis a much higher excited state energy.

3.1.4.4 Theoretical Calculations and Investigations

Photoinduced intramolecular charge transfer (ICT) and ESIPT in HBO were investigated theoretically by Sun *et al.*[50] The authors found that HBO is a planar molecule due to a strong intramolecular hydrogen bond. Upon excitation intramolecular proton transfer takes place and causes a change in the HOMO and LUMO energies and alters the electron density of the HOMO as illustrated in Figure 3.8.

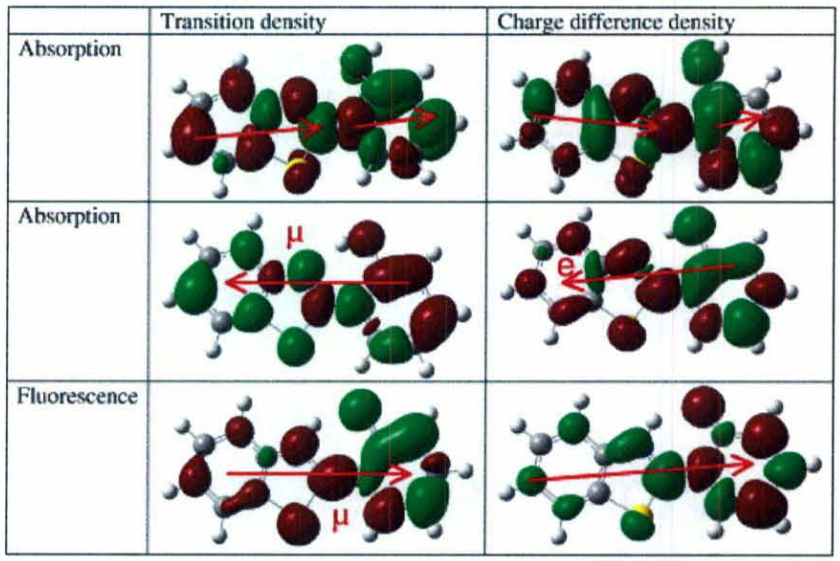

Figure 3.8. Transition density and charge difference density for the normal, enol and keto forms.[50]

2-(2′-hydroxyphenyl)benzimidazole (HBI) has been investigated in the ground and excited state by several authors.[51-54] Mosquera *et al.*[34] have suggested that HBI exhibits ground state tautomeric equilibria between the enol form and the keto form in aqueous solution. The authors have studied the acid-base conformational equilibria of HBI in the ground state in aqueous solution as shown in Scheme 3.5

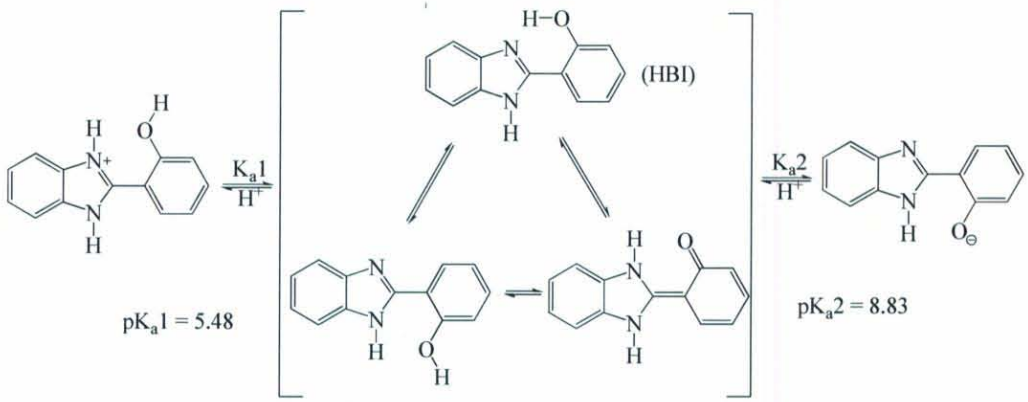

Scheme 3.5. Acid-base ground state conformational equilibria of HBI.[34]

3.1.5 Bbim Studies in this Chapter

In this work, investigations have been conducted into the structural dynamics of bbim using a combination of ^{1}H NMR spectroscopy and theoretical calculations. We also report the study of the ESIPT and CT behavior of bbim in DMSO and THF solvents.

Absorption maxima, extinction coefficients, emission spectra, quantum yields and emission lifetimes for bbim have been tabulated together with comparative literature data in Table 3.1.

3.2 Results

The 2,5-Bis(benzimidazoyl)-1,4-dihydroxybenzene (bbim) molecule has been investigated primarily with the objective of studying the ground state, excited state and the difference in the ground and excited state potential energy surfaces. In the following discussion, the ground and excited state properties will be described and the interaction of bbim with electrolytes will be documented.

3.2.1 Ground State Properties

Characterization of the solution structure using NMR spectroscopy is presented prior to discussing the excited electronic state properties. The crystal structure of bbim[55] shows a planar structure at room temperature ascribed to intramolecular hydrogen bonding which plays an important role in stabilizing the planar structure.

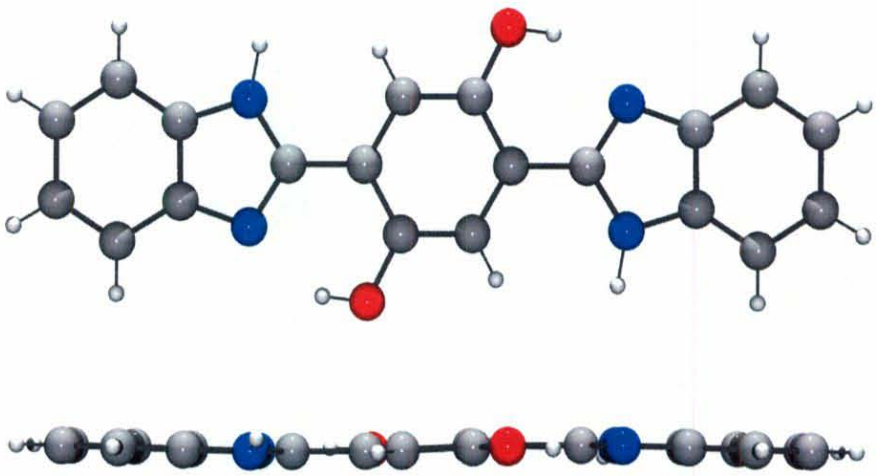

Figure 3.9. (Top) Front and (Bottom) side-view ORTEP representation of 2,5-bis(2-Benzimidazolyl)hydroquinone (bbim) (50% probability ellipsoids). Grey = carbon, light grey = hydrogen, red = oxygen, blue = nitrogen; lattice solvent DMF molecule been omitted for clarity.[55]

The theoretical and experimental IR spectra of bbim, shown in Figure 3.10, show very intense bands at 3020 cm^{-1} and 3300 cm^{-1} respectively, assigned as the asymmetric R-OH stretch. The intensity of the OH stretch provides the evidence for a hydrogen bonding interaction with the imidazole nitrogen which is the dominant H bonded motif at room temperature, Figure 3.10.[56,57]

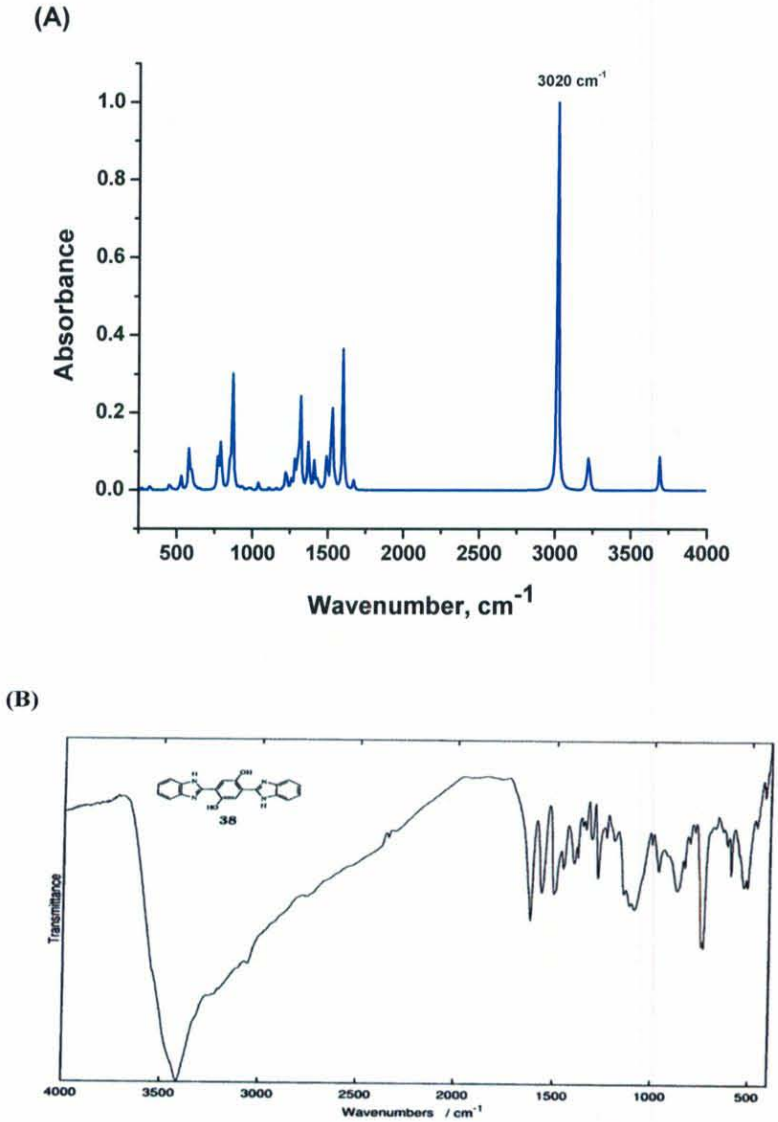

Figure 3.10. (A) predicted IR spectrum of the bbim molecule.[57] (B) experimental IR spectrum of the bbim molecule.[56]

The ground state structure of bbim at 298 K in DMSO-d_6 solution was probed using ^{1}H NMR spectroscopy. Assignment of the ^{1}H resonances and coupling constants are outlined in Figure 3.11.

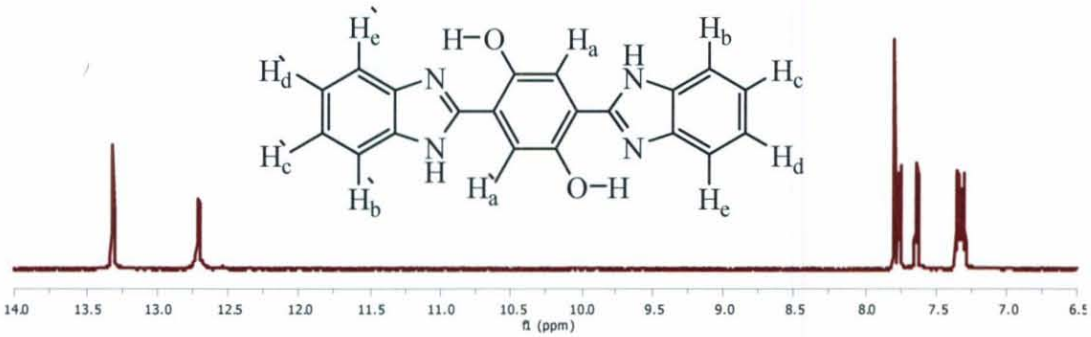

Figure 3.11. The ^{1}H-NMR spectrum of bbim, insert chemical structure of bbim. The peaks were assigned as: ^{1}H NMR: δ ppm 7.32-7.20 (H_c and H_d, m), 7.63 (H_e , d, $3J$ = 6 Hz). 7.75 (H_b,d, $3J$ = 6 Hz), 7.79 (H_a, s), 12.70 (NH, s), 13.31 (OH, s).

3.2.2 Temperature Dependent ^{1}H NMR

The ^{1}H NMR spectra temperature dependence for bbim in DMSO-d_6 solution was investigated from room temperature to 365 K. These experiments demonstrate that the rotation between the bisbenzimidazole and hydroquinone bond axis increases with temperature. As the temperature was increased above approximately 328 K for bbim, the signals at 7.32-7.20, 7.63, and 7.75 ppm became increasingly broader and band intensities were attenuated. Similar behaviour was observed for the NH and OH bands which shift toward TMS. However, cooling the sample back to room temperature restored the original peaks as shown in Figure 3.12.

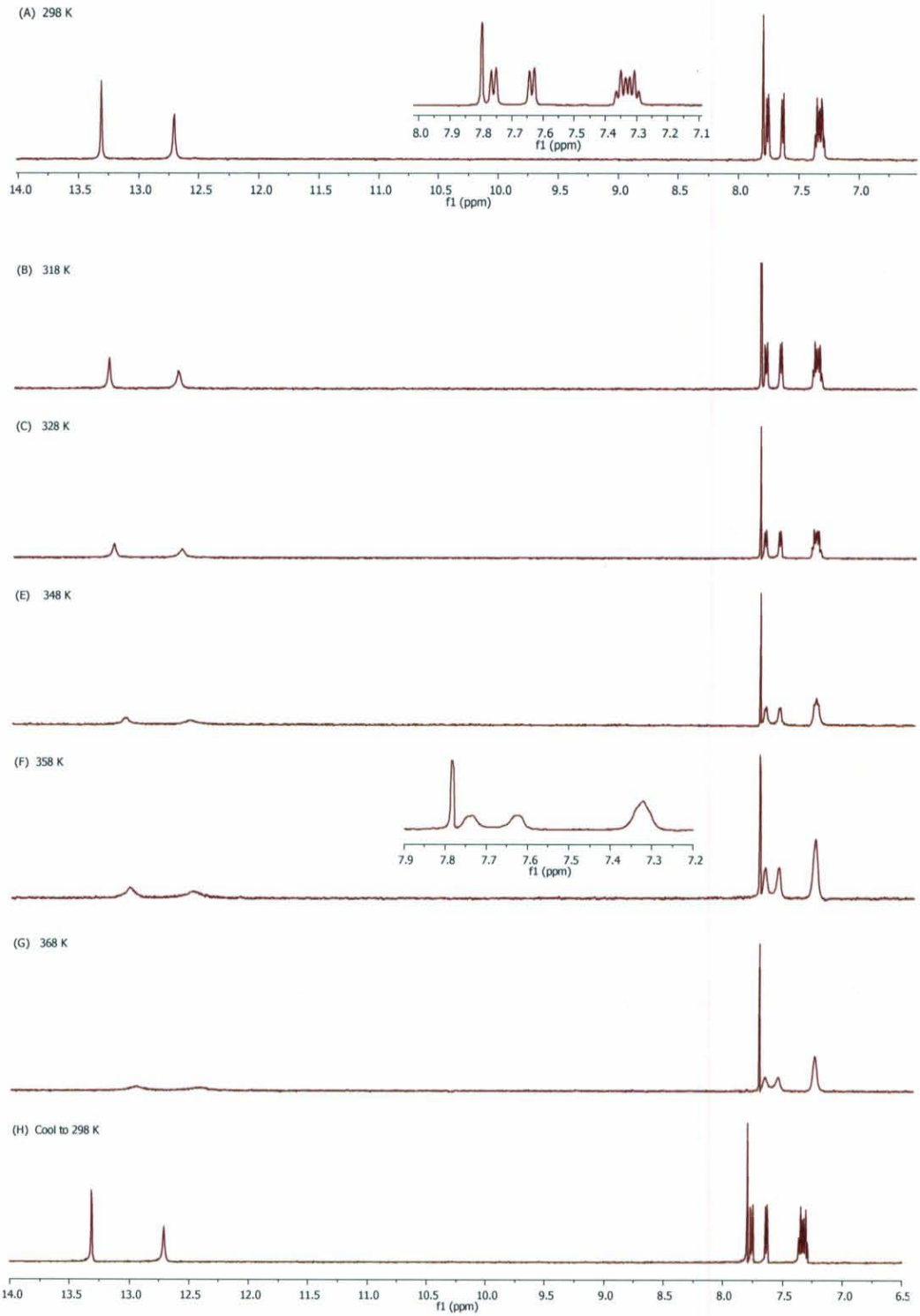

Figure 3.12. ^{1}H NMR temperature dependence of bbim in DMSO-d_6 solution.

The values of the chemical shifts for the hydroxyl proton of bbim DMSO-d_6 as a function of the temperature are given in Table 3.2. The corresponding plot of the observed chemical shift changes $\Delta\delta$ for OH and NH against T gave a linear fit (Figure. 3.13).

Table 3.2. ^{1}H NMR shifts as a function of temperature (±2 K) in DMSO-d_6

	δ, ppm[b]						
[a]Tempreature (K)	H_a	H_b	H_c	H_d	H_e	OH	NH
289	7.789	7.626	7.320	7.320	7.751	13.303	12.701
308	7.787	7.622	7.318	7.318	7.745	13.257	12.667
318	7.785	7.621	7.318	7.318	7.744	13.207	12.628
328	7.782	7.620	7.317	7.317	7.741	13.164	12.589
338	7.780	7.617	7.316	7.316	7.738	13.109	12.550
348	7.777	7.617	7.315	7.315	7.734	13.063	12.508
358	7.774	7.610	7.312	7.312	7.725	13.025	12.491
368	7.770	7.608	7.307	7.307	7.718	12.956	12.416

(a) The thermal equilibration time required between experiments was 5-10 mins based on the stability of the temperature reading.

(b) 500 MHz Bruker peaks are referenced relative to the DMSO-d_6 signal at 2.500 ppm. This peak arises since the isotopic enrichment of deuterium in the DMSO is slightly less than 100%.

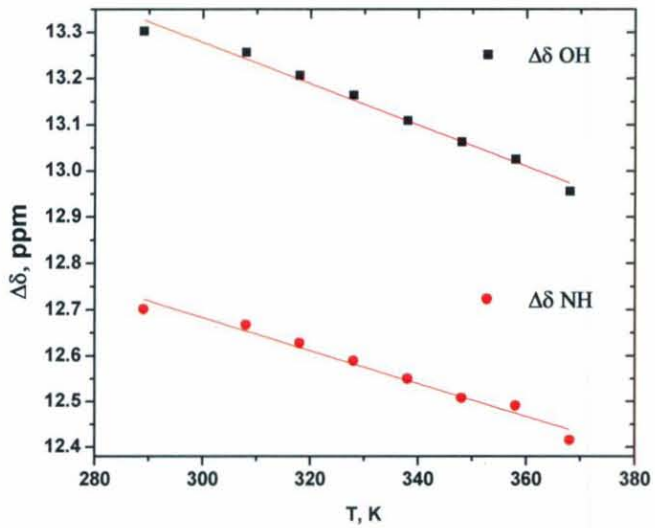

Figure 3.13. Temperature dependence of the ^{1}H NMR shifts assigned to the OH and NH groups of bbim in DMSO solution.

Table 3.2 shows that the chemical shifts of the hydroxyl proton shift with increasing temperature to higher field values. Figure 3.13 shows an inverse dependence of the chemical shifts on the temperature for bbim in DMSO-d_6 solution, leading to a nearly linear plot with a slope of -0.0044 ppm/°C with an increase in temperature (298-368 K). The chemical shift of the hydroxyl proton to higher field is attributed to both an increase in the exchange kinetics and an increase in conformational degrees of freedom with increasing temperature. The small value of the slope $\left(d\delta/_{dT}\right)$ means that bbim is associated with different compounds in equilibrium and that the equilibrium lies to the left side (enol-form) as shown in Scheme 3.6.

Enol form Zwitterion form

Scheme 3.6. Ground state intramolecular hydrogen bond equilibrium in bbim.

The rates of the dynamic chemical exchange processes (k_c) of intramolecular proton transfer along the strong internal hydrogen bond of the hydroquinone OH and benzimidazole subunits were estimated from the temperature dependence of ^{1}H NMR spectra as shown in Figure 3.13. Lifetimes of the contributing species (t_c), and the Gibbs free energies ($\Delta G^{\ddagger}$) at the coalescence temperature (T_c) are given in Table 3.3.

Table 3.3. Thermodynamic parameters of dynamic exchange of the proton on the phenol moiety to the amine on the benzimidazole for bbim at different temperatures.

Temperature	$\Delta\nu$	${k_c}^a$	${t_c}^b$
K	Hz	s^{-1}	ms
298	4.46	9.91	101
318	10.75	23.88	42
328	17.26	38.34	26
338	22.49	49.96	20
348	24.34	54.07	18
358	35.02	77.49	13
368	30.28	67.26	15

[a] The rate constants (k_c) were calculated at the coalescence temperature using Eq 3.1.[b] Lifetimes were calculated at the coalescence temperature (T_c) using Eq 3.2. Estimation of the activation energy barrier ($\Delta G^{\ddagger}$) at the coalescence temperature was made using Eq 3.3, ($\Delta G^{\ddagger} = 75\ kJmol^{-1}$).

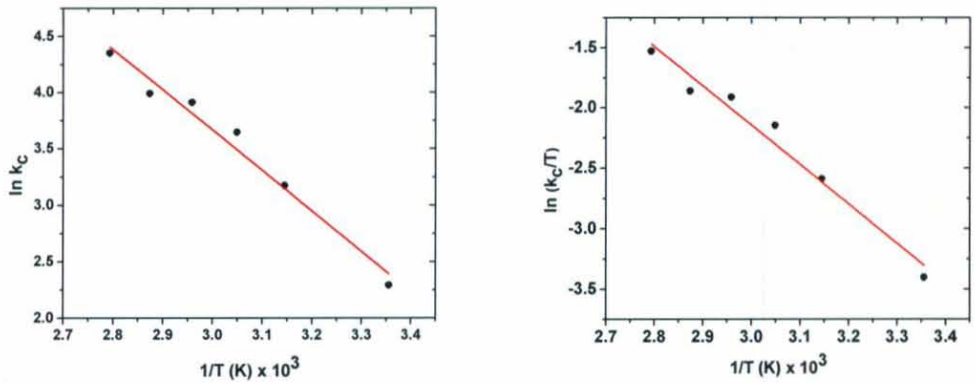

Figure 3.14. Left: an Arrhenius plot, the slope (-3580 K) of which gives the Arrhenius activation energy E_a. Right: an Eyring plot, the slope (-3254 K) and intercept (7.62) of which give the activation enthalpy $\Delta H^{\ddagger}$ and activation entropy $\Delta S^{\ddagger}$ respectively.

$$k_c = \frac{\pi \Delta \nu}{\sqrt{2}} \qquad (3.1)$$

where $\Delta \nu$ is the half linewidth of the resonance frequency of the OH NMR peak in Hz

$$t_c = \frac{1}{k_c} \qquad (3.2)$$

$$\Delta G^{\ddagger} = 19.143\, T_c \left(10.318 - log \frac{k_c}{T_c}\right) \qquad (3.3)$$

where T_c is the coalescence temperature (T_c = 358 K). The free energy of activation was determined by an *Eyring plot.*

$$k_c = \frac{k_B T}{h} exp\, -[\Delta H^{\ddagger} - T\Delta S^{\ddagger}]/_{RT} \qquad (3.4)$$

3.2.3 Conformational Analysis

AM1 and Hartree-Fock (HF) calculations for geometry optimizations and single-point energy (HOMO-LUMO gap) calculations were performed with Gaussian 03. Semi-empirical calculations for interpretation and graphical representation were carried out using Yet another Extended Hückel Molecular Orbital Package (YaEHMOP).[58] These

calculation tested a rotation about the dihedral angle between O and N (Figure 3.15), showing an H-bonding bridge maintained even past angles of 30°. However, deprotonation of bbim does not significantly change the character of the HOMO and LUMO energies following removal of one or more protons in any sequence. The calculations show there is no significant change in the HOMO-LUMO gap or in the total energy with the transfer of the hydrogen bonded proton from O to N.

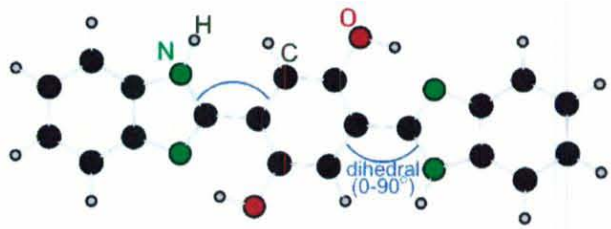

Figure 3.15. Idealized structure of the isomeric (enol-form) of bbim molecule indicating bonds about which rotation can occur.

The isomer (enol-form) and tautomer (keto-form) structures for bbim were optimized by using density functional theory (DFT) using the MP2/6-31G(d) basis set was used for subsequent single point calculations. The LUMO shows significant π-bonding character across the C-C bridge between fragments, suggesting tautomerization as shown in Figure 3.16.

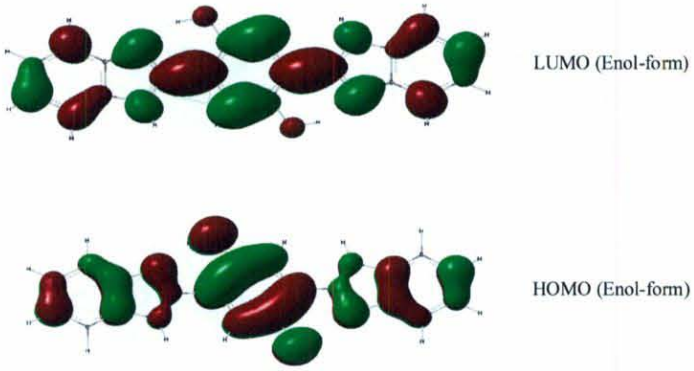

Figure 3.16. The structure of the HOMO and LUMO orbitals for the enol form, which is responsible for the isomer and tautomer energy transition in the emission spectrum of bbim.

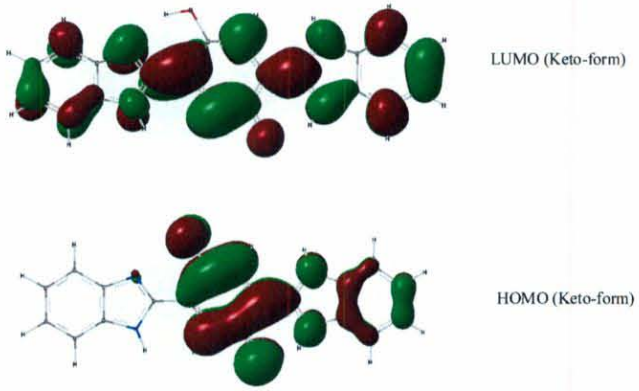

Figure 3.17. Calculated DFT structures of the HOMO and LUMO orbitals for the bbim keto tautomer structure.

3.2.4 Absorption Spectroscopy

The UV-Vis absorption spectra of bbim in DMSO, DMF and THF solutions are illustrated in Figure 3.19. The UV-Vis spectra are dominated by strong absorption bands at 404 nm (ε, = 38000 $M^{-1}cm^{-1}$), 385 nm (ε, = 35000 $M^{-1}cm^{-1}$), 334 nm (ε, = 52000 $M^{-1}cm^{-1}$) and 318 nm (ε, = 39000 $M^{-1}cm^{-1}$) respectively. The overall band envelopes are relatively insensitive to the nature of the solvents used. The limited solubility of bbim

precluded a more detailed solvent study. Spectroscopic data for bbim is summarized in Table 3.4.

A more detailed analysis of the UV-Vis spectrum of bbim by deconvolution of underlying transitions was undertaken. The UV-Vis spectral envelopes were deconvoluted using the procedure outlines in Chapter 2, section 2.5.1.

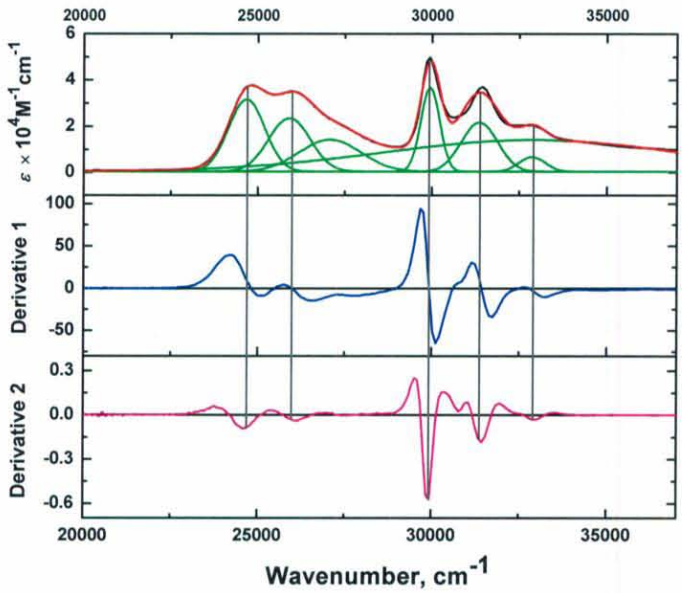

Figure 3.18. Absorption spectra showing the results of Gaussian deconvolution calculations for bbim in DMSO solution at 298 (± 2) K under 1 atm N_2.

The spectral envelope of bbim consists of 6 transitions as deduced from the deconvolution procedure. It is apparent that the complexity of the UV-Vis spectrum arises from a series of overlapping transitions and their vibronic components. The key transitions at 24750 cm^{-1} and 25975 cm^{-1} are assigned to $\pi - \pi^*$ transitions localized on the benzoimidazaole fragments of bbim. The transitions at 29940 cm^{-1} and 31445 cm^{-1} are due to the 1,4-dihydroxybenzyl bridge (H_2Q), and higher energy transitions are

vibronic progressions associated with the symmetric ring breathing mode of the bridging H_2Q with $v = 0 \rightarrow v' = 0$ at 318 nm; $v = 0 \rightarrow v' = 1$ at 334 nm and $v = 0 \rightarrow v' = 2$ at 385 nm respectively.

The benzoimidazole and H_2Q bridge are relatively uncoupled electronically (weak coupling limit); the intensity of the H_2Q progressions are directly due to the dominant planar conformation as a result of H-bonding.

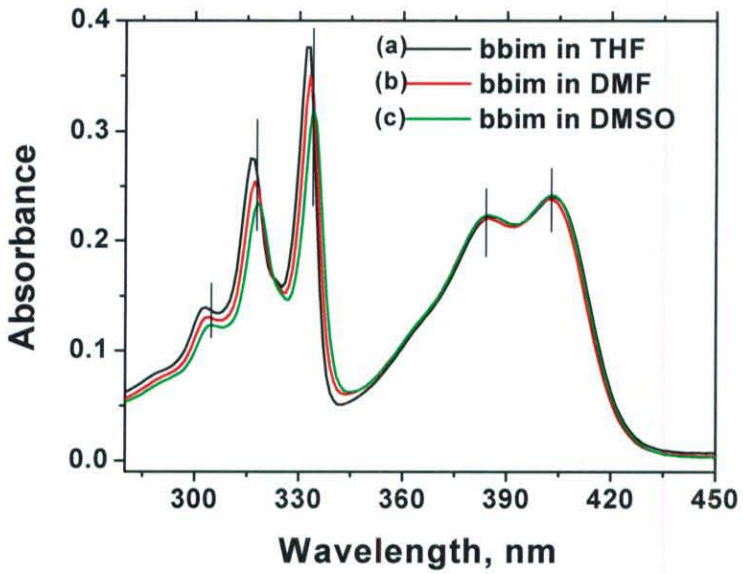

Figure 3.19. Absorption spectra of bbim in (a) THF; (b) DMF and (c) DMSO solvents under 1 atm N_2 298 (± 2) K.

3.2.5 Excited States Properties

3.2.5.1 Photochemistry

Air saturated DMSO solutions of bbim are extremely photosensitive as evidenced by the changes in the UV-Vis spectrum of bbim shown in Figure 3.20 upon extended broad band white light irradiation. There was a bleaching of the bands at 404, 385, 334

and 318 nm and the growth of two new bands at ~ 355 and 375 nm respectively. The photolysis of bbim was found to give the same final spectrum independent of the concentration. Attempts were made to characterize the products using UV-Vis spectroscopy and ^{1}H NMR. However, the NMR spectra illustrated a number of peaks due to a complex mixture of products, and no further attempts to characterize products was undertaken. In this work, a significant attenuation of the photodegradation of bbim was achieved by purging the DMSO solutions of bbim with N_2 for at least 50 minutes. Air saturated DMSO solutions of bbim that were not exposed to light lasted for weeks with no change in the UV-Vis spectrum.

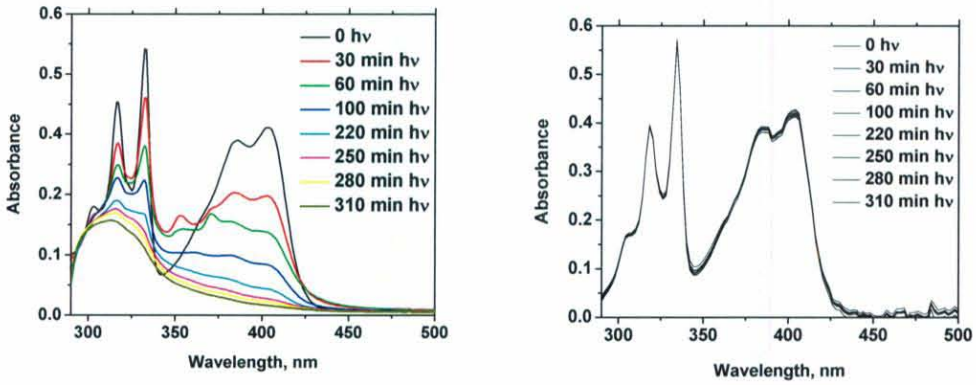

Figure 3.20. (Left) UV-Vis absorbance spectra of bbim in the presence of air before and after broad white light exposure. (Right) UV-Vis absorbance spectra of bbim in the absence of air at 298 (± 2) K under 1 atm 50 min N_2.

3.2.5.2 Emission/ Excitation/ Absorbance

Excitation of bbim (λ_{exc} = 404 nm) in N_2 purged DMSO solution gives rise to two major emission bands at 427 nm (23365 cm^{-1}) and 550 nm (18180 cm^{-1}). The excitation spectra of bbim (λ_{mon} = 427 and 550 nm) displayed identical band envelope shapes.

Interestingly, the absorption bands at 334 and 318 nm do not show vibronic progressions in the excitation spectra.

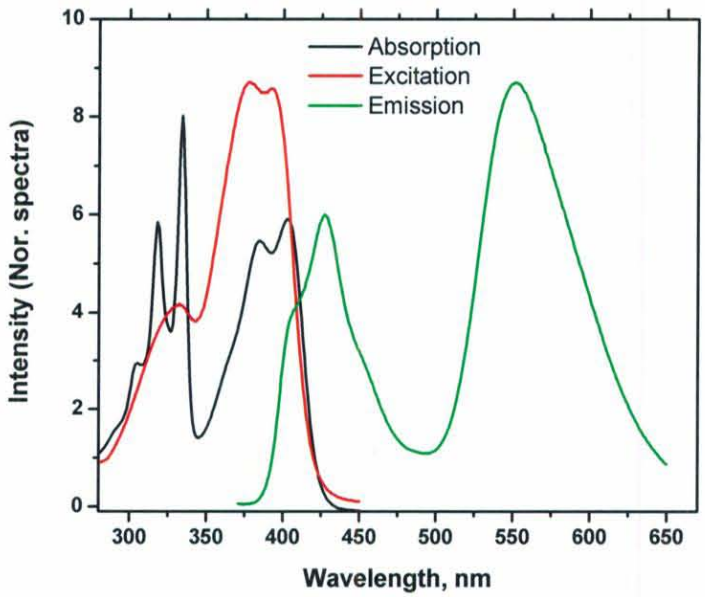

Figure 3.21. Absorption, excitation, and emission spectra of bbim in DMSO solution at 298 (± 2) K under 1 atm N_2.

From the spectral data shown in Figure 3.21, the following observations were made: excitation of bbim at $\lambda = 370$ nm results in dual emission with the high energy emission at 427 nm and long wavelength emission at 550 nm. The emission spectral envelopes were found to be independent of the excitation wavelength.

Comparison of the absorption spectra and excitation spectra monitored at 550 nm reveals that the vibronic progressions found in the absorption spectra are absent in the excitation spectra. The excitation spectral band envelope differed from that observed for the absorption spectra consistent with wavelength dependent non-radiative pathways.

3.2.5.3 Time-Resolved Emission

Laser flash emission experiments were performed to determine the lifetimes for the excited states of bbim. Following pulsed laser excitation at 337 nm (pulse width 350 ps), the emission decay kinetics were monitored at 428 nm and 550 nm. The emission decay kinetics after deconvolution from the laser pulse was adequately modeled by an exponential decay function (Eq. 3.5).

$$I_t = I_0 \exp -kt \qquad (3.5)$$

where I_0 and I_t are the emission intensity at time 0 and time t respectively. However, the rate constants were dependent on the monitoring wavelength, Figure 3.21. Monitoring the emission at 427 nm and 550 nm yielded k = 5.9($\pm$0.2) x 10^8 s^{-1} (τ = 1.9 ns), and k = 1.4($\pm$0.1) x 10^8 s^{-1} (τ = 7.3 ns) respectively with χ^2 close to 1.0. Nanosecond transient absorption experiments using 355 nm pulse excitation revealed that there were no long-lived transient species that might be assignable to any species such as a triplet based excited state between 360 and 650 nm.

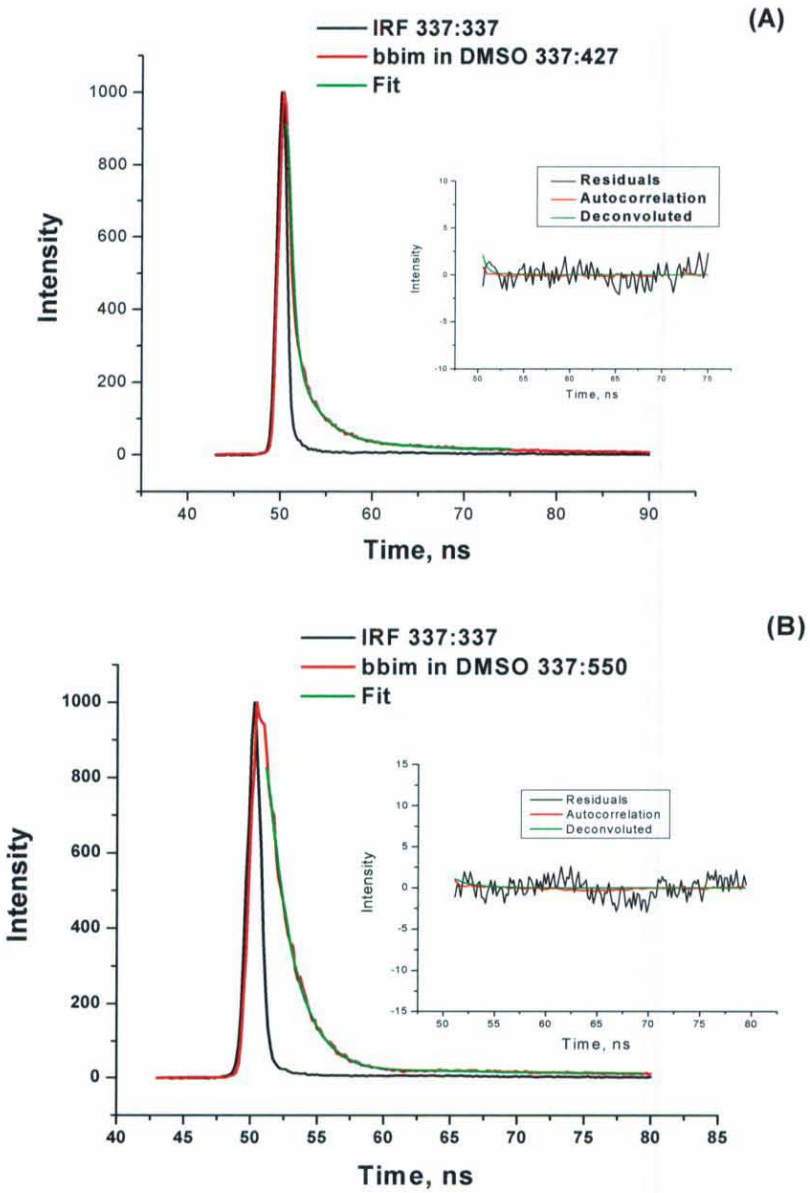

Figure 3.22. (A) Fluorescence decay of the enol-form bbim emission at 427 nm, (B) Fluorescence decay of the keto-form bbim tautomer emission at 550 nm in DMSO solution at 298 (± 2) K under 1 atm N_2.

Table 3.4: Ground and excited state parameters of bbim in DMSO and THF at room temperature.

bbim	DMSO	THF	Assignment
λ_{max} (ε, $cm^{-1}M^{-1}$)	304nm ($2.38x10^4$)	303nm	$\pi \rightarrow \pi^*$
	318nm ($3.87x10^4$)	316nm	$\pi \rightarrow \pi^*$
	334nm ($5.16x10^4$)	332nm	$\pi \rightarrow \pi^*$
	385nm ($3.48x10^4$)	385nm	$\pi \rightarrow \pi^*$
	403nm ($3.77x10^4$)	403nm	$\pi \rightarrow \pi^*$
λ_{max} (Em.)	427 nm	419 nm	Isomer (enol)
	550 nm	555 nm	Tautomer (keto)
Φ_{em}	0.027	0.0045	Φ_{enol}
	0.091	0.0053	Φ_{keto}
τ	1.9 ns	1.5 ns	τ_{enol}
	7.4 ns	6.4 ns	τ_{keto}
E_{ss}	1395 cm^{-1}	947 cm^{-1}	Isomer Stokes shift
	6632 cm^{-1}	6795 cm^{-1}	Tautomer Stokes shift

3.2.5.4 Emission Spectral Fitting

The emission spectra for bbim were subjected to Franck-Condon line-shape analysis as described in Chapter 2, and given by

$$I(\bar{\nu}) = \sum_{\nu_M} \left[\left(\frac{E_0 - \nu_M \hbar\omega}{E_0} \right)^3 \left(\frac{S^\nu}{\nu!} \right) exp\left(-4ln2 \left(\frac{\bar{\nu} - E_0 + \nu_M \hbar\omega}{\Delta\upsilon_{1/2}} \right)^2 \right) \right] \qquad (3.6)$$

where E_0 is energy of the $\nu' = 0 \rightarrow \upsilon = 0$ transition, $\hbar\omega$ is the quantum spacing and is the average energy of all vibrations that deactivate the excited state, $\Delta\upsilon_{1/2}$ is full width at half maximum for each individual vibronic component (typically S), and S is the electron-vibrational coupling constant or Huang-Rhys factor and the vibrational reorganization energy for the medium to high frequency modes. $\Delta\upsilon_{1/2}$ is given by

$$\left(\Delta\bar{\nu}_{1/2}\right)^2 = 16k_BT\lambda_o ln(2) \qquad (3.7)$$

where λ_o is the solvent reorganization energy. The model assumes that $\hbar\omega$ for the excited and ground states are similar and the equation is valid at the high temperature weak coupling limit ($k_BT \ll \hbar\omega$). The emission and fits are shown in Figure 3.23.

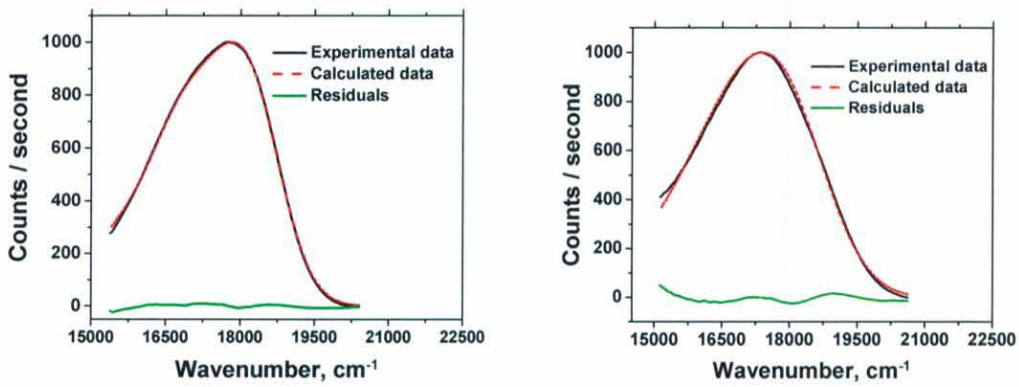

Figure 3.23. (Left) Corrected emission of the tautomer emission spectrum of bbim in DMSO solution at 298 (± 2) K under 1 atm N_2. (solid black line) and the corresponding one-mode spectral fit (red dashed line). (Right) Corrected emission of the tautomer emission spectrum of bbim in THF solution at 298 (± 2) K under 1 atm N_2. (solid black line) and the one-mode spectral fit (red dashed line), at room temperature.

The parameters derived from the spectral fitting procedure can be used to calculate the Franck-Condon weighted density of states.

The parameters from the fitting procedure are given in Table 3.5. The parameters derived from the fitting procedure are related to the non-radiative rate constant k_{nr} by

$$\ln(k_{nr}) = \ln\beta_o + \ln[F(calc)] \qquad (3.8)$$

where β_0 contains the vibrationally induced electronic coupling matrix element which dynamically couples the initial and final electronic states.

Table 3.5. Emission spectral fitting parameters, Franck–Condon factors, and reorganization energies for bbim in DMSO and THF at room temperature.

Quantity	DMSO	THF
	Tautomer	Tautomer
E_{em} (cm^{-1})	18182	18018
$\hbar\omega_M$ (cm^{-1})	1200	1200
E_0 (cm^{-1})	18160 ±3.0	17990 ±20
S	1.012 ±0.004	1.028 ±0.03
$\Delta\bar{\nu}_{1/2}$ (cm^{-1})	1545 ±7.2	2200 ±27
$\ln[F(\text{calc})]^a$	-27.19	-25.57
γ^b	1.70	1.68
$\lambda_{o,}$ (cm^{-1})^c	1039	2107
λ_i (cm^{-1})^d	1214	1233
λ_t (cm^{-1})^e	2253	3340

[a] Calculated from Eq. 3.9. b Calculated from Eq. 3.10.[c] Calculated from Eq. 3.13. [d] Calculated from Eq. 3.11. [e] Calculated from Eq. 3.12.

$$\ln[F(calc)] = -\frac{1}{2}\ln\left[\frac{\hbar\omega E_o}{(1000\ cm^{-1})^2}\right] - S - \left(\frac{\gamma E_o}{\hbar\omega}\right) + (\gamma+1)^2\left(\frac{\Delta\bar{\nu}_1}{\hbar\omega}\right)^2 /16\ln 2 \qquad (3.9)$$

$$\gamma = ln\left(\frac{E_o}{S\hbar\omega}\right) - 1 \qquad (3.10)$$

In Eq 3.9, the factor of 1000 cm^{-1} is an arbitrary scaling factor to make the logarithmic term unitless, and E_0, $\hbar\omega$ and $\Delta\bar{\nu}_{1/2}$ are in cm^{-1}.

The Stokes shift is given by

$$E_{abs} - E_{em} = 2(\lambda_i - \lambda_o) \qquad (3.11)$$

where the total reorganization energy, λ_t is a linear combination of the solvation (λ_o) and vibration (λ_i) energies.

$$\lambda_t = \lambda_i + \lambda_o \qquad (3.12)$$

and solvent reorganization energy, λ_o, is given by

$$\lambda_o = \frac{\left(\Delta\bar{\nu}_{1/2}\right)^2}{16k_B T ln(2)} \qquad (3.13)$$

3.3 Discussion

3.3.1 Ground State Structure and Conformational Dynamics

The structural dynamics of bbim were investigated using a combination of ^{1}H NMR absorption spectroscopic measurements coupled to the DFT calculations described in section 3.2.3 to characterize the conformational dynamics and probe the dominant solution structure of bbim in the ground state.

There exists an equilibrium between the isomeric enol form and a zwitterionic form (Scheme 3.6). But ^{1}H NMR spectroscopic results provided no evidence for tautomer formation even at the highest temperature. The ground state spectra are due to one species, the enol form, for which the structured absorption bands at 304 nm (32895 cm^{-1}), 318 nm (31446 cm^{-1}), and 334 nm (29940 cm^{-1}) are assigned to vibronic progressions from the symmetric ring breathing mode of hydroquinone (H_2Q) where

$\hbar\omega = 1300\ cm^{-1}$.[57] The appearance of the bands in bbim is unique and indicative of H-bonding interactions between bridging H_2Q and benzimidazole N. DFT calculations by C. Javier[57] suggest that the oscillator strength at 3020 cm^{-1} is enhanced by intramolecular H-bonding with the imidazole H^+ acceptor.

3.3.2 Thermodynamics

The intramolecular hydrogen bond between imidazole $N\cdots HO-R$ donor/acceptor plays an important role in stabilizing the planar structure of bbim in room temperature solution (Figure 3.9).[55]

The thermodynamic parameters deduced from an Eyring plot of variable temperature ^{1}H NMR data are free energy of activation $\Delta G^{\ddagger} = 75\ kJmol^{-1}$ with $\Delta H^{\ddagger} = 27\ kJmol^{-1}$ and $\Delta S^{\ddagger} = -133\ JK^{-1}mol^{-1}$. These values indicate that the rate constant is favoured entropically and disfavoured enthalpically. The broad peaks observed above 318 K (Figure 3.12) may be due to fast exchange of the H-bond between the hydroquinone and imidazole. Subtle changes in frequency for a ^{1}H resonance would be expected as a consequence of increased torsional motion (Scheme 3.7). These broad peaks return back to the original structure when the sample was cooled to room temperature. This temperature dependence of the NMR spectrum suggests thermally activated torsional motion with increasing temperature as depicted in Scheme 3.7. Calculation by S. Fatima indicate that a H-bonding bridge is maintained even at torsion angle of 30°.

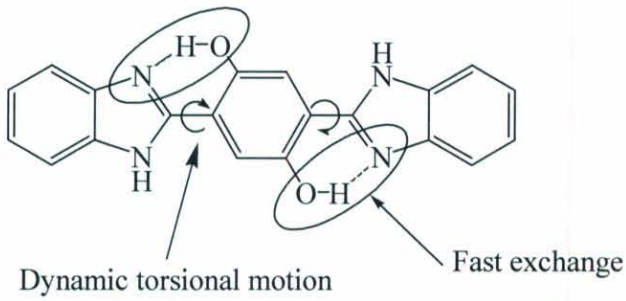

Scheme 3.7. Torsional motion and rapid proton exchange between intramolecular H-bonding in the bbim molecule.

3.3.3 Photostability

The bbim is extremely photosensitive as evidenced by the changes in the UV-Vis spectrum in the presence of air shown in Figure 3.20. The photosensitivity in the presence of O_2 is counter-intuitive given that this family of compounds is utilized as photostabilizers in polymeric media.

The hypothesis is that the mechanism of the intersystem crossing to the triplet state localized on hydroquinone (HQ) is competitive with excited state decay to low-lying bbim excited states. Once the triplet is formed energy transfer to $^3\sum O_2$ generates $^1O_2$,[59] which is highly reactive. Removal of O_2 by N_2 purging significantly attenuates the photochemistry.

The observation for photoinstability of bbim in the presence of O_2 following excitation is presumed to involve a sensitization of a triplet bbim (^{3}bbim) excited state, as reaction of H_2Q with O_2 is spin forbidden as the O_2 has a triplet ground state. A mechanism is suggested below to account for the photoinstability. In the absence of an obvious source of spin orbit coupling, spin interconversion to form a triplet ($\Delta S = 2$)

must proceed via a mechanism where spin and orbital angular momentum are conserved during the transition. At this juncture, it is proposed that the intersystem crossing occurs as given by Eq. 3.14 and 3.15

$$^1(\pi\pi^*)_{H_2Q} \rightarrow {}^3(n\pi^*)_{H_2Q} \quad (3.14)$$

$$^3(n\pi^*)_{H_2Q} \rightarrow {}^3(\pi\pi^*)_{H_2Q} \quad (3.15)$$

where the tautomeric C=O mediates via a low-lying $(n\pi^*)$ excited state. The ground state spectra do not show a transition that is assignable to $n\pi^*$ as this transition is disallowed and its low oscillator strength makes observation of this transition difficult relative to other overlapping intense bands. In the excited state, the mechanism of non-radiative decay can be drastically changed by the presence of an $(n\pi^*)$ state. Once $^3(n\pi^*)$ is formed (Eq 3.14), there is an internal conversion to the $^3(\pi\pi^*)$ state (Eq 3.15). In this mechanism, spin and orbital angular momentum are conserved during intersystem crossing and this process has been designated as following El-Sayed's Rules. When the $^3O_2$ oxidizes the HQ the consequence is the creation of radicals which may be undergoing very rapid reactions in solution[60]. In contrast, in the absence of air (the solution purged with N_2 for around one hour) the bbim shows substantially increased photostability. This gives an indication that in the absence of O_2 no BQ or other products were formed.

3.3.4 Excited States

3.3.4.1 Solvent Effects

No significant changes in absorption spectra were seen in different solvents. The most stable form of bbim in DMSO solution in the ground state is the intramolecularly hydrogen bonded form but there may be another conformation which is hydrogen

bonded to the DMSO solvent. In the case of DMSO as solvent, the conversion of the enol-form to the keto-form via ultrafast proton transfer takes place along an intramolecular hydrogen bond (closed form). The formation of the tautomer in the excited state gives rise to a red-shifted excitation spectrum obtained at wavenumber (18182 cm^{-1}). Other emission bands such as the blue emission band with an emission maximum at (23420 cm^{-1}) may be assumed to be due to an enol-form in which the intramolecular hydrogen bond is not strong enough to convert all of the enol-form species to the tautomer (keto-form) species.

It is suggested that the higher energy structured emission spectrum (enol-form) is due to other conformations such as an open form (intermolecularly hydrogen bonded with the solvent) and as well the *trans*-enol form which is formed when the hydroquinone ring is rotated. Douhal *et al.*[52] argue that, by internal rotation, the molecule would form the *trans*-enol form or open system which would intermolecularly hydrogen bond to the solvent. These conformations would be less likely to undergo ESIPT.

Upon excitation of the enol-form to its first excited singlet state, the enhanced acidity of the hydroxyl group causes an ultrafast intramolecular proton transfer from the hydroquinone OH group to the benzimidazole N. This may lead to a loss of the planar structure for the excited state which leads to losing the vibrational structure as illustrated in the excitation spectra shown in Figure 3.21. The bbim in DMSO solution exhibits a more intense enol-form peak compared with bbim in DMF and THF solutions. This can be attributed to stabilization of the enol-form moiety by a hydrogen bond between bbim

and the DMSO molecule. This changes the rate of excited state proton transfer and also changes the intensity ratio between the enol isomer and the keto tautomer.

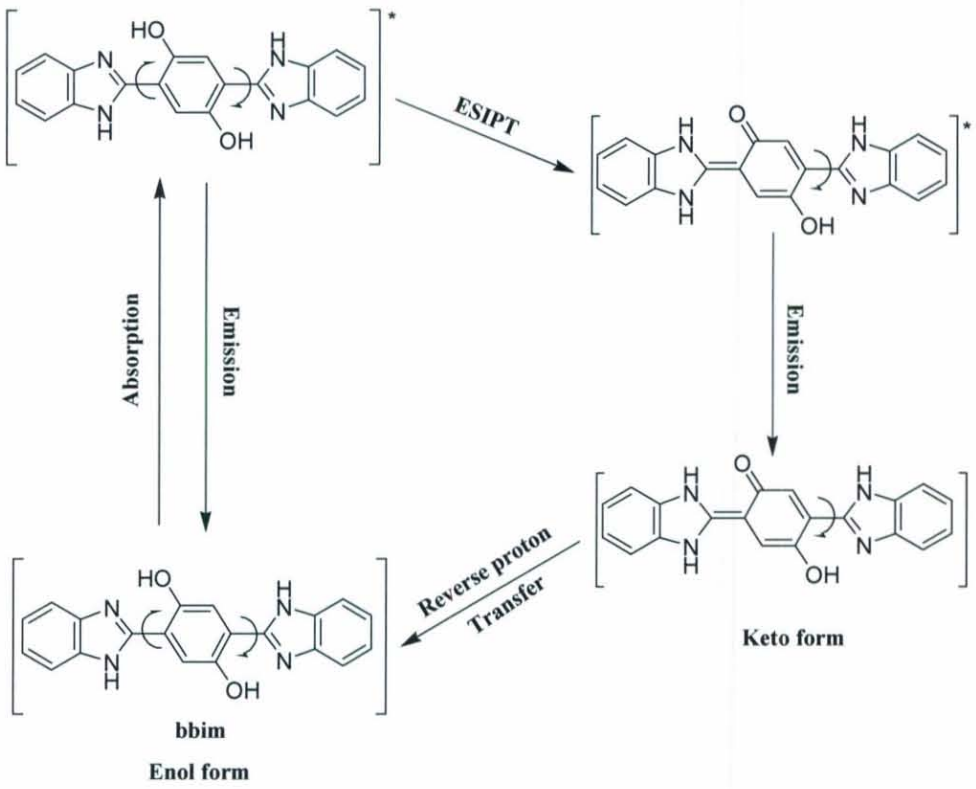

Scheme 3.8. The accepted mechanism for excited state intramolecular proton transfer process for bbim molecule.

More investigations have been done on this issue for molecules similar to the bbim. For instance, the effect of rotation on the photophysics of similar molecules was investigated by Stephan *et al.*[61] The contribution to the observed spectrum from the molecule with a "closed conformation" emits actually no isomer (enol-form) fluorescence. The fluorescence emission of such molecules is totally due to the excited keto-form. This strongly suggests that the blue emission by bbim is due to the open *trans*-enol form and that there is an intermolecular hydrogen bond to solvent for the *trans*-enol

form. This leads us to conclude that all the fluorescence deriving from the *cis*-enol conformer of bbim must similarly be due to the keto-form.

3.3.4.2 Role of Charge Transfer on the Radiationless Decay of the bbim Tautomer

The bbim molecule undergoes excited state intramolecular proton transfer along the internal hydrogen bonds (strong hydrogen bonds exist on both sides of the molecule). This leads to the possibility of double proton transfer with the possible formation of a zwitterionic structure which subsequently undergoes electron transfer. The ground state redox potential for bbim is known.[62] ESIPT brings about changes in the ability of the electron donor (deprotonated hydroquinone moiety) and electron acceptor (protonated benzazole) to respectively donate and accept electrons. The new excited state structure with a proper redox pair can undergo a charge transfer process. In this case, the intramolecular charge transfer process takes place after an ultrafast ESIPT occurs as shown in Scheme 3.9. The single proton transfer process already occurs to a slight extent in the ground state based on the temperature dependent NMR data described above.

Previous research has been devoted to studying single versus double proton transfer.[10,11,14,16,20,22,47,48] Previous investigators have suggested that only a single proton is transferred in the excited state forming the keto-enol tautomer because the di-keto tautomer has the highest energy of the other possible forms of the tautomer in the excited electronic state. In our hypothesis, we proposed that no di-keto tautomer will form, but that a double proton transfer takes place in the first singlet excited state without a potential barrier. Upon excitation of bbim, the intramolecular hydrogen transfer occurs on one side of the molecule producing the tautomer conformation after a proton is transferred while on the other side of the molecule, a zwitterionic conformation is

produced. The new zwitterionic structure can undergo an intramolecular charge-transfer process (on one side of the molecule) as shown in Scheme 3.9.

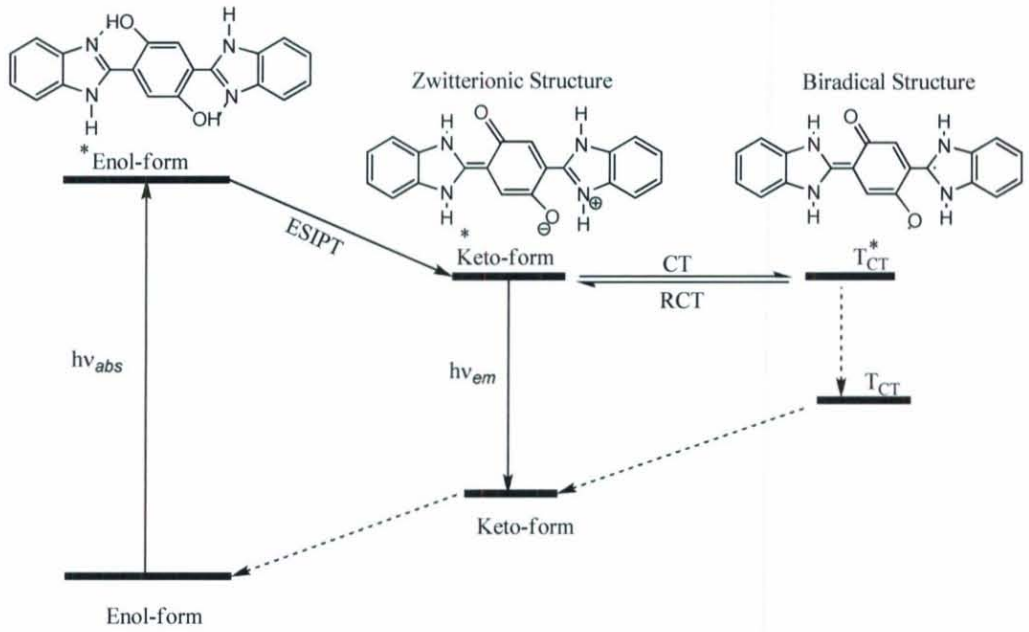

Scheme 3.9. Proposed mechanism of the coupled intramolecular proton and charge transfer in the first excited singlet state of bbim.

The solubility of bbim is generally very low. This hindered attempts to study the effects of solvent polarity and viscosity on the rate constant of electron transfer. In this work a study of solvent effects on the excited state behavior of bbim was carried out using just the two solvents, DMSO and THF. We found that the process of proton transfer plays a role in charge transfer. Changes in the solvent polarity could affect several factors such as the rate of solvent relaxation, the internal charge transfer, proton transfer, and changes in the radiative and non-radiative decay rates. It will be difficult to predict which effect is dominant. However, the figure below shows that the fluorescence emission maximum of the tautomer decreases from DMSO to THF (18018 and 17482

cm^{-1} respectively). This prediction is in good agreement with the experimental results showed that the fluorescence quantum yield of the tautomer decreases (Table 3.4) and therefore that the radiationless decay process is more efficient ($\Phi_{bbim\ in\ DMSO} > \Phi_{bbim\ in\ THF}$).

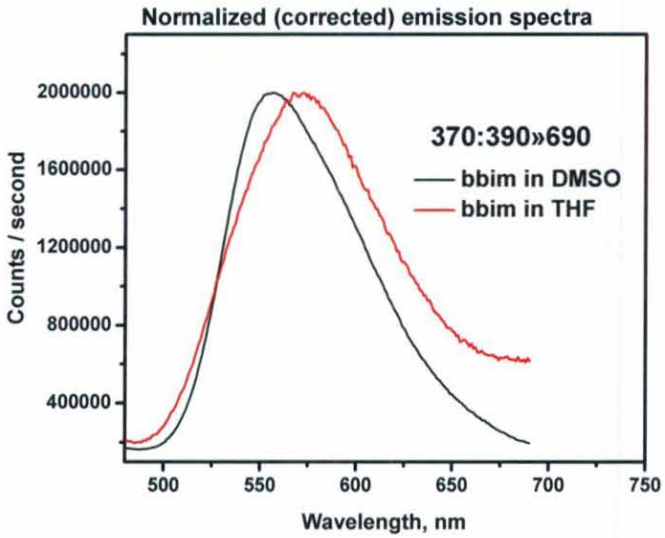

Figure 3.24. Tautomer emission peak solvent dependence of bbim.

Generally, the excited state has a larger dipole moment than the ground state. Highly polar solvent molecules can reorient around the excited state molecules. However, the bbim molecule contains hydroquinone as an electron donor and benzimidazole as an electron acceptor group which, upon excitation, will increase their donor and acceptor character. Therefore, the excited state can be more effective at accepting or donating electrons than the ground state. Following excitation, the intramolecular proton transfer induced internal charge transfer takes place. Prieto *et al.*[63] found that the new species after charge transfer is the lower energy state.

The role of the solvent polarity is not only to lower the energy of the excited state. The small red shift in the case of THF is evidence that the tautomer might undergo charge transfer in the excited state. In agreement with the CT hypothesis, a limited correlation between the observed fluorescence quantum yield and the solvent polarity is observed for the tautomer of bbim in DMSO and THF. The experimental results confirm the hypothesis that, for the tautomer form of bbim, the radiationless decay observed involves an intramolecular CT from the dissociated hydroquinone (donor) to the protonated benzimidazole (acceptor). The structure of T^*_{CT} shown in Scheme 3.9 is our proposed mechanism. The proton transfer generates a molecular structure with the appropriate intramolecular redox properties (Scheme 3.9), and proton transfer is required for CT to occur.

We did not note the fluorescence due to the charge transferred species which possibly is due to ultrafast radiationless decay. It is possible that there is minimal fluorescence, possibly overlaid with the fluorescence of the tautomer species. This seems reasonable in view of the reported quantum mechanical calculations.[64-68] Hence, changing the polarity of the media for the ESIPT process supports the charge transfer from the hydroquinone (proton donor) to the benzimidazole (proton acceptor). This will decrease the quantum yield of bbim in THF in comparison to bbim in DMSO. The decreasing quantum yield probably is due to increasing nonradiative decay in the case of bbim in THF solution. Therefore, the observed results can be interpreted under the hypothesis of a CT process. The rate constant of the charge transfer in the excited tautomer decreases when moving from bbim in DMSO to bbim in THF. Therefore, it is suggested that a zwitterionic structure is more favorable in the case of bbim in DMSO than in THF media.

3.4 Conclusion

The excited-state behavior of the 2,5-Bis(benzimidazoly)-1,4-dihydroxybenzene (bbim) has been investigated by means of steady-state and time-resolved fluorescence. The fluorescence quantum yield and lifetime of the tautomer generated after ESIPT have been found to be solvent dependent. The bbim exists in the ground state in the *trans*-enol form and intermolecularly hydrogen-bonded (open form) in DMSO solvent. It is suggested that the blue emission comes from these species. The *cis*-enol form undergoes an ultrafast ESIPT from the hydroxyl group to the benzimidazole nitrogen to give the tautomer, which, in the excited state, experiences fast excited-state intramolecular proton transfer (ESIPT) from the OH group to the benzimidazole nitrogen to yield the zwitterionic tautomer from which a charge transfer species TC^* is formed. The excited state tautomer of bbim exhibits a solvent polarity dependent radiationless transition which is the change that the tautomer is most likely to undergo following a charge migration from the deprotonated hydroquinone ring (donor) to the protonated benzimidazole (acceptor) (leading to the charge-transfer species, TC^*, whose emission was not detected). The intramolecular proton transfer step provides the excited state structure with the suitable electron donor and electron acceptor pairs to lead to internal charge transfer and conformational changes in bbim. Therefore, the process described may be considered to be an example of a proton-coupled charge transfer.

The energetics of the excited state can be altered by the solvent polarity, thus affecting solvent reorganizational energies. In this work, we show how the rate constant of electron transfer for the tautomer species slows down due to the effect of solvent (faster in THF than in DMSO).

3.5 References

(1) Tolbert, L. M.; Solntsev, K. M. *Acc. Chem. Res.* **2001**, *35*, 19-27.

(2) Bamford, C. H.; Tipper, C. F. H. *"Proton Transfer"*; Elsevier Scientific Publishing Company: Amsterdam, 1977; Vol. 8.

(3) Cohen, A. O.; Marcus, R. A. *J Phys. Chem.* **1968**, *72*, 4249-4256.

(4) Marcus, R. A. *J. Phys. Chem.* **1968**, *72*, 891-899.

(5) Marcus, R. A. *J Am. Chem. Soc.* **1969**, *91*, 7224-7225.

(6) Al-Soufi, W.; Grellmann, K. H.; Nickel, B. *J. Phys. Chem.* **1991**, *95*, 10503-10509.

(7) Balamurali, M. M.; Dogr, S. K. J. *Photochem. Photobio. A: Chem.* **2002**, *154*, 81-92.

(8) Fahrni, C. J.; Henary, M. M.; VanDerveer, D. G. *J. Phys. Chem. A* **2002**, *106*, 7655-7663.

(9) Gelabert, R.; Moreno, M.; Lluch, J. M. *J. Phys. Chem. A* **2006**, *110*, 1145-1151.

(10) Grabowska, A.; Mordzinski, A.; Kownacki, K.; Gilabert, E.; Claude, R. *Chem. Phys. Lett.* **1991**, *177*, 17-22.

(11) Grabowska, A.; Mordzinski, A.; Tamai, N.; Yoshihara, K. *Chem. Phys. Lett.* **1990**, *169*, 450-456.

(12) Hosoi, H.; Mizuno, H.; Miyawaki, A.; Tahara, T. *J. Phys. Chem. B* **2006**, *110*, 22853-22860.

(13) Iijima, T.; Momotake, A.; Shinohara, Y.; Sato, T.; Nishimura, Y.; Arai, T. *J. Phys. Chem. A* **2010**, *114*, 1603-1609.

(14) Kaczmarek, K. K.; Grabowska, A. *Chem. Phys. Lett.* **1993**, *210*, 373.

(15) Luzina, E.; Kauffman, J. M.; Mordzinski, A. *Chem. Phys. Lett.* **2004**, *400*, 1-6.

(16) Mordzinski, A.; Grabowska, A. *Chem. Phys. Lett.* **1982**, *90*, 122-127.

(17) Mordzinski, A.; Kuehnle, W. *J. Phys. Chem.* **1986**, *90*, 1455-1458.

(18) Nagoaka, S.; Nakamura, A.; Nagashima, U. J. *Photochem. Photobio. A: Chem.* **2002**, *154*, 23-32.

(19) Roberts, E. L.; Dey, J.; Warner, I. M. *J. Phys. Chem. A* **1997**, *101*, 5296-5301.

(20) Waluk, J.; Bulska, H.; Grabowska, A.; Mordzinski, A. *Nouveau Journal de Chimie* **1986**, *10*, 413-420.

(21) Wu, P.-W.; Hsieh, W.-T.; Cheng, Y.-M.; Wei, C.-Y.; Chou, P.-T. *J. Am. Chem. Soc.* **2006**, *128*, 14426-14427.

(22) Mordzinski, A.; Grabowska, A.; Teuchner, K. *Chem. Phys. Lett.* **1984**, *111*, 383-388.

(23) Catalan, J.; Diaz, C. *J Phys. Chem. A* **1998**, *102*, 323-328.

(24) Kim, T. G.; Topp, M. R. *J. Phys. Chem. A* **2004**, *108*, 10060-10065.

(25) Wan, P.; Shukla, D. *Chem. Rev.* **1993**, *93*, 571-584.

(26) Acuna, A. U.; Costela, A.; Munoz, J. M. *J. Phys. Chem.* **1986**, *90*, 2807-2808.

(27) Kim, S.; Park, S. *Advanced Materials* **2003**, *15*, 1341.

(28) Tong, H.; Zhou, G.; Wang, L.; Jing, X.; Wang, F.; Zhang, J. *Tetrahedron Lett* **2003**, *44*, 131-134.

(29) Keck, J.; Horst, E. A.; Port, H.; Hirsch, T.; Fischer, P.; Rytz, G. *J. Phys. Chem.* **1996**, *100*, 14468-14475.

(30) Kim, S.; Chang, D. W.; Park, S.; Kim, K.; Jin, J. *Korean Chem. Soc.* **2001**, *22*, 1407.

(31) Joubert, A.; Sun, X.; Johansson, E.; Bailly, C.; Mann, J.; Neidle, S. *Biochem.* **2003**, *42*, 5984-5992.

(32) Ashok, M.; George, L.; Nicholas, J. T.; Ravi, R.; Suhadolnil, J. C.; DeBellis, A.; Wood, M. G.; Lue, J. *J. Phys. Chem. A* **2002**, *106*, 7680-7689.

(33) Satoru, S.; Rie, K.; So, T.; Haruo, S.; Seiji, T. *J. Photochem. Photobio. A: Chem.* **2002**, *154*, 53-60.

(34) Mosquera, M.; Penedo, J. C.; Rios Rodriguez, M. C.; Rodriguez-Prieto, F. *J. Phys. Chem.* **1996**, *100*, 5398-5407.

(35) Beens, H.; Grellmann, K. H.; Gurr, M.; Weller, H. *Discuss. Faraday Soc.* **1965**, *39*, 183.

(36) Weller, H. *Elektrochemistry* **1956**, *60*, 1144.

(37) Weller, H. *Prog. React. Kinet.* **1961**, *1*, 187.

(38) Grellmann, K. H.; Mordzinski, A.; Heinrich, A. *Chem. Phys.* **1989**, *136*, 201.

(39) Krishnamurthy, M.; Dogra, S. K. *J. Photochem.* **1986**, *32*, 235.

(40) Mordzinski, A.; Grellmann, K. H. *J. Phys. Chem.* **1986**, *90*, 5503.

(41) Rodriguez-Prieto, M. F.; Nickel, B.; Grellmann, K. H.; Mordzinski, A. *Chem. Phys. Lett.* **1988**, *146*, 387.

(42) Woolfe, G. J.; Melzing, M.; Schneider, S.; Dorr, F. *Chem. Phys.* **1983**, *77*, 213.

(43) Itoh, M.; Fujiwara, Y. *j. Am. Chem. Soc.* **1985**, *107*, 1561.

(44) Abou-Zied, O. K.; Jimenez, R.; Thompson, E. H. Z.; Millar, D. P.; Romesberg, F. E. *J. Phys. Chem. A* **2002**, *106*, 3665-3672.

(45) Iijima, T.; Momotake, A.; Shinohara, Y.; Sato, T.; Nishimura, Y.; Arai, T. *J Phys. Chem. A* **2010**, *114*, 1603-1609.

(46) Grabowska, A.; Mordzinski, A.; Tamai, N.; Yoshihara, K. *Chem. Phys. Lett.* **1988**, *153*, 389-392.

(47) Mordzinski, A.; Grabowska, A.; Kuehnle, W.; Krowczynski, A. *Chem. Phys. Lett.* **1983**, *101*, 291-296.

(48) Mordzinski, A.; Grabowska, A. J. *Mole. Struct.* **1984**, *114*, 337-341.

(49) Weiß, J.; May, V.; Ernsting, N. P.; Farztdinov, V.; Mühlpfordt, A. *Chem. Phys. Lett.* **2001**, *346*, 503-511.

(50) Sun, D.; Fang, J.; Yu, G.; Ma, F. *J. Mole. Struct. THEOCHEM* **2007**, *806*, 105-112.

(51) Das, K.; Sarkar, N.; Ghosh, A. K.; Majumdar, D.; Nath, D. N.; Bhattacharyya, K. *J. Phys. Chem.* **1994**, *98*, 9126-9132.

(52) Douhal, A.; Amat-Guerri, F.; Lillo, M. P.; Acuña, A. U. *J. Photochem. Photobio. A: Chem.* **1994**, *78*, 127-138.

(53) Kalnin'sh, K. K.; Glebovskii, D. N.; Bedrina, M. E.; Roschina, E. K. *J. Struct. Chem.* **1992**, *33*, 636.

(54) Sinha, H.; Dogra, S. K. *Chem. Phys.* **1986**, *102*, 337.

(55) Weber, E.; Klomfas, D.; Csoregh, I.; Kristallogr, Z. *New Cryst.Struct.* **2007**, *222*, 299.

(56) Colin, C., Ph.D. Dissertation, Memorial University of Newfoundland, 2000.

(57) Javier Concepcion *The University of North Carolina, Chapel Hill private communication.*

(58) Landrum, G. Web Page, p http://yaehmop.sourceforge.net/.

(59) Li, C.; Hoffman, M. Z. *J. Phys. Chem. A* **2000**, *104*, 5998-6002.

(60) Patai, S. *"The Chemistry of the Hydroxyl Group"*; Interscience: New York, 1971.

(61) Stephan, J. S.; Rodríguez, C. R.; Grellmann, K. H.; Zachariasse, K. A. *Chem. Phys.* **1994**, *186*, 435-446.

(62) Colin, C., Ph.D. Dissertation, Memorial University of Newfoundland, PP. 97, 2000.

(63) Ríos Vázquez, S.; Ríos Rodríguez, M. C.; Mosquera, M.; Rodríguez-Prieto, F. *J. Phys. Chem. A* **2007**, *111*, 1814-1826.

(64) Estévez, C. M.; Bach, R. D.; Hass, K. C.; Schneider, W. F. *J. Am. Chem. Soc.* **1997**, *119*, 5445-5446.

(65) Âreca, D. L.; Kharlanovb, V.; Browna, R. G.; Rettigb, W. *J. Photochem. Photobio. A: Chem.* **1998**, *117*, 209-216.

(66) LeGourriérec, D.; Kharlanov, V. A.; Brown, R. G.; Rettig, W. *J. Photochem. Photobio. A: Chem.* **2000**, *130*, 101–111.

(67) Paterson, M. J.; Robb, M. A.; Blancafort, L.; DeBellis, A. D. *J. Am. Chem. Soc.* **2004**, *126*, 2912-2922.

(68) Paterson, M. J.; Robb, M. A.; Blancafort, L.; DeBellis, A. D. *J. Phys. Chem. A* **2005**, *109*, 7527-7537.

Chapter 4

Interactions of the Ground and the Excited States of 2,5-Bis(benzimidazoyl)-1,4-dihydroxybenzene with Electrolytes

4.1 Introduction

The introduction presents the main principles relevant to the chemistry involved in ground and excited state intermolecular proton transfer (ESIPT) as a function of solvents and electrolytes.

4.1.1 Inter and Intramolecular Interactions with Electrolytes

Intermolecular proton transfer processes in which a proton is transferred from a hydrogen-bond donor to proton acceptor such as fluoride can produce a color change.[1-6] Many studies have involved double benzoxazole derivatives which exhibit apparently only single proton transfer in the first excited state.[7-10]

Compounds that undergo proton transfer through an intramolecular hydrogen bond have many applications.[11,12] Various authors have demonstrated the use of these compounds as fluorescent and colorimetric chemosensors for anions such as acetate, phosphate, fluoride etc. where the response is detectable by UV-Vis absorption, fluorescence and ^{1}H NMR methods. Scheme 4.1 illustrates ground state stepwise changes for phenyl-1H-anthra[1,2-d]imidazole-6,11-dione (PAI) which occur following electronic excitation and subsequently proton transfer. The ^{1}H NMR fluoride ion titration spectra of PAI indicated the existence of a new species that was ascribed to the FHF^- unit at 16.15 ppm; the FHF^- ion causes the deprotonation of the NH group in PAI. Scheme 4.2 shows the excited state stepwise changes for PAI. The deprotonation of the PAI excited state was facile due to increased excited state acidity and the high stability of the FHF^- unit. The fluorescence spectra showed a new emission peak for PAI at 600 nm with an isoemissive point at 568 nm. The authors demonstrated that PAI is a colorimetric and

ratiometric fluorescence chemosensor for fluoride anion.

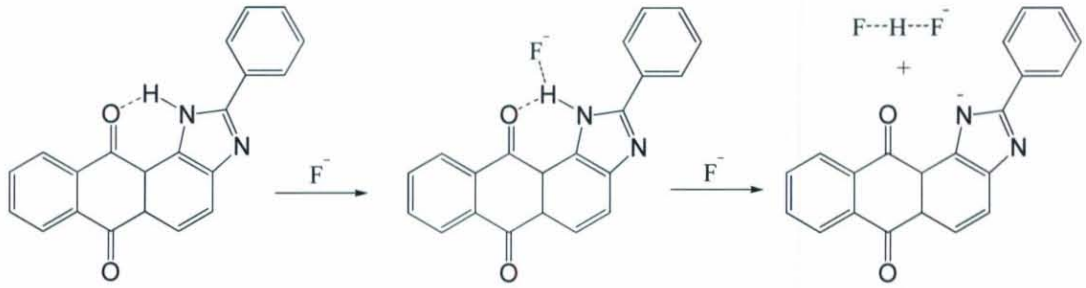

Scheme 4.1. Ground state stepwise changes for PAI with fluoride interaction.[11]

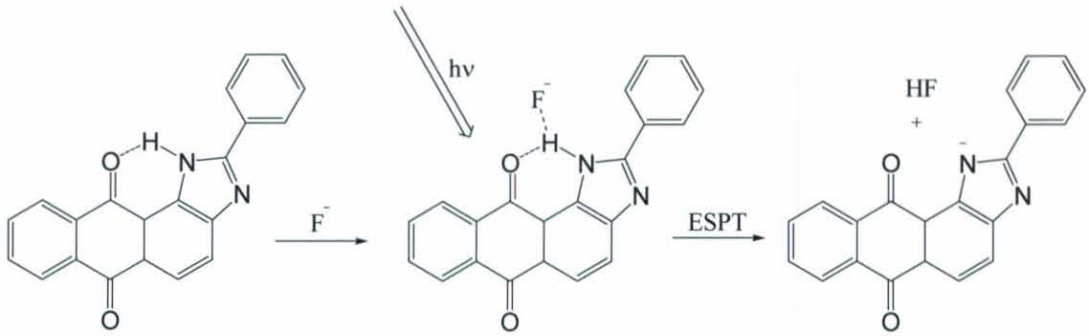

Scheme 4.2. Excited state stepwise changes for PAI with fluoride interaction.[11]

In this work, the effects of electrolytes on the ground and excited state of bbim, and inter-intramolecular proton transfer from bbim have been investigated. Ground and excited state mechanisms have been proposed to describe the spectra observed for bbim in the presence and absence of added electrolytes. The effect of H_2O and D_2O on the ground and excited state has been investigated.

Absorption maxima, extinction coefficients, emission spectra, quantum yields and emission lifetimes for bbim have been tabulated in Chapter 3, Table 3.4.

4.2 Results

In the previous chapter, the ground state and excited state dynamics for bbim were studied in solution. In this chapter, the interactions of bbim with Tetra-*n*-butylammonium salts $[N(nC_4H_9)_4]X$, where X is fluoride (F^-), chloride (Cl^-), bromide (Br^-), iodide (I^-), acetate (Ac^-), hydrogen sulphate (HSO_4^-), hexafluorophosphate (PF_6^-), are delineated. It is known that systems which undergo ESIPT are sensitive to the nature of electrolytes.

The ground state properties as a function of $[N(nC_4H_9)_4]X$ were studied using ^{1}H NMR and absorption spectroscopy, which includes titrations of bbim with $[N(nC_4H_9)_4]X$. The excited state properties will be presented later on in the chapter.

4.2.1 Electrolytes Interactions with the bbim Ground State

4.2.1.1 ^{1}H NMR Studies

The ^{1}H NMR and peak assignments of bbim were discussed in Chapter 3 section 3.2.1, Figure 3.11. The N-H and O-H peaks for bbim are clearly evident at 13.30 and 12.70 respectively at room temperature in DMSO-d_6 solution (Figure 4.1). The peak position for both N-H and O-H are substationally shifted downfield as expected for significant H-bonding.

The addition of one equivalent $[N(nC_4H_9)_4]F$ to a mM solution of bbim in DMSO-d_6 results in the lost of the N-H peak at 12.70 ppm and O-H peak at 13.30 ppm. The concomitant loss of both resonances is presumably due to increased exchange broading due to competitive H-bonding interactions with F^-. The argument for increased exchange is supported by the broadening of the peak assigned to H_a on the bridging

hydroquinone and the loss of resolution for the NMR signals on the bbim moiety. The rate constant for proton exchange at room temperature is 9.91 s^{-1} from analysis of temperature dependent experiments as described in Chapter 3 section 3.2.2.

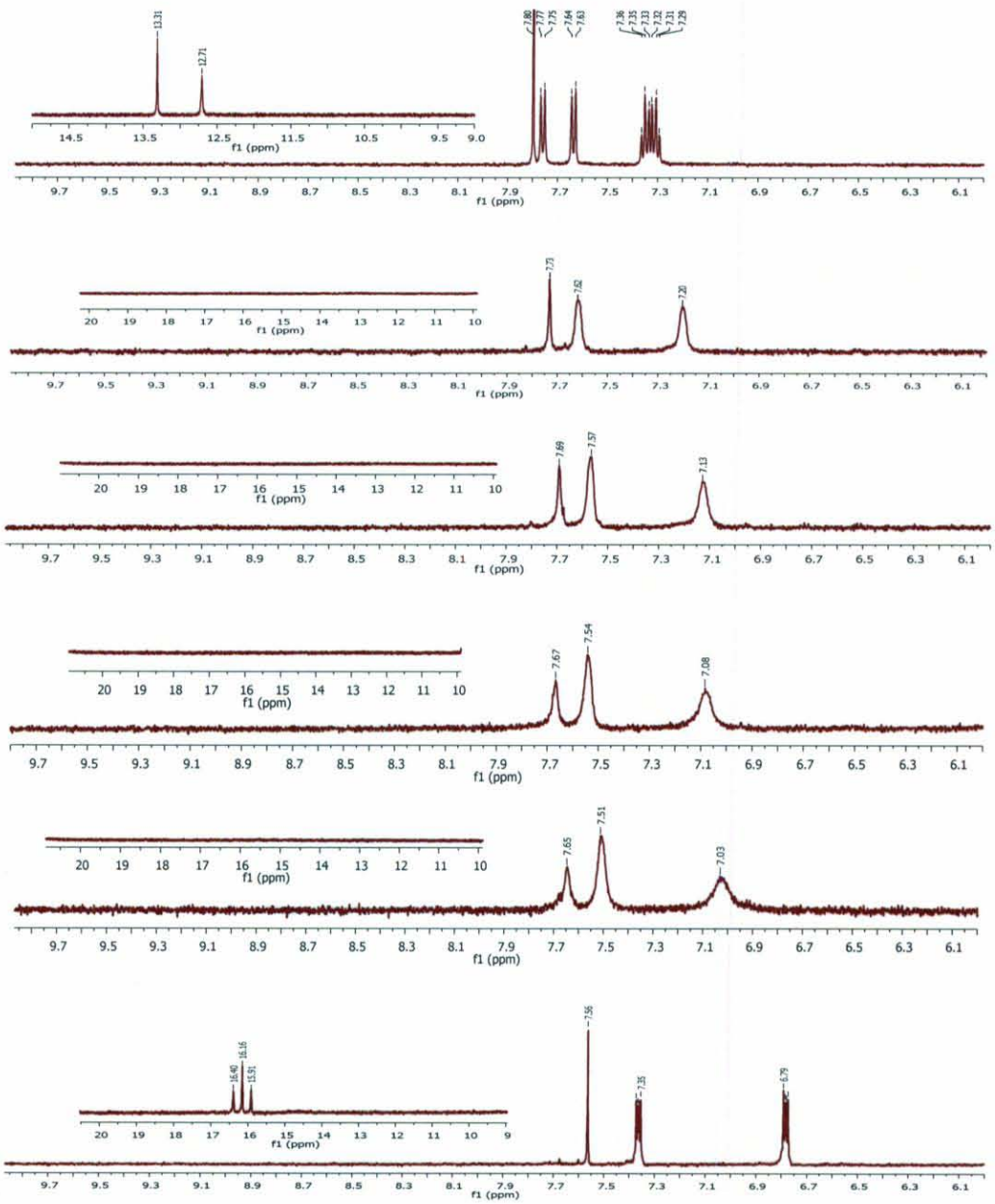

Figure 4.1. From top to down ^{1}H NMR spectra for 0, 1, 2, 3, 4 and 10 equivalents of $[Bu_4N]F$ added to bbim in DMSO-d_6.

Upon addition of 10 equivalents of F^-, a new peak at 16.1 ppm started to appear (Figure 4.1) and, with this change, the doublet peak at 7.758-7.742, and 7.634-7.608 ppm became one sharp multiplet peak from 7.363 to 7.344 ppm. Meanwhile, the sextet of peaks at 7.355-7.273 ppm became a sharp quartet of peaks at 6.781-6.763 ppm. ^{1}H NMR titration spectra of bbim with OH^- gave a similar result to the titration with F^- except no new peak was observed at 16.1 ppm.

4.2.1.2 Absorption Study

The absorption spectra of DMSO solutions containing bbim (10 μM, $\varepsilon = 3.48 \times 10^4$ cm^{-1} M^{-1} at $\lambda = 385\ nm$) in the presence of $[Bu_4N]X$ (X= F^-, OH^-, Ac^-, Cl^-, Br^-, I^-, PF_6^-, and HSO_4^-) is shown in Figure 4.2. The UV-Vis spectral data as a function of electrolyte are summarized in Table 4.1

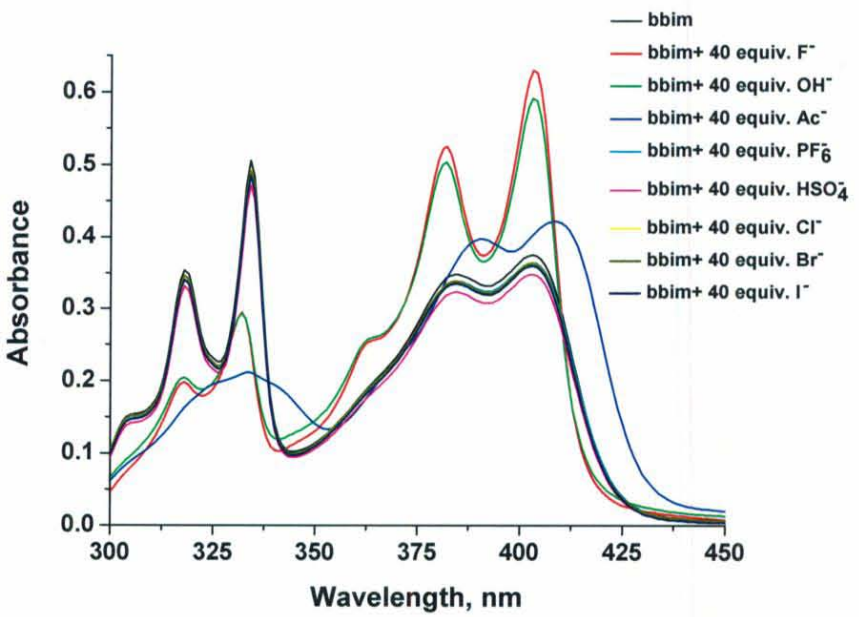

Figure 4.2. Effect of 40 equivalents of all of the different anions under study on the absorption spectra bbim in DMSO solution at 298 (± 2) K under 1 atm N_2.

Table 4.1. . Absorption spectra maxima, ionic radii and electronegativity values of the anions used for titration of bbim in DMSO at 298 (± 2) K under 1 atm N_2.

$[Bu_4N]X$	λ_{Abs}^{max}, nm	E_{em}, (cm^{-1})	Ionic radii, pm	Electronegativity
F^-	319	31350	133	4.0
	332	30120		
	383	26110		
	403	24814		
OH^-	318	31447		
	332	30120		
	382	26178		
	403	24814		
Ac^-	304	32895		
	319	31350		
	334	29940		
	390	25640		
	409	24450		
PF_6^-	Like bbim No Change	-		
HSO_4^-	Like bbim No Change	-		
Cl^-	Like bbim No Change	-	181	3.0
Br^-	Like bbim No Change	-	196	2.8
I^-	Like bbim No Change	-	220	2.5

Addition of 2 equivalents of F^- to a DMSO solution of bbim results in distinct changes in the UV-Vis spectra (Figure 4.3) assigned to the formation of an adduct between bbim and 2 F^-, Eq 4.1. The adducts are characterized by large attenuation of the band intensities at 318 and 334 nm. In the 350-450 nm region, the π-π^* transitions increased in intensity and moved to slightly longer wavelength.

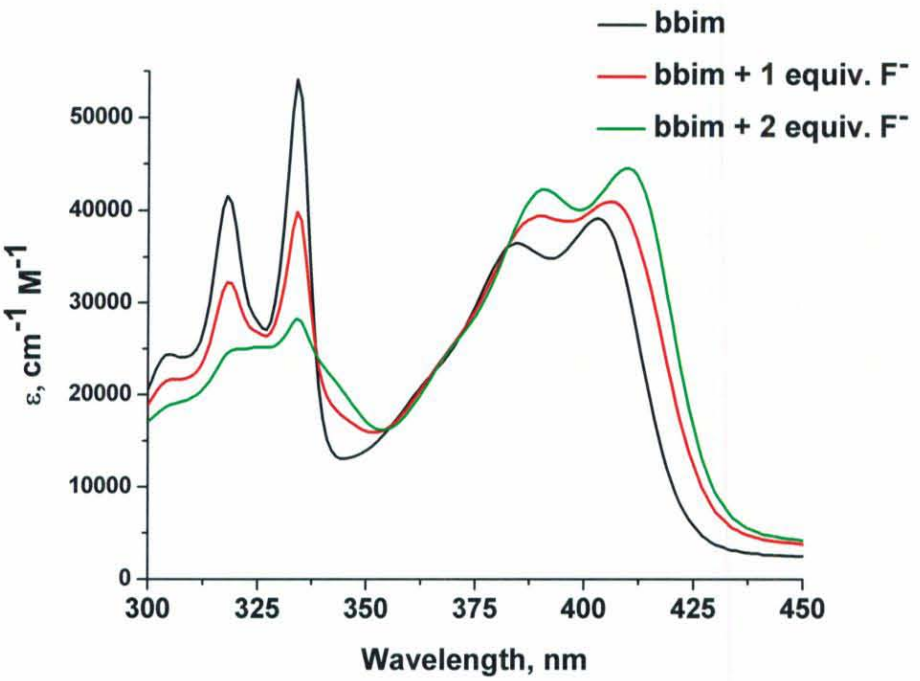

Figure 4.3. Spectrophotometric titration of bbim in DMSO solution at 298 (± 2) K under 1 atm N_2 with one and two equivalents of $[Bu_4N]F$ added to bbim.

Upon further addition of F^- (from 3 to 40 equivalents), systematic changes in the UV-Vis spectra were observed with five isosbestic points being seen at 335, 350, 388, 395, and 408 nm (Figure 4.4).

$$bbim + 2F^- \rightleftharpoons [bbim(F^-)_2] \qquad (4.1)$$

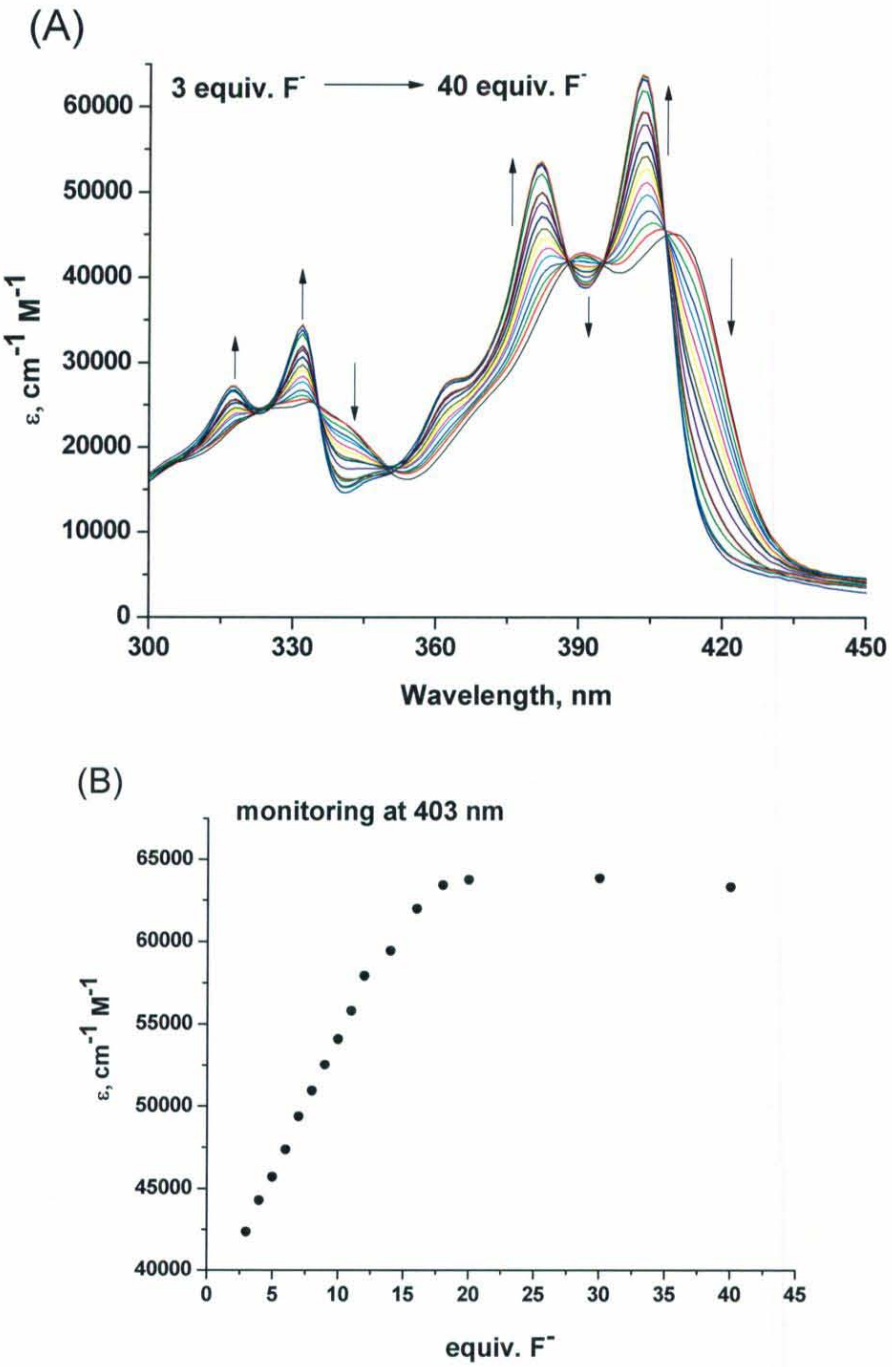

Figure 4.4. (A) Spectrophotometric titration of bbim in DMSO solution at 298 (± 2) K under 1 atm N_2 with $[Bu_4N]F$. (B) Absorbance change at 403 nm vs equivalents of F^-.

4.2.2 Emission/ Excitation/ Absorbance

Excitation of bbim (λ_{exc} = 404 nm) in N_2 purged DMSO solution gives rise to two major emission bands at 427 nm (23365 cm^{-1}) and 550 nm (18180 cm^{-1}) independent of excitation wavelength. The absorption, emission and excitation spectra for bbim shown in Chapter 3 (Figure 3.21), are repeated in Figure 4.5 for the reader's convenience.

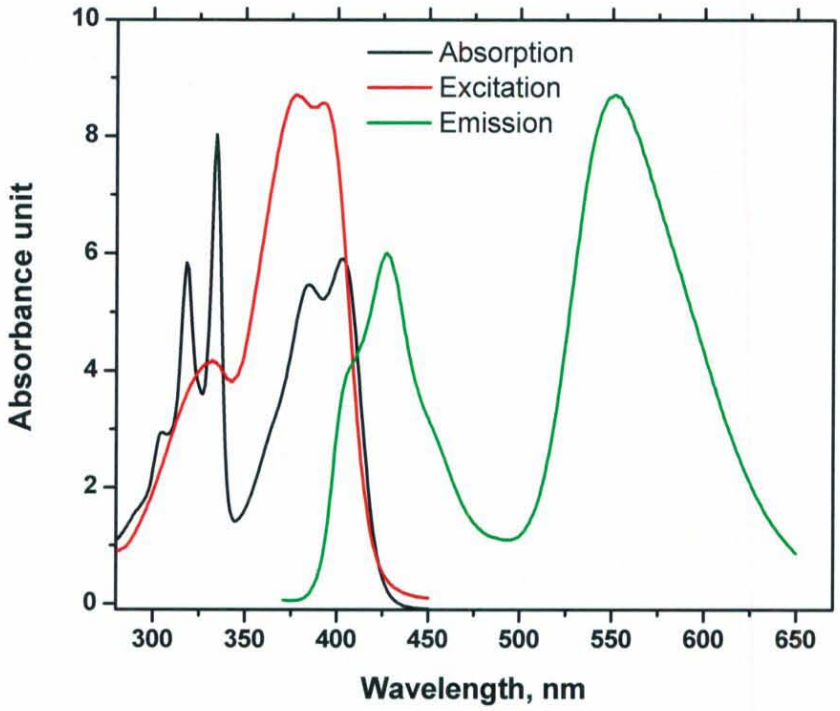

Figure 4.5. Absorption (black line), excitation monitoring at 550 (red line), and emission (green line) spectra of bbim in DMSO at 298 (± 2) K under 1 atm N_2.

4.2.3 Electrolyte Interactions with the Excited State of bbim

The emission spectra for bbim with F^-, OH^-, and Ac^- provide evidence that the excited state of bbim interacts with anions, as illustrated in Figure 4.6. However, the less basic anions such as PF_6^-, HSO_4^-, Cl^-, Br^-, and I^- in a DMSO solutions of bbim do not induce detectable changes in the fluorescence spectra.

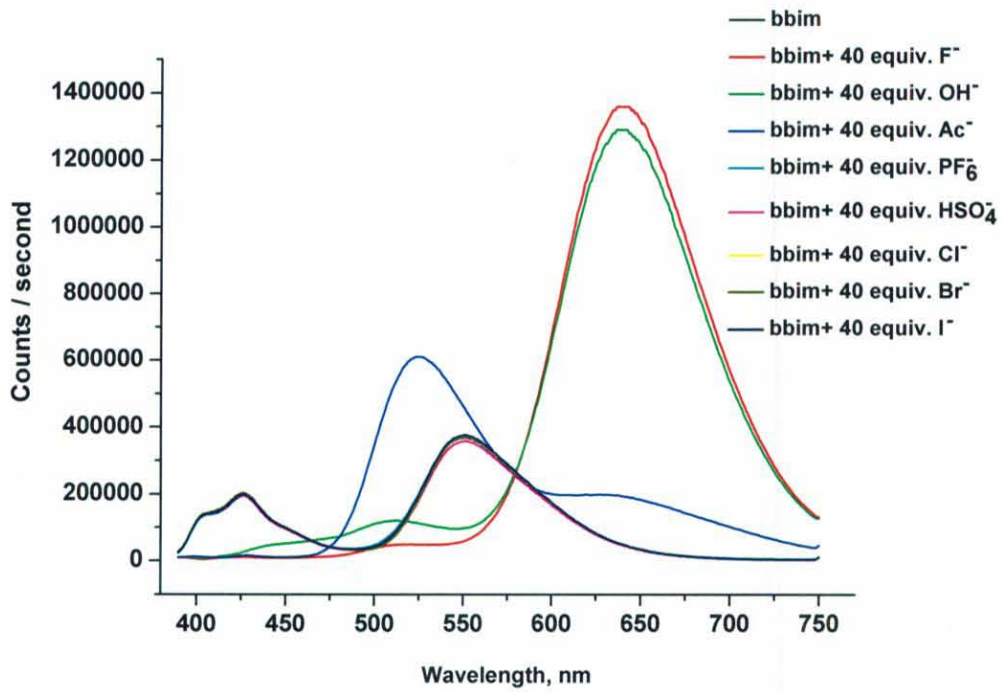

Figure 4.6. Effect of 40 equivalents of all of the different anions under study on the emission spectra of bbim in DMSO solution at 298 (± 2) K under 1 atm N_2.

The fluorescence spectrum of bbim is dependent on the nature and concentration of X^-. The emission spectra of bbim (10 μM in DMSO) as a function of [F^-] is shown in Figure 4.7. The emission spectra appear to be due to two distinct phases depending on the [F^-] in a manner closely analogous to that observed in the absorption data. In the first

phase of the titration, ([F^-]: 0 - 5 equivalents), the emission spectrum of bbim increases in intensity and shifts to slightly higher energy (λ_{max} = 525 nm; 19048 cm^{-1}).

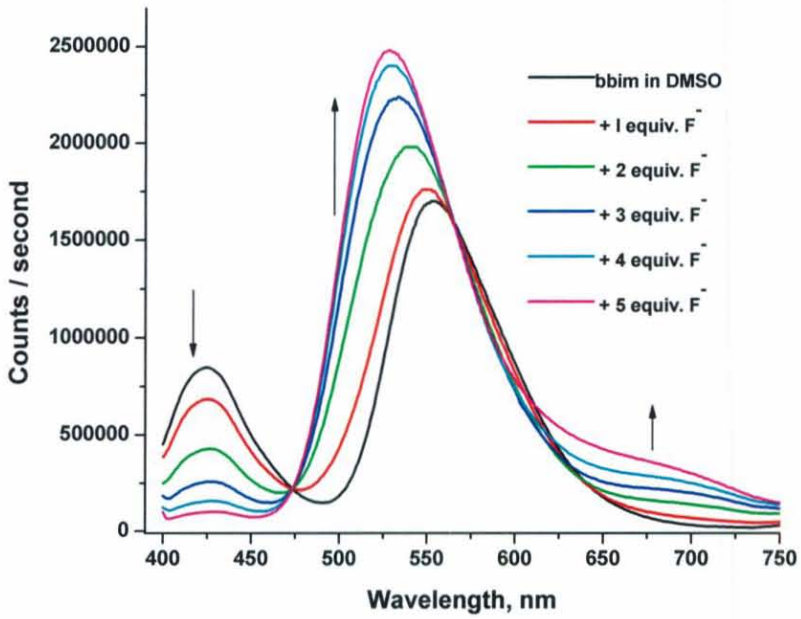

Figure 4.7. Emission changes of bbim DMSO solution at 298 (± 2) K under 1 atm N_2 upon addition 0, 1, 2, 3, 4 and 5 equivalents of TBAF.

In the second phase ([F^-]: 5-40 equivalents), the emission intensity at 525 nm decreases while a new emission maximum appears at 635 nm (15748 cm^{-1}) with a shoulder at 525 nm (Figure 4.9). In comparison, the emission of free bbim is a weak green (ϕ_{em} = 0.091, λ_{em} = 550 nm; 18182 cm^{-1}). Enhanced emission, a new emission at the longer wavelength, an extremely large Stokes shift (9065 cm^{-1}) and a clear isoemissive point at 570 nm (17544 cm^{-1}) are observed. In fact, when bbim was treated with base ($[Bu_4N]OH$), a similar red-shifted emission was observed. However, beyond a

critical [OH^-], quenching of the emission peak at 635 nm was observed after more than 20 equivalents (Figure A-4 appendix).

The emission spectral data were subjected to a Stern-Volmer analysis and the dependence of $^{I_o}/_{I}$ as a function of F^- is shown in Figure 4.8. The data were adequately described by the Stern-Volmer equation given by

$$^{I_o}/_{I} = 1 + K_{SV}[Q] \qquad (4.2)$$

Here I_o is the fluorescence intensity of bbim free of OH^- and I is the emission intensity of bbim with addition of excess of OH^-, K_{SV} is the Stern-Volmer constant, and [Q] is the concentration of the quencher. K_{SV} is given by $^{k_q}/_{\tau}$ where k_q is the rate constant for quenching of the excited state and τ is the lifetime in the absence of quencher. A Stern-Volmer quenching constant was calculated as K_{SV} = 5.5x10^3 M^{-1}.

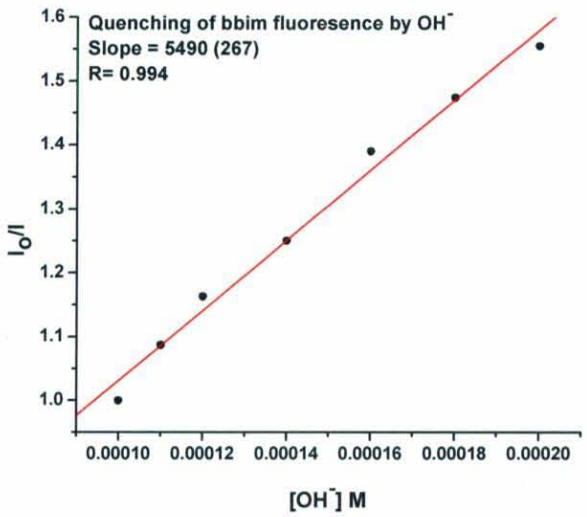

Figure 4.8. Stern-Volmer plot of bbim in DMSO solution at 298 (± 2) K under 1 atm N_2 with addition of OH^-.

In contrast, upon addition of other halide anions, i.e. Cl^-, Br^-, I^-, and also upon addition of PF_6^- and HSO_4^-, no distinct changes were observed except for small decreases in the emission intensity (Figure A-8 in appendix).

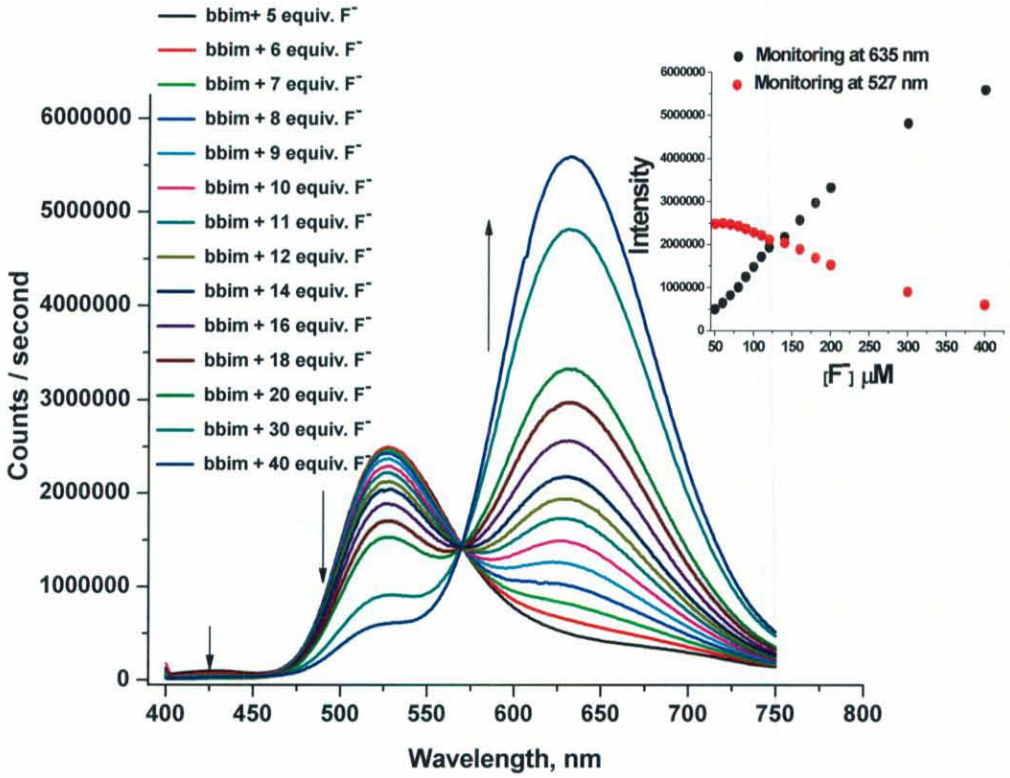

Figure 4.9. Emission changes of bbim in DMSO solution at 298 (± 2) K under 1 atm N_2 upon addition of TBAF from 5 to 40 equivalents; insert emission change at 527 and 632 nm vs. equivalents of F^-.

4.2.4 Analysis of Spectroscopic Data

Isosbestic absorption and isoemissive emission spectra are seen upon addition of one of F^-, OH^- or Ac^-. This may be due to intermolecular hydrogen bonding or deprotonation of bbim in the ground and/or excited state, depending on the basicity, size, and electronegativity of the titrant and the stability of the leaving group. In order to determine the equilibrium constant (K) of the bbim adduct anions the titration spectra are subjected to singular value decomposition (SVD) global analysis with the SPECFIT/32 program as described in Chapter 2. The global analysis places the measured spectra data in a matrix Y, which can be decomposed into a product of matrices A (molar absorptivities) and C (concentration) of initial species.[13,14] The matrices are related by given equation

$$Y = CA + R \qquad (4.3)$$

where R is the matrix of the residuals due to the instrumental and experimental errors.

Global analysis can predict the presence of unknown species and their equilibrium constants and molar absorptivities by fitting the data.[13,14]

For example, the interaction of bbim with F^- produces multiequilibria for the protonation and deprotonation of the four hydrogens of bbim (Scheme 4.4). The reaction model and the parameters are illustrated in Table 4.2, assuming the simplest model that adequately describes the data and which is consistent with the ^{1}H NMR titration experiment.

Table 4.2. Results of the ground and excited states equilibrium constants ($logK$ and $logK^*$ respectively) obtained by global analysis of the series of absorption and emission data of bbim titration with F^-

Reaction model	$logK$	$logK^*$
$bbimH_4 + F^- \rightleftarrows bbimH_4F^-$	2.23	3.66
$bbimH_4F^- + F^- \rightleftarrows bbimH_3^- + FHF^-$	4.67	6.97
$bbimH_3^- + F^- \rightleftarrows bbimH_3^-F^-$	7.56	9.47
$bbimH_3^-F^- + F^- \rightleftarrows bbimH_2^{2-} + FHF^-$	11.12	12.87
$bbimH_2^{2-} + F^- \rightleftarrows bbimH_2^{2-}F^-$	14.35	17.17
$bbimH_2^{2-} + F^- \rightleftarrows bbimH_1^{3-} + FHF^-$	17.50	22.36
$bbimH_1^{3-} + F^- \rightleftarrows bbimH_1^{3-}F^-$	19.49	25.99
$bbimH_1^{3-}F^- + F^- \rightleftarrows bbim^{4-} + FHF^-$	23.57	30.98

The absorption spectra changes upon addition of F^- is shown in Figure 4.10. Addition of OH^- displays similar changes as F^-; on the other hand addition of Ac^- displays attenuation of the peaks (Figure 4.11). The correlations between the parameters are shown in the appendix (Table A-2, Table A-3 and Table A-4).

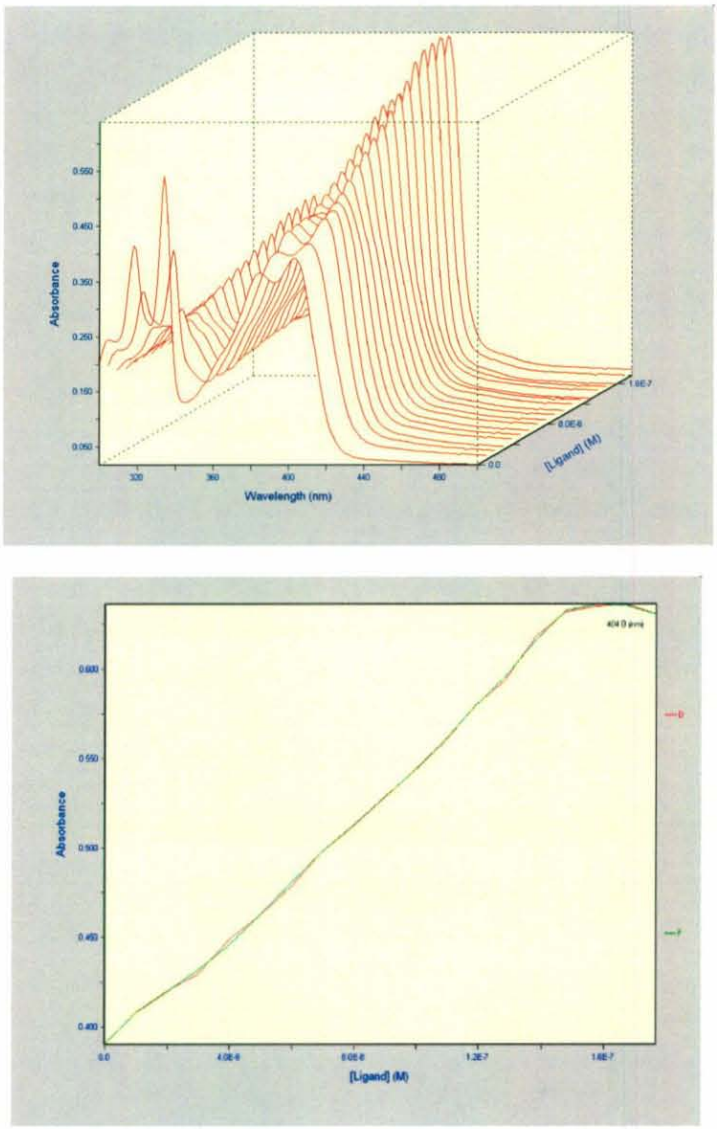

Figure 4.10. Titration of bbim in DMSO solution at 298 (± 2) K under 1 atm N_2 with F^-. Using SPECFIT/32 results in a good fit to the data at 404 nm.

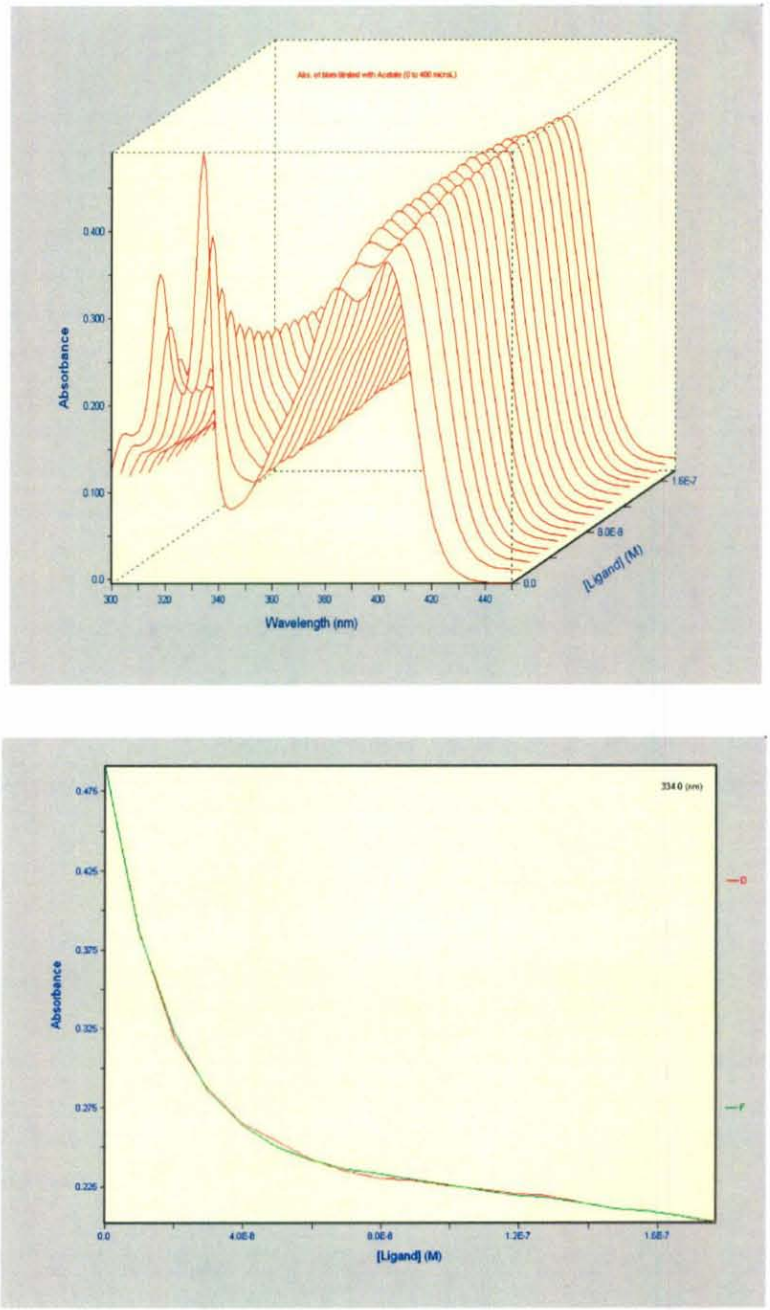

Figure 4.11. Titration of bbim in DMSO solution at 298 (± 2) K under 1 atm N_2 with acetate anion. Using SPECFIT/32 results in a good fit to the data at 334 nm.

Table 4.3. Ground state global analysis measurements of binding constants (log K_n) for bbim titrated with fluoride, hydroxide, and acetate anions.

Anions	log K_1	log K_2	log K_3	log K_4	log K_5	log K_6	log K_7	log K_8
F^-	2.23	4.67	7.56	11.12	14.35	17.50	19.49	23.57
OH^-	2.56	6.39	10.27	15.07	18.09	21.77	26.03	28.94
Ac^-	2.59	11.28	17.77	25.17	-	-	-	-

The data shown in Figure 4.12 were analyzed using the global analysis SPECFIT/32 program to extract the equilibrium constant (K) of the excited state.

Table 4.4. Ground state global analysis measurements of the excited state binding constants (log K_n) for bbim titrated with fluoride, hydroxide, and acetate anions.

Anions	log K_1	log K_2	log K_3	log K_4	log K_5	log K_6	log K_7	log K_8
F^-	3.66	6.97	9.47	12.87	17.17	22.36	25.99	30.98
OH^-	10.01	12.30	15.04	18.21	22.47	27.72	-	-
Ac^-	2.37	11.40	19.68	24.53	-	-	-	-

Absorption, excitation, and emission spectra of bbim with 40 equivalents of F^- in a N_2 purged DMSO solution are shown in Figure 4.13. This solution gives rise to two major emission bands at 520 nm (19230 cm^{-1}) and 635 nm (15748 cm^{-1}). The excitation spectrum of bbim (λ_{mon} = 635 nm) displayed identical band envelope shapes to the absorption spectra.

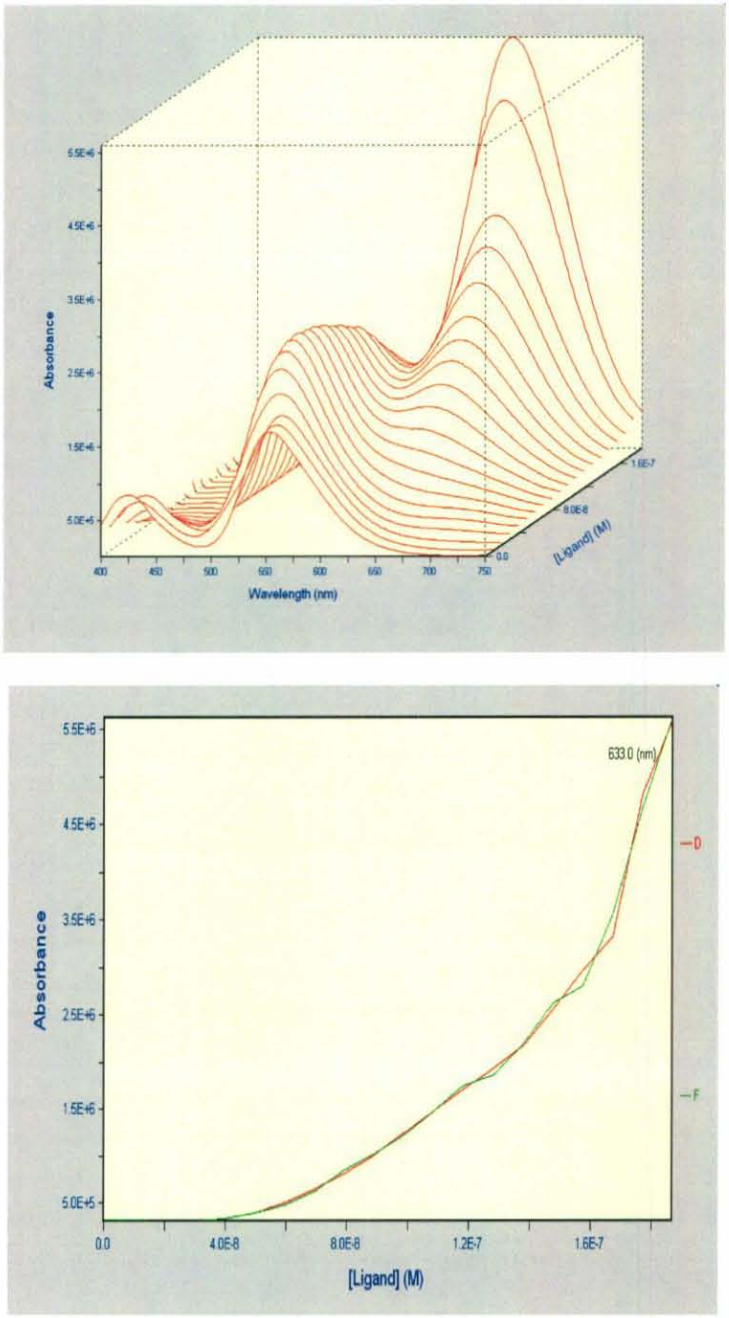

Figure 4.12. Titration of bbim in DMSO solution at 298 (± 2) K under 1 atm N_2 with fluoride anion. Using SPECFIT/32 program results in a good fit to the data at 633 nm.

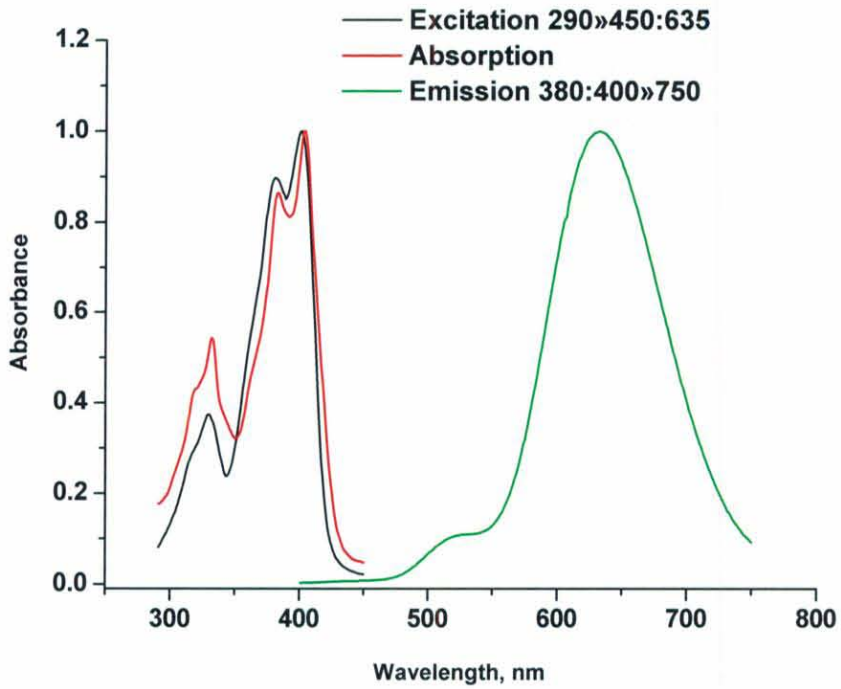

Figure 4.13. Absorption, excitation, and emission spectra of bbim in DMSO solution at 298 (± 2) K under 1 atm N_2 with addition of 40 equivalents of TBAF.

The emission spectra of bbim (10 μM in DMSO) demonstrated dependence on the concentration of D_2O, with the intensity of the enol form peak at 426 nm decreasing with increasing keto-form (tautomer). A small new emission peak arises at about 635 nm when excess D_2O was added, as shown in Figure 4.14.

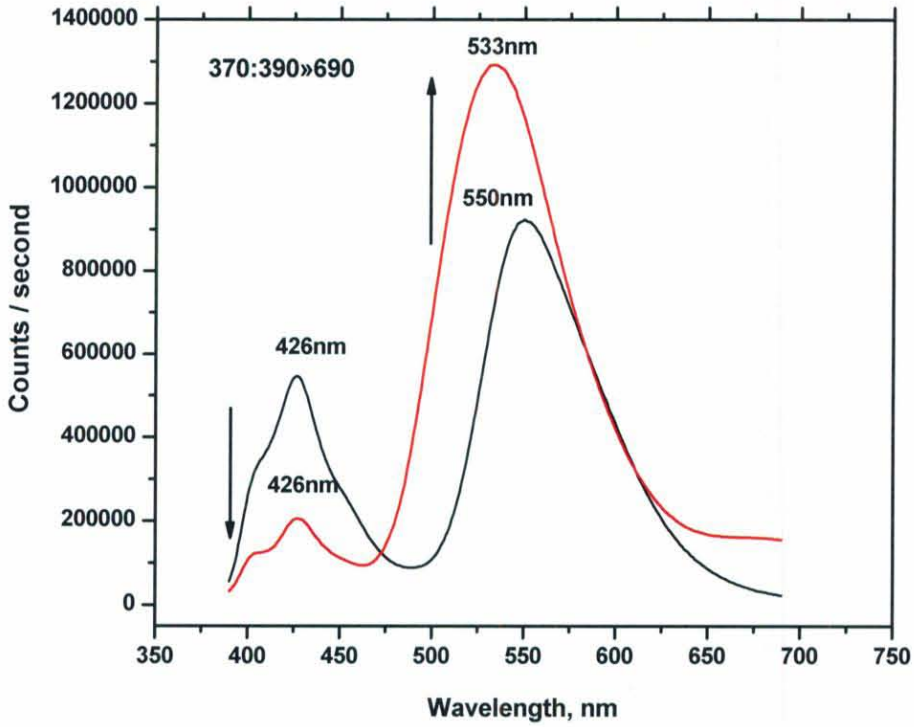

Figure 4.14. Emission spectrophotometric titration of bbim in DMSO solution at 298 (± 2) K under 1 atm N_2 with D_2O 10 equivalents (red spectrum line), free bbim is the black spectrum line.

4.3 Discussion

Supramolecular interaction between chromophores and ions in solution constitute one of the most active areas of research in the molecular sciences. Cation/anion–donor/acceptor dynamics with suitable acceptors can alter the physical properties of a given system. The chemistry may be exploited for the detection of analytes in solution, thereby forming the basis for a chemosensor.

4.3.1 Electrolyte Interactions

The effect of ions on the ground state properties of bbim in DMSO (10μM solution, 1 atm N_2) was studied by adding tetraalkylammonium salts of Cl^-, I^-, Br^-, PF_6^- and HSO_4^-. These electrolytes did not significantly alter the UV-Vis spectra of bbim (Figure A-7 in the appendix). In contrast, addition of tetrabutylammonium salts with F^- or OH^- affects the absorption spectra in two ways. Upon addition of 1 and 2 molar equivalents of fluoride ions to the bbim, the band shifts (Figure 4.3) suggest that the bbim formed an intermolecular hydrogen bond with F^- as shown in Scheme 4.3.

Scheme 4.3. Proposed mechanism illustrate the adduct complex between bbim in DMSO solution at 298 (± 2) K under 1 atm N_2 and 2 equivalents of F^-.

However, with further addition of fluoride from 3 to 40 molar equivalents, systematic changes in the UV-Vis spectra were observed with five isobestic points, suggesting that binding of F^- with bbim must be described by multiple equilibra This

was confirmed by absorption spectra changes and NMR changes, with observation of FHF^- after addition of more than four equivalents of F^-(Figure 4.1). To determine the equilibrium constants, the spectral data were subjected to global analysis (Figure 4.10). The best fitting of the spectral data is obtained on the assumption of multiple stepwise equilibria (Scheme 4.4).

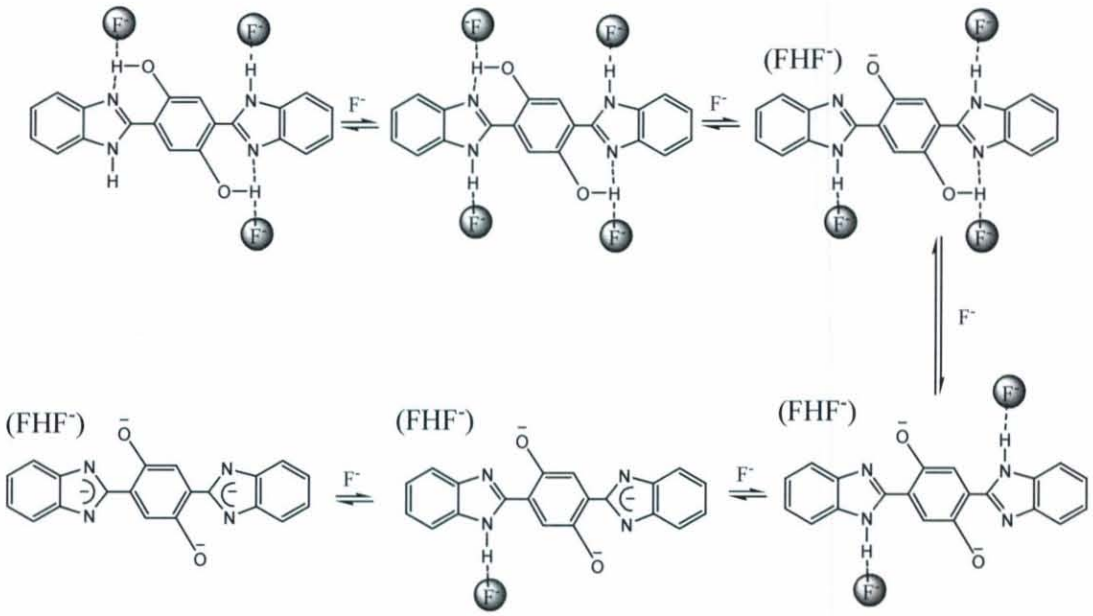

Scheme 4.4. Proposed ground state mechanism of the interaction of bbim in DMSO solution at 298 (± 2) K under 1 atm N_2 with F^-.

In Figure 4.4, the fluoride titration in DMSO solutions results in spectral changes which suggest the formation of a $[bbim \ldots . F^-]$ interaction through hydrogen bonding and intermolecular proton transfer (IPT) between the bridging hydroquinone OH and benzimidazole NH upon further addition of F^-. These deprotonations lead to an increased negative charge on the ion state of bbim, i.e. from a neutral state to one that is

negatively charged. The interaction of F^- with bbim is also clear from ^1H NMR studies which are consistent with Schemes 4.3 and 4.4, and demonstrate the presence of strong hydrogen bonding involving both the OH and NH groups with fluoride anion in the ground state. Upon addition of F^-, the hydroquinone OH proton signal (13.31 ppm) and benzimidazole NH proton signal (12.71 ppm) disappear completely from the NMR spectrum (0-20 ppm) as shown in Figure 4.1. These observations demonstrate that the proton transfer interaction between bbim and F^- involves both the OH and NH moieties.[15] One also sees broadening of all of the other peaks at 7.75, 7.62 and 7.36 ppm, and a downfield shift for the H_a, H_b, H_c, H_d and H_e protons (Figure 4.15) in the benzimidazole ring, indicating the formation of O-H···F and N-H···F hydrogen bonds.[16-18]

The appearance of a new peak at 16.15 ppm indicates that the deprotonation of both the OH and NH groups has occurred. After the addition of 8 equivalents of F^-, the system has lost all hydrogen bonds to F^- which causes the broad NMR peaks (observed after the addition of one equivalent of F^-) to form a sharp multiplet peak from 7.362 to 7.344 ppm, and the other broad peak became a sharp quartet peak at 6.781-6.764 ppm, which indicates that bbim has became more symmetrical. With ten molar equivalents of F^-, low field signals at 16.15 ppm with a triplet resonance appears, which is assigned to bifluoride ion (FHF^-) (Figure 4.16(B)).[11,19-33] This is consistent with Scheme 4.4. Occurrence of the O-H and N-H deprotonation is confirmed by: (a) complete disappearance of both O-H and N-H NMR peaks from 0-20 ppm, and (b) an upfield shift for all aromatic protons (Figure 4.16(B)).

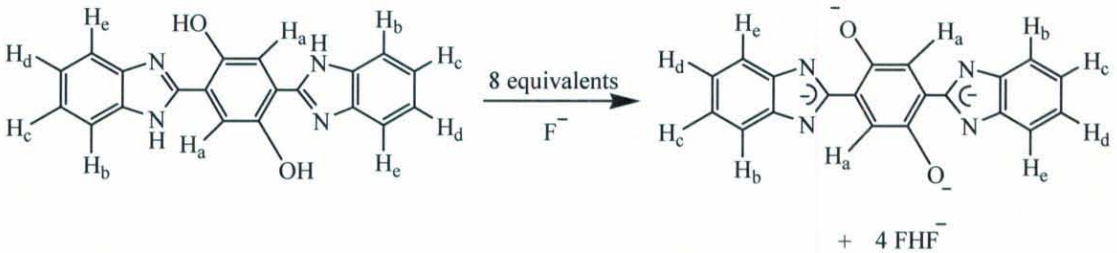

Figure 4.15. Deprotonation of bbim in DMSO-d_6 solution at 298 (± 2) K by adding more than 8 equivalents of $[Bu_4N]F$.

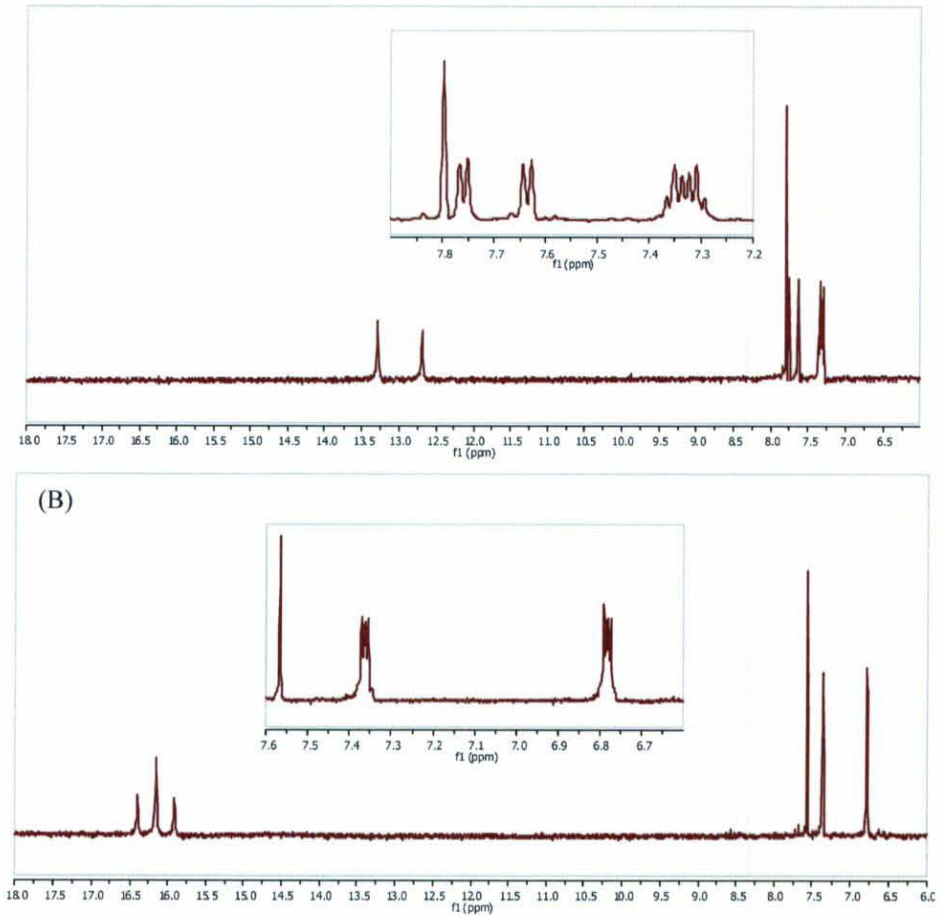

Figure 4.16. (A) ^{1}H NMR spectra for bbim in DMSO-d_6 at room temperature. The peaks were assigned as: ^{1}H NMR: δ ppm 7.32-7.20 (H_c and H_d, m), 7.63 (H_e , d, $3J$ = 6 Hz). 7.75 (H_b,d, $3J$ = 6 Hz), 7.79 (H_a, s), 12.70 (NH, s), 13.31 (OH, s). (B) ^{1}H NMR spectra for bbim in DMSO-d_6 with 10 equivalents of F^-. The peaks were assigned as: ^{1}H NMR: δ ppm 6.78-6.76 (H_c and H_d, m), 7.36-7.34 (H_e and H_b m), 7.55 (H_a, s) and 16.39-16.91 (FHF^-, t).

Titrations of bbim with $[Bu_4N]OH$, display similar behaviour to that of F^-: the OH and NH peaks completely disappear upon addition of 1 equivalent of OH^-, and there is no resonance peak at 16.15 ppm. With other less basic anions such as Cl^-, I^-, Br^-, PF_6^- and HSO_4^-, no evidence of deprotonation was observed in the ground and excited states. However, this is not unexpected. The interaction of bbim with anions is related to the basicity of anions which in the case of Ac^- induced gradual spectral changes, however, the sensitivity of spectral responses were as not large as those seen for F^- and OH^-. The best global analysis fitting of the absorption titration data for Ac^- included four equilibria. This suggests that the acetate ion cannot deprotonate bbim in the ground state, but upon Ac^- addition deprotonation of just the hydrogen from hydroquinone occurs in the excited state. The factors that govern the deprotonation are not only the acidity of the hydrogen donor and the basicity of the anion acceptor, but also the stability of the leaving group. The F^- ion is able to extract more than one proton from the same molecule by producing a very stable hydrogen bonded complex $[FHF^-]$.[19,20,23,31,35]

The emission spectrum of bbim exhibits anion dependent behavior as shown in Figure 4.7 and 4.9. In the case of titration of bbim in DMSO with F^- shown in Figure 4.9, the intensity of the peak at 427 nm (23420 cm^{-1}) decreases in intensity while the intensity of the tautomer peak at 550 nm (18182 cm^{-1}) increases with slight shifts to higher energy. Further addition of F^- results in the peak at 427 nm being completely quenched, while the peak at 550 nm is quenched and shifts to 525 nm (19048 cm^{-1}) giving rise to a new bright and deep red emission with a maximum at 635 nm. The increased emission yield, especially the observation of a new emission at the longer

wavelength and the extremely large Strokes shift (236 nm, 9165 cm^{-1}) suggests that an intermolecular proton transfer to basic fluoride occurs in both the ground and the excited states.[20,30] When the data were fit using the SPECFIT/32 global analysis program, the association constants were determined resulting in a good fit to the data at 635 nm. The resulting equilibrium constants are consistent with the NMR titration experiments performed in DMSO-d_6, and also reasonably consistent with the mechanism shown in Scheme 4.4. This is reasonably interpreted as well by considering the molecular structure of bbim which has OH and NH groups both capable of hydrogen bonding to the fluoride ion.[32] The postulated mechanism in Scheme 4.5 predicts that, in the presence of F^-, competition between the excited state intramolecular proton transfer and excited state intermolecular proton transfer occurs. Further addition of F^- causes complete quenching of the isomer (enol-form) emission peak and also quenched the tautomer (keto-form) emission peak with a new emission band (red shifted) being seen which increased in intensity gradually upon addition of F^-. A possible explanation of the significant red shift is that a series of proton transfers occurs to form four negative charges on the bbim complex in the excited state. The formation of a new red shifted emission after addition of 8 equivalents of F^- is indicative of complete deprotonation of bbim. This causes a loss of the inter and intramolecular hydrogen bonds, a conclusion supported by the increase in the quantum yield of the new emission peak at 635 nm compared to the tautomer emission peak at 550 nm (ϕ_{em} 635nm=0.362 and ϕ_{em} 550nm=0.091 respectively). These results are also supported by a paper published by Barbara and Flom,[36] in which they confirmed that nonradiative decay rates of the tautomer will

increase in the presence of intramolecular hydrogen bonding. The acidity of the OH in the hydroquinone in the excited state is higher than in the ground state. Because of this difference the stability constant in the excited state is not the same as the ground state stability constant (Tables 4.3 and 4.4).

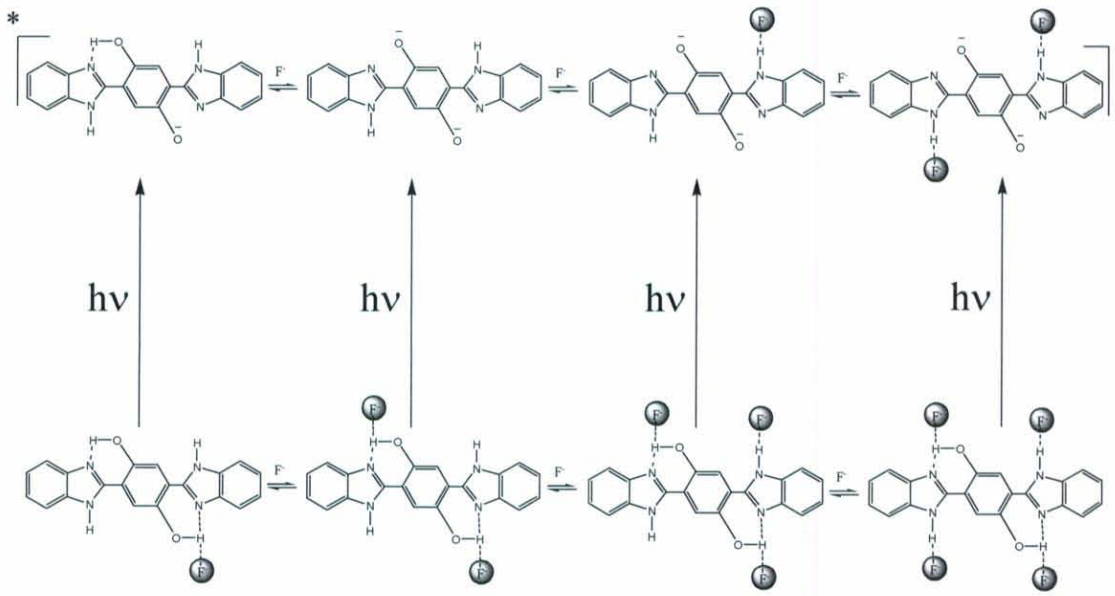

Scheme 4.5. Proposed excited state mechanism of the first set of interactions of bbim with F^- ion.

The effect of OH^- ion in the excited state is not exactly the same as that of F^- ion even though both anions (F^-, OH^-) gave the same ground state results (absorbance and ^1H NMR titration). In the excited state, there is a slight difference which is not fully understood. From the excited state measurements the F^- ion is shown to be able to deprotonate the hydroquinone OH of bbim by forming a 1:1 adduct, and to deprotonate the benzimidazole NH of bbim by forming a 2:1 adduct. Therefore, it is postulated that

the nature of the excited state of *bbimH···[F]$_2$* is dramatically different than that of the 1:1 adduct.

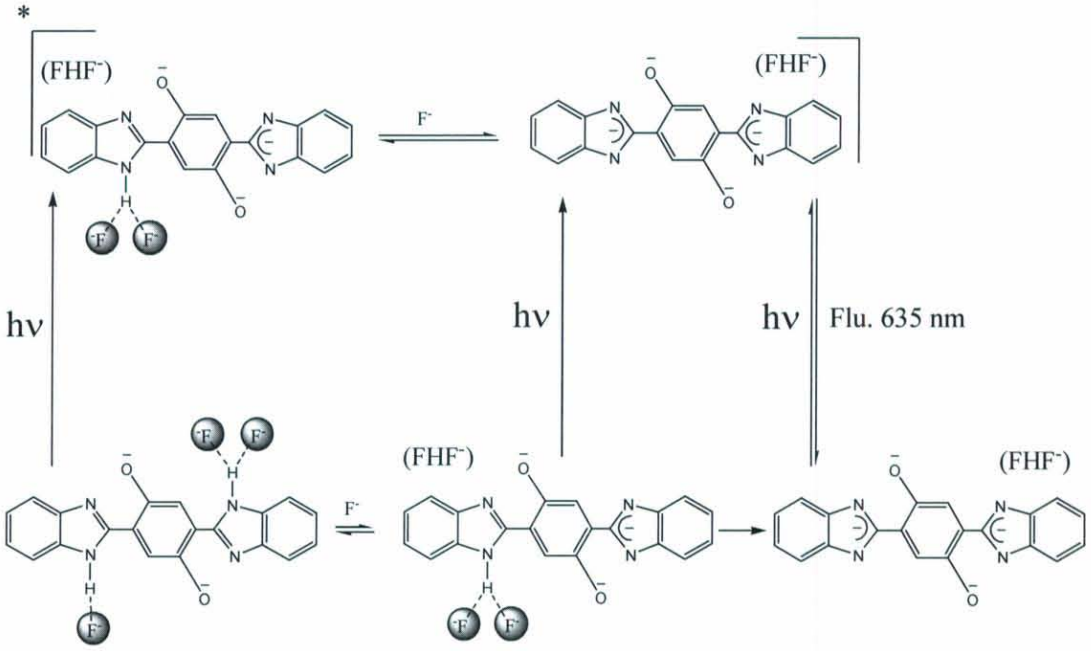

Scheme 4.6. Proposed excited state mechanism of the second set of interactions between bbim and F^-ions.

Addition of $[Bu_4N]OH$ results in a similar red-shifted emission being observed together with the eventual quenching of the emission peak at 635 nm after addition of 18 equivalents of OH^-. The Stern-Volmer plot[37] of bbim with addition of OH^- displays a close to linear relationship (Figure 4.8). The fluorescence intensity of bbim is quenched upon addition of excess OH^-, which maybe indicates a strong excited state interaction between bbim and OH^- (hydrogen-bond interaction) or could be attributed to a photoinduced electron transfer process (PET).[38-40]

Previous work on a related system has been done by Fabbrizzi *et al.* in 2005.[32] They performed titrations of urea by tetrabutylammonium fluoride and hydroxide and found that these anions induced double deprotonation from urea. They used the UV-vis absorption and ^{1}H NMR spectra as evidence for their conclusions. On the other hand, addition of a large amount of acetate induced only one deprotonation. These observations are consistent with our results for titration of bbim by the same anions.

Addition of an excess amount of the less basic anions such as PF_6^-, HSO_4^-, Cl^-, Br^-, and I^- to a DMSO solution of bbim do not induce detectable changes in the fluorescence spectra excluding a small decrease in emission intensity which may be indicative of a heavy atom effect (Figure A-8 in appendix).[37] Upon addition of H_2O or / and D_2O, the fluorescence intensity of the tautomer increases in DMSO solution (Figure 4.14). This is likely due to formation of the intermolecular hydrogen bonded tautomer. To extract a proton from bbim requires the assistance of several H_2O molecules to assist proton transfer from the bbim molecule (Scheme 4.7).[41] The number of H_2O molecules which participate cannot be determined from our experiments. Deprotonation of bbim by H_2O or D_2O could not occur unless a large excess of water molecules were added. In our experiments, we saw evidence of strong hydrogen bonds between bbim and a cluster of hydrogen bonded water molecules but no clear evidence for deprotonation. The emission spectra show a growing new emission peak at 635 nm in the same position as seen in titrations of bbim with F^-, OH^-,and Ac^-. Therefore, we can conclude that bbim deprotonation needs a cluster of H_2O molecules to accept a proton from bbim.

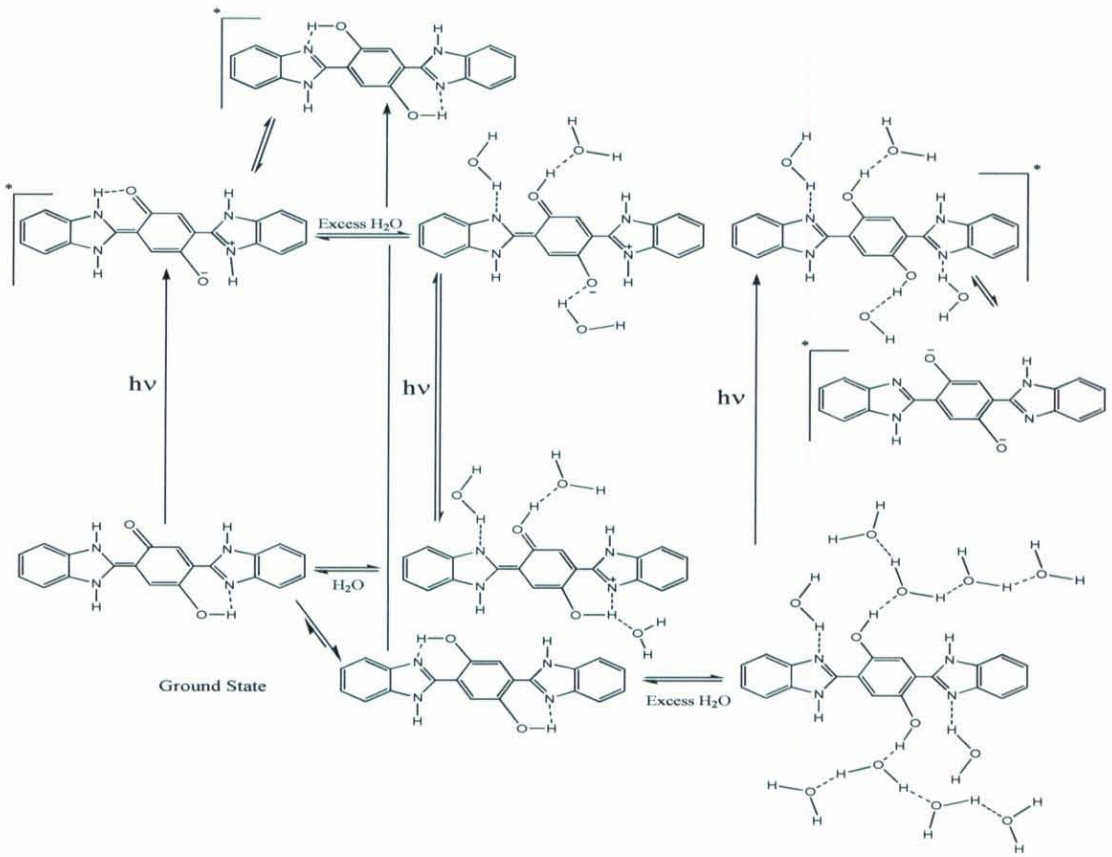

Scheme 4.7. Proposed ground and excited state proton transfer mechanism of interaction bbim with H_2O.

4.4 Conclusion

In this work, the behavior of bisbenzimidazolyl-hydroquinone in the presence of basic anions has been studied. Both the ground and the excited-state behavior of bbim were shown to be anion dependent. The fluoride and hydroxide effect on bbim is significantly higher than that observed for other halide anions (Ac^-, PF_6^-, HSO_4^-, Cl^-, Br^-, and I^-). Moreover, the effect of F^- and OH^- dramatically changes the emission color from weak green to bright red and gives about a 5-fold enhanced emission for F^- and OH^- and a small effect for Ac^- in the UV-Vis and fluorescence emission. For the other anions such as PF_6^-, HSO_4^-, Br^-, Br^-, and I^- there is no significant change in the ground and excited state emission.

4.5 References

(1) Boiocchi, M.; Del Boca, L.; Gomez; abbrizzi, L.; Licchelli, M.; Monzani, E. *J. Am. Chem. Soc.* **2004**, *126*, 16507-16514.

(2) Boiocchi, M.; Del Boca, L.; Gomez, D. E.; Fabbrizzi, L.; Licchelli, M.; Monzani, E. *J. Chem. Eur* **2005**, *11*, 3097-3104.

(3) Costero, A. M.; Banuls, M. J.; Aurell, M. J.; Ward, M. D.; Argent, S. *Tetrahedron* **2004**, *60*, 9471-9478.

(4) Esteban-Gmez, D.; Fabbrizzi, L.; Licchelli, M. *J. Org. Chem.* **2005**, *70*, 5717-5720.

(5) Evans, L. S.; Gale, P. A.; Light, M. E.; Quesada, R. *Chem. Commun* **2006**, 965-967.

(6) Gunnlaugsson, T.; Kruger, P. E.; Jensen, P.; Pfeffer, F. M.; Husset, G. M. *Tetrahedron Lett* **2003**, *44*, 8909-8913.

(7) Grabowska, A.; Mordzinski, A.; Tamai, N.; Yoshihara, K. *Chem. Phys. Lett.* **1988**, *153*, 389-392.

(8) Grabowska, A.; Sepiol, J.; Rulliere, C. *J. Phys. Chem.* **1991**, *95*, 10493-10495.

(9) Mordzinski, A.; Grabowska, A.; Kuehnle, W.; Krowczynski, A. *Chem. Phys. Lett.* **1983**, *101*, 291-296.

(10) Mordzinski, A.; Grabowska, A. J. *Mol. Struct.* **1984**, *114*, 337-341.

(11) Peng, X.; Wu, Y.; Fan, J.; Tian, M.; Han, K. *J. Org. Chem.* **2005**, *70*, 10524-10531.

(12) Tong, H.; Zhou, G.; Wang, L.; Jing, X.; Wang, F.; Zhang, J. *Tetrahedron Lett* **2003**, *44*, 131-134.

(13) Martell, A. E.; Motekaitis, R. J. *"Determination and Use of Stability Constants"*; Verlag Chemie, Weinheim,, 1988.

(14) Polster, J.; Lachmann, H. *"Spectrometric Titrations"*; Verlag Chemie, Weinheim, 1989.

(15) Cho, E. J.; Moon, J. W.; Ko, S. W.; Lee, J. Y.; Kim, S. K.; Yoon, J.; Nam, K. C. *J. Am. Chem. Soc.* **2003**, *125*, 12376-12377.

(16) Zhang, X.; Guo, L.; Wu, F.-Y.; Jiang, Y.-B. *Org. Lett.* **2003**, *5*, 2667-2670.

(17) Jose, D. A.; Kumar, D. K.; Ganguly, B.; Das, A. *Org. Lett.* **2004**, *6*, 3445-3448.

(18) Lin, C.-I.; Selvi, S.; Fang, J.-M.; Chou, P.-T.; Lai, C.-H.; Cheng, Y.-M. *J. Org. Chem.* **2007**, *72*, 3537-3542.

(19) Amendola, V.; Boiocchi, M.; Fabbrizzi, L.; Palchetti, A. *J. Chem. Eur.* **2005**, *11*, 5648 –5660.

(20) Amendola, V.; Esteban-GÃ³mez, D.; Fabbrizzi, L.; Licchelli, M. *Acc. Chem. Res.* **2006**, *39*, 343-353.

(21) Descalzo, A. B.; Rurack, K.; Weisshoff, H.; Martínez-Máñez, R.; Marcos, M. D.; Amorós, P.; Hoffmann, K.; Soto, J. *J. Am. Chem. Soc.* **2005**, *127*, 184-200.

(22) Fang, L.; Chan, W.-H.; He, Y.-B.; Kwong, D. W. J.; Lee, A. W. M. *J. Org. Chem.* **2005**, *70*, 7640-7646.

(23) Gunnlaugsson, T.; Ali, H.; Glynn, M.; Kruger, P. E.; Hussey, G. M.; Pfeffer, F. M.; Cid´alia, M. G.; D., S.; Tierney, J. *Journal of Fluorescence* **2005**, *15*, 287-299.

(24) Gunnlaugsson, T.; Glynn, M.; Tocci, G. M.; Kruger, P. E.; Pfeffer, F. M. *Coord. Chem. Rev.* **2006**, *250*, 3094–3117.

(25) Gunnlaugsson, T.; Kruger, P. E.; Jensen, P.; Tierney, J.; Ali, H. D. P.; Hussey, G.

M. *J. Org. Chem.* **2005**, *70*, 10875-10878.

(26) Hudnall, T. W.; Chiu, C.-W.; GabbaiÌˆ, F. o. P. *Acc. Chem. Res.* **2009**, *42*, 388-397.

(27) Kumar, S.; Luxami, V.; Kumar, A. *Org. Lett.* **2008**, *10*, 5549-5552.

(28) Miskolczya, Z.; Biczók, L. *J. Photochem. Photobio. A: Chem.* **2006**, *182*, 82-87.

(29) Shenderovich, I. G.; Tolstoy, P. M.; Golubev, N. S.; Smirnov, S. N.; Denisov, G. S.; Limbach, H.-H. *J. Am. Chem. Soc.* **2003**, *125*, 11710-11720.

(30) Wu, C.-Y.; Chen, M.-S.; Lin, C.-A.; Lin, S.-C.; Sun, S.-S. *J. Chem. Eur.* **2006**, *12*, 2263 –2269.

(31) Wu, Y.; Peng, X.; Fan, J.; Gao, S.; Tian, M.; Zhao, J.; Sun, S. *J. Org. Chem.* **2006**, *72*, 62-70.

(32) Zhao, Y.-P.; Zhang, B.-g.; Duan, C.-Y.; Lin, Z.-H.; Meng, Q.-J. *New J. Chem.* **2006**, *30*, 1207-1213.

(33) Zhao, Y.-P.; Zhao, C.-C.; Wu, L.-Z.; Zhang, L.-P.; Tung, C.-H.; Pan, Y.-J. *J. Org. Chem.* **2006**, *71*, 2143-2146.

(34) Bordwell, F. G. *Acc. Chem. Res.* **1988**, *21*, 456-463.

(35) Zhang, B.-g.; Xu, J.; Zhao, Y.-g.; Duan, C.-y.; Cao, X.; Meng, Q.-j. *Dalton Trans.* **2006**, 1271-1276.

(36) Flom, S. R.; Barbara, P. F. *J. Phys. Chem.* **1985**, *89*, 4489-4494.

(37) Lakowicz, J. R. *"Principle of Fluorescence Spectroscopy"*; Spronger Science/ kluwer: New York, 2006; Vol. 3rd.

(38) Miao, Y.-J.; Bazan, G. C. *J. Am. Chem. Soc.* **1994**, *116*, 9379-9380.

(39) De Silva, A. P.; Gunaratne, H. Q. N.; Gunnlaugsson, T.; Huxley, A. J. M.;

McCoy, C. P.; Rademacher, J. T.; Rice, T. E. *Chem. Rev.* **1997**, *97*, 1515-1566.

(40) Li, P.; Shaw, B. R. *Org. Lett.* **2002**, *4*, 2009-2012.

(41) Penedo, J. C.; Mosquera, M.; Rodriguez-Prieto, F. *J. Phys. Chem. A* **2000**, *104*, 7429-7441.

Chapter 5

Characterization of the Ground and Excited State Properties in a Series of 3-aminocoumarins (3-AC)

5.1 Introduction

5.1.1 The Properties of Coumarin and its Derivatives

The coumarin molecule (1,2-benzopyrone) was isolated from plants in 1820.[1] A variety of coumarin derivatives have been synthesized and particularly investigated for their biological effects and medical usefulness. For example, coumarins are formed in response to traumatic injury and are widely used in the fields of polymer science.[2-16] Coumarins are also found in which the pharmacological therapy and photodynamic properties depend upon the pattern of ring substitution.[2-16]. Examples of coumarin structures that contain substituents are illustrated in Figure 5.1.

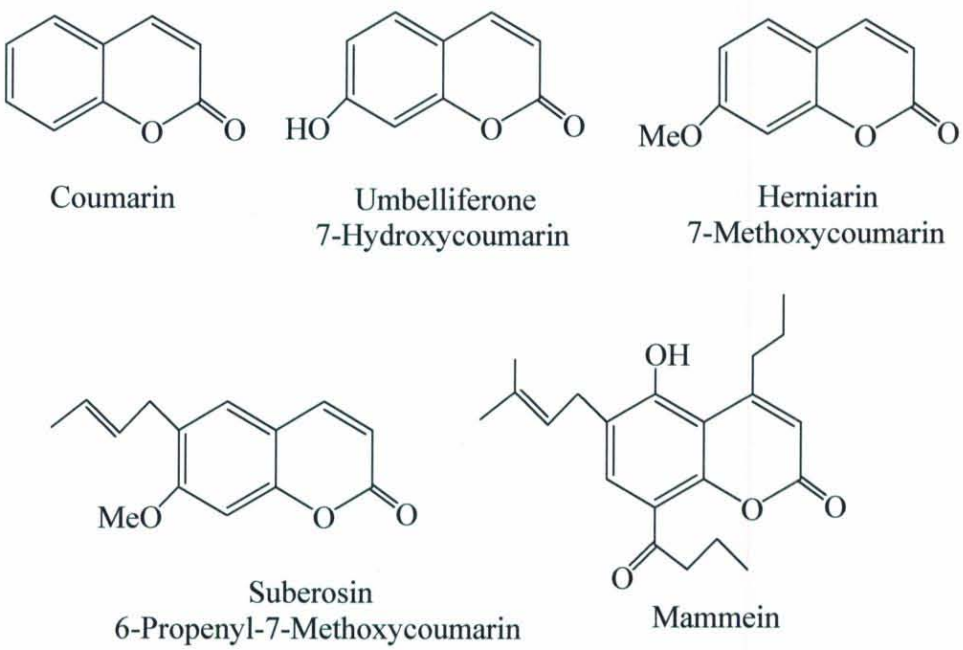

Figure 5.1. Examples of simple coumarins.

Coumarins exhibit sensitivity to their local structure. For example, changes in solvent polarity alters the fluorescence wavelength, quantum yield, and excited state lifetime of the coumarin laser dyes.[9,17,18] As a result of this sensitivity to the environment/medium, coumarins have found widespread applications. For instance, coumarins having a strong electron donating substituent, such as the amino group (7-position), comprise a class of efficient laser dyes, and coumarins with 3, 4 and 6-substituted electron withdrawing groups provide a large number of laser emitting lines in the blue-green region of the visible spectrum.[13,19] In total, over one hundred coumarin laser dyes are presently known.[20,21]

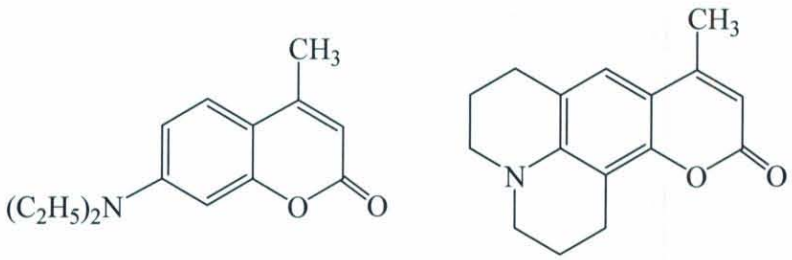

Coumarin 460 Coumarin 480

Figure 5.2. Examples of the chemical structures of some coumarin laser dyes.

Jones *et al.*[22] have studied the solvent effects for the coumarins shown in Figure 5.2. They observed a strong red-shift and a reduced fluorescence quantum yield in polar solvents. The authors attributed these changes with increasing solvent polarity to an increased nonradiative decay rate (k_{nr}) via formation of a twisted intramolecular charge-transfer (TICT) state, which will be discussed in a later section.

5.1.2 Spectroscopic Properties of Coumarin and its Derivatives

The photophysical properties of coumarin based chromophores have been documented since the 1940s.[13] The excited states generally can undergo many excitation and relaxation processes. However, some of these processes can be represented using a modified Jablonski diagram or energy state diagram for a typical chromophore molecule.

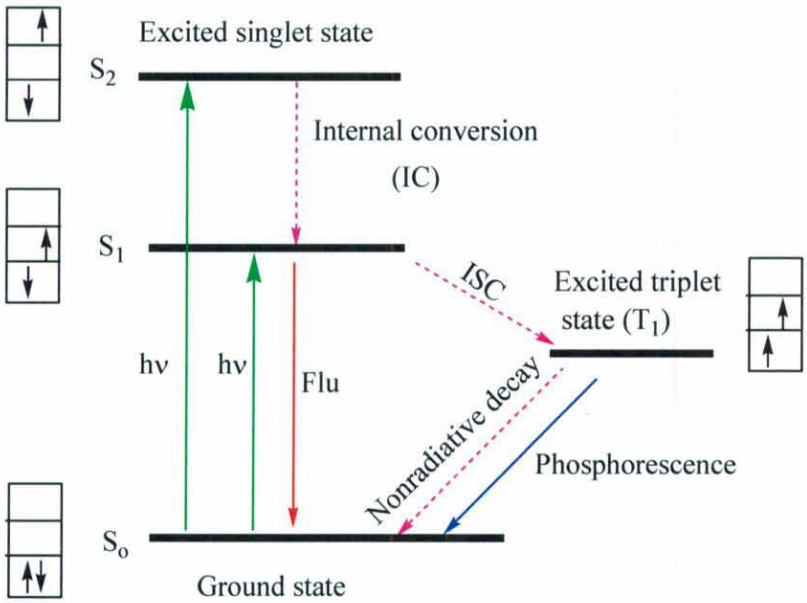

Figure 5.3. A modified Jablonski diagram illustrates excited state decay.

The photophysics and photochemistry of coumarins are dependent on solvent polarity, substituents and substituent placement. The numbering system for substituent placement is shown in the figure below.

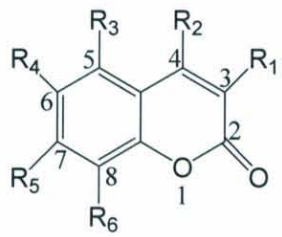

Figure 5.4. Structure and numbering scheme for coumarin with substituents.

The absorption spectrum of coumarin or 6-methylcoumarin has one transition at 275 nm $\left(E_{op} = 36364\ cm^{-1}\right)$ assigned to a $^{1}[(\pi)^2 \rightarrow (\pi\pi^*)]$ or L_B^1 transition using the Platt notation, and a second transition at 321 nm $\left(E_{op} = 31150\ cm^{-1}\right)$ assigned to a $^{1}[(\pi)^2 \rightarrow {}^{1}(\pi\pi^*)]$ transition or a L_a^1 transition using the Platt notation. The expected $[(n)^2 \rightarrow {}^{1}(\pi\pi^*)]$ transition localized on the CO moiety is not observed, as it is a forbidden transition. Emission is observed at 370 nm $(E_{em} = 27030\ cm^{-1})$ in dioxane with $\tau < 0.3\ ns$ and is assigned to $S_0 \leftarrow S_1$ fluorescence.

5.1.2.1 Triplet State

Coumarins often possess a long-lived triplet $^{3}(\pi\pi^*)$ which arises from intersystem crossing from the singlet $^{1}(\pi\pi^*)$ state. In the absence of an obvious source of spin-orbit coupling (e.g. heavy metals), the singlet-triplet transition is counterintuitive. Coumarin derivatives such as 3-aminocoumarin (3-AC) can undergo the spin forbidden process of intersystem crossing (ISC). The law of conservation of momentum dictates that in an isolated system or molecule the momentum may be transferred but must be conseved.[23] However, the total change in the angular momentum and linear momentum must be constant. Thus the forces within a molecule that can bring about a spin change without violating the law of conservation of momentum can be summarized. Spin-orbit coupling (SOC), in which torque on an electron spin is created by orbital angular momentum, is the dominant intramolecular force which facilitates ISC. Figure 5.5 illustrates the relative orientations of the two electron spins for the single and the triplet state.[24]

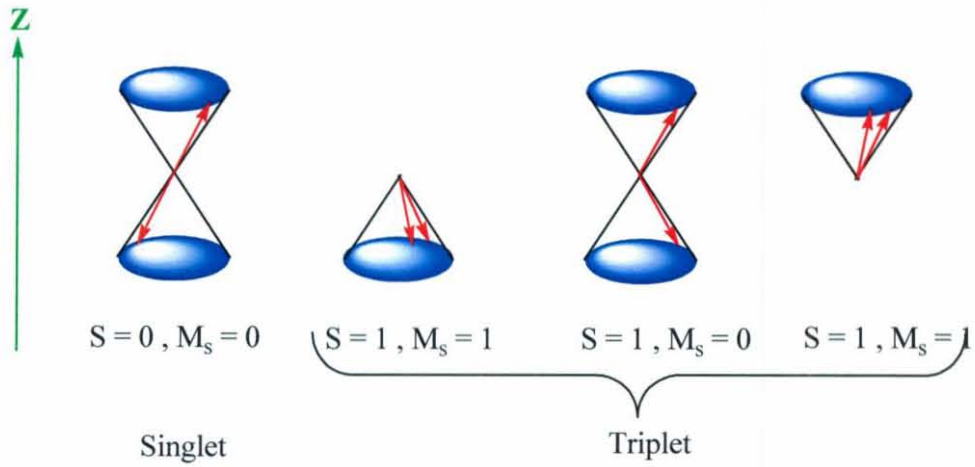

Figure 5.5. Schematic representation of electron spin for the single and the triplet state.[24]

Benzophenone as described above undergoes facile intersystem processes. The benzophenone molecule has a small energy gap between the singlet excited state and the lowest triplet state ($\sim 2000\ cm^{-1}$)[25] and undergoes a rapid intersystem crossing ($k_{ISC} = 10^{11} s^{-1}$)[26,27] from the lowest excited singlet state of the $^1n - \pi^*$ to the two triplet states $^3\pi - \pi^*$ as shown in the Figure 5.6.

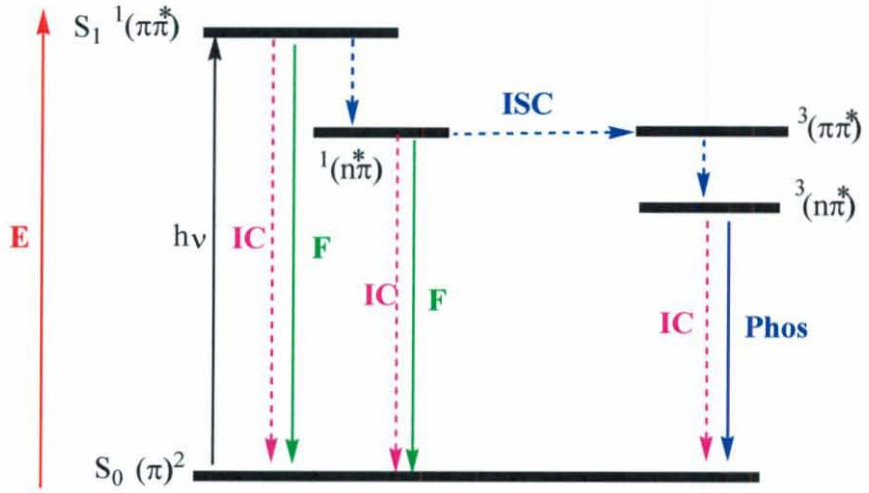

Figure 5.6. Schematic representation of the energy levels of benzophenone in the excited states.[23]

The intersystem crossing yield to the triplet (ϕ_{isc}) is negligible; however, the coumarin based triplet is efficiently sensitized by benzophenone. The $^3(\pi\pi^*)$ state is at 420 nm (23810 cm^{-1}). The $[(n)^2 \rightarrow {}^1(\pi\pi^*)]$ transition is a forbidden transition and does not contribute to ground state absorption spectra. Once the $^1(\pi\pi^*)$ is formed the $(n\pi^*)$ plays an important role and mediates the $^1(\pi\pi^*)$ to $^3(\pi\pi^*)$ transition. The mechanism known as El-Sayed's rules[i] is shown in Figure 5.7.

The singlet-triplet intersystem crossing of some coumarin derivatives has been studied using several spectroscopic methods.[28,29] In such cases the triplet emission (T_1) of substituted coumarin derivatives has been assigned to the $\pi - \pi^*$ transition from the excited state. The Jablonski diagram energy levels of coumarin's excited state for orientations of singlet and triplet states of substituted coumarin derivatives is shown in Figure 5.7.[30]

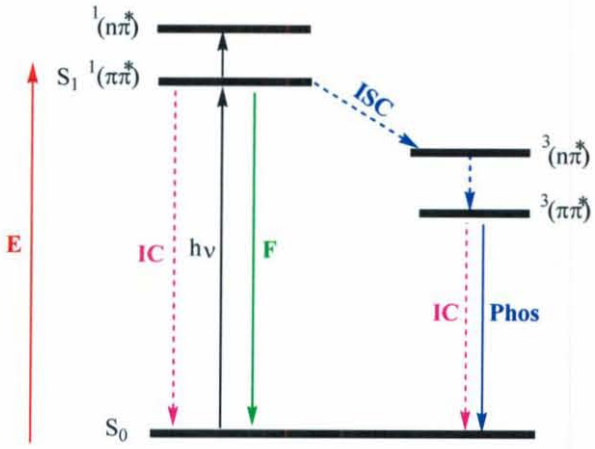

Figure 5.7. Schematic representation of the energy levels of the substituted coumarin derivatives in the excited state.[30]

[i] The rate of intersystem crossing is relatively large if the radiationless transition involves a change of orbital type. A typical case is the transition from the lowest singlet state to the triplet manifold, e.g., $^1\pi\pi^* \rightarrow {}^3n\pi^*$

5.1.2.2 Substituent Effects

The absorption spectrum of an unsubstituted coumarin displays absorption bands at 274 nm and 311 nm,[31] the lower wavelength band being the more intense. Wavelength shifts occur due to the effect of different substituents. For example, a bathochromic shift is observed in the absorption spectrum in the presence of the electron-withdrawing nitro group in position 6 or 8.[31] The nature and position of the substituents influence the magnitude of the spectral shift. Wheelock[32] noted the substituent influenced electronic energies of 7-methoxycoumarin, resulting in emission shifts to longer wavelength (red shifts). The effect of the substitution, in the case of electron-donating groups (EDG) in the 4, 6, or 7 positions of the coumarin molecule, is that red shifts will be observed. On the other hand, in the case of an electron-withdrawing group (EWG) in position number 3 the fluorescence band will red shift as well. In general, coumarin and its derivatives such as 7-aminocoumarins are of particular interest because they possess an electron donating group (amino group) and an electron withdrawing group (carbonyl group). These compounds reveal strong fluorescence in UV-Vis light which makes their identification easy.[19,33,34] However, the substitutions may contribute to excited state decay by providing another kinetic pathway.[9,35]

Changing the solvent polarity and the pH may affect the fluorescence spectra. For instance, upon changing solvent polarity for the 7-aminocoumarins one observes a blue shift and a slight reduction in the molar extinction coefficient. The photophysical properties of thirteen coumarin derivatives in a variety of organic solvents have been investigated by Jones *et al.*[9,10] They found that increasing solvent polarity causes a red shift in the absorption spectrum and both a red shift and broadening in the fluorescence

emission. Solvent polarity can shift both the emission and absorption peaks and a large shift has been observed by Sharma *et al.*[36] for 4- and 7-substituted coumarin derivatives. They also observed a large shift in the emission spectra due to a large increase in the dipole moment on photoexcitation, subsequently giving rise to large Stokes' shifts which are solvent-dependent.[36,37]

5.1.2.3 Types of Excited States and Excited State Dynamics and Energetics in Coumarin and its Derivatives

When a fluorophore contains both an electron donor and an acceptor group, it undergoes intramolecular charge transfer (ICT) from the donor to the acceptor upon excitation by light. The photoinduced ICT reaction between the two distinct parts of a molecule is currently one of the most important reactions in photochemistry and finds use in laser applications,[21] nonlinear optical properties,[38] fluorescence sensors,[39] etc. The ICT leads to a consequent change in dipole moment and results in a Stokes shift that depends on the polarity of the medium.[40,41] ICT in a conjugated donor-acceptor assembly may be accompanied by internal rotation or other conformational changes leading to twisted intramolecular charge transfer (TICT) states[42]. Lippert *et al.*[43] were the first to report a dual emission band from 4N,N-dimethylaminobenzonitrile (DMABN) assigned to an intramolecular charge transfer (ICT). Lippert initially proposed that there are two excited states, one of which is highly polar and the other of low polarity, responsible for the short and long wavelength fluorescence bands respectively. Later Grabowski *et al.*[37,44-48] proposed that the dual fluorescence from DMABN could be explained using the concept of a TICT state. They also investigated the role of solvent in the twisting of the bichromophoric molecule in the excited state. The TICT state arises from a rotation of the

donor group to 90° leading to donor and acceptor sites that are electronically uncoupled ($V = 0$). In this limit, there is complete intramolecular electron transfer in the donor acceptor assembly.[42,49,50] The TICT state has a significant dipole moment which is stabilized in polar solvents. The fluorescence from TICT states is usually weak because the radiative decay rate constant (k_r) value is small and the ϕ_{em} value for TICT emission should decrease with an increase in solvent polarity.

Results from experimental studies on compounds such as DMABN have been rationalized using the TICT model to explain the observed dual-fluorescence. Grabowski's model of the TICT state arrangement is shown in Figure 5.8. The locally excited state of DMABN is almost planar and solvent relaxation takes place with an associated rotation of the dimethylamino group in DMABN ultimately increasing the dihedral angle between the donor and acceptor to the point where excited relaxation is predominantly radiative. The π-electronic decoupling of the twisted donor and acceptor moieties leads to a large dipole moment as a result of a full charge separation and a significant increase in solvent reorganization energies.

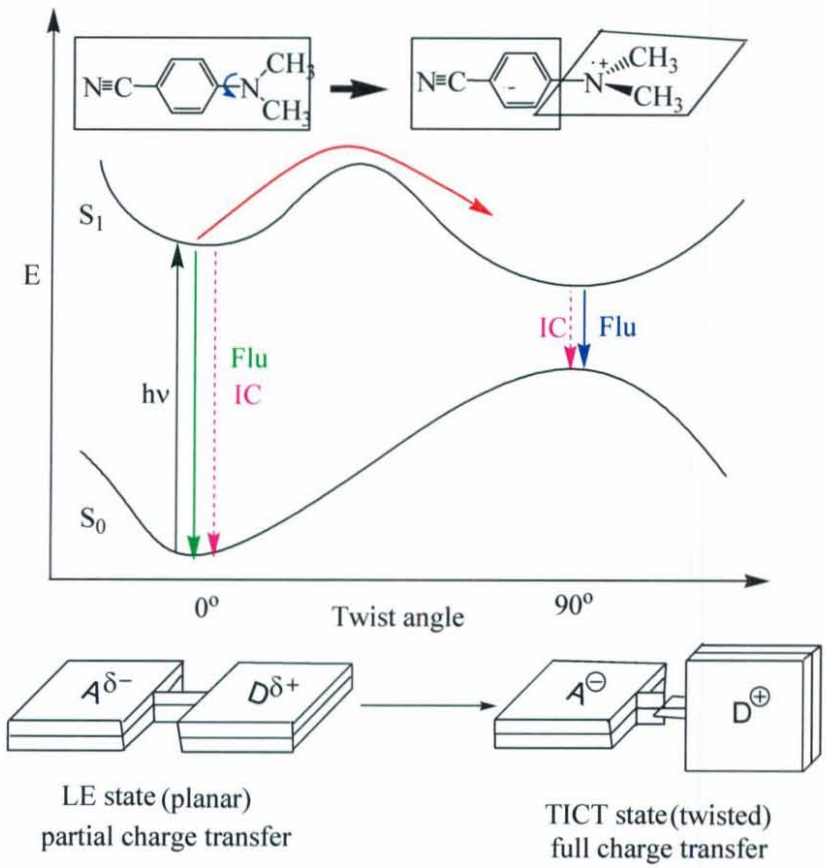

Figure 5.8. Potential energy diagram of DMABN and model of a molecular rotor consisting of two different moieties (donor and acceptor) in a TICT excited state for a D-A molecule.[51,52]

Even though the TICT state of DMABN was invoked to accommodate the dual fluorescence, it was realized that the TICT state may not always fluoresce. The photophysical behaviors of a vast number of coumarins have been examined and the involvement of the nonradiative TICT state has been ascertained.[9,17,53-57] However, coumarin dyes with an electron withdrawing group (EWG) are good electron acceptors[58-61] which in some cases leads to formation of an intramolecular charge transfer structure that subsequently relaxes to a non-fluorescent TICT state.[9] For example, 7-

aminocoumarin in polar solvents undergoes charge transfer and excitation twisting around the C-N bond (an excited state torsional motion) linking the amino group to the aromatic ring. However, coumarin compounds that contain an electron donating group undergo ICT upon optical excitation. Consequently this process leads to an increase in the dipole moment in the excited state that exhibits a large Stokes shift in the fluorescence emission.[62] The excited state character of 7-aminocoumarin has been intensively studied by several authors.[9,10,62-70] They found that in the excited state 7-aminocoumarin undergoes rapid torsional motion involving the amino group at the C-7 position on the coumarin ring which results in the formation of the TICT state.[9,10,62-70] While an increase in the solvent viscosity may attenuate charge transitions by conformational gating effects such as amino group rotation, it could be argued that the solvent polarity stabilizes either ICT or TICT states due to the magnitude of the dipole moment change ($\Delta\vec{\mu}$).[55] Scheme 5.1 shows the structures of the ICT and TICT states for 7-aminocoumarin.

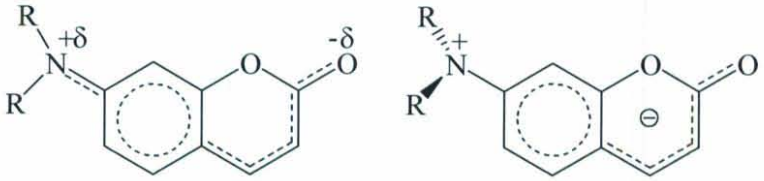

ICT TICT

Scheme 5.1. Planar ICT structure and nonplanar TICT structure.[68]

Figure 5.9 illustrates the potential energy diagram for the ground and excited states, where the excited states have three distinct minima. These three minima represent different configurations which are solvent dependent and can exist at different values of

the reaction coordinate as shown in Figure 5.10.[68] The numbers from (1) to (6) represent the following: (1) Photon capture and formation of the Franck-Condon (FC) state. (2) Radiative and non-radiative decay to reform the ground state. (3) Vibrational cooling within the excited state (S_1) and a thermally activated transition from S_1 →ICT. (4) Radiative decay from the ICT state. (5) Thermally induced activation barrier crossing between the ICT and TICT states. (6) The relaxation of the TICT state to the ground state by non-radiative decay in most cases by emitting a photon.

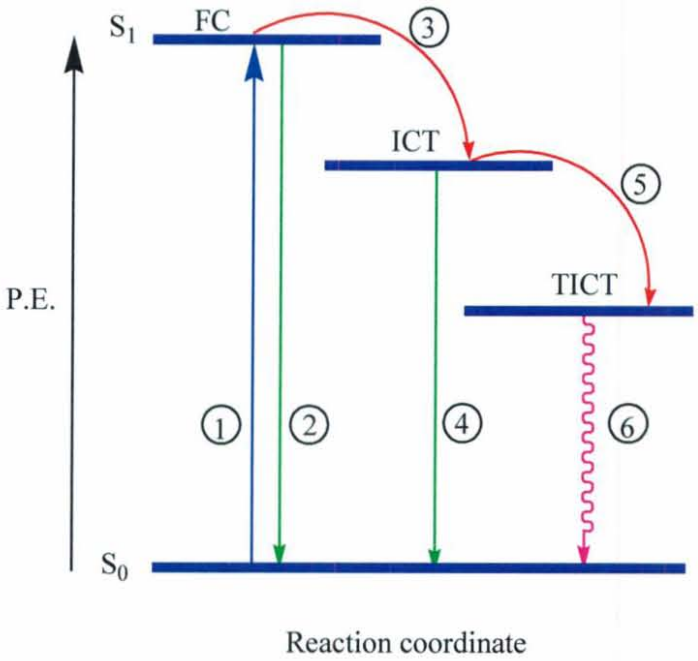

Figure 5.9. Potential energy diagram of a molecule undergoing structural change in the excited state.

Since the TICT state is essentially highly polar in character it is expected to become more stable in higher polarity solvents.[71-75] Figure 5.10 illustrates how the potential energy surface for the 7-aminocoumarin dye changes with different solvent dielectric properties.

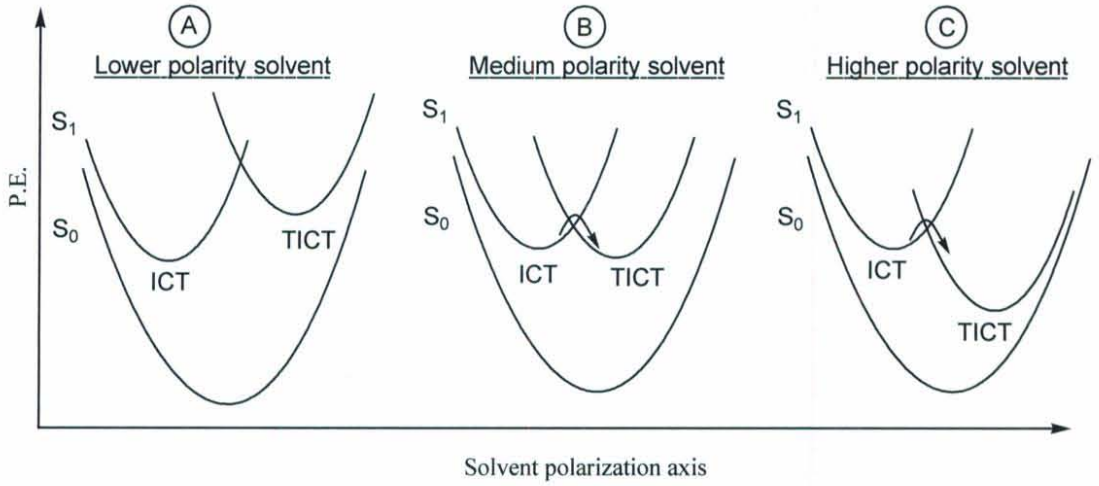

Figure 5.10. Potential energy diagrams for 3-AC showing the proposed changes in excited state configurations with a change in the solvent polarity.

Pal *et al.*[76] have studied electron transfer from aromatic amines to excited coumarin dyes in acetonitrile (MeCN) solution using steady state and time resolved spectroscopic techniques. They observed formation of an amine cation radical using laser flash photolysis excitation. The fluorescence of the electron acceptor 4-CF_3-7-dimethylaminocoumarin (C152) was significantly quenched by addition of electron donor aromatic amines such as *N,N*-diethylaniline (DEAN). The appearance of a radical anion of C152 is consistent with electron transfer quenching of the C152 excited state, Scheme 5.2. A transient absorption measurement shows an absorption peak at 450 nm, which was attributed to the DEAN cation radical. The authors observed a bleach or negative absorption peak at 500-550 nm that was attributed to stimulated emission from the C152 excited state. They also observed a broad absorption peak at around 600 nm which they attributed to the coumarin anion radical.

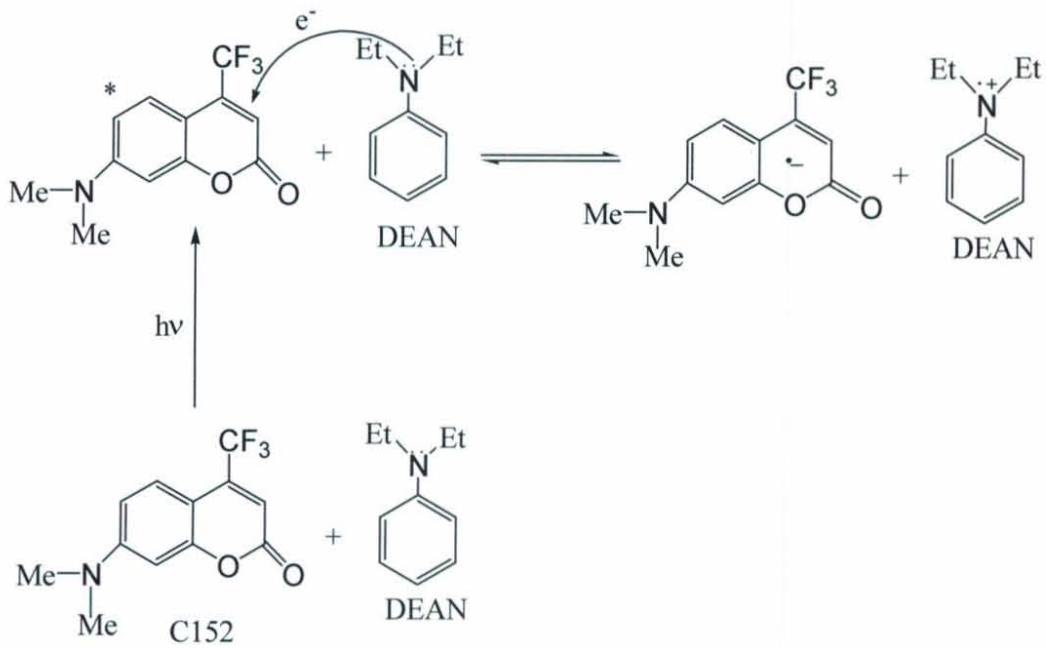

Scheme 5.2. Electron transfer mechanism from *N,N*-diethylaniline donor to 4-CF_3-7-dimethylaminocoumarin photoexcited acceptor.

Coumarin can also undergo photodimerization. The photodimerization and photochemical properties have been investigated by several authors.[77-83] They found that electronically excited coumarin derivatives yielded a variety of different dimers in solution of which cis-head-to-head, trans-head-to-head, cis-head-to-tail and trans-head-to-tail, were identified, Scheme 5.3.

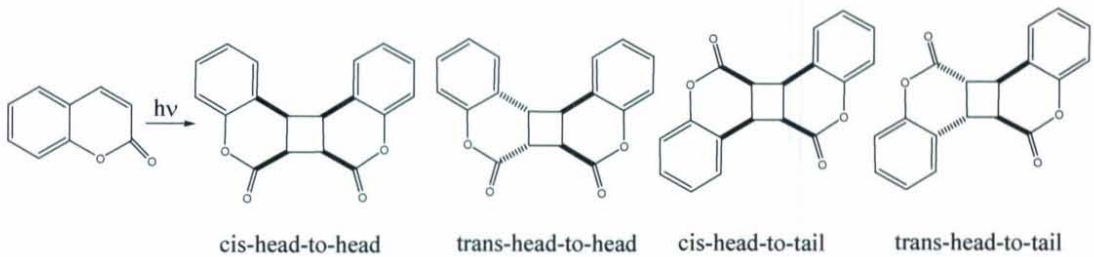

Scheme 5.3. Photodimerization products of coumarin.[30]

5.1.3 Scope of this Study

This study is focused on the excited state dynamics of 3-aminocoumarin (3-AC) and the derivatives shown in Scheme 5.4. The effects of solvent polarity and substituent effects in the C-6 position of the coumarin on the excited state properties were investigated. Intramolecular charge transfer (ICT) in 3-aminocoumarin and its derivatives were studied in an attempt to determine the role of ICT and to ascertain the presence of twisted photoinduced intramolecular charge transfer (TICT).

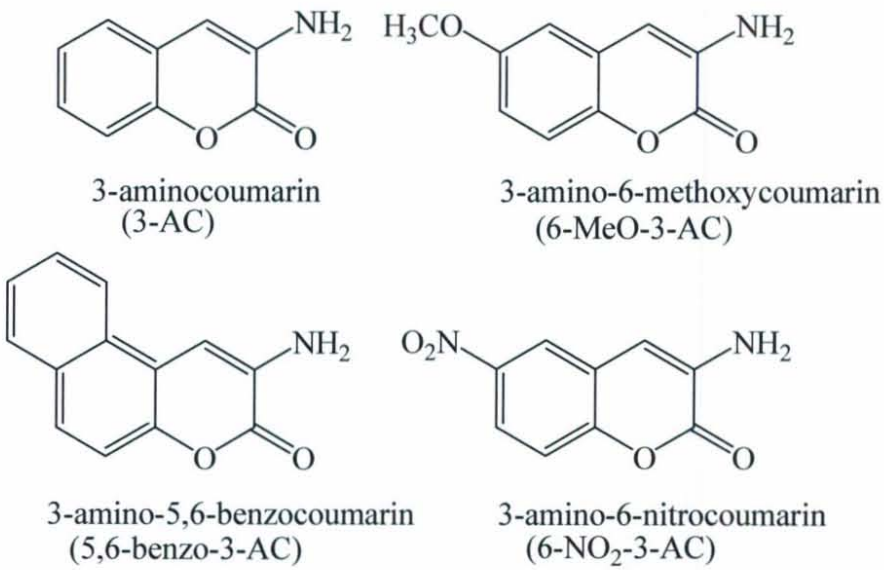

Scheme 5.4. Structures of coumarin derivatives studied in this work.

Ground and excited states literature data examples are given in Tables 5.1 and 5.2

Table 5.1. Selected literature examples of absorption spectra of coumarin and its derivatives.

Quantity	Solvent	λ_{Abs} (nm)	E_{op} (cm^{-1})	ε_{max} $M^{-1}cm^{-1}$
Coumarin [a]	Cyclohexane	272	36765	11400
		311	32154	5700
HOCou [b]	ethanol	326	30675	1.63×10^4
C151 [c]	MeCN	367	27248	
C120 [d]	MeCN	343	29155	
C152 [e]	MeCN	393	25445	
C500 [f]	MeCN	385	25974	
C481 [e]	MeCN	399	25063	
Dye 1 [g]	MeCN	367	27248	
Dye 2 [h]	$CHCl_3$	446	22422	
Dye 3 [b]	ethanol	323	30960	3.52×10^4
Dye 4 [h]	$CHCl_3$	449	22272	
Dye 5 [h]	$CHCl_3$	446	22422	
Dye 6 [g]	MeCN	354	28249	
Dye 7 [g]	MeCN	383	26110	
Dye 8 [i]	MeCN	334	29940	1.44×10^4
Dye 9 [g]	MeCN	380	26316	
Dye 10 [g]	MeCN	418	23923	
Dye 11 [g]	MeCN	405	24691	
Dye 12 [g]	MeCN	454	22026	
Dye 13 [g]	MeCN	403	24814	
Dye 14 [j]	EtOH	454	22026	9.1×10^4
Dye 15 [k]	MeCN	450	22222	
Dye 16 [l]	$CHCl_3$	500	20000	
Dye 17 [l]	$CHCl_3$	455	21978	

[a] J. Phys. Chem. **1994**, 98, 6054-6058. [b] *Dyes and Pigments* 80 **(2009)** 115–120. [c] *J. Phys. Chem. A*, **2001**, **105**, 1097–1106. [d] *J. Chem. Phys.*, 119, **2003** 443-452. [e] *J. Phys. Chem. A* **2003,** *107,* 4808-4816. [f] *J. Phys. Chem. A* **2003,** *107,* 501-507. [g] *J. Phys. Chem.* ***1985****,89,* 294-300. [h] *J. Phys. Chem.* ***1994****,98,* 8903-8905. [i] *Journal of Photochemistry and Photobiology A: Chemistry*, 117, **1998**, 67-74. [j] Tetrahedron Letters 40, **1999**, 82551-8555. [k] *Journal of Photochemistry and Photobiology A: Chemistry*, 116, **1998**, 135-142. [l] *J. Phys. Chem. A* **1997,** *101,* 981-987.

Table 5.2. Selected literature examples of photophysical properties of coumarin and its derivatives.

Quantity	Solvent	$\lambda_{em}, (nm)$	E_{em}, cm^{-1}	ϕ_{em}	τ, ns	k_r, ns^{-1}	k_{nr}, ns^{-1}
Coumarin [a]				0.0004	< 0.10	> 0.004	> 10.0
HOCou [b]	ethanol	390	25641	0.28	-	-	-
C151[c]	MeCN	461	21692	0.57	5.13	1111	838
C120 [d]	MeCN	412	24272	0.63	3.10	2032	1194
C152 [e]	MeCN	504	19841	0.22	1.92	1146	4063
C500 [f]	MeCN	485	20619	0.56	5.23	1071	841
C481[e]	MeCN	504	19841	0.08	0.66	1242	13909
Dye 1 [g]	MeCN	430	23256	1.00	3.4	30.3	< 1.0
Dye 2 [h]	$CHCl_3$	486	20576	0.34	2.75	12.4	24.0
Dye 3 [b]	ethanol	458	21834	0.11	-	-	-
Dye 4 [h]	$CHCl_3$	512	19531	0.43	2.43	17.7	23.4
Dye 5 [h]	$CHCl_3$	522	19157	0.43	2.39	18.0	23.8
Dye 6 [g]	MeCN	420	23810	0.80	3.5	23.0	5.7
Dye 7 [g]	MeCN	481	20790	0.58	7.7	7.5	5.5
Dye 8 [i]	MeCN	418	23923	0.130			
Dye 9 [g]	MeCN	450	22222	0.91	3.3	-	-
Dye 10 [g]	MeCN	521	19194	0.56	5.6	10.0	7.9
Dye 11 [g]	MeCN	510	19608	0.87	5.6	15.0	2.3
Dye 12 [g]	MeCN	501	19960	0.63	3.2	20.0	1.2
Dye 13 [g]	MeCN	480	20833	0.67	2.8	24.0	1.2
Dye 14 [j]	EtOH	498	20080	0.52	2.4		20.0
Dye 15 [k]	MeCN	528	18939	0.64	2.46	26.3	14.8
Dye 16 [l]	$CHCl_3$	571	17513	0.82	4.14	19.8	4.4
Dye 17 [l]	$CHCl_3$	497	20121	0.67	1.93	34.7	17.1

[a] J. Phys. Chem. **1994**, 98, 6054-6058. [b] *Dyes and Pigments* 80 **(2009)** 115–120. [c] *J. Phys. Chem. A*, **2001**, **105**, 1097–1106. [d] *J. Chem. Phys.*, 119, **2003** 443-452. [e] *J. Phys. Chem. A* **2003,** *107,* 4808-4816. [f] *J. Phys. Chem. A* **2003,** *107,* 501-507. [g] *J. Phys. Chem.* ***1985****,89,* 294-300. [h] *J. Phys. Chem.* ***1994****,98,* 8903-8905. [i] *Journal of Photochemistry and Photobiology A: Chemistry*, 117, **1998**, 67-74. [j] Tetrahedron Letters 40, **1999**, 82551-8555. [k] *Journal of Photochemistry and Photobiology A: Chemistry*, 116, **1998**, 135-142. [l] *J. Phys. Chem. A* **1997,** *101,* 981-987.

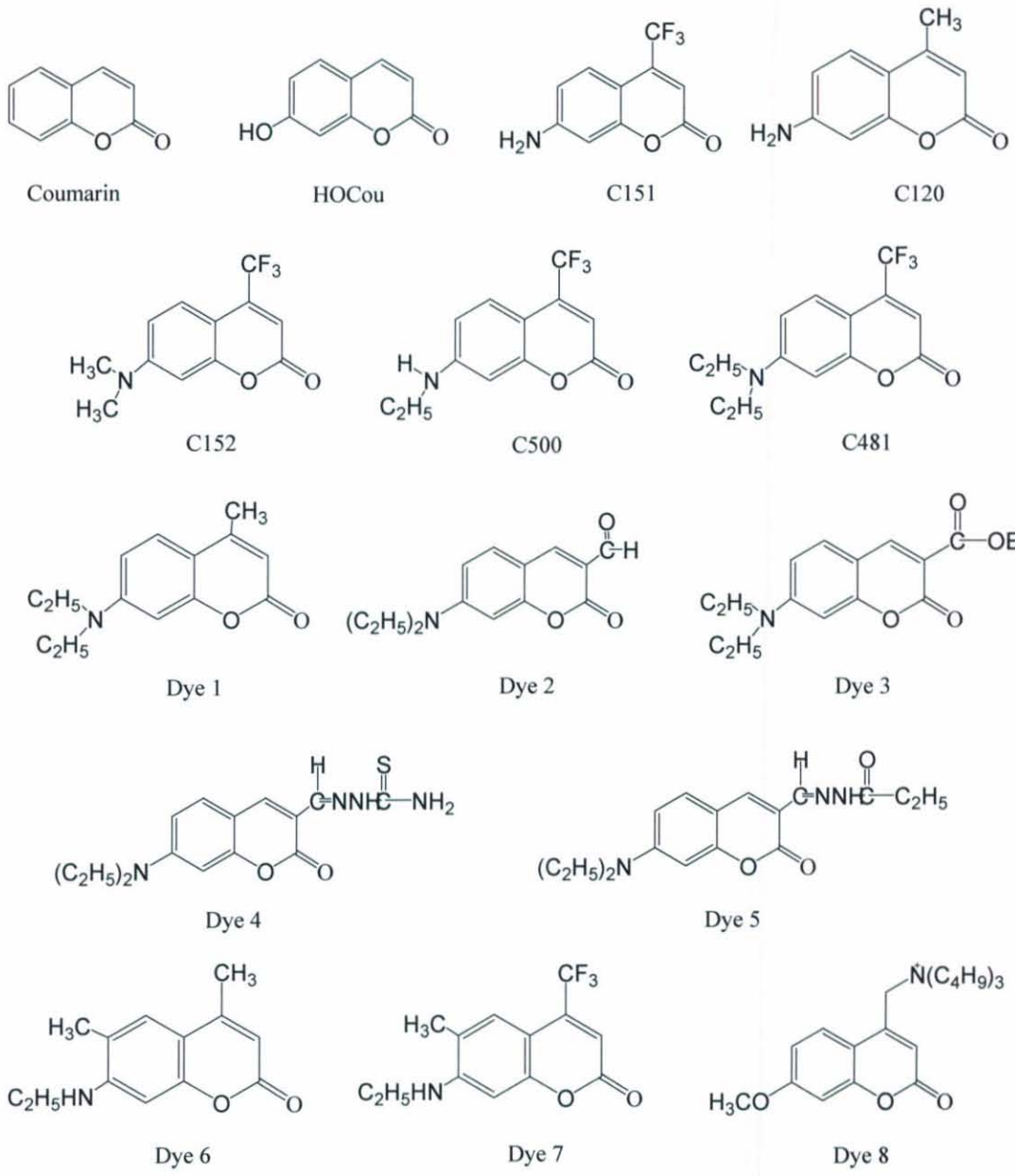

Figure 5.11. Chemical structure of coumarin and its derivatives.

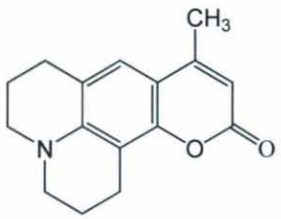

Dye 9

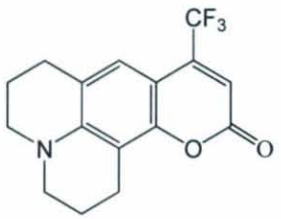

Dye 10

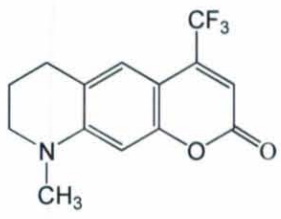

Dye 11

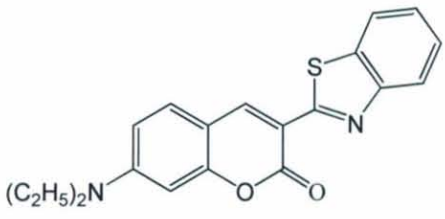

Dye 12

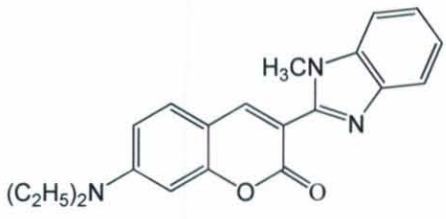

Dye 13

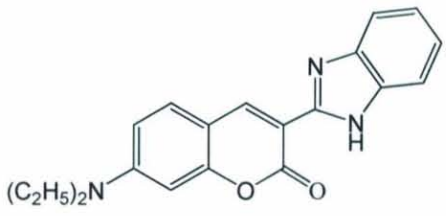

Dye 14

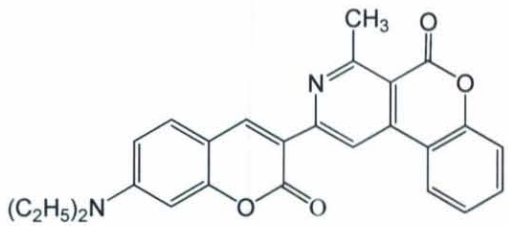

Dye 15

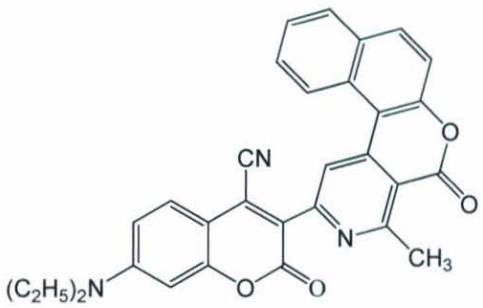

Dye 16

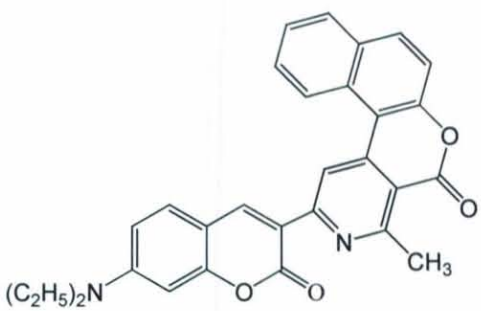

Dye 17

(Continued)
Figure 5.11. chemical structure of coumarin and its derivatives.

5.2 Results

The ground and excited electronic state properties of 1,2-benzopyrone (coumarin) and its derivatives have in this work been subjected to detailed spectroscopic analysis. The absorption properties are presented first using 3-aminocoumarin (3-AC) as a standard paradigm followed by the presentation and results from the studies of excited state dynamics as a function of substituent electron properties and the effect of extended π-systems.

5.2.1 Absorption Spectra

The absorption spectral envelopes for the coumarin compounds described below are characterized by a number of resolved peaks and shoulders due to several overlapping electronic transitions and their vibronic components.

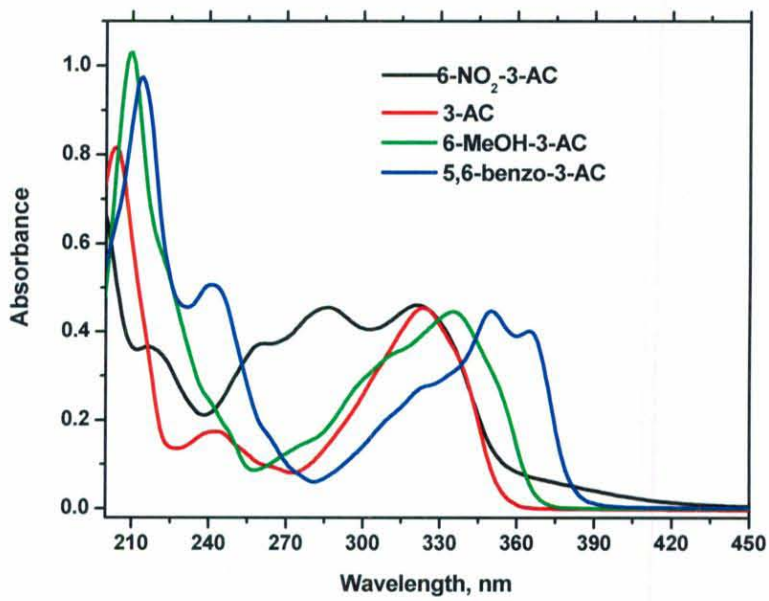

Figure 5.12. Absorbance of 3-AC substituent in MeCN solution at 298 (± 2) K under 1 atm N_2.

For example, the lowest energy transition of the absorption spectrum for 3-AC in acetonitrile (MeCN) solution at 324 nm (30864 cm^{-1}, $\varepsilon = 1.3\,x\,10^4\,M^{-1}cm^{-1}$) is attributed to a π-π^* transition localized on the coumarin ring.[31,84] The shoulder at 337 nm (29673 cm^{-1}, $\varepsilon = 9.6 \times 10^3\,M^{-1}cm^{-1}$) is attributed to a charge transfer (ICT) band as is expected for molecules containing an accepting group (carbonyl group)[85,86] and donating group (amino group). The intensities of the absorption bands found for 3-AC are consistent with electric dipole allowed ICT transitions.[ii] The integrated intensity for an electronic transition is given by

$$\int \varepsilon(v)dv = \frac{4\pi^2 N_A v}{3000cn\hbar(ln10)}\left|\vec{M}\right|^2 \qquad (5.1)$$

where M is the transition moment. M is directly related to $\vec{\mu}$ the dipole moment and the ground and excited state wavefunctions by

$$M = \left\langle \psi_{el}^* \middle| e\sum \vec{r} \middle| \psi_{el} \right\rangle \langle \psi_{vib}^* | \psi_{vib} \rangle \qquad (5.2)$$

The intensity of the transition is related to $\vec{\mu}$

$$\vec{\mu} = \left\langle \psi_{el}^* \middle| e\sum \vec{r} \middle| \psi_{el} \right\rangle \qquad (5.3)$$

and the band shape is governed by the Franck-Condon overlap factors, $\langle \psi_{vib}^* | \psi_{vib} \rangle$.

Time dependent density functional theory (TD-DFT) was used to calculate the energies and orbital contributions of the UV-Vis spectrum. Analysis of the absorption spectral data for 3-AC and its derivatives were calculated from the first and second

[ii] In this particular charge transfer (ICT) transition, electron density has been redistributed from the amino group (NH_2) donor substituent to an electron deficient carbonyl group ($C = O$) moiety. These differ from $\pi - \pi^*$ transitions in that the ICT transition has a large degree of σ-bonding / lone pair character.

derivative of the absorption spectrum as described in the Chapter 2. The calculated and the observed spectral envelopes are shown in Figure 5.13.

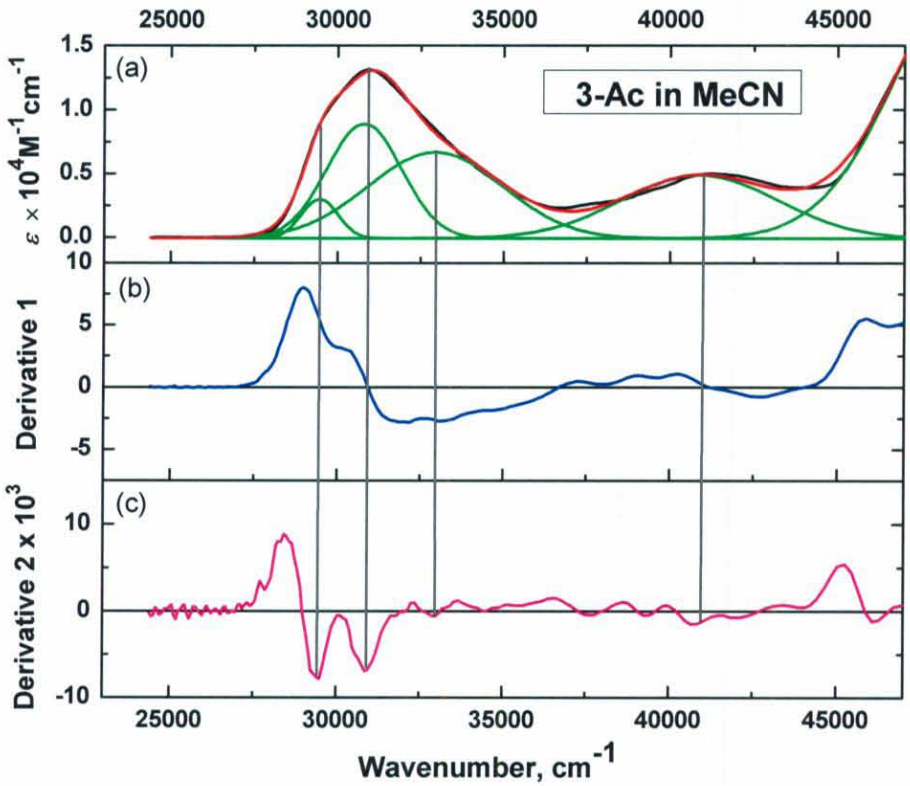

Figure 5.13. Absorption Spectral Deconvolution for 3-AC in MeCN solution at 298 (± 2) K under 1 atm N_2. (a) Observed and calculated spectral envelope from the deconvolution. (b) The first derivative and (c) second derivative. Band maxima are indicated by the vertical lines.

Absorption spectral data from the deconvolution procedure, transition energies, oscillator strengths and the dipole moment are given in Table 5.3.

Table 5.3. Absorption spectral data for 3-AC and some of its derivatives in MeCN solution. Transition energies assignments, oscillator strengths and dipole moments for 3-AC and some of its derivatives.

Entry	Observed			Trans.	From deconvolution				
	λ_{abs} (nm)	E_{op} (cm^{-1})	ε_{max} $M^{-1}cm^{-1}$		E_{op} (cm^{-1})	$\Delta\bar{\nu}_{1/2}$ (cm^{-1})	ε_{max} $M^{-1}cm^{-1}$	f_{osc}	$\bar{\mu}$ D
1[a]	337	29674	$9.95x10^3$	①	29522	1178	3109	0.017	4.17
	324	30864	$1.32x10^4$	②	30887	2343	9033	0.098	1.78
	244	40984	$4.80x10^3$	③	33218	4227	6023	0.117	1.68
2[b]	355	29850	$1.35x10^4$	①	28397	975	2693	0.011	5.08
	311	32154	$1.06x10^4$	②	29691	2108	8102	0.068	2.09
	209	47847	$3.00x10^4$	③	32352	4802	9570	0.184	0.42
3[c]	321	31153	$1.55x10^4$	①	27736	4273	2073	0.035	2.82
	285	35088	$1.53x10^4$	②	30970	2549	11379	0.116	1.63
	260	38462	1.25×10^4	③	29702	1316	2543	0.013	4.78
4[d]	364	27473	$1.70x10^4$	①	27205	896	11126	0.040	6.80
	350	28571	$1.88x10^4$	②	28428	1288	10665	0.055	5.17
	323	30960	1.70×10^4	③	29762	3290	7517	0.099	3.01

[a] (3-AC), [b](6-MeO-3-AC), [c](6- NO_2-3-AC), and [d](5,6-Benzo-3-AC)

The absorption of a photon leads to formation of the Franck-Condon state where the molecule has the electronic co-ordinates of the excited state but still possesses the ground state nuclear and solvent co-ordinates. Inspection of the data shown in Table 5.3 reveals

that generally the optical energy of the absorption increases as the transition dipole moment decreases as described in Eq. 5.1. The observation indicates that the lowest energy transitions possesses a large degree of charge transfer (CT) character whereas the higher energy transitions are $\pi - \pi^*$ and are not expected to possess large dipole moments. The exception is the NO_2 derivative which will be discussed further in section 5.3.

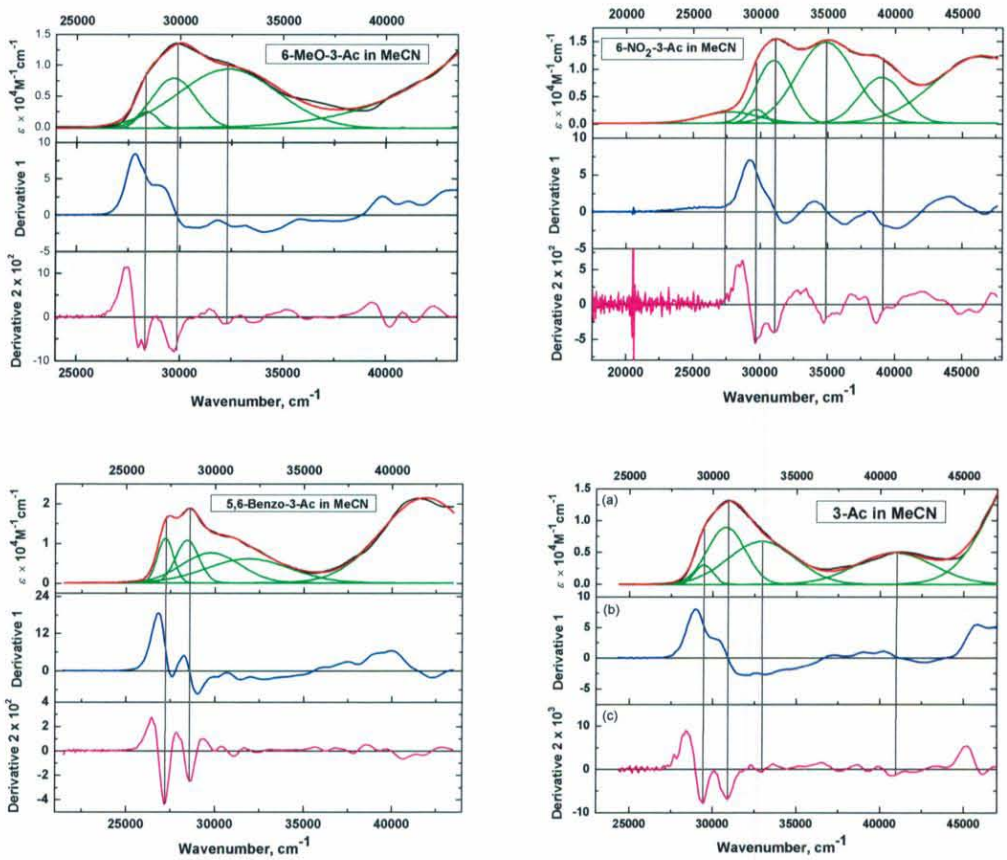

Figure 5.14. Absorption Spectral Deconvolution for top left 6-MeO-3-AC, top right 6-NO_2-3-AC and immediately below left 5,6-Benzo-3-AC and below right 3-AC in MeCN solution at 298 (± 2) K under 1 atm N_2.

5.2.2 Emission and Emission Spectral Fitting

Excitation of 3-AC (λ_{exc}= 324 nm) in MeCN solution at room temperature gives rise to emission bands at 386 nm (25906 cm^{-1}). The excitation spectrum displayed one emission peak at 328 nm within the $\lambda = 300 \rightarrow 400\, nm$ spectral window. The excitation, fluorescence, and phosphorescence spectra of 3-AC in MeCN solution are shown in Figure 5.15.

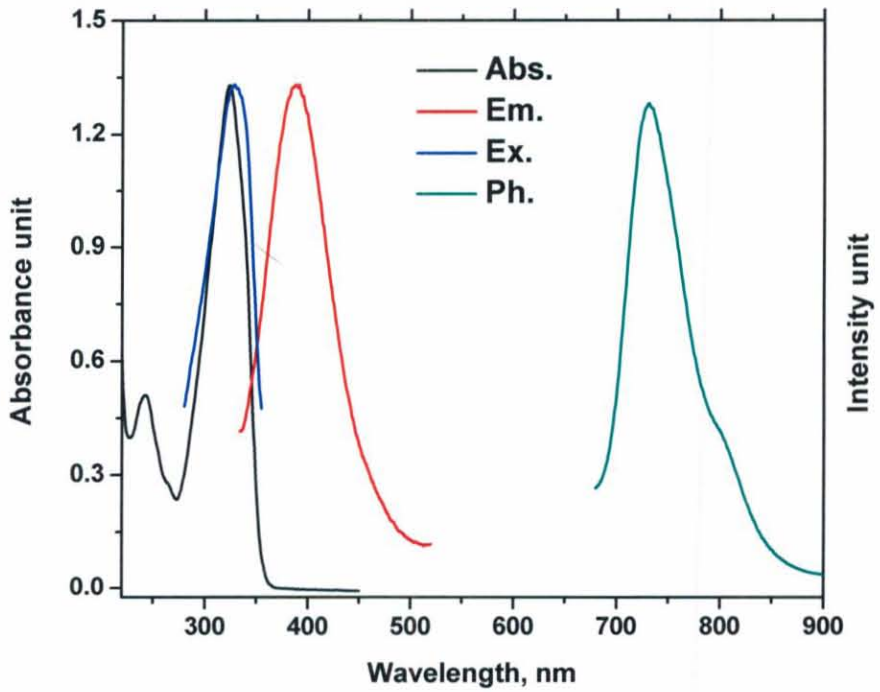

Figure 5.15. Normalized absorption spectrum (black line), fluorescence spectrum $\lambda_{exc} = 324\, nm$ (red line), excitation spectrum $\lambda_{mon} = 368\, nm$ (blue line), and phosphorescence spectrum (green line) of 3-AC in MeCN solution at 298 (± 2) K under 1 atm N_2.

Table 5.4. Photophysical properties of 3-AC and its derivatives in MeCN 10 μM solution

Quantity	λ_{em} nm	E_{em} cm^{-1}	ϕ_{em}	τ ns	k_r ns^{-1}	k_{nr} ns^{-1}	$E_{abs} - E_{em}$ cm^{-1}
1[a]	386	25974	0.005	< 0.40	> 0.0125	> 2.50	4686
2[b]	408	24510	0.02	< 0.40	> 0.050	> 2.45	5043
3[c]	346	28902	< 0.001	< 0.40	> 0.0025	> 2.50	13393
4[d]	405	24691	0.15	1.18	0.127	0.72	2678

[a] (3-AC), [b](6-MeO-3-AC), [c](6- NO_2-3-AC), and [d](5,6-Benzo-3-AC)

Emission spectra of 3-AC and its derivatives were fit by application of single, average mode Franck-Condon analysis utilizing the line shape analysis methodology described in the experimental section (Chapter 2). Emission spectra and fits are shown in Figure 5.16. The fits and their interpretation rely on the magnitude of errors associated with the data, and a well-defined minimum on the error surface. Based on a rigourous analysis of error surfaces by Juan Claude[87], there exist shallow minima. Furthermore, several of the parameters are mathematically correlated and care must be exercised in the interpretation of these data. It should be noted that the emission spectral fitting analysis has been widely utilized for d^6 polypyridyl complexes of Re, Rh, Ru, Os, etc.[88] The use of spectral fitting in this work represents one of the few such studies on organic based chromophores. The fitting methodolgy employed has evolved over time to reduce problems associated with multiparameter fits and employs the following steps:

- Minimization of the number of parameters that are allowed to vary in the fits. For example, E_o may be estimated from where the normalized absorption and emission spectra intersect one another, or by drawing a tangent on the high energy side of the emission envelope and E_o is then estimated from the energy axis.
- If the emission spectra exhibit vibronic structure, $\hbar\omega_M$ is fixed.
- Careful examination of the correlation matrices to assess the degree of mathematical correlation between parameters.
- The use of several different initial guesses in the fitting routine to see if the fitting parameters converge to produce the same results, thereby providing evidence for a well-defined minimum on the error surface.

The fit parameters are given in Table 5.5. In the case of 6-NO_2-3-AC dual emission was observed and the emission data will be presented below. Unfortunately the fitting was difficult because this dye has very weak emission.

Table 5.5. One-mode emission spectral fitting for 6-R-3-AC (R = H, OCH_3 and benzo) in chloroform at room temperature.[a]

Quantity	3-AC	6-MeO-3-AC	5,6-Benzo-3-AC
$E_o, (cm^{-1})$	27840 (15)	26505 (50)	25748 (10)
S_M	1.88 (0.02)	2.41 (0.02)	1.77 (0.01)
$\Delta\nu_{1/2}, (cm^{-1})$	1915 (30)	2340 (80)	1733 (15)
$\hbar\omega_M, (cm^{-1})$	1350	1350	1350

[a] Error estimates are in parentheses.

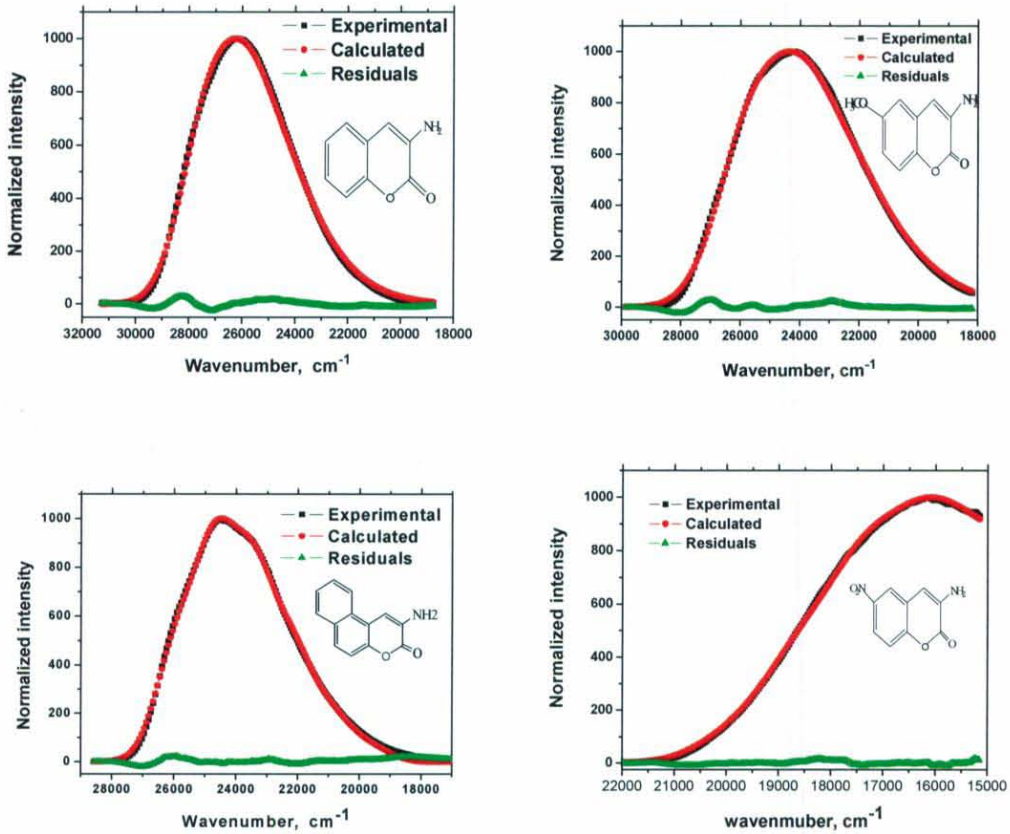

Figure 5.16. Normalized corrected emission of 3-AC, 6-MeO-3-AC, 6-NO_2-3-AC and 5,6-benzo-3-AC in chloroform solution at 298 (± 2) K under 1 atm N_2 (solid black line) and one-mode spectral fit (red dashed line). The residuals are shown in green.

5.2.3 Excited State Decay

Laser flash emission experiments were performed to determine the lifetime for the excited states of 3-AC and its derivatives. Following pulsed laser excitation at 337 nm (pulse width 350 ± 50 ps), the emission decay kinetics were monitored at the emission maxima. The fluorescence decay kinetics for 3-AC, 6-MeO-3-AC, and 6-NO_2-3-AC rate constants were convoluted with the laser pulse obtained by using the deconvolution protocols as described in Chapter 2. In contrast, the 5,6-benzo-3-AC exhibits an emission

lifetime of 1.18 ns. The emission lifetime of 5,6-benzo-3-AC was described by a single-exponential function of the decay in MeCN (Figure 5.17) and was adequately fit to Eq. 5.4,

$$I_t = I_o exp - kt \quad (5.4)$$

where I_t and I_o were the emission intensities at time t and $t = 0$ respectively. The photophysical properties of 3-AC and its derivatives are summarized in Table 5.4 along with extensive data found for other systems.

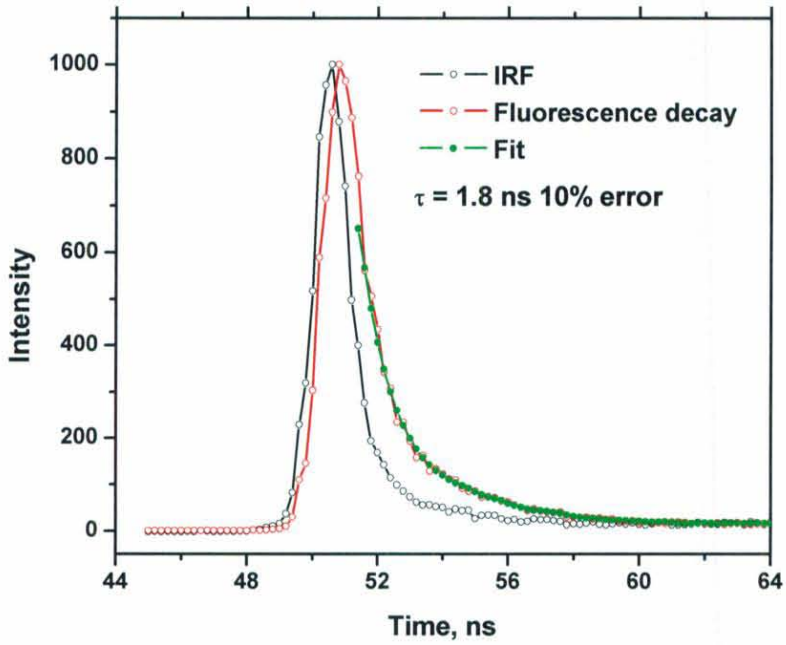

Figure 5.17. Fluorescence decay of 5,6-Benzo-3-AC in MeCN solution at 298 (± 2) K under 1 atm N_2 following laser excitation at 337 nm, 0.3 ns pulse width at room temperature, laser pulse profile decay (black dot), and the best fit (green dot).

5.2.4 Non-radiative Decay

There are four parameters given in Table 5.5. E_0 is the energy gap for the $v'= 0 \rightarrow v = 0$ transition. S_m is the Huang-Rhys factor or vibrational coupling constant given by

$$S_j = \frac{1}{2}\left(\frac{M_j \omega_j}{\hbar}\right)(\Delta Q_j)^2 \quad (5.5)$$

where M_j and ω_j are the reduced mass and the vibrational frequency of the j^{th} vibrational mode and ΔQ_j is the change in equilibrium displacement for the j^{th} mode. In the one mode approximation S is given by

$$S = \sum_{1}^{j} S_j \quad (5.6)$$

For coupled vibrational mode with ω_j, and $\hbar\omega$ is the average quantum spacings for all modes given by

$$\hbar\omega = \frac{\sum S_j \hbar\omega_j}{\sum S_j} \quad (5.7)$$

The vibrational reorganization energy (λ_{vib}) is given by

$$\lambda_{vib} = S.\hbar\omega \quad (5.8)$$

The term $\Delta\nu_{1/2}$ contains information about the solvent reorganization energy

$$(\Delta\nu_{1/2})^2 = (\Delta\nu_{0,1/2})^2 + \lambda_{oL} 16 k_B T(ln2) \quad (5.9)$$

where $\Delta\nu_{0,1/2}$ is the intrinsic band width and λ_{oL} is the the solvent reorganization energy and the low frequency vibrational modes are treated classically ($k_B T \gg \hbar\omega_L$)

$$\lambda_o = \frac{(\Delta\nu_{1/2})^2}{16 k_B T(ln2)} \quad (5.10)$$

The fitting parameters can be used to calculate the Franck-Condon weighted density of states for non-radiative decay. With the average mode approximation $[F(calc)]$ is given by

$$\ln[F(calc)] = -\frac{1}{2}\ln\left[\frac{\hbar\omega E_o}{(1000\ cm^{-1})^2}\right] - S - \left(\frac{\gamma E_o}{\hbar\omega}\right) + (\gamma+1)^2\left(\frac{\Delta\bar{\nu}_{1/2}}{\hbar\omega}\right)^2 /16\ln 2 \qquad (5.11)$$

This expression is valid in the weak coupling case, $E_0 \gg S\hbar\omega$, and assumes equal quantum spacing in the initial and final electronic states, $\hbar\omega = \hbar\omega'$. In Eq. 5.11, the factor of 1000 cm^{-1} is an arbitrary scaling factor to make the logarithmic term unitless; E_0, $\hbar\omega$, and $\Delta\bar{\nu}_{1/2}$ are in cm^{-1}, and γ is given by

$$\gamma = ln\left(\frac{E_o}{S\hbar\omega}\right) - 1 \qquad (5.12)$$

Calculated values for $\ln[F(calc)]$ are listed in Table 4.6. They are related to the rate constant for nonradiative decay, k_{nr}, by Eq. 5.13.[89]

$$\ln(k_{nr}) = \ln\beta_o + \ln[F(calc)] \qquad (5.13)$$

where β_o contains the vibrationally induced electronic coupling matrix element which dynamically couples the initial and final electronic states. Following excitation and

relaxation of the lowest lying excited state, the electronic wavefunctions for the excited state (ψ_{el}^{*}) and ground states (ψ_{gs}), are orthogonal. Low frequency promoting vibrational modes allow mixing of the ground and excited state wavefunctions by facilitating electronic coupling. In this limit, the Born-Oppenheimer approximation is no longer valid as electron motion occurs on the time scale of vibrational motion. The Stokes shift between the absorbing and emitting states is given by

$$E_{ss} = E_{abs} - E_{em} = 2\,\lambda_t \qquad (5.14)$$

where λ_t is the total reorganization energy, which is the sum of the vibrational (λ_{vib}) and solvent (λ_o) reorganization energies.

$$\lambda_t = \lambda_{vib} + \lambda_o \qquad (5.15)$$

The free energy content of the emitting state (ΔG_{Es}^{o}) is given by

$$\Delta G_{Es}^{o} \cong E_o + \lambda_o \qquad (5.16)$$

The absorption band energy (E_{abs}) is related to emission spectral fitting and the emission maximum as described in Eq. 5.17.

$$E_{abs} \approx E_{em} + 2S\hbar\omega + 2\lambda_o \qquad (5.17)$$

The radiative rate constant (k_r) is related to the emission quantum yield and lifetime by

$$k_r = \frac{\phi_{em}}{\tau} \qquad (5.18)$$

The electronic coupling between the electron donor and acceptor (H_{DA}) is related to k_r as given by.

$$H_{DA} = \left(\frac{E_{abs}}{nd}\right)[(1.39 \times 10^5)k_r\langle\bar{\nu}^{-3}\rangle]^{1/2} \qquad (5.19)$$

where n is the refractive index of the solvent, $n_{MeCN} = 1.3441, and\ n_{CHCl3} = 1.446$ at room temperature and d is the electron-transfer distance between the electron donor and acceptor which is determined using the DFT method, d = 2.7 Å.

Table 5.6. Emission spectral fitting parameters, Franck–Condon factors, and reorganization energies for 3-AC and its derivatives in $CHCl_3$ at 298 (± 2) K.

Quantity	3-AC	6-MeO-3-AC	5,6-Benzo-3-AC
γ [a]	1.40	1.10	1.38
$ln[F(calc)]$ [b]	-31.52	-24.60	-28.02
$\lambda_o, (cm^{-1})$ [c]	1596	2383	1307
$\lambda_{vib}, (cm^{-1})$ [d]	2538	3253	2390
$\lambda_t, (cm^{-1})$ [e]	4134	5636	3697
$\Delta G^o_{Es}, (cm^{-1})$ [f]	29436	28888	27055
$(\bar{\nu}^{-1})^{-3}, (cm^{-1})^{-3}$ [g]	1.74 x 10^{13}	1.47 x 10^{13}	1.49 x 10^{13}
$E_{abs}, (cm^{-1})$ [h]	34242	35783	32084
$k_r, (s^{-1})$ [i]	1.25 x 10^7	2.63 x 10^7	1.27 x 10^8
$H_{DA}, (cm^{-1})$ [j]	2980	4917	9623

[a] Calculated from Eq. 5.12. [b] Calculated from Eq. 5.11. [c] Calculated from Eq. 5.10. [d] Calculated from Eq. 5.8. [e] Calculated from Eq. 5.15. [f] Calculated from Eq. 5.16. [g] $\left\langle \bar{\nu}^3 \right\rangle^{-1} \approx E^3_{em}$ [90,91]. [h] E_{abs} Calculated from Eq. 5.17. [i] Calculated from Eq. 5.18. [j] Calculated from Eq. 5.19.

5.2.5 Triplet States

Nanosecond transient absorption experiments as described in Chapter 2 were performed by using pulsed 355 nm excitation. These experiments revealed that there

were no long-lived transient species that might be assignable to a triplet based excited state in the wavelength range 360 to 650 nm for 3-AC and 5,6-benzo-3-AC. However, in the case of 6-MeO-3-AC and 6-NO_2.3-AC the laser flash experiments indicate the presence of transient species between $\lambda = 300 \rightarrow 600$ nm. Transient absorption difference spectra following 355 nm (8 ns pulse, 5-10 mJ/pulse) excitation on 6-MeO-3-AC are shown in Figure 5.18. The transient absorption spectra of 6-MeO-3-AC exhibit a broad absorption peak in the range 360-520 nm. The decay of the maximum absorption at 440 nm (Figure 5.18(b)) was analyzed using a single exponential fit which gave k_{obs} = 3.84 x 10^4 s^{-1} ($\tau = 26\ \mu s$), and bleaching of the absorption band at 340 nm. The decay is single exponential with k_{obs} = 3.92 x 10^4 s^{-1} ($\tau = 25.5\ \mu s$).

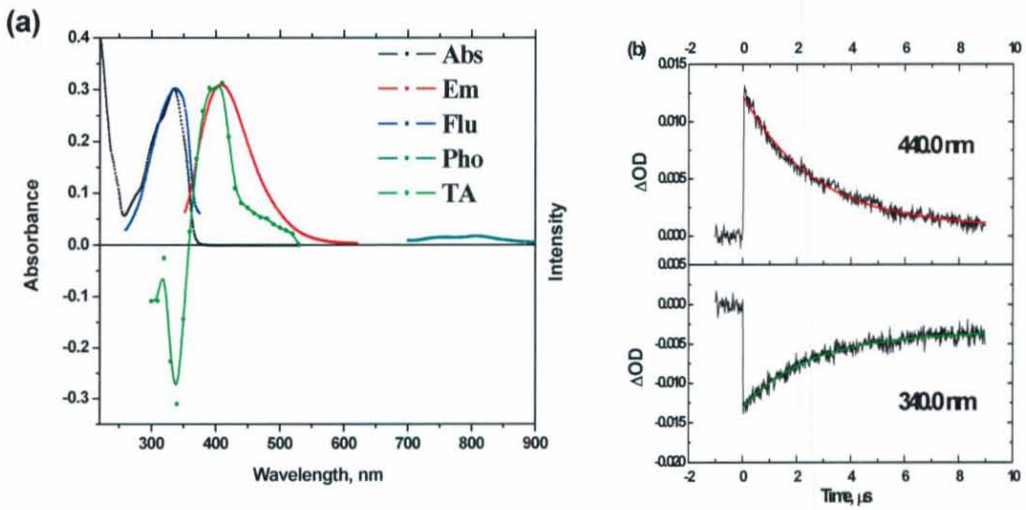

Figure 5.18. (a) The green line is the nanosecond transient absorption difference spectrum of a 10^{-5} M solution of 6-MeO-3-AC in MeCN solution at 298 (± 2) K under 1 atm N_2. The black line is absorption, the red line is the fluorescence, the blue line is the excitation, and the dark cyan is the phosphorescence spectra of 6-MeO-3-AC in MeCN solution at 298 (± 2) K under 1 atm N_2. (b) Single wavelength kinetic decay traces of a sample excited at 355 nm and probed at 340 and 440 nm.

Figure 5.19 shows the time-resolved UV-vis spectra of 6-NO_2-3-AC which exhibit an absorption peak in the range 360-500 nm. The absorption decay at 380 nm (right Figure 5.19) was fit using a single exponential model and gave k_{obs} = 1.38 x 10^5 s^{-1} (τ = 7.25 μs), and bleaching of the absorption band at 320 nm. The decay is single exponential with k_{obs} = 1.52 x 10^5 s^{-1} (τ = 6.6 μs).

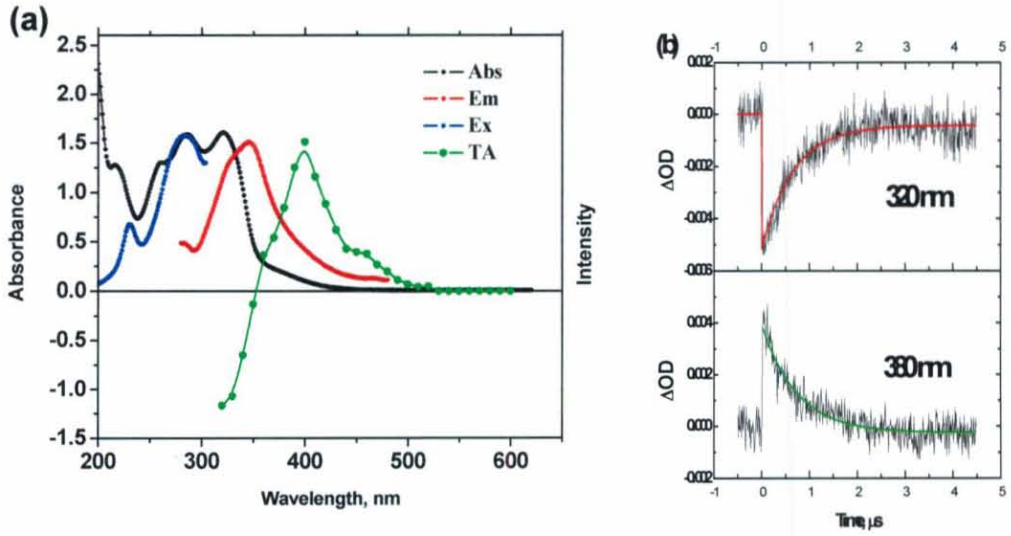

Figure 5.19. (a) The green line is nanosecond transient absorption difference spectrum of a 10^{-5} M solution of 6-NO_2-3-AC in MeCN solution at 298 (± 2) K under 1 atm N_2. the black line is absorption, the red line is the fluorescence, the blue line is the excitation spectra of 6-NO_2-3-AC in MeCN solution at 298 (± 2) K under 1 atm N_2. (b) Single wavelength kinetic decay traces of a sample is excited at 355 nm and probed at 320 and 380 nm.

Table 5.7. Absorption and emission data for 3-AC and its derivatives in MeCN at 298±2K.

Quantity	3-AC	6-MeO-3-AC	6-NO_2-3-AC	5,6-Benzo-3-AC
λ_{abs}^{max}, nm	324	335	321	364
$\lambda_{em}^{max}, nm\ (S_1 \rightarrow S_0)$	386	408	346	405
$\lambda_{em}, nm\ (T_1 \rightarrow S_0)$	730	807	-	809
$\lambda_{\Delta OD}^{max}, nm\ (T_1 \rightarrow T_n)$	-	420	400	-
E_{00}, cm^{-1}	28985	27855	30030	26455

5.2.6 Solvent Effects

Absorption and emission spectra of 3-AC as a function of solvent are shown in Figures 5.20 and 5.22 respectively. Variations in the absorption spectra are generally slight in the case of the solvents toluene, chloroform, ethyl acetate, and MeCN and these do not correlate with solvent polarity. On the other hand, in the cases of DMF and DMSO, the absorption spectra show more sensitivity to the changes in solvent polarity than for the other solvents. For MeCN, the $E_{op} = 30864\ cm^{-1}$; $E_{op} = 30395\ cm^{-1}$ in the case of DMF, and in the case of DMSO the $E_{op} = 30120\ cm^{-1}$. It has been reported that the hydrogen bonding interaction is primarily responsible for the enhanced Stokes shift in solvents that are able to interact with solutes by hydrogen bonding such as water and alcoholic solvents.[92]

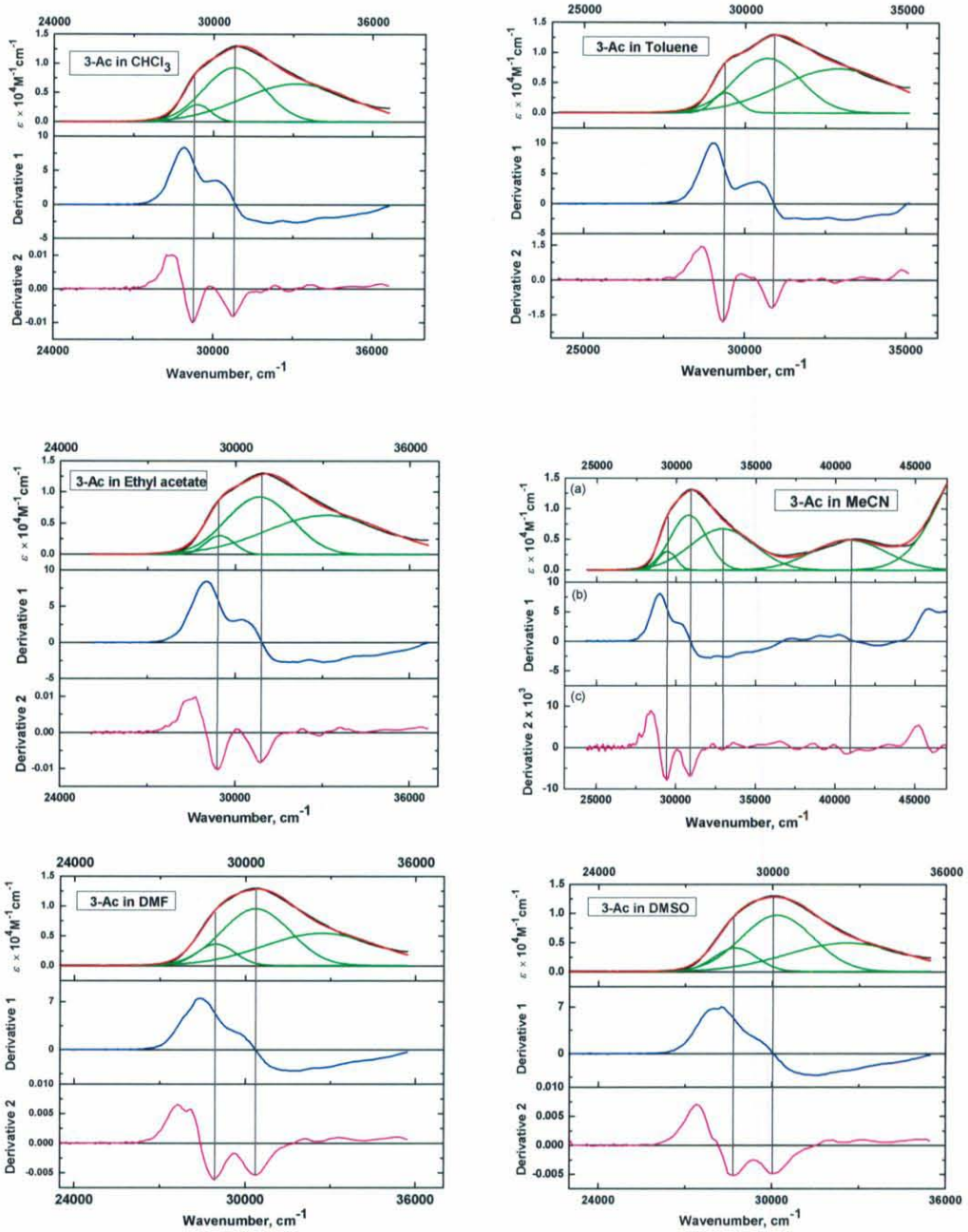

Figure 5.20. Absorption spectral deconvolution for 3-AC in different solvents at 298 (± 2) K under 1 atm N_2.

Table 5.8. Absorption maxima of 3-AC dye as estimated by absorption spectral deconvolution.

Solvent	Δf	$\bar{\upsilon}_{S_0 \leftarrow S_1}$, ($cm^{-1}$)	$\bar{\upsilon}_{S_0 \leftarrow S_2}$, ($cm^{-1}$)
Toluene	0.015	29371	30680
Chloroform	0.148	29365	30772
Ethyl acetate	0.201	29453	30809
MeCN	0.305	29512	30875
DMF	0.275	28975	30368
DMSO	0.267	28717	30171

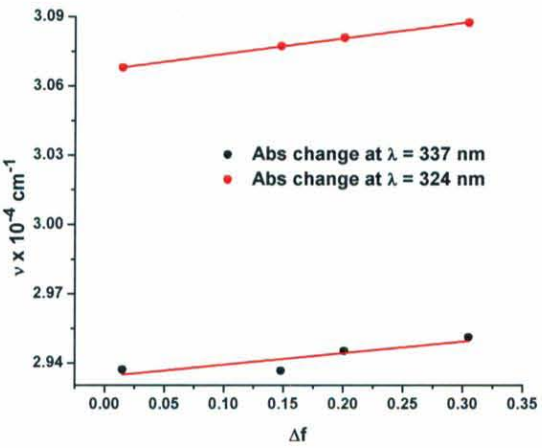

Figure 5.21. Plot of the ν for 3-AC dye vs the solvent polarity function Δf.

The solvent effect on the emission for 3-AC at 324 nm excitation is given in Figure 5.22. As this figure illustrates, a slight shift in the emission is observed with increased solvent polarity as is expected for charge transfer states. In addition, an increase in the

solvent polarity results in a dramatic attenuation of the emission intensity. The emission band shifts from 26667 to 25063 cm^{-1} on going from toluene to DMSO.

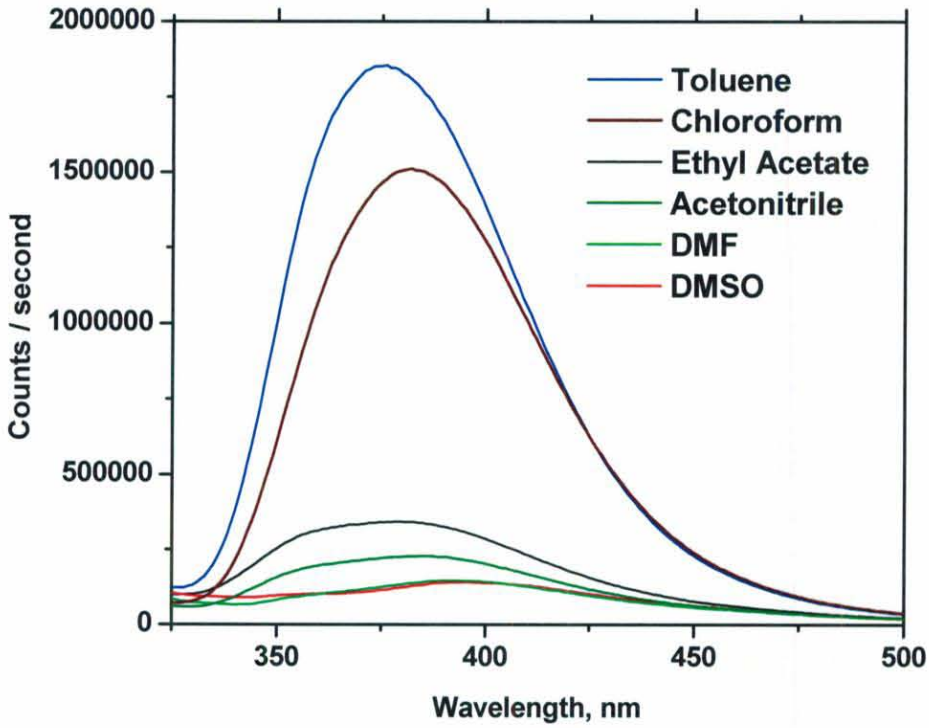

Figure 5.22. Solvent effects on the fluorescence intensity of 3-AC solutions at 298 (± 2) K under 1 atm N_2 at 324 nm excitation.

The dependence of the spectral properties of 3-AC on the solvent polarity is reported in Table 5.9. The Lippert-Mataga solvent polarity parameter (Δf) is defined by Eq. 5.20,[63-65,70,93,94]

$$\Delta f = \frac{\varepsilon - 1}{2\varepsilon + 1} - \frac{n^2 - 1}{2n^2 + 1} \qquad (5.20)$$

where ε and n are the static dielectric constant and refractive index of the solvent.

The Stokes' shift $\left(\Delta\bar{\nu} = \Delta\bar{\nu}_{abs}^{max} - \Delta\bar{\nu}_{flu}^{max}\right)$ of 3-AC is anticipated to be linear according to Lippert-Mataga, Eq. 5.21, which is related to Δf and $\Delta\mu$ where $\Delta\mu$ is the difference in dipole moments between the excited and ground states, $\Delta\mu = \mu_e - \mu_g$

$$\Delta\bar{\nu} = const. + \frac{2\Delta\mu^2}{hca^3}\Delta f \qquad (5.21)$$

where h is Planck's constant, c is the speed of light, and a is the Onsager radius of the solute molecule, taken as the distance between the amino N atom and the carbonyl O atom (2.7 Å) in the optimized geometry (Figure 5.23). The ground-state dipole moment $\mu_g = 3.73\ Debye\ (D)$, obtained using density function theory (DFT).[iii]

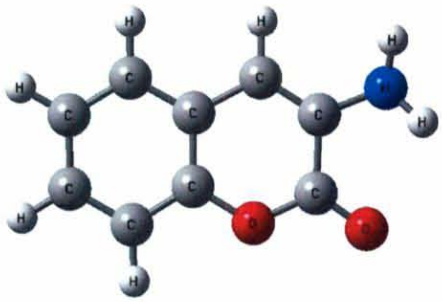

Figure 5.23. DFT optimized structure of 3-AC.

The Onsager radius corresponds to the maximum distance across which charge separation occurs.[95] The $\Delta\mu$ magnitude can be obtained from the slope of the $\Delta\bar{\nu}$ versus Δf plot using Eq. 5.21 giving the change in the dipole moments as $\Delta\mu = 2.22\ D$ for 3-AC which is similar to the reported $\Delta\mu$ values of some related amino coumarin derivatives.[55,92] The μ_e value thus calculated for the 3-AC dye is about 5.95 D.

[iii] Calculation carried out by Dr. Csaba E. Szakacs using DFT with the B3LYP functional and 6-31G(d) basis set.

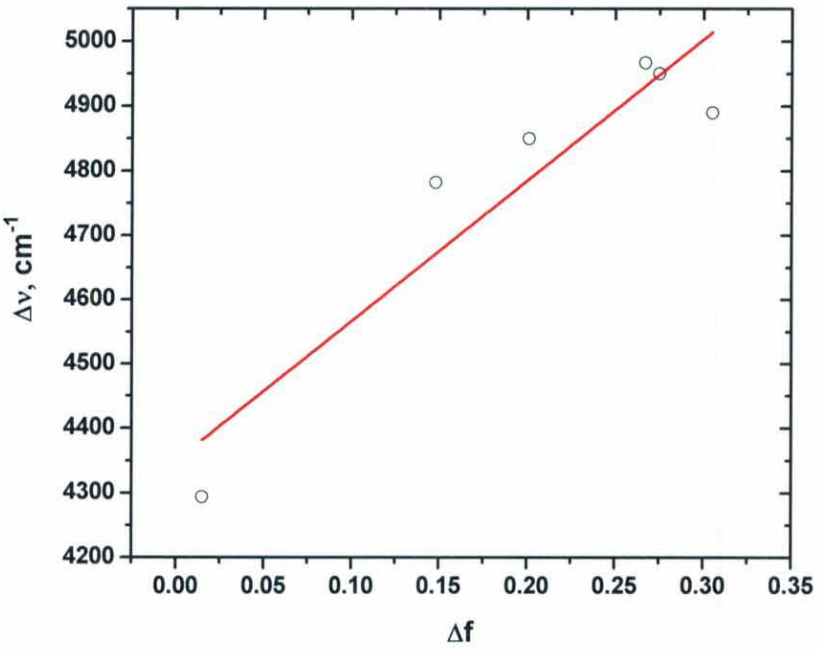

Figure 5.24. Plot of the $\Delta\bar{\nu}$ for 3-AC dye vs the solvent polarity function Δf.

Table 5.9. Absorption and fluorescence maxima of 3-AC dye as estimated in different solvents.

Solvent	λ_{max}^{Abs}	$\bar{\nu}_{Abs}\, cm^{-1}$	λ_{max}^{Em}	$\bar{\nu}_{Em} cm^{-1}$	Δf	$\Delta\bar{\nu}, cm^{-1}$
Toluene	323	30960	375	26666	0.015	4294
Chloroform	323	30960	382	26178	0.148	4782
Ethyl acetate	323	30960	383	26110	0.201	4850
Acetonitrile	324	30864	386	25974	0.305	4890
DMF	329	30395	394	25445	0.275	4950
DMSO	333	30030	399	25063	0.267	4967

Furthermore, the transition dipole moment for absorption (M_{abs})[96] as given by Eq. 5.22 was found to be $M_{abs} = 3.8\ D$.

$$M_{abs} = 0.0958\left(\frac{\varepsilon_{max}\Delta\bar{\nu}_{1/2}}{\bar{\nu}_{max}}\right)^{1/2} \qquad (5.22)$$

where ε_{max} is the extinction coefficient at the maximum intensity of the absorption peak (1.3×10^4 cm^{-1} M^{-1}), $\Delta\bar{\nu}_{1/2}$ is the full width at half maximum of the absorption band as determined by Gaussian fitting (3810 cm^{-1}), and $\bar{\nu}_{max}$ is the wavenumber of the maximum absorption peak (30864 cm^{-1}).

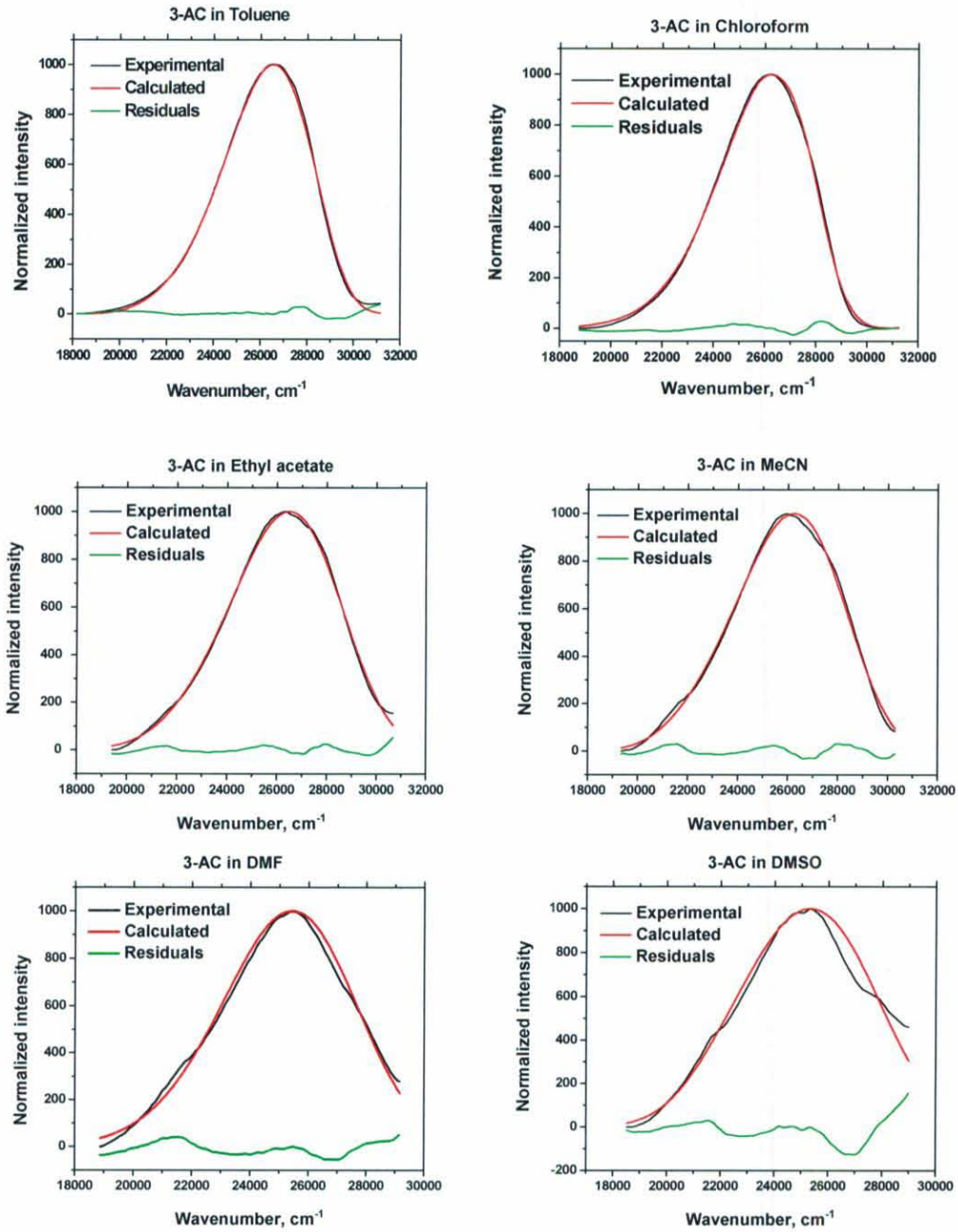

Figure 5.25. Normalized corrected emission of 3-AC in different solvents at 298 (± 2) K under 1 atm N_2 (solid black line) and the corresponding one-mode spectral fit (red dashed line) at room temperature.

Table 5.10. One-mode emission spectral fitting and emission spectral fitting parameters, Franck–Condon factors, and reorganization energies for 3-AC in different solvents at room temperature.

Quantity	Toluene	Chloroform	Ethyl acetate	MeCN	DMF	DMSO
$E_o, (cm^{-1})$	28154	27840	28502	28438	26801	28453
S_M	1.86	1.88	2.12	2.34	1.43	3.15
$\Delta\nu_{1/2}, (cm^{-1})$	2330	1915	3346	2891	4293	3550
$\hbar\omega_M, (cm^{-1})$	1350	1350	1350	1350	1350	1350
$\lambda_o, (\mathrm{cm}^{-1})$	2363	1596	4874	3638	8023	5487
γ	1.41	1.40	1.30	1.20	1.63	1.00
$ln[F(calc)]$	-31.52	-31.52	-28.46	27.44	-29.27	-23.56
$E_{abs} - E_{em}, (\mathrm{cm}^{-1})$	4294	4782	4850	4890	4950	4967
$\lambda_i, (\mathrm{cm}^{-1})$	-	795	-	-	-	-
$\lambda_t, (\mathrm{cm}^{-1})$	2147	2391	2425	2445	2475	2484
$\Delta G_{ES}, (\mathrm{cm}^{-1})$	30517	29436	33376	32076	34824	33940

5.2.7 Ground and Excited State Proton Transfer Reactions

The reaction between 3-AC and TFA was investigated by UV-Vis and emission spectroscopy in MeCN solution. Addition of TFA results in a remarkable effect on the absorption spectrum of 3-AC in MeCN solution as demonstrated in Figure 5.26. There was a decrease in the intensity of the transitions at 324 nm (30864 cm^{-1}), while the intensity of the transitions at 280 nm (35714 cm^{-1}) increased with an isosbestic point observed at 296 nm (33784 cm^{-1})

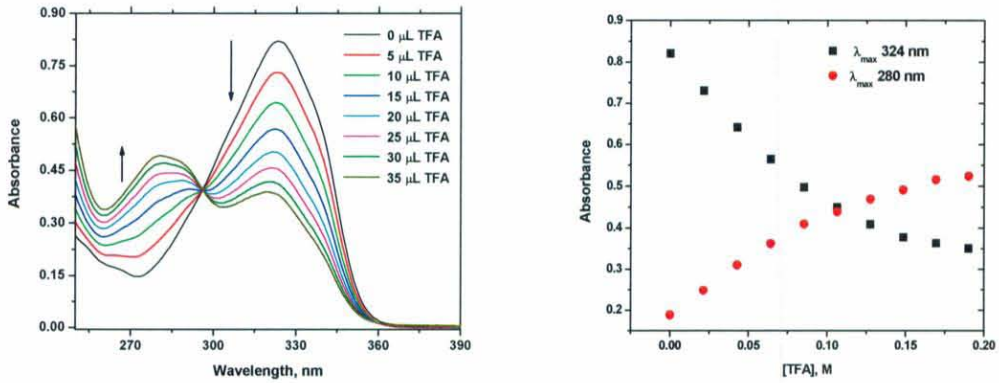

Figure 5.26. (Left) spectrophotometric titration of 3-AC in MeCN solution at 298 (± 2) K under 1 atm N_2 with TFA. (Right) absorbance change at 324 and 280 nm vs equivalents of TFA.

Using global analysis (described in Chapter 2) for estimation of the equilibrium constant for the ground (pK_a) and the excited state (pK_a^*), pK_a and pK_a^* were determined to be 3.44 and 5.71 respectively.

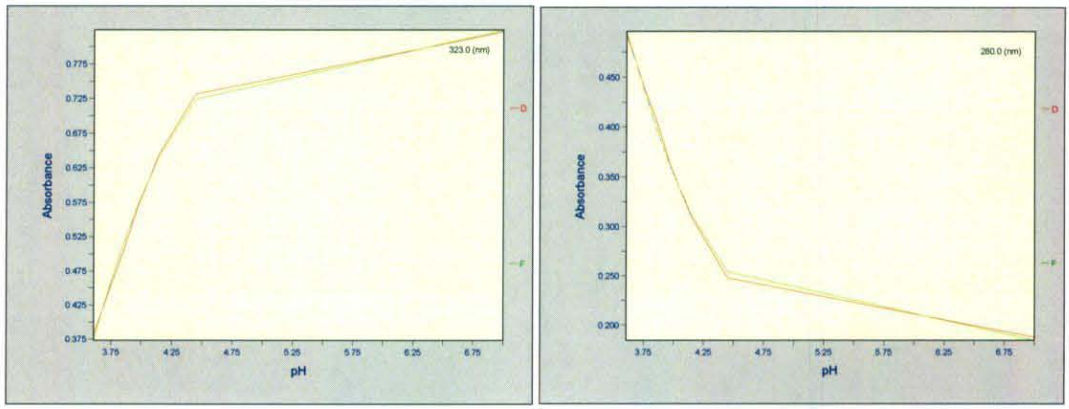

Figure 5.27. Equilibrium constant determination using the global analysis fitting program.

The fluorescence spectrum of 3-AC exhibits acidic dependent behavior, as shown in Figure 5.28. Upon addition of TFA, the emission spectrum of 3-AC increases in intensity and shifts to slightly higher energy from λ_{max} 386 nm to 399 nm.

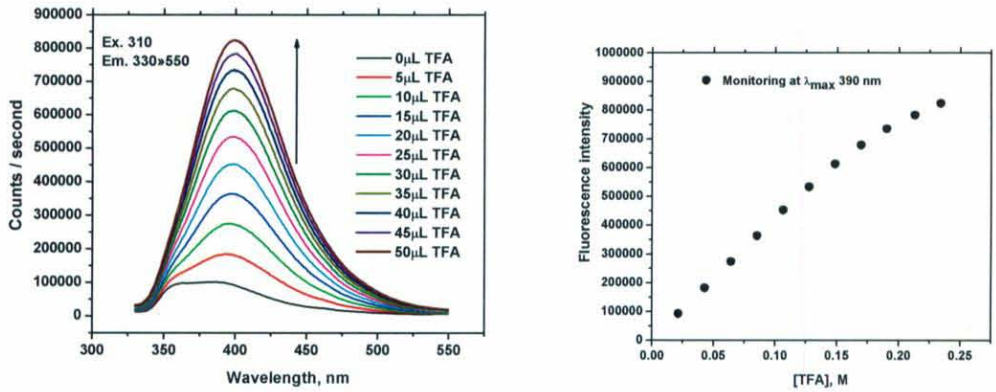

Figure 5.28. (Left) emission changes of 3-AC in MeCN solution at 298 (± 2) K under 1 atm N_2 upon addition of TFA. (Right) Fluorescence change at 390 nm vs equivalents of TFA.

5.2.8 Estimation of pK_a^* Using the Förster Cycle

By using Förster cycle calculations, one can estimate the pK_a^* of 3-AC following the protonation of the amino group by titration of 3-AC with trifluoroacetic acid (TFA) as described in section 5.1.3. The protonated amino group is in equilibrium with the neutral species in the excited state. Förster cycle calculations were done using fluorescence spectra for the deprotonated (neutral 3-AC) and protonated (cation 3-AC) species. For comparison with the pK_a^* that was obtained by global analysis of all of the equations, the calculated constants are shown below.

Förster equation:

$$pK_a^* = pK_a - \frac{N_A h}{2.3RT}(\upsilon_1 - \upsilon_2) \quad (5.23)$$

For T = 298.15 K, Avogadro's number (N_A), Planck's constant (h), and the ideal gas constant (R) Eq. 5.23 becomes

$$pK_a^* = pK_a - 6.999 \times 10^{-14}\, s\, (\upsilon_1 - \upsilon_2) s^{-1} \quad (5.24)$$

3-AC	λ_{max}^{em}, nm	υ / s^{-1}	pK_a	pK_a^*
Neutral	386	7.7666×10^{14}		
Cation	399	7.5136×10^{14}	3.44	5.21

The estimated error for pK_a^* between the global analysis and the Förster cycle calculation is less than 10 %.

5.3 Discussion

5.3.1 Intramolecular Charge Transfer (ICT) and Twisted Intramolecular Charge Transfer State (TICT) Formation in 3-AC

The photophysical properties of 3-AC may be delineated from the steady-state absorption and emission spectral data which were shown in Figure 5.15. The absorption spectrum shows a maximum absorption peak at 324 nm which is attributed to a $\pi - \pi^*$ transition localized on the coumarin ring. The shoulder at 337 nm is attributed to a charge transfer (CT) band from the amino moiety (donor) into the carbonyl moiety (acceptor) of the coumarin ring. The emission spectrum shows one emission peak at 386 nm that is assigned to a radiative charge transfer transition ($S_1 \rightarrow S_0$). This state exhibits a very short emission lifetime ($\tau < 400\ ps, k > 2.5 \times 10^9 s^{-1}$). However, no emission peak has been observed from a TICT state which is consistent with the results reported by Lippert *et al.*[97] These authors have theoretically calculated the coupling for a bichromophoric molecule. They observed that the radiative relaxation from the TICT state is disallowed because the π-system of the donor and acceptor are decoupled from each other. Therefore detection of fluorescence from the TICT state would be attenuated. Alternatively, it should be noted if $E_o^{TICT} < S\hbar\omega$, fluorescence would not be observed as the ground and excited TICT states would be highly distorted with respect to one another. 3-AC exhibits a fluorescence quantum yield ($\phi_{em} = 0.005$) which is consistent with intersystem crossing from the CT state to the close lying triplet state (from singlet to triplet state), showing a phosphorescence band at 730 nm (Figure 5.15). The presence of $n \rightarrow \pi^*$ states, while making only a small contribution to the ground state spectral envelope, may

facilitate intersystem crossing in the excited state by a series of transitions between states in a manner described using El-Sayed's rule.[27] There are other non-radiative pathways that may be present, but at the present time there is little evidence to invoke such behavior. Bangar Raju[53] has studied the photophysical properties of some substituted bicoumarins in different solvents. The author concludes that excited triplet states have low probability of formation in the absence of a mechanism which lifts the spin restriction of a $\Delta S = 2$ spin interconversion. A proposed energy level diagram derived from the emission spectroscopic data is given in Figure 5.29

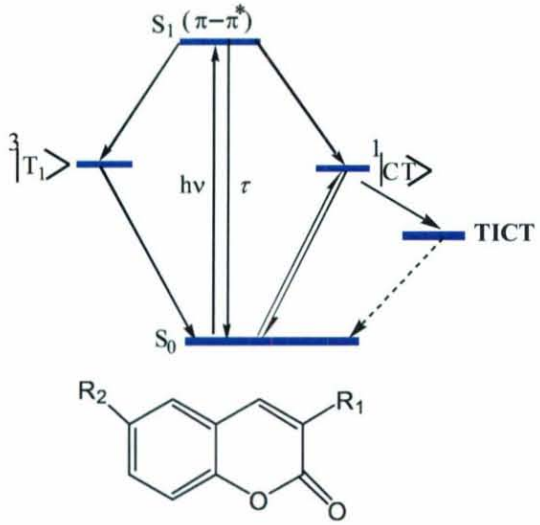

Figure 5.29. Energy diagram illustrating the excited state transitions of 3-AC substitution.

5.3.2 Effect of Solvent Polarity on the ICT and TICT States

Spectroscopic data for 3-AC in different solvents are shown in Figures 5.20 and 5.26 and emission spectral fitting parameters, Franck–Condon factors, and reorganization energies data are collated in Table 5.10. Absorption and fluorescence spectra of 3-AC were found to be dependent on the dielectric properties of the solvent. The absorption

spectra exhibit a red shift with an increase in the solvent polarity which is expected based on the polarity of a charge transfer state. In DMSO and DMF, which are able to hydrogen bond with a solute, the observed Stokes' shifts are much larger than those seen in other solvents of lower polarity. This is indicative of a specific solute-solvent interaction. It has been reported that the hydrogen bonding interaction is primarily responsible for the enhanced Stokes' shift and therefore enhanced ICT character for the dye in such solvents.[64,98] The fluorescence spectra show slight shifts in polar solvents and a pronounced decrease in the emission intensity with increasing solvent polarity (Figure 5.22) as is expected for charge transfer. The dramatic quenching of fluorescence in highly polar solvents is consistent with a mechanism where k_{nr} is increased due to the energy gap law considerations or to the new non-radiative channels such as the ICT → TICT transitions as shown in Figure 5.31. The ability of solvents to specifically interact with a chromophore is due to the presence of electron lone pairs, either in the solvent or the solute (Figure 5.30). Since dielectric continuum theory treats the solvent as a continuum characterized by the bulk solvent properties D_{op} and D_s, and does not consider specific solute / solvent interactions, it is not appropriate in this case.[89]

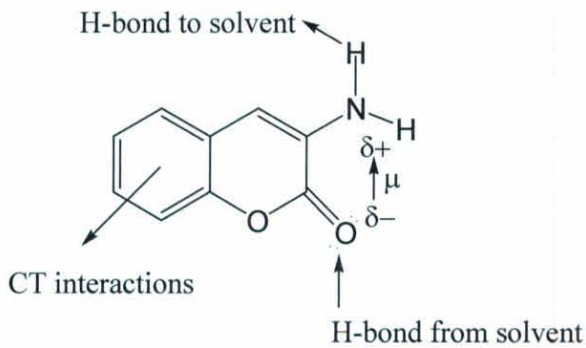

Figure 5.30. Structure of 3-AC forming a H-bond with solvent.

More importantly, the ordering of electronic states in 3-AC is predicated on several factors which dictate the structure of the ground and excited state electronic manifolds. Coumarins have been extensively investigated as solvation probes for the reasons described above. The nature of the solvent effect on the energy gap is illustrated in a proposed potential energy surface in Figure 5.31.

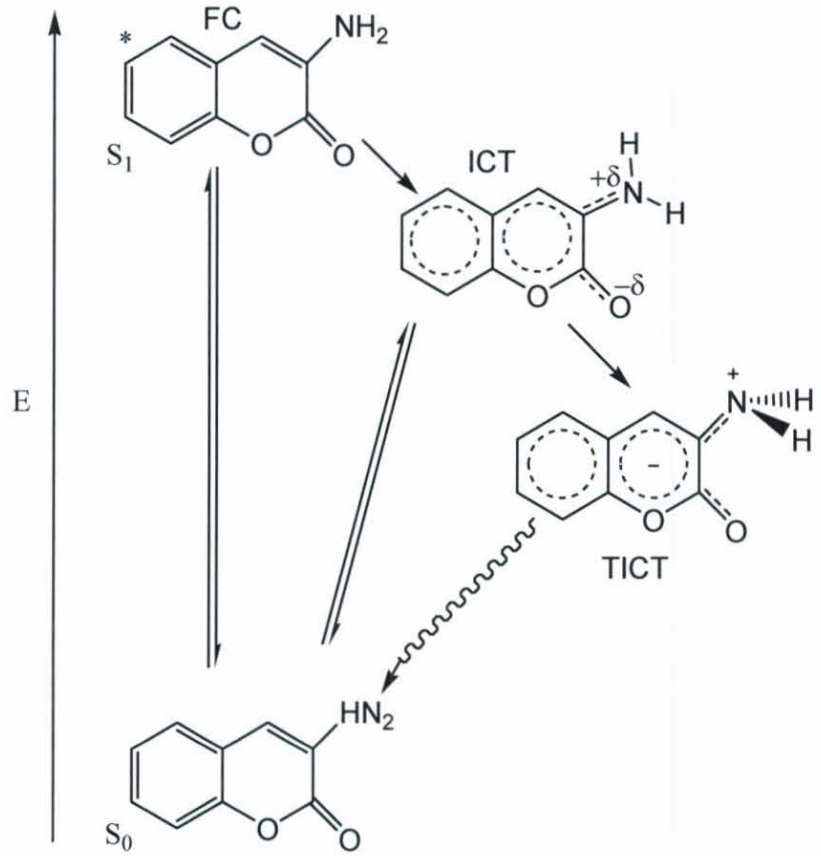

Figure 5.31. Proposed mechanism for 3-AC in polar solvent, depicting a Franck-Condon (FC) transition and internal conversion from the CT state to the twisted conformation TICT state.

One other important property that may be estimated is the change of dipole moment($\Delta\vec{\mu}$) following excitation. This value is important because it provides a measure

of the electronic redistribution in the excited state compared to the ground state. To understand spectral shifts with solvent polarity, it is important to correlate Stokes' shifts, Δν, with Δf, which are expected to follow the linear Lippert-Mataga relationship, Eq. 5.21. Figure 5.24 shows the Δν vs Δf plot for 3-AC. The value of the dipole moment of the excited state ($\mu_e = 5.95$ D) indicates that the excited state is more polar than the ground state, which is attributed to the ICT state, and corresponds to the proposed mechanism in Figure 5.31.

5.3.3 The Effect of Trifluoroacetic Acid (TFA) on the ICT and TICT States

3-AC acts as a proton acceptor and the addition of TFA to 3-AC leads to a decrease in the absorption intensity at 324 nm which is consistent with the enhancement observed in the fluorescence intensity with increasing H-bond capacity. This implies a considerable decrease in the efficiency of intersystem crossing (ISC) or internal conversion (IC) of 3-AC in such media because the rate of IC between $n-\pi^*$ and $\pi-\pi^*$ states is dependent to a significant extent on the vibrational overlap integral (Franck-Condon factor) between the states. The vibrational overlap integral between the $n-\pi^*$ and $\pi-\pi^*$ states decreases as a result of the decrease in the charge density of the nonbonding electrons of the amine moiety of 3-AC following H-bond formation.[99] These changes in the absorption and emission intensities due to protonation of the amino group in 3-AC decrease the k_{nr}, because the lone pair of the NH_2 group is not accessible after the amino moiety has been protonated. The protonated amino substituent then becomes electron withdrawing and increases the energy of the intramolecular charge transfer state.

This is also why the emission intensity increases (with a slight red shift). One sees a larger k_r value and decreased internal conversion from the ICT to the TICT state.[97,100,101] Subba Aro *et al.*[102] conclude from a similar observation on 3-AC that the emission intensity increases when 3-AC is protonated; they also investigated the acid-base equilibria of 3-AC in aqueous solution for the ground and excited state.[102] Their experiments and ours were conducted at different temperatures making direct comparisons of the derived quantities difficult.

5.3.4 Substitutions Effect on the ICT and TICT States

Substituents at the 6 position of the coumarin ring have a noticeable effect on the absorption and fluorescence energies and the quantum yield for emission. The UV-vis absorption and fluorescence spectra of 3-AC and its derivatives in MeCN are shown in Figure 5.32. The results are also given in Tables 5.3 and 5.4. The fluorescence intensity depends on the electron donating or withdrawing nature of the substituent.

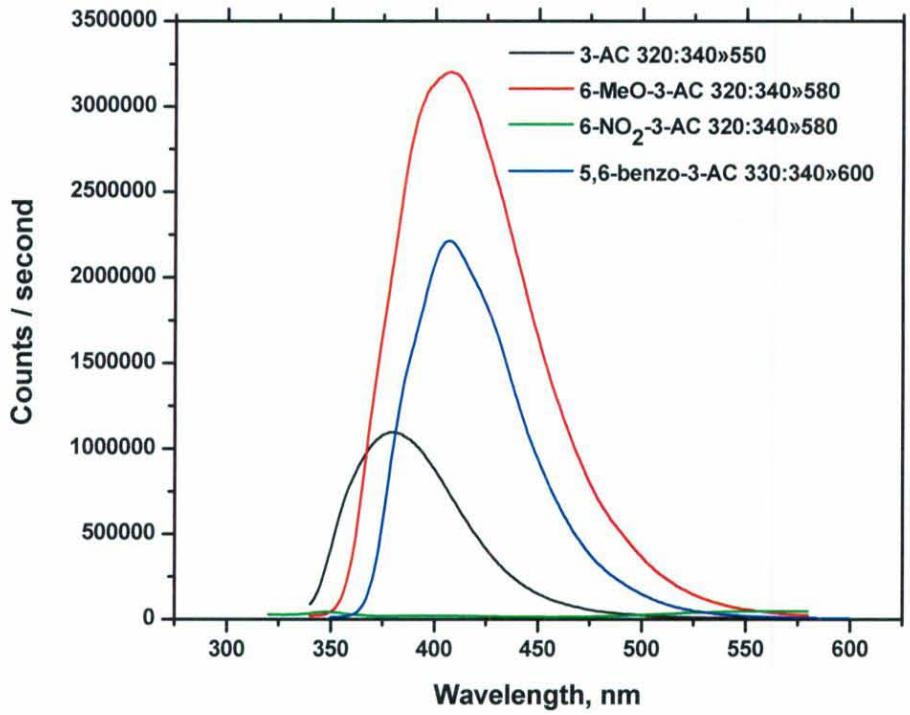

Figure 5.32. Fluorescence of 3-AC with substituents in MeCN solution at 298 (± 2) K under 1 atm N_2.

The substituent study provides additional evidence that 3-AC forms the ICT and TICT state, where the solvent polarity has a similar effect to the substituent effect. The latter depends on the nature of the substituent. An electron-withdrawing substituent at the 6 position such as one finds in 6-NO_2-3-AC may act as a charge stabilizer, which tends to diminish the barrier between the ICT and TICT states and increases k_{nr} via a temperature dependent thermal crossing. This is exactly analogous to the solvent dependence of the $Ru(bpy)_3^{2+*}$ which undergoes non-radiative relaxation through highly distorted Ru^{II*} localized excited states (i.e. dd states) and which attenuates the lifetime of the

chromophore.[103] The energy gap between the ground and the excited state decreases as the polar TICT state is stabilized relative to the ground state (Figure 5.10) via inductive substituent effects. On the other hand, the electron-donating substituents such as one finds in 6-MeO-3-AC would provide an additional electron density which energetically facilitates forming the ICT state. Thus, the substituent behavior of 3-AC can be understood on the basis of conventional inductive substituent effects that give rise to variations in k_{nr}. This is illustrated schematically in Figure 5.10

The extension of the aromatic framework in 5,6-benzo-3-AC increases electron delocalization. Effectively, the excited state spin density is spread over a larger nuclear framework and results in a significant attenuation in Δr_e. This in turn lowers S_M and the potential energy surfaces become nested. Also, spreading the excited state electron spin density over the aromatic rings should reduce electron-electron repulsion. The net effect is understood within the framework of non-radiative decay theory. With this structural feature (the larger aromatic ring system) the k_{nr} value is attenuated and k_r becomes more prominent. Hence the fluorescence quantum yield increases with decreasing internal conversion from the FC to the ICT state, Table 5.4.

Transient absorption of 3-AC substituted with methoxy and nitro groups in position 6 shows significant differences compared to the transient absorption of 3-AC and 5,6-benzo-3-AC. This indicates that the electron-donating and electron-withdrawing groups have significant influence on the nature of the excited states. The methoxy group supports the ICT state, and the nitro group supports the TICT state. Transient difference spectra of 6-MeO-3-AC (Figure 5.18) show bleaching $at\ \lambda_{max}$= 340 nm due to loss of

ground state absorption and the positive peak $at\ \lambda_{max}$= 400 nm is attributed to either the triplet state or the ICT state. The suggested mechanism is shown in Figure 5.33.

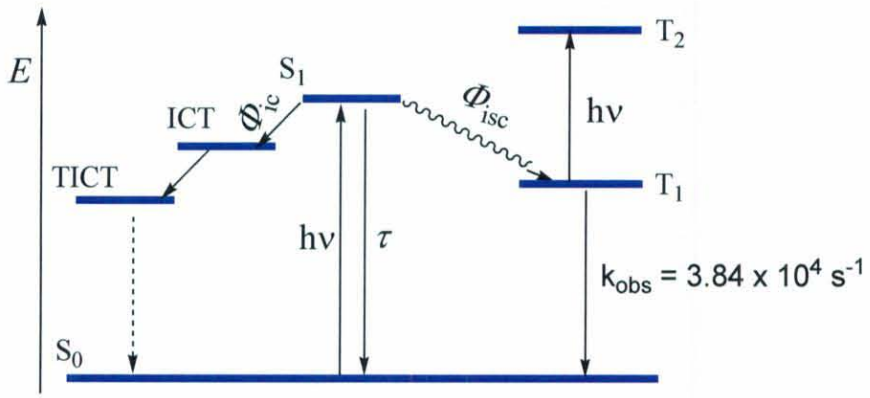

Figure 5.33. Schematic energy level diagram showing the proposed mechanism for relaxation and interconversion of ICT and TICT states and illustrating the energetics of the singlet and triplet states in 6-MeO-3-AC.

The emission spectrum of 6-NO_2-3-AC exhibits a dual emission at 380 nm and 555 nm in $CHCl_3$ solutions as shown in Figure 5.34. The emission peak at 555 nm corresponds with the TICT emission. The emergence of a TICT emission band for 6-NO_2-3-AC can be interpreted as being due to the nitro group (NO_2) substituent. Since NO_2 is a withdrawing group, this group causes an increase in the dipole moment between the donor and acceptor moieties. The TICT state generally has a large dipole moment and its energy is expected to decrease with presence of a withdrawing group such a NO_2 group. Consequently, this group will stabilize the TICT state by reducing the energy of the TICT state as shown in Figure 5.10.

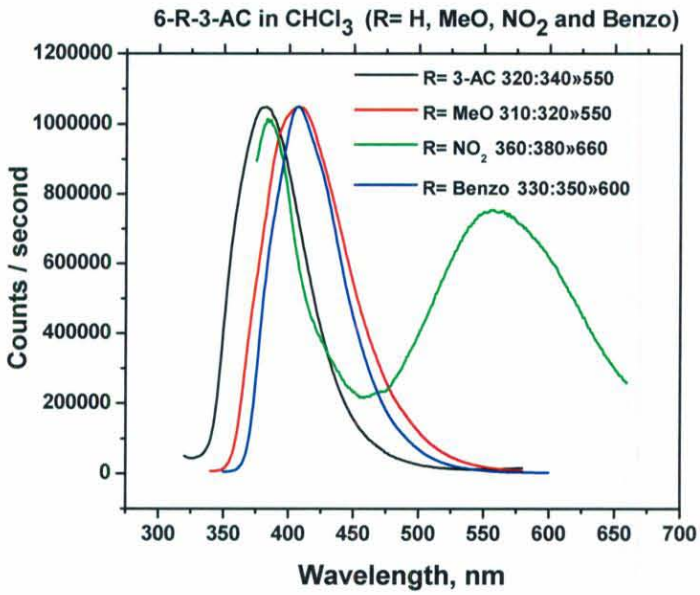

Figure 5.34. Emission spectra of 3-AC bearing various substituents in $CHCl_3$ solution at 298 (± 2) K under 1 atm N_2.

Transient difference spectra of 6-NO_2-3-AC (Figure 5.19) show that the bleach at 320 nm is due to a loss of ground state absorption and the positive peak at 380 nm is attributed to the TICT state. The mechanism is shown in Figure 5.35.

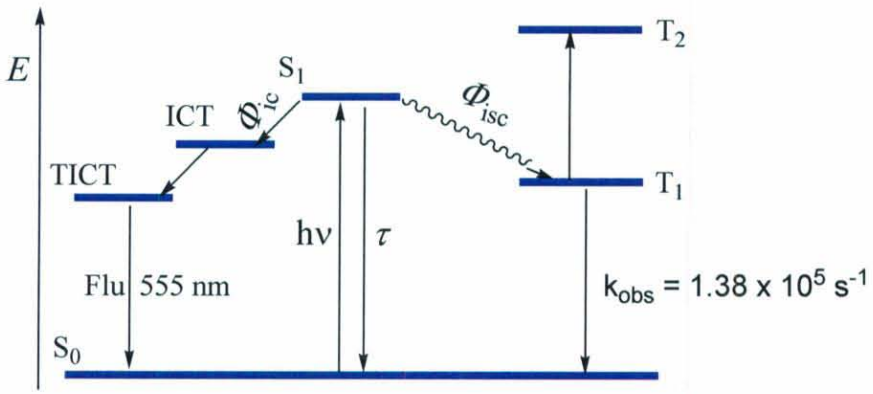

Figure 5.35. Schematic energy level diagram showing the proposed mechanism for relaxation for ICT and TICT states and illustrating the energetics of the singlet and triplet states in 6-NO_2-3-AC.

The fitting of the emission spectra was accomplished using a single mode Franck-Condon analysis. The photophysical parameters for 3-AC, 6-MeO-3-AC and 5,6-benzo-3-AC are listed in Table 5.4 and the fits are shown in Figure 5.16. The values of the quantum spacings ($\hbar\omega_M$) for 3-AC and 6-MeO-3-AC are significantly larger than the value obtained for 5,6-benzo-3-AC. It is proposed that the emission spectra for these chromophores is due to a charge transfer state in which an increase in the value for $\hbar\omega_M$ is caused by an increase in the vibrational frequency of the carbonyl group following substitution of an electron-withdrawing group.[104-106] It is difficult to calculate the electronic coupling (H_{DA}) between the electron donor and acceptor because these compounds have short emission lifetimes and only an upper limit of the lifetimes can be estimated. Therefore, the estimates of H_{DA} represent lower limits. Thus the electronic coupling matrix element, H_{DA}, has values > 1000 cm^{-1} and of a magnitude that indicates that donor-acceptor electron transfer will be adiabatic in nature.

5.4 Conclusions

In conclusion, the absorption and emission spectral properties of 3-AC and its substituted derivatives show a significant dependence on both the coumarin molecular structure and the chosen solvent. In the solvent polarity studies on the photophysical properties of 3-AC we observed increased nonradiative decay in high polarity solvents which suggests that the excited state relaxes from the TICT state to the ground state rather than the ICT state. Also, particular substituents such as electron withdrawing groups stabilize the TICT state by increasing the nonradiative decay. Protonation of the 3-AC dye leads to an increase in the emission intensity by decreasing the nonradiative decay. From these observations, we conclude that 3-AC has a planar ICT structure in solvents of moderate polarities, but in a highly polar solvent which could hydrogen-bond with the dye, the TICT state is stabilized. This interpretation is consistent with what has been previously reported.[53,64-67,70,107]

5.5 References

(1) Kvoschwitz, J. I.; Kirk-Othmer *"Encyclopedia of Chemical Technology"*; 3rd ed.; Wiley: New York, **1978**, pp. 196–206.

(2) Cohen, B.; Huppert, D. *J. Phys. Chem. A* **2001**, *105*, 7157.

(3) de Melo, J. S.; Fernandes, P. F. *J. Mol. Struct.* **2001**, *565*, 69-78.

(4) de Melo, J. S. S.; Becker, R. S.; Macanita, A. L. *J. Phys. Chem.* **1994**, *98*, 6054.

(5) Eckardt, T.; Hagen, V.; Schade, B.; Schmidt, R.; Schweitzer, C.; J., B. *J. Org. Chem.* **2002**, *67*, 703.

(6) Hoshiyama, M.; Kubo, K.; Igarashi, T.; Sakurai, T. *J. Photochem. Photobio. A-Chem.* **2001**, *138*, 227.

(7) Izquierdo, M. E. F.; Granados, J. Q.; Mir, V. M.; Martinez, M. C. L. *Food Chemistry* **2000**, *70*, 251.

(8) Jakubiak, R.; Bunning, T. J.; Vaia, R. A.; Natarajan, L. V.; Tondiglia, V. P. *Advanced Materials* **2003**, *15*, 241.

(9) Jones, G.; Jackson, W. R.; Choi, C. Y.; Bergmark, W. R. *J. Phys. Chem.* **1985**, *89*, 294-300.

(10) Jones, G.; Rahman, M. A. *J. Phys. Chem.* **1994**, *98*, 13028-13037.

(11) Killard, A. J.; O'Kennedy, R.; Bogan, D. P. *J. Pharm. Biomed. Anal.* **1996**, *14*, 1585.

(12) Stathatos, E.; Lianos, P.; Stangar, U. L.; Orel, B. *Chem. Phys. Lett.* **2001**, *345*, 381.

(13) Trenor, S. R.; Shultz, A. R.; Love, B. J.; Long, T. E. *Chem. Rev.* **2004**, *104*, 3059-3077.

(14) Yamazaki, H.; Tanaka, M.; Shimada, T. *J. Chromatography B* **1999**, *721*, 13.

(15) Yourick, J. J.; Bronaugh, R. L. *J. Appl. Toxicol.* **1997**, *17*, 153.

(16) Zhang, R. F.; Zheng, H. P.; Shen, J. C. *Synthetic Metals* **1999**, *106*, 157.

(17) Jones, G.; Jackson, W. R.; Halpem, A. H. *Chem. Phys. Lett.* **1980**, *72*, 391.

(18) Jones, G.; Jackson, W. R.; Kanoktanapom, S. *Optics Commun* **1980**, *33*, 315.

(19) Drexhage, K. H. *Dye Lasers*; Springer-Verlag: New York, **1977**.

(20) Kauffman, J. M. *Applied Optics* **1980**, *19*, 3431-3435.

(21) Maeda, M. *"Laser dyes : properties of organic compounds for dye lasers"* Academic Press New York, **1984**.

(22) Jones, G.; Jackson, W. R.; Kanoktanaporn, S.; Halper, A. M. *Opt. Commun.* **1980**, *33*, 315-320.

(23) Turro, N. J. *"Modern Molecular Photochemistry"*; University Science Books: Sausalito, California, **1991**.

(24) Köhler, A.; Bässler, H. *Materials Science and Engineering* **2009**, *66*, 71-109.

(25) Ohmori, N.; Suzuki, T.; Ito, M. *J Phys. Chem.* **1988**, *92*, 1086-1093.

(26) Anderson, R. W.; Hochstrasser, R. M.; Lutz, H.; Scott, G. W. *J. Chem. Phys.* **1974**, *61*, 2500.

(27) El-Sayed, M. A.; Leyerle, R. *J. Chem. Phys.* **1975**, *62*, 1579.

(28) Chou, P.-T.; Martinez, M. L.; Studer, S. L. *Chem. Phys. Lett.* **1992**, *188*, 49-53.

(29) Land, E. J.; Truscott, T. G. *Photochem. Photobio.* **1979**, *29*, 861-866.

(30) Kitamura, N.; Kohtani, S.; Nakagaki, R. *J. Photochem. Photobio. C: Photochem. Rev.* **2005**, *6*, 186-185.

(31) Christie, R. M.; Lui, C.-H. *Dyes and Pigments* **1999**, *42*, 85-93.

(32) Wheelock, C. *J. Am. Chem. Soc.* **1959**, *81*, 1348.

(33) Kamiski, M.; Kartanowicz, R.; Kartanowicz, M. M. x.; Królicka, A.; Sidwa-Gorycka, M.; ojkowska, E.; Gorze, W. *J. Sep. Sci.* **2003**, *26*, 1287–1291.

(34) Pryor, B. A.; Palmer, P. M.; Chen, Y.; Topp, M. R. *Chem. Phys. Lett.* **1999**, *299*, 536-544.

(35) Atkins, R. L.; Bliss, D. E. *J. Org. Chem.* **1978**, *43*, 1975-1980.

(36) Sharma, V. K.; Saharo, P. D.; Sharma, N.; Rastogi, R. C.; Ghoshal, S. K.; Mohan, D. *Spectrochim. Acta, Part A: Mol. Biomol. Spectrosc.* **2003**, *59*, 1161.

(37) Grabowski, Z. R.; Rotkiewicz, K.; Rettig, W. *Chem. Rev.* **2003**, *103*, 3899-4032.

(38) Chemla, D. S.; Zyss, J. *"Nonlinear Optical Properties of Organic Molecules and Crystals"*; Academic Press: New York, **1987**.

(39) Kim, J.; Morozumi, T.; Kurumatani, N.; Nakamura, H. *Tetrahedron Lett.* **2008**, *49* 1984-1987.

(40) Rosenthal, S. J.; Jimenez, R.; Fleming, G. R.; Kumar, P. V.; Maroncelli, M. *J. Mol. Liq.* **1994**, *60*, 25-56.

(41) Samanta, A.; Fessenden, R. W. *J. Phys. Chem. A* **2000**, *104*, 8577-8582.

(42) Rettig, W. *Angew. Chem. Int. Ed. Engl.* **1986**, *25*, 971.

(43) Lippert, E.; Luder, W.; Moll, F.; Nagele, W.; Boos, H.; H., P.; Seibold-Blankenstein, I. *Angew. Chem.* **1961**, *73*, 695.

(44) Grabowski, Z. R. *Pure and Appl. Chem.* **1993**, *65*, 1751-1756.

(45) Grabowski, Z. R.; Dobkowski, J. *Pure Appl. Chem* **1983**, *55*, 245.

(46) Huppert, D.; Rand, S. D.; Rentzepis, P. M.; Barbara, P. M.; Struve, W. S.; Grabowski, Z. R. *J. Chem. Phys.* **1981**, *75*, 5714.

(47) Rotkiewicz, K.; Grellmann, K. H.; Grabowski, Z. R. *Chem. Phys. Lett.* **1973**, *19*, 315.

(48) Siemiarczuk, A.; Grabowski, Z. R.; Asher, M.; Ottolenghi, M. *Chem. Phys. Lett.* **1977**, *51*, 315.

(49) Dobkowski, J.; Michl, J.; Waluk, J. *Phys. Chem. Chem. Phys.* **2003**, *5*, 1027-1031.

(50) Rotkiewicz, K.; Herbich, J.; Salgado, F. P.; Rettig, W. *Proc. Indian Acad. Sci.* **1992**, *2*, 105-115.

(51) Herbich, J.; Perez Salgado, F.; Rettschnick, R. P. H.; Grabowski, Z. R.; Wojtowicz, H. *J. Phys. Chem.* **1991**, *95*, 3491-3497.

(52) Paczkowski, J.; Neckers, D. C. *Macromolecules* **1991**, *24*, 3013-3016.

(53) Raju, B. B. *J. Phys. Chem. A* **1997**, *101*, 981-987.

(54) Ramakrishna, G.; Ghosh, H. N. *J. Phys. Chem. A* **2002**, *106*, 2545-2553.

(55) Rechthaler, K.; Köhler, G. *Chem. Phys.* **1994**, *189*, 99-116.

(56) Satpati, A. K.; Kumbhakar, M.; Nath, S.; Pal, H. *Photochem. Photobio.* **2009**, *85*, 119-129.

(57) Van Gompel, J. A.; Schuster, G. B. *J. Phys. Chem.* **1989**, *93*, 1292-1295.

(58) Nagasawa, Y.; Yartsev, A. P.; Tominaga, K.; Bisht, P. B.; Johnson, A. E.; Yoshihara, K. *J. Phys. Chem.* **1995**, *99*, 653-662.

(59) Pal, H.; Nagasawa, Y.; Tominaga, K.; Yoshihara, K. *J. Phys. Chem.* **1996**, *100*, 11964-11974.

(60) Pal, H.; Shirotab, H.; Tominagac, K.; Yoshiharad, K. *J. Chem. Phys.* **1999**, *110*, 11454.

(61) Shirota, H.; Pal, H.; Tominaga, K.; Yoshihara, K. *J. Phys. Chem. A* **1998**, *102*, 3089-3102.

(62) Nad, S.; Pal, H. *J. Phys. Chem. A* **2003**, *107*, 501-507.

(63) Bangar Raju, B. *J. Phys. Chem. A* **1997**, *101*, 981-987.

(64) Barik, A.; Kumbhakar, M.; Nath, S.; Pal, H. *Chem. Phys.* **2005**, *315*, 277-285.

(65) Barik, A.; Nath, S.; Pal, H. *J. Chem. Phys.* **2003**, *119*, 10202.

(66) Dahiya, P.; Kumbhakar, M.; Kukherjee, T.; Pal, H. *Chem. Phys. Lett.* **2005**, *414*, 148-154.

(67) Kaholek, M.; Hrdlovic, P. *J Photochem. Photobiol. A: Chem.* **1999**, *127*, 45-55.

(68) Nad, S.; Kumbhakar, M.; Pal, H. *J. Phys. Chem. A* **2003**, *107*, 4808-4816.

(69) Raju, B. B.; Varadarajan, T. S. *J. Photochem. Photobiol. A: Chem.* **1995**, *85*, 263-267.

(70) Senthilkumar, S.; Nath, S.; Pal, H. *Photochem. Photobiol.* **2004**, *80*, 104-111.

(71) Cornelissen-Gude, C.; Rettig, W. *J. Phys. Chem. A* **1998**, *102*, 7754.

(72) Druzhinin, S. I.; Bursulaya, B. D.; Uzhinov, B. M. *J. Photochem. Photobiol. A* **1995**, *90*, 53.

(73) Fonseca, T.; Kim, H. J.; Hynes, J. T. *J. Photochem. Photobiol. A* **1994**, *82*, 67.

(74) Lafemina, J. P.; Duke, C. B.; Paton, A. *J. Chem. Phys.* **1987**, *87*, 2151.

(75) Maus, M.; Rettig, W. *Chem. Phys.* **1997**, *218*, 151.

(76) Nad, S.; Pal, H. *J Phys. Chem. A* **2000**, *104*, 673-680.

(77) Carreira, E. M. *"Organic photochemistry"* Thieme: New York, **2001**.

(78) Hammond, G. S.; Stout, C. A.; Lamola, A. A. *J. Am. Chem. Soc.* **1964**, *86*, 3103-3106.

(79) Hoffman, R.; Wells, P.; Morrison, H. *J Org. Chem.* **1971**, *36*, 102-108.

(80) Karthikeyan, S.; Ramamurthy, V. *J Org. Chem.* **2006**, *71*, 6409-6413.

(81) Lewis, F. D.; Barancyk, S. V. *J. Am. Chem. Soc.* **1989**, *111*, 8653-8661.

(82) Moorthy, J. N.; Venkatesan, K.; Weiss, R. G. *J Org. Chem.* **1992**, *57*, 3292-3297.

(83) Muthuramu, K.; Ramnath, N.; Ramamurthy, V. *J Org. Chem.* **1983**, *48*, 1872-1876.

(84) Farooqui, A. S.; Zaidi, Z. H. *Spectro. Lett.* **2001**, *34*, 301-309.

(85) Samanta, A. *Proc Indian Natn Sci Acad* **2003**, *69*, 95-107.

(86) Wang, Y. *J. Phys. Chem.* **1985**, *89*, 3799-3805.

(87) Claude, J. P., Ph.D. Thesis, University of North Carolina, Chapel Hill, **1996**.

(88) Barqawi, K. R.; Murtaza, Z.; Meyer, T. J. *J. Phys. Chem.* **1991**, *95*, 47-50.

(89) Chen, P.; Meyer, T. J. *Chem. Rev.* **1998**, *98*, 1439-1477.

(90) Cohen, B.; Crespo-Hernández, C. E.; Kohler, B. *Faraday Discuss.*, **2004**, *127*, 137.

(91) Kestell, J. D.; Williams, Z. L.; Stultz, L. K.; Claude, J. P. *J. Phys. Chem. A* **2002**, *106*, 5768-5778.

(92) McCarthy, P. K.; Blanchard, G. J. *J. Phys. Chem.* **1993**, *97*, 12205-12209.

(93) Lakowicz, J. R. *Principles of Fluorescence Spectroscopy*; 3rd ed.; Springer: New York, **2006**.

(94) Lippert, E. Z. *Naturforsch.* **1955**, *10a*, 541.

(95) Mukherjee, S.; Chattopadhyay, A.; Samanta, A.; Soujanya, T. *J. Phys. Chem.* **1994**, *98*, 2809-2812.

(96) Tsubomura, H.; Lang, R. P. *J. Am. Chem. Soc.* **1961**, *83*, 2085-2092.

(97) Lippert, E.; Rettig, W.; Bonacic-Koutecky, V.; Heisl, F.; Miehe, J. *Adv. Chem. Phys.* **1987**, *68*, 1.

(98) Nakagaki, R.; Kitamura, N.; Aoyama, I.; Ohtsubo, H. *J. Photochem. Photobiol.*, **1994**, *80*, 113.

(99) Lim, E. C. *"Molecular Luminescence"*; ed by E. C. Lim, W. A. Benjamin: New York, **1969**, P. 475.

(100) Grabowski, Z. R.; Rotkiewicz, K.; Siemiarczuk, A.; Cowley, D. J.; Baumann, W. N. *J. Chem.* **1979**, *3*, 443.

(101) Kato, S.; Amatatsu, Y. *J. Chem. Phys.* **1990**, *92*, 7241.

(102) Subba Rao, R. V.; Krishnamurthy, M.; Dogra, S. K. *J. Photochem.* **1986**, *34*, 55-61.

(103) Thompson, D. W.; Fleming, C. N.; Myron, B. D.; Meyer, T. J. *J. Phys. Chem. B* **2007**, *111*, 6930-6941.

(104) Chen, P.; Duesing, R.; Graff, D. K.; Meyer, T. J. *J. Phys. Chem.* **1991**, *95*, 5850-5858.

(105) Kober, E. M.; Caspar, J. V.; Lumpkin, R. S.; Meyer, T. J. *J. Phys. Chem.* **1986**, *90*, 3722-3734.

(106) Tutt, L.; Tannor, D.; Schindler, J.; Heller, E. J.; Zink, J. I. *J. Phys. Chem.* **1983**, *87*, 3017-3019.

(107) Satpati, A. K.; Kumbhakar, M.; Maity, D. K.; Pal, H. *Chem. Phys. Lett.* **2005**, *407*, 114-118.

Chapter 6

Summary and Conclusion

6.1 Summary and Conclusion

The primary goal of this work was to understand at a very fundamental level, the molecular properties that dictate chemical reactivity so as to quantify the important factors which influence the charge transfer excited-state dynamics. In this work, we have applied a variety of different techniques to study the properties and the mechanism of ground state and excited state intermolecular and intramolecular proton transfer and charge transfer in chromosphere assemblies. The salient points and conclusion are point form below.

In Chapter 3 investigations have been conducted into the structural dynamics of the excited state intramolecular proton transfer (ESIPT) and charge transfer (CT) behavior of 2,5-Bis(benzimidazoyl)-1,4-dihydroxybenzene (bbim) in DMSO and THF solvents. The effects of electrolytes on the ground and excited state of bbim have been investigated in Chapter 4. The important conclusions from Chapter 3 and 4 are as follows:

- The bbim molecule exhibits similar photophysical properties to those described for the same family of compounds that contain intramolecular hydrogen bonds within the molecule.
- The bbim molecule exhibits photodegradation in the presence of air.
- After excitation, the bbim molecule can undergo facile ESIPT from the hydroxyl group to the benzimidazole nitrogen to give the excited electronic state tautomer.
- The fluorescence quantum yield and lifetime of the excited state tautomer have been found to be solvent dependent.

- A double excited state intramolecular proton transfer takes place leading to charge migration from the deprotonated hydroquinone ring (donor) to the protonated benzimidazole (acceptor).
- We consider that the bbim molecule might be an example of a proton-coupled electron transfer. These reactions are the most important photoinduced phenomena yet studied.
- The bbim molecule displays highly sensitive and selective fluorescence towards fluoride, hydroxide, and acetate relative to halide anions other than fluoride. This is facilitated by the strong hydrogen bonding involving both the NH and the OH groups.
- Moreover, the dramatic change of the emission color from weak green to bright red illustrates the effect of anions on bbim.

In Chapter 5, investigations have been conducted into 3-aminocoumarin (3-AC) and its derivatives by steady state and transient absorption. The conclusions of Chapter 5 can be summarized as follows:

- The photophysical properties of 3-AC dye show a significant dependence on the position of the amino group in position 3, which is seen to display a sharp decrease in the fluorescence quantum yield and emission lifetime relative to 7-aminocoumarin. Thus the 3-AC dye is not technically important as a laser dye, in contrast to 7-aminocoumarin. With the amino group in position 7 one sees significant differences, where the fluorescence quantum yield of 7-aminocoumarin is very high compared to that seen for 3-amniocoumarin dyes.[2-4]

- The 3-AC exhibits a decrease in the emission intensity in highly polar solvents. This effect could be due to relaxation of the ICT state to a low lying TICT state, which opens a new radiationless pathway for deactivation of the excited state.
- Protonation of the amino and / or the carbonyl group of 3-AC by trifluoroacetic acid (TFA) leads to enhancement of the fluorescence quantum yield by reducing the radiationless channel.
- The ground and excited state acidity constants for the protonated 3-AC via TFA equilibria were evaluated with the help of the Förster cycle and global analysis methods using the fluorescence titration data. Both analyses produced consistent results.
- Substituents which either donate or withdraw electrons from the aromatic ring have a marked effect on the absorption and emission maxima. For example, with a nitro group in position 6, the molecule exhibits a dual emission. This was explained as being due to formation of a twisted intramolecular charge transfer state following rotation around the single bond of the amino group.
- From these observations, we conclude that 3-AC has a planar ICT structure in solvents of moderate polarities. However, in a highly polar solvent there is clear evidence of a solvent stabilized TICT state. This interpretation is consistent with what has been previously reported.[1-9]

6.2 References

(1) Barik, A. K., M.; Nath, S.; Pal, H. *Chem. Phys.* **2005**, *315*, 277-285.

(2) Kumbhakar, M.; Singh, P. K.; Satpati, A. K.; Nath, S.; Pal, H. *J. Phys. Chem. B* **2010**, *114*, 10057-10065.

(3) Samanta, A.; Fessenden, R. W. *J. Phys. Chem. A* **2000**, *104*, 8577-8582.

(4) Barik, A. N., S.; Pal, H. *J. Chem. Phys.* **2003**, *119*, 10202.

(5) Dahiya, P. K., M.; Kukherjee, T.; Pal, H. *Chem. Phys. Lett.* **2005**, *414*, 148-154.

(6) Kaholek, M. H., P. *J Photochem. Photobiol. A: Chem.* **1999**, *127*, 45-55.

(7) Raju, B. B. *J. Phys. Chem. A* **1997**, *101*, 981-987.

(8) Satpati, A. K. K., M.; Maity, D. K.; Pal, H. *Chem. Phys. Lett.* **2005**, *407*, 114-118.

(9) Senthilkumar, S. N., S.; Pal, H. *Photochem. Photobiol.* **2004**, *80*, 104-111.

Appendix

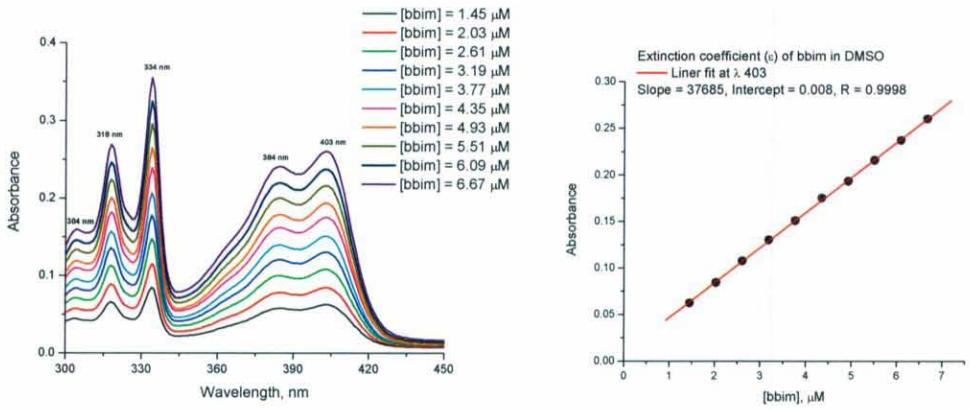

Figure A-1. (a) Visible spectra observed following concentration changes of bbim in DMSO at 298 (± 2) K, (b) Beer's Law Plot for bbim in DMSO at 403 nm.

Table A-1. Absorption, emission spectra maxima, and emission lifetime values for bbim in DMSO titrated with 40 equivalents of different anions at 298 (± 2) K.

Anions	λmax (Abs.) ε = (3.48x104 cm^{-1} M^{-1})	λmax (Em.)	τ ns	χ^2
F^-	319nm 332nm 383nm 403nm	520 635	6.3 7.2	1.0 1.1
OH^-	318nm 332nm 382nm 403nm	509 638	- 6.2	- 1.1

Ac^-	304nm 319nm 334nm 390nm 409nm	429 524 635	- - -	- - -
PF_6^-	Like bbim No Change	427 550	-	-
HSO_4^-	Like bbim No Change	427 550	-	-
Cl^-	Like bbim No Change	427 550	1.5 6.5	1.0 1.5
Br^-	Like bbim No Change	427 550	1.6 6.6	1.1 1.2
I^-	Like bbim No Change	427 550	1.6 6.5	1.3 1.1

Continued **Table A-1**. Absorption, emission spectra maxima, and emission lifetime values for bbim in DMSO titrated with 40 equivalents of different anions at 298 (± 2) K.

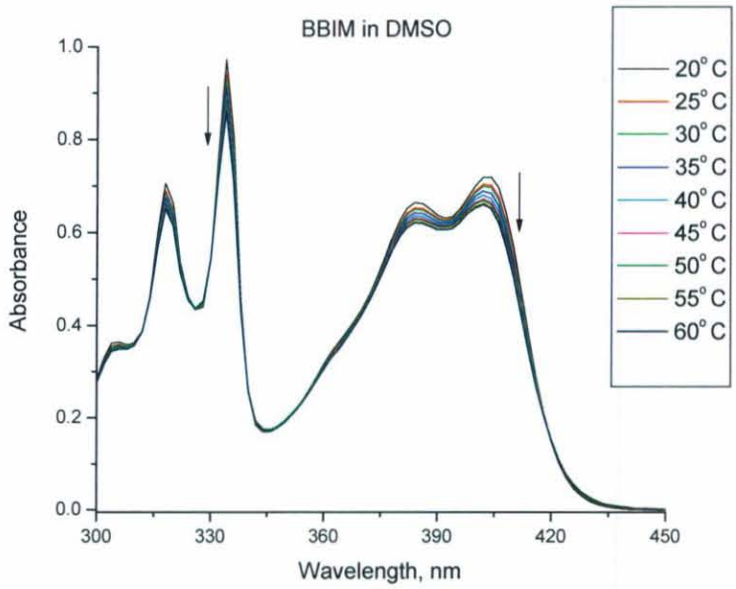

Figure A-2. Temperature dependence-band intensity decreases as temperature is increased (from 293 to 333 K gradually using 5 K temperature increments).

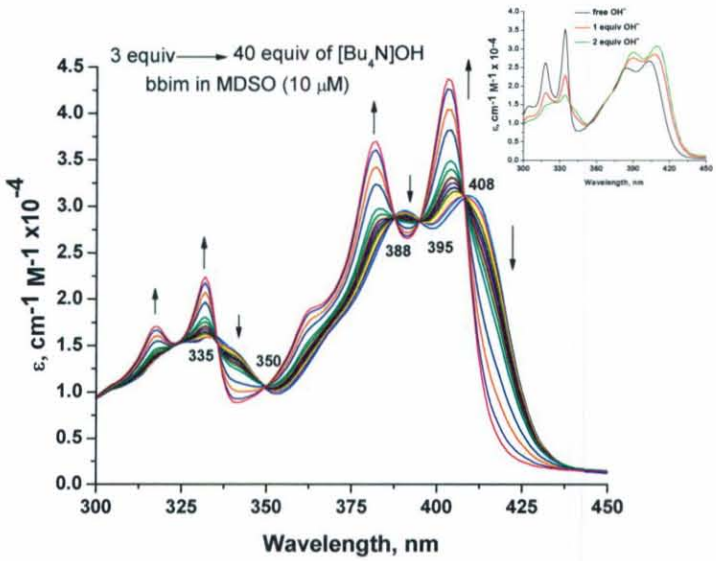

Figure A-3. Spectrophotometric titration of bbim in DMSO solution (10 x10^{-6} M) with [Bu4N]OH. Insert: First set of titration with one and two equiv of OH^- to bbim.

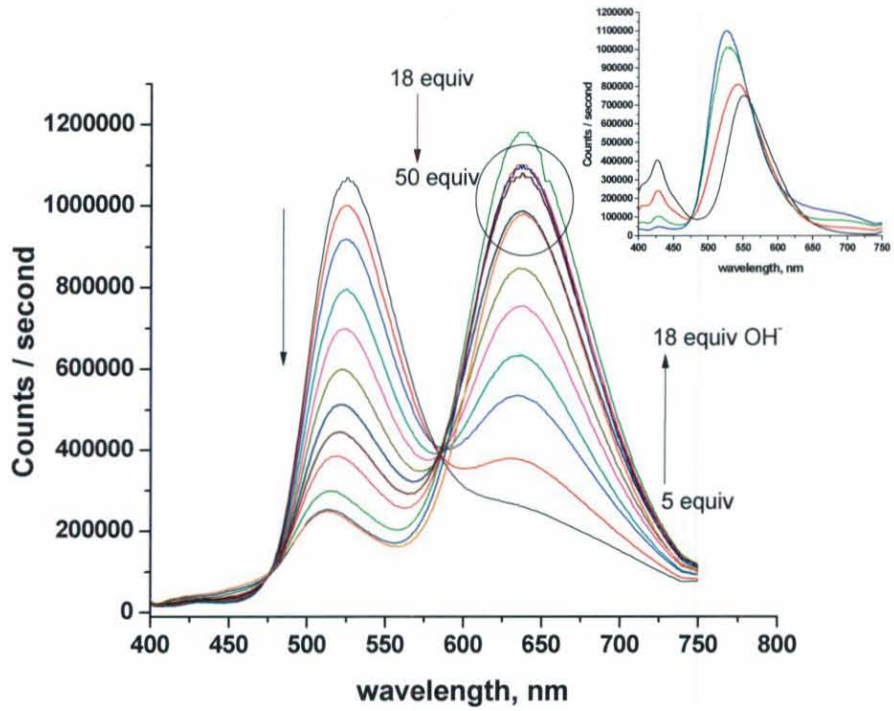

Figure A-4. Emission changes of bbim (DMSO, 10 μM) upon addition of [Bu4N]OH from 5 to 40 equivalents; insert: First set of titrations with 0, 1, 2, 3, 4 and 5 equivalents of OH^-.

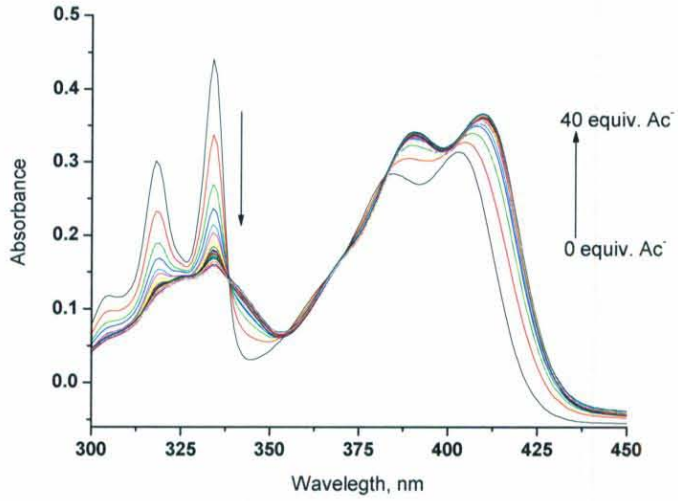

Figure A-5. Spectrophotometric titration of bbim in DMSO solution (10 x10^{-6} M) with Ac^- from zero to 40 equivalents.

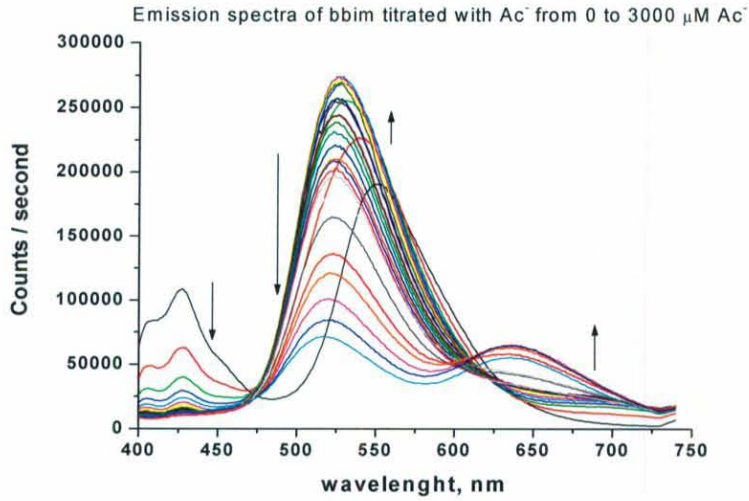

Figure A-6. Emission changes of bbim (DMSO, 10 μM) upon addition of [Bu4N]Ac from 0 to 40 equivalents Ac^- .

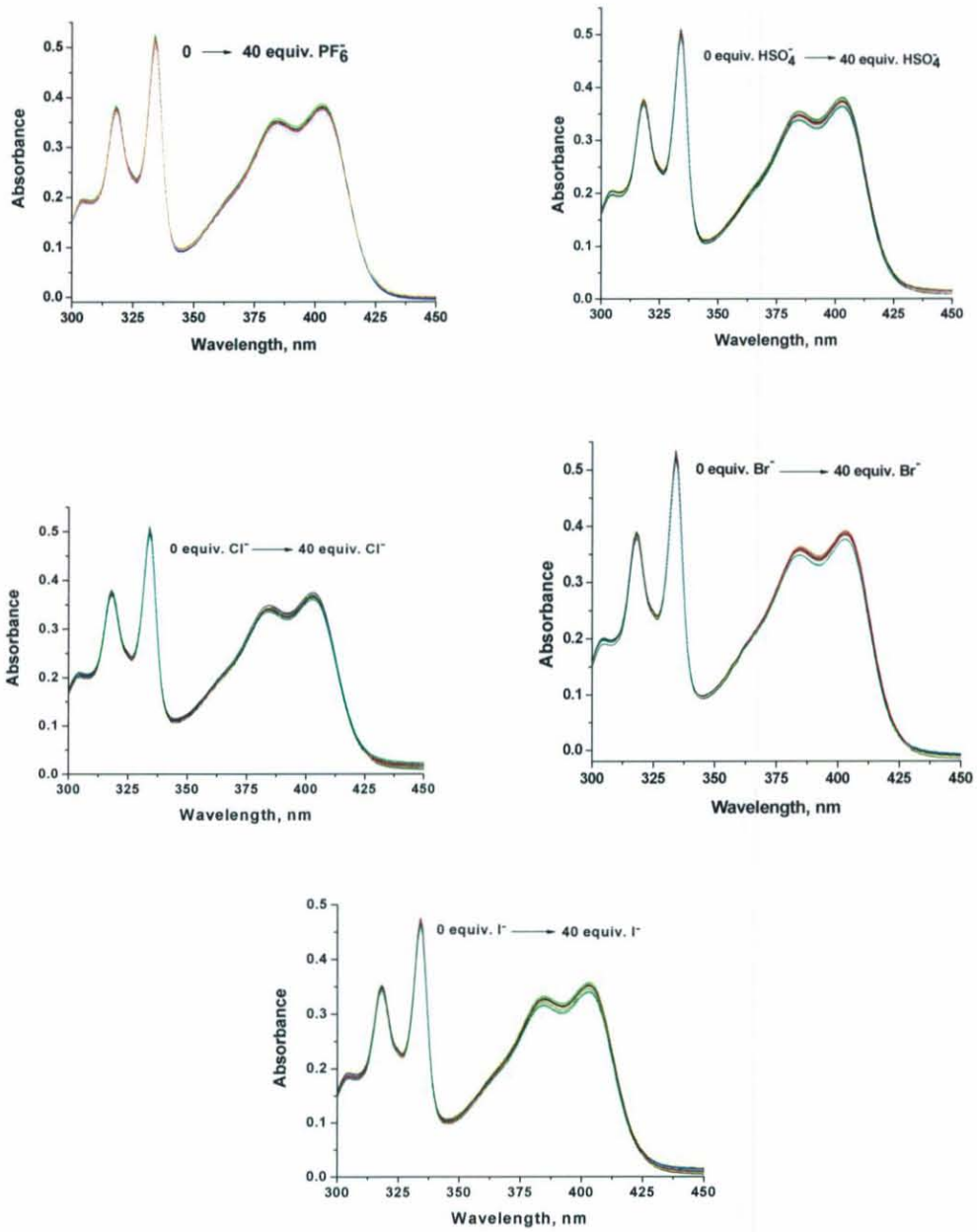

Figure A-7. Absorption spectrophotometric titration of bbim in DMSO (10 x10^{-6} M) solution with (a) PF_6^- from zero to 40 equivalents, (b) HSO_4^- from zero to 40 equivalents, (c) Cl^- from zero to 40 equivalents, (d) Br^- from zero to 40 equivalents, (e) I^- from zero to 40 equivalents.

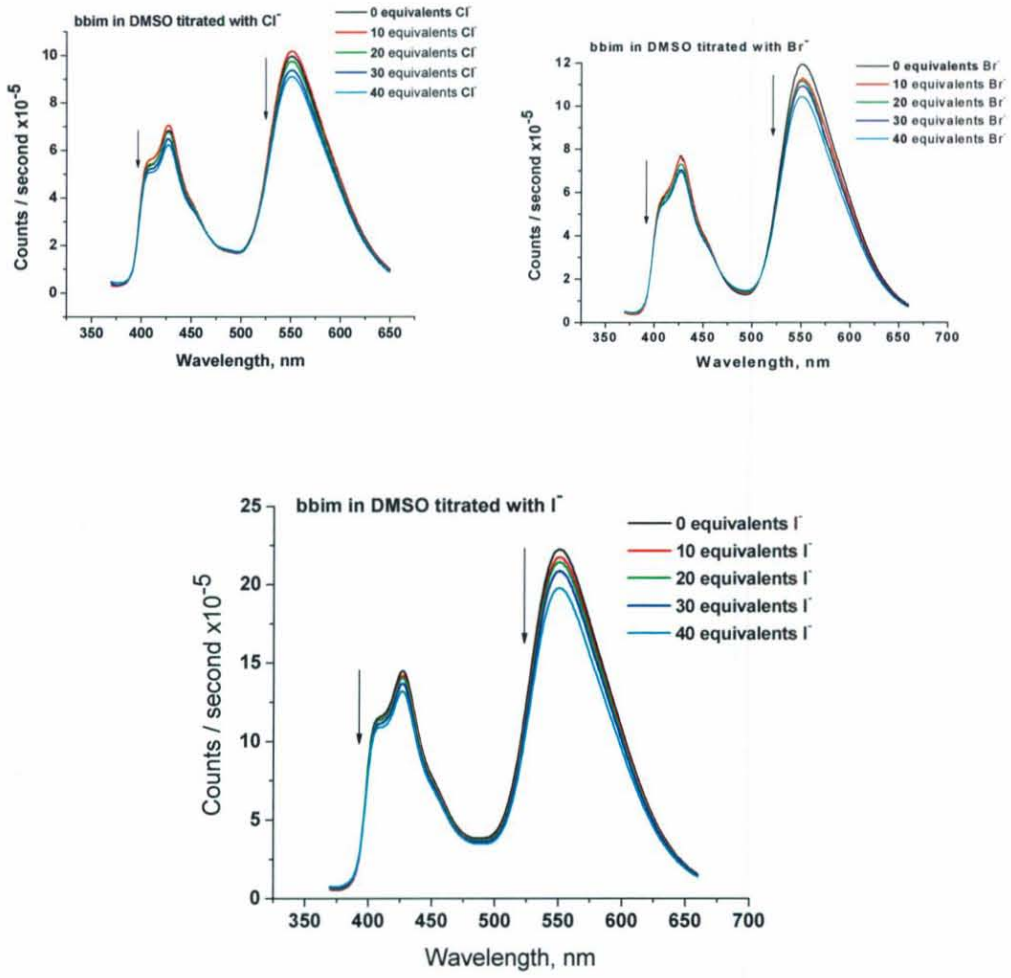

Figure A-8. Emission spectrophotometric titration of bbim in DMSO (10 x10^{-6} M) solution with (a) Cl^- from zero to 40 equivalents, (b) Br^- from zero to 40 equivalents, (c) I^- from zero to 40 equivalents.

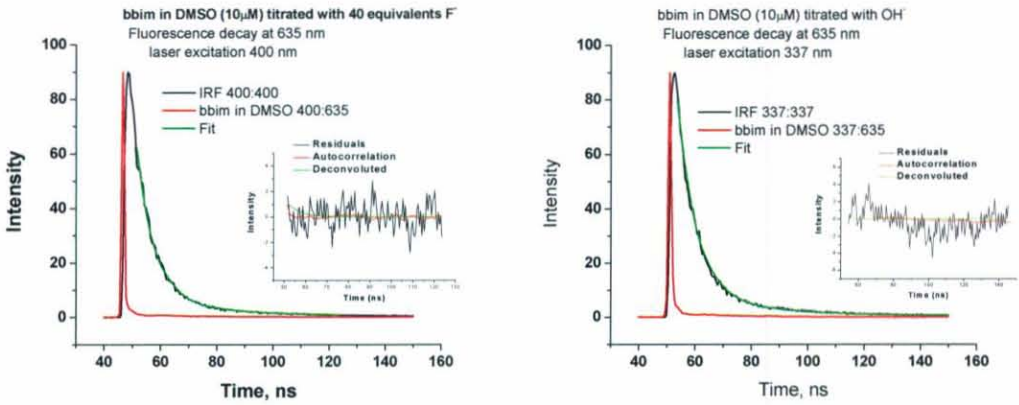

Figure A-9. Fluorescence decay of the new emission spectrum of bbim titrated with F^- at 635 nm, laser excitation at 400 nm. (Right) Fluorescence decay of the new emission spectrum of bbim titrated with OH^- at 635 nm, laser excitation at 337 nm.

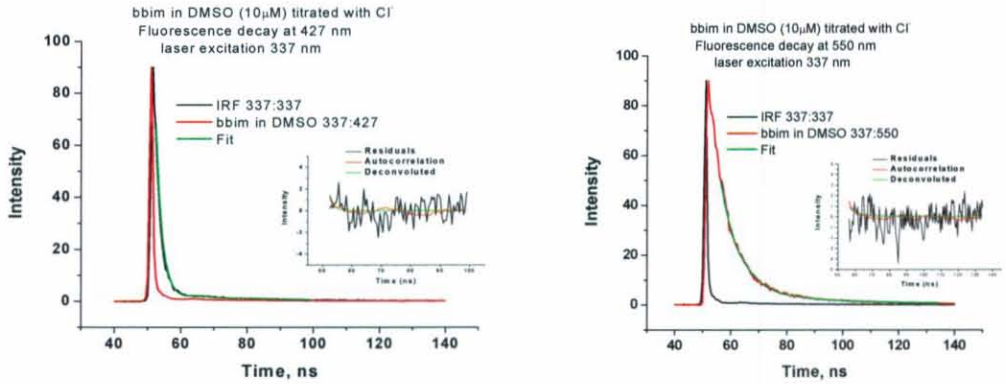

Figure A-10. (a) Fluorescence decay of the isomer bbim emission at 427 nm, titrated with 40 equivalents of Cl^-, (b) Fluorescence decay of the tautomer bbim emission at 550 nm, titrated with 40 equivalents of Cl^-.

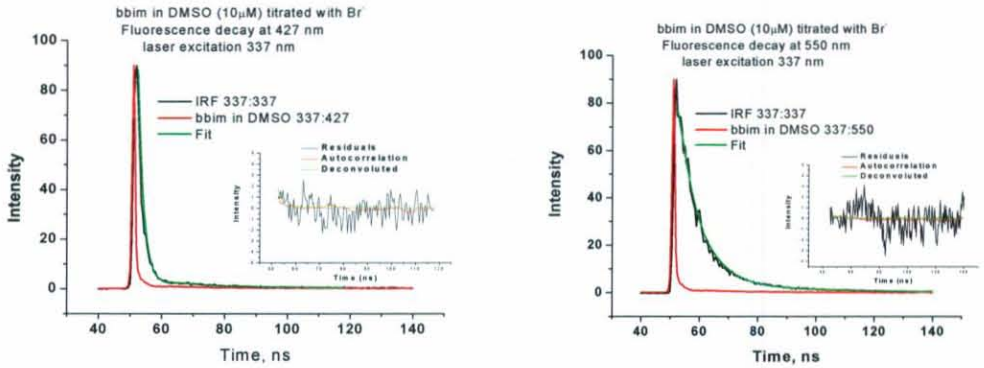

Figure A-11. (a) Fluorescence decay of the isomer bbim emission at 427 nm, titrated with 40 equivalents of Br^-, (b) Fluorescence decay of the tautomer bbim emission at 550 nm, titrated with 40 equivalents of Br^-.

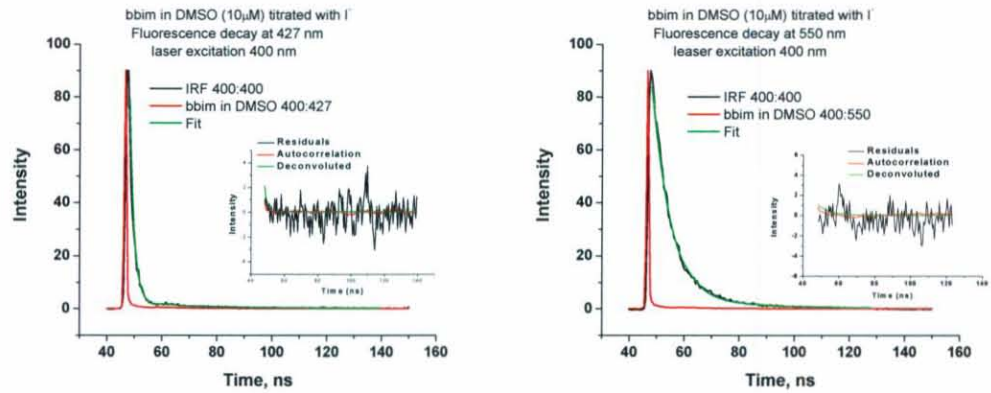

Figure A-12. (a) Fluorescence decay of the isomer bbim emission at 427 nm, titrated with 40 equivalents of I^-, (b) Fluorescence decay of the tautomer bbim emission at 550 nm, titrated with 40 equivalents of I^-.

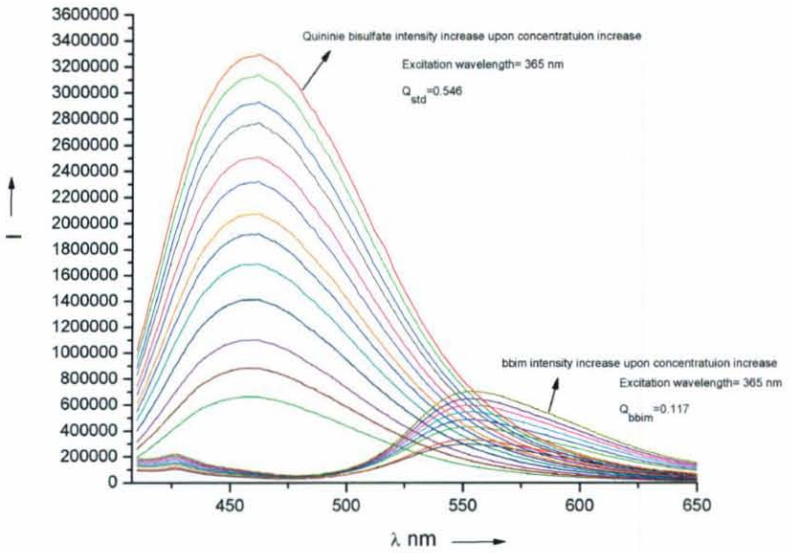

$$Q_{bbim} = Q_{std}\left(\frac{Grand_{bbim}}{Grand_{std}}\right) x \left(\frac{\eta^2_{bbim}}{\eta^2_{std}}\right)$$

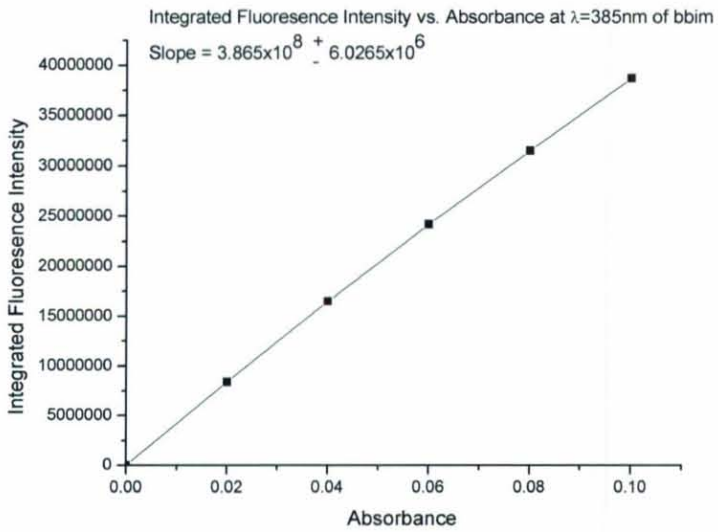

Figure A-13. (a) Emission data set obtained for different concentrations of bbim in DMSO solution (10 μM) and for standard solution (quinine bisulfate in 0.1 H2SO4), (b) linear plots of integrated fluorescence intensity versus absorbance at excitation wavelength 385 nm of bbim in DMSO 10 μM solution.

Table A-2. Correlation matrix from global analysis fitting for absorption spectra of bbim titrated with acetate ion.

[PROGRAM] Name = SPECFIT, Version = 3.0

[SPECIES]	[FIXED]	[PARAMETER]	[ERROR]
1 0 0	True	0.00000E+00 +/-	0.00000E+00
0 1 0	True	0.00000E+00 +/-	0.00000E+00
1 1 0	False	2.59103E+00 +/-	7.31262E-02
1 2 0	False	1.12825E+01 +/-	3.29986E-01
1 3 0	False	1.77754E+01 +/-	8.46218E-01
1 4 0	False	2.51695E+01 +/-	3.76104E-01

[CORRELATION]

1.000E+00	1.075E-01	-2.373E-01	2.893E-01
1.075E-01	1.000E+00	-8.681E-01	7.696E-01
-2.373E-01	-8.681E-01	1.000E+00	-9.537E-01
2.893E-01	7.696E-01	-9.537E-01	1.000E+00

Table A-3. Correlation matrix from global analysis fitting for absorption spectra of bbim titrated with fluoride ion.

[PROGRAM]

Name = SPECFIT, Version = 3.0

[SPECIES]	[FIXED]	[PARAMETER]	[ERROR]
1 0 0	True	0.00000E+00 +/-	0.00000E+00
0 1 0	True	0.00000E+00 +/-	0.00000E+00
1 1 0	False	2.22999E+00 +/-	1.01004E-01
1 2 0	False	4.67139E+00 +/-	1.31750E+00
1 3 0	False	7.56134E+00 +/-	1.14736E+00
1 4 0	False	1.11207E+01 +/-	8.16714E-01
1 5 0	False	1.43498E+01 +/-	6.57686E-01
1 6 0	False	1.75007E+01 +/-	6.98942E-01
1 7 0	False	1.95005E+01 +/-	8.85919E-01
1 8 0	False	2.35783E+01 +/-	1.14921E+00

[CORRELATION]

1.000E+00	-9.974E-01	-9.568E-01	-6.673E-01	3.017E-01	4.155E-01	-1.471E-01	-4.483E-01
-9.974E-01	1.000E+00	9.576E-01	6.658E-01	-3.012E-01	-4.132E-01	1.445E-01	4.410E-01
-9.568E-01	9.576E-01	1.000E+00	8.336E-01	-1.394E-01	-4.297E-01	3.717E-02	3.448E-01
-6.673E-01	6.658E-01	8.336E-01	1.000E+00	3.807E-01	-2.102E-01	-1.707E-01	4.272E-03
3.017E-01	-3.012E-01	-1.394E-01	3.807E-01	1.000E+00	6.316E-01	-5.444E-02	-3.462E-01
4.155E-01	-4.132E-01	-4.297E-01	-2.102E-01	6.316E-01	1.000E+00	6.322E-01	2.473E-01
-1.471E-01	1.445E-01	3.717E-02	-1.707E-01	-5.444E-02	6.322E-01	1.000E+00	9.004E-01
-4.483E-01	4.410E-01	3.448E-01	4.272E-03	-3.462E-01	2.473E-01	9.004E-01	1.000E+00

Table A-4. Correlation matrix from global analysis fitting for absorption spectra of bbim titrated with hydroxide ion

[PROGRAM] Name = SPECFIT, Version = 3.0

[SPECIES]	[FIXED]	[PARAMETER]	[ERROR]
1 0 0	True	0.00000E+00 +/-	0.00000E+00
0 1 0	True	0.00000E+00 +/-	0.00000E+00
1 1 0	False	2.56456E+00 +/-	1.07947E-01
1 2 0	False	6.39541E+00 +/-	1.27586E+00
1 3 0	False	1.02727E+01 +/-	1.14288E+00
1 4 0	False	1.50665E+01 +/-	8.47209E-01
1 5 0	False	1.80917E+01 +/-	5.29284E-01
1 6 0	False	2.17680E+01 +/-	4.22901E-01
1 7 0	False	2.60325E+01 +/-	6.73512E-01
1 8 0	False	2.89358E+01 +/-	1.00719E+00

[CORRELATION]

1.000E+00	-9.977E-01	-9.719E-01	-8.733E-01	-4.707E-01	-2.989E-01	-7.209E-01	-7.491E-01
-9.977E-01	1.000E+00	9.696E-01	8.679E-01	4.697E-01	3.043E-01	7.127E-01	7.348E-01
-9.719E-01	9.696E-01	1.000E+00	9.542E-01	5.806E-01	3.286E-01	7.238E-01	7.693E-01
-8.733E-01	8.679E-01	9.542E-01	1.000E+00	7.715E-01	4.363E-01	6.365E-01	6.713E-01
-4.707E-01	4.697E-01	5.806E-01	7.715E-01	1.000E+00	7.536E-01	3.185E-01	2.174E-01
-2.989E-01	3.043E-01	3.286E-01	4.363E-01	7.536E-01	1.000E+00	5.163E-01	2.600E-01
-7.209E-01	7.127E-01	7.238E-01	6.365E-01	3.185E-01	5.163E-01	1.000E+00	9.485E-01
-7.491E-01	7.348E-01	7.693E-01	6.713E-01	2.174E-01	2.600E-01	9.485E-01	1.000E+00

Table A-5. Correlation matrix from global analysis fitting for emission spectra of bbim titrated with fluoride ion.

[PROGRAM] Name = SPECFIT, Version = 3.0

[SPECIES]	[FIXED]	[PARAMETER]	[ERROR]
1 0 0	True	0.00000E+00 +/-	0.00000E+00
0 1 0	True	0.00000E+00 +/-	0.00000E+00
0 0 1	True	0.00000E+00 +/-	0.00000E+00
1 1 0	False	3.66108E+00 +/-	1.83650E-02
1 2 0	False	6.96773E+00 +/-	6.04631E-01
1 3 0	False	9.47320E+00 +/-	5.25986E-01
1 4 0	False	1.28752E+01 +/-	3.72809E-01
1 5 0	False	1.71726E+01 +/-	3.30310E-01
1 6 0	False	2.23639E+01 +/-	3.24048E-01
1 7 0	False	2.59952E+01 +/-	3.21389E-01
1 8 0	False	3.09817E+01 +/-	5.07877E-01

[CORRELATION]

1.000E+00	-9.996E-01	-9.285E-01	-5.766E-01	8.563E-02	2.277E-01	-2.125E-01	-5.424E-01
-9.996E-01	1.000E+00	9.294E-01	5.773E-01	-8.780E-02	-2.320E-01	2.105E-01	5.460E-01
-9.285E-01	9.294E-01	1.000E+00	8.071E-01	1.297E-01	-1.345E-01	2.020E-01	5.216E-01
-5.766E-01	5.773E-01	8.071E-01	1.000E+00	6.558E-01	3.217E-01	2.574E-01	2.356E-01
8.563E-02	-8.780E-02	1.297E-01	6.558E-01	1.000E+00	8.761E-01	3.861E-01	-1.949E-01
2.277E-01	-2.320E-01	-1.345E-01	3.217E-01	8.761E-01	1.000E+00	6.434E-01	-8.107E-02
-2.125E-01	2.105E-01	2.020E-01	2.574E-01	3.861E-01	6.434E-01	1.000E+00	6.855E-01
-5.424E-01	5.460E-01	5.216E-01	2.356E-01	-1.949E-01	-8.107E-02	6.855E-01	1.000E+00

Table A-6. Correlation matrix from global analysis fitting for emission spectra of bbim titrated with hydroxide ion.

[PROGRAM] Name = SPECFIT, Version = 3.0

[SPECIES]	[FIXED]	[PARAMETER]		[ERROR]
1 0 0	True	0.00000E+00	+/-	0.00000E+00
0 1 0	True	0.00000E+00	+/-	0.00000E+00
1 1 0	False	1.00134E+01	+/-	9.32702E-01
1 2 0	False	1.23028E+01	+/-	2.47098E+00
1 3 0	False	1.50406E+01	+/-	2.63658E+00
1 4 0	False	1.82062E+01	+/-	2.75024E+00
1 5 0	False	2.24755E+01	+/-	2.86887E+00
1 6 0	False	2.77199E+01	+/-	2.98217E+00

[CORRELATION]

1.000E+00	-9.999E-01	-9.066E-01	-6.672E-01	-4.081E-01	-2.109E-01
-9.999E-01	1.000E+00	9.075E-01	6.693E-01	4.113E-01	2.150E-01
-9.066E-01	9.075E-01	1.000E+00	9.139E-01	7.344E-01	5.630E-01
-6.672E-01	6.693E-01	9.139E-01	1.000E+00	9.448E-01	8.424E-01
-4.081E-01	4.113E-01	7.344E-01	9.448E-01	1.000E+00	9.718E-01
-2.109E-01	2.150E-01	5.630E-01	8.424E-01	9.718E-01	1.000E+00

Table A-7. Correlation matrix from global analysis fitting for emission spectra of bbim titrated with acetate ion.

[PROGRAM] Name = SPECFIT, Version = 3.0

[SPECIES]	[FIXED]	[PARAMETER]		[ERROR]
1 0 0	True	0.00000E+00	+/-	0.00000E+00
0 1 0	True	0.00000E+00	+/-	0.00000E+00
1 1 0	False	2.36520E+00	+/-	2.46340E-01
1 2 0	False	1.14010E+01	+/-	6.14215E-01
1 3 0	False	1.96800E+01	+/-	3.12898E-01
1 4 0	False	2.45320E+01	+/-	1.87033E+00

[CORRELATION]

1.000E+00	-1.867E-01	1.538E-01	-3.991E-01
-1.867E-01	1.000E+00	-7.751E-01	4.188E-01
1.538E-01	-7.751E-01	1.000E+00	-3.240E-01
-3.991E-01	4.188E-01	-3.240E-01	1.000E+00